THE UNIVERSITY of ADELAIDE

Thorium substitution in monazite: case studies and forward modelling

Megan A. Williams

Department of Earth Sciences
School of Physical Sciences
University of Adelaide

This Thesis is submitted in fullfillment of the
requirements for the degree of Doctor of Philosophy

December 2019

Table of Contents

Abstract

The accessory mineral monazite [(REE, Th, U, Y, Ca)(P, Si)O_4] is the major host of the heat producing element Th in the high temperature (>500 °C) continental crust, hosted predominantly in peraluminous rock types. It is also an important geochronometer for high temperature crustal processes. As monazite forms, it often preserves multiple chemical and isotopic zones which can be used to infer the timing and conditions of formation. These zones can be preserved through multiple cycles of metamorphism and partial melting. While some aspects of monazite chemistry (e.g. LREE and Y) are well understood, studies which have focussed on Th in particular are few. This has resulted in a lack of clarity on the partitioning of Th into monazite with progressive metamorphism as well as a limited understanding of the solid-solution behaviour of the two Th-bearing endmembers of monazite, cheralite and huttonite.

To expand the utility of this mineral, this thesis first presents two detailed and comprehensive case studies of chemical zoning in monazite from compositionally homogeneous suites of progressively metamorphosed metasediments, Mt Stafford, central Australia and the Ivrea–Verbano Zone, Italy. These studies also present the chemistry of associated minerals, modal abundance of accessory minerals, bulk rock chemistry and mineralogy. These case studies have a particular focus on Th, and compare trends observed in monazite from progressively metamorphosed terranes to bulk rock Th and mineralogy trends. These studies show that monazite in granulite-facies and UHT rocks is not depleted in Th with respect to amphibolite-facies monazite. In all samples, cheralite is the dominant Th-endmember of monazite. Monazite modal proportion is also observed to increase with metamorphic grade in both terranes. The case studies are then integrated with a global dataset of over 5000 monazite chemical analyses spaning a wide range of pressure and temperature conditions. This analysis shows that Th in monazite shows systematic behaviour with temperature with limited effect from pressure and that the trends observed in the case studies can be considered universal.

This new understanding of Th partitioning in monazite is used to build and calibrate a predictive and readily adaptable thermodynamic framework for modelling the chemistry and abundance of monazite and associated minerals. This framework is tested on representative pelite compositions to explore the bulk compositional and pressure–temperature controls on monazite stability and composition. Closed- and open-system melting scenarios are also explored. Finally, the thermodynamic framework is used to calculate models for one sample from each case study to provide the proof-of-concept that these models adequately predict the complexity of monazite compositions in natural systems and to provide new insights into the formation of this mineral.

Declaration

I certify that this work contains no material which has been accepted for the award of any other degree or diploma in my name, in any university or other tertiary institution and, to the best of my knowledge and belief, contains no material previously published or written by another person, except where due reference has been made in the text. In addition, I certify that no part of this work will, in the future, be used in a submission in my name, for any other degree or diploma in any university or other tertiary institution without the prior approval of the University of Adelaide and where applicable, any partner institution responsible for the joint-award of this degree.

The author acknowledge that copyright of published works contained within this thesis resides with the copyright holder(s) of those works.

I also give permission for the digital version of my thesis to be made available on the web, via the University's digital research repository, the Library Search and also through web search engines, unless permission has been granted by the University to restrict access for a period of time.

I acknowledge the support I have received for my research through the provision of an Australian Government Research Training Program Scholarship.

MEGAN WILLIAMS DATE

Publications arising from this thesis

Journal articles

Williams, M. A., Kelsey, D. E., Baggs, T., Hand, M., & Alessio, K. L. (2018). Thorium distribution in the crust: Outcrop and grain-scale perspectives. *Lithos*, **320**, 222-235.

Williams, M. A., Kelsey, D. E., & Rubatto, D. (submitted and reviewed). Thorium zoning in monazite: a case study from the Ivrea–Verbano Zone, NW Italy. *Journal of Metamorphic Geology.*

Williams, M. A., Kelsey, D. E., Hand, M., Raimondo, T., Morrissey, L. J., Tucker, N. M., & Dutch, R. A. (2018). Further evidence for two metamorphic events in the Mawson Continent. *Antarctic Science,* **30**(1), 44-65.

Alessio, K. L., Hand, M., Kelsey, D. E., **Williams, M. A.,** Morrissey, L. J., & Barovich, K. (2018). Conservation of deep crustal heat production. *Geology*, **46**(4), 335-338.

Conference abstracts

Williams, M. A., Kelsey, D. E., Hand, M., Rubatto, D., Alessio, K. L., 2018. Keeping the deep crust hot: the role of monazite. *Australian Geoscience Council Convention 2018*, Adelaide, Australia.

Williams, M. A., Kelsey, D. E., Hand, M., Rubatto, D., Spear, F. S., 2018, Where's the heat? How a tiny mineral keeps the deep crust hot. *GSA Earth Science Student Symposium of South Australia*, 2018, Adelaide, Australia.

Williams, M. A., Kelsey, D. E., Hand, M., Rubatto, D., Bockmann, K. L., 2017. Th–U distribution in the crust: outcrop and grain scale approaches. *GSA Earth Science Student Symposium of South Australia, 2017*, Adelaide, Australia.

Williams, M. A., Kelsey, D. E., Rubatto, D., Hand, M., Bockmann, K., 2017, Thorium distribution in the crust: outcrop and grain scale approaches. *Goldschmidt 2017*, Paris, France.

Williams, Megan A., Hand M. & Kelsey D. E. 2016. Are spatially variable records of overprinting metamorphism related to inherited zones of retrogression and structural weakness? Unravelling polymetamorphism in the Terre Adélie Craton (east Antarctica) and formerly contiguous Gawler Craton (South Australia). *Australian Earth Sciences Convention 2016*, Adelaide, Australia.

Acknowledgements

Firstly, thank you to Dave. You have been an outstanding supervisor. I thougroughly appreciate you for supporting and encouraging me, always providing thoughtful critque of my work and giving me the licence to drive this project. To Martin, thanks for giving me your all in the early stages of this process. Your enthusiasm for new ideas is infectious and was a great motivator for me to question and to be open minded about metamorphic processes. I gratefully appreciate Stijn for stepping up near the end of this process and giving me the support I needed to submit. To my co-authors, particularly Daniela and Frank, your perspectives have been invaluable in my development as a scientist. You have each made contributions without which this thesis would be both lacking and incomplete and for those contributions I am considerably grateful. Also to all of the reviewers of my work – thank you. Your comments, criticisms and suggestions have made me both a better scientist and a better communicator of science.

I would like to thank the many people who were part of the field work for these projects: Kiara and Martin at Mt Stafford; Daniela, Mahyra, Arnaud in the Ivrea Zone; Laura, Roberto, Tato, Alfonso and Pablo in the Sierra de Quilmes. Thanks very much to Daniela, Tato and Alfonso for assistance with getting samples back to Aus – without your help and those rocks there wouldn't be much in this thesis. Thanks to Kiara and Alec for assisting me with cutting and processing my samples – there were a lot and you both saved me weeks of time. Thanks to Tom for assisting me with the collection and processing of data for the Mt Stafford and Ivrea samples. Thanks are due to Ben, Sarah, Ken and Aoife at Adelaide Microscopy for the many, many hours contributed to assisting me with the collection of data. Thanks for your wisdom, patience and kindness. It made the long days of analytical work enjoyable and profitable. My thanks go to Kiara, Frank, Joe, Chris, Frederico and Philippe for the provision of complete monazite datasets and to the many respondents to my requests for published data.

I am eternally grateful for the funding that I have received to complete this work and to present the findings at various conferences. So to the Department of Earth Sciences (UofA) (Alderman-Kleeman Travel Scholarship), GSA South Australian division (Divisional Scholarship for AESC), ARC (DP grant DP160101006 to DEK) and Australian government (AGRTPS), thank you.

I am greatful to the various people I have shared offices with over the years – Kam, Drew, Richard, Kiara, Kieran and Naomi – thank for putting up with me and sharing the good times and bad. Thanks to Rachel, Haidee, Briony, Claire, Pavan and the rest of the morning tea regulars. I have really enjoyed getting to know you all and having friendly faces for a chat and a cup of tea on a Monday. Thanks for sticking with it. Thanks also to Alec, Kam, Jack and Gilby for chatting science with me. To mum and dad and the rest of my extended family and family by choice – it's been a long journey. Thanks for sticking with me to the end. I know you didn't necessarily get it, but I know you're proud anyway. And finally to Alec. Thanks for supporting me. For pushing me when I didn't want to move, loving an encouraging me when I was feeling down (and when I was up!), not letting me be too proud to ask for help and generally coming along for the ride. I couldn't have done this without you and I'm a very different person to the one you first met in the basement. Thanks for not letting me believe my own nonsense.

Chapter 1

Significance and aims of this thesis

Monazite ([REE,Y,Th,U,Ca] [Si,P]O_4) is a common accessory mineral in aluminous pelitic and psammitic metasedimentary and peraluminous granitic rock types. Monazite is an important geochronometer for high temperature (>500 °C) processes and is a major host of the heat producing element thorium in the deep crust. For these reasons, it is crucial to have a good understanding of how thorium partitions into monazite at different pressures and temperatures as well as what controls the retention of thorium in monazite and in the deeper crust. This requires an understanding of the behaviour (stability and composition) of monazite as a function of pressure, temperature and rock composition (*P–T–X*) in the context of the *P–T–X* behaviour of major silicate minerals and other accessory minerals. However, uncertainty remains about when monazite grows in relation to the bulk silicate mineral assemblage of rocks. There are various ways in which monazite can be linked to the growth and consumption of major minerals, some of which are more reliable than others (e.g. microstructural location vs idealised 'equilibrium' partitioning coefficients; see Engi, 2017). In addition, monazite commonly preserves several chemical and isotopic zones (see Taylor, Kirkland, & Clark, 2016; Williams, Jercinovic, & Hetherington, 2007) which complicates the establishment of links to the major silicate assemblages, but also provides a potential solution, as investigated in this thesis. If such chemical and isotopic zones can be reconciled and correlated with pressure, temperature and bulk composition (*P–T–X*), monazite could potentially become a powerful tool for understanding in detail the pressure and temperature conditions of the growth of metamorphic assemblages and the controls on retention of heat production in the deep crust.

In order to develop a comprehensive framework of understanding of the behaviour of monazite chemistry with progressive metamorphism, the information required is the composition of monazite and coexisting minerals (e.g. apatite, allanite, xenotime, garnet, feldspar etc.) at well constrained pressure and temperature conditions, as well as full whole rock geochemistry (major and trace elements). Such studies should ideally be conducted in locations where protolith (bulk rock chemistry) is consistent at all metamorphic grades to limit the effect of bulk composition on the apparent effects of progressive metamorphism. However, few studies exist that have presented all of this data, therefore making the development of a detailed understanding of monazite growth behaviour challenging. Although the REE composition of monazite is commonly used to infer the *P–T–X* characteristics and coexisting silicate minerals during monazite formation, comprehensive studies with a specific focus on Th have not been conducted, mostly as such studies require significant investment and appropriate natural laboratories are rare. Recent works have partially addressed these deficiencies by providing detailed studies including much of the necessary information (Skrzypek, Bosse, Kawakami, Martelat, & Štípská, 2017; Skrzypek et al., 2018) and highly detailed natural datasets are becoming more common with the rise of large electronic appendices to published papers (e.g. Berry, Chmielowski, Steele, & Meffre, 2007; Foster, Kinny, Vance, Prince, & Harris, 2000; Laurent, Duchene, Bingen, Bosse, & Seydoux-Guillaume, 2018; Martins, Vlach, & de Assis Janasi, 2009; Schulz, 2017; Skrzypek et al., 2017; Yakymchuk et al., 2015). In particular, studies with a specific focus on Th-in-monazite remain rare, despite the acknowledgement that Th is critical to the stability of monazite. Previous studies have reported monazite chemical trends, such as REE-rich, Th-poor monazite observed at low temperatures (e.g. Rasmussen & Muhling, 2007) trending to more Th-rich monazite at higher temperatures (e.g. Bea & Montero, 1999; Foster et al., 2000; Overstreet, 1967). However, studies focussing on Th in particular report seemingly contradictory results (e.g. Th-rich rims surrounding Th-poor cores and visa-versa; e.g. Kohn & Malloy, 2004; Skrzypek et al., 2018), sometimes even within the same samples (e.g. Franz, Andrehs, & Rhede, 1996), and give qualitative statements about monazite composition or thorium solid-solution which cannot be interrogated with the available quantitative data (e.g. Allaz, Selleck, Williams, & Jercinovic, 2013; Bial, Buettner, Schenk, & Appel, 2015; Bial, Büttner, v& Appel, 2016; Finger, Broska, Roberts, & Schermaier, 1998; Franz et al., 1996). This lack of clarity about monazite composition as a function of *P–T–X* is commonly the result of small sample sets and use of samples that vary – sometimes significantly – in their major and trace element chemistry as a function of

metamorphic grade. Indeed, the issue of changing bulk rock composition in studies investigating monazite behaviour adds one more layer of complexity to resolving monazite behaviour. This thesis aims to improve the clarity on this issue.

Thermodynamic phase equilibria modelling is currently one of the most widely used approaches for investigating metamorphic rocks and processes. One of the outstanding challenges in this approach is to (more) directly link the modelled major silicate mineral assemblages to high temperature geochronology, which is an important step in understanding the significance of age data for metamorphic minerals. This is because the addition of accessory minerals (especially monazite) used to date high temperature processes to thermodynamic datasets requires the expansion of such datasets to include (many) elements that are only present in trace amounts in most common rock-forming silicate minerals (e.g. Zr, P, REE, Th, U). However, some such attempts have been done, with zircon and other Zr-bearing phase end-members added to the THERMOCALC dataset (Kelsey & Powell, 2011) and Ce, Y and P added to the GIBBS dataset (Spear, 2010; Spear & Pyle, 2010). However, in regard to monazite, Ce and Y do not adequately represent the full complexity of real monazite solid solution compositions, and so for this reason further work is required to incorporate other REE elements and also, especially, Th, to more thoroughly and adequately explore and understand monazite behaviour in metamorphic systems. For the most part, studies investigating the behaviour of zircon and monazite in the context of metamorphic rock evolution (*P–T–X*) have been done by performing calculations external to the thermodynamic modelling software, utilising experimentally-derived solubility equations (Harrison & Watson, 1984; Stepanov, Hermann, Rubatto, & Rapp, 2012; Watson & Harrison, 1983; Wolf & London, 1994) for the accessory minerals (e.g. Kelsey, Clark, & Hand, 2008; Yakymchuk, 2017; Yakymchuk & Brown, 2014, 2019; Yakymchuk, Kirkland, & Clark, 2018). The Yakymchuk & Brown (2019) study included Th and U in the calculations on monazite and zircon (and apatite) behaviour and provided great insight into how accessory mineral behaviour controls Th and U (heat production) in the residual part of partially melted rocks in the crust. However, this study used solubility expressions to derive the accessory phase behaviour, whereas in this thesis the alternative approach of developing an equilibrium thermodynamic approach for modelling accessory phase behaviour is taken.

The overall aim of this thesis is to present the first comprehensive, quantitative and predictive equilibrium thermodynamic tool-set that systematically links Th concentrations to the primary mineralogical, melt and rock composition controls on the stability of Th-bearing phases, specifically monazite, thus building on the framework of the seminal Spear (2010) and Spear and Pyle (2010) studies. In order to achieve this, it is first necessary to establish that such a pursuit is warranted. Therefore, this study also collates and adds to the current global dataset of monazite chemistry with individual analyses tied to metamorphic grade and bulk rock chemistry of samples. This is firstly achieved through two detailed case studies of the response of monazite to progressive metamorphism within a whole-rock context, with a particular focus on the trends of Th and the two Th-bearing monazite end-members, cheralite ($Ca_{0.5}Th_{0.5}PO_4$) and huttonite ($ThSiO_4$), with progressive metamorphism. These case studies contribute detailed and comprehensive datasets of monazite chemistry, the chemistry of associated minerals, monazite geochronology, modal abundance of accessory minerals, bulk rock composition and mineralogy. Secondly, it compares these detailed and well constrained records to other available monazite data from the published literature to understand in a global context the response of the composition of monazite to progressive metamorphism. Finally, these data, obtained from natural samples, are used to calibrate and test a quantitative, predictive thermodynamic framework for monazite and associated phases within a chemical system that adequately reflects the complexity of natural systems.

The specific aims of this thesis are to:

1. *Comprehensively characterise the natural record of thorium in monazite and rocks in different tectonic settings in detail to understand the interplay between the behaviour of thorium in monazite and in the bulk rock as a function of metamorphism, partial melting and melt loss (Chapters 2 and 3);*

2. *Establish the global trends in monazite chemistry with pressure and temperature, including understanding the solid-solution chemistry changes and the relative proportions of the two Th-bearing endmembers of monazite (Chapter 4);*

3. *Create a readily adaptable thermodynamic calculation framework that explicitly incorporates the major elemental components of monazite (Ce, La, Nd, Th, Y, Ca, Si and P) and systematically predicts the pressure, temperature and rock composition (P–T–X) controls on the stability of Th-bearing phases including monazite (Chapter 5);*

4. *Apply the thermodynamic model to determine P–T–X (metamorphic reaction) controls on monazite chemistry and stability in representative and natural bulk compositions (Chapter 5);*

5. *Apply the thermodynamic model to determine P–T–X controls on retention versus extraction of Th from the lower crust during metamorphism involving crustal melting (Chapter 5).*

CHAPTER OUTLINES

Chapter 1 *Introduction and thesis aims*

Chapter 2 *Thorium distribution in the crust: Outcrop and grain-scale perspectives*

Chapter 2 provides the first of two case studies, examining the distribution of Th at the outcrop scale (centimeter to metre) at Mt Stafford, central Australia, and comparing this with changes to Th-in-monazite at the sub-grain scale (microns to millimetres). Mt Stafford is a well characterised crustal section with a high metamorphic field gradient. These two datasets are used to show that whole rock thorium is preserved to the highest grades of metamorphism at Mt Stafford (granulite facies) and this is facilitated by Th sequestered by monazite which remains stable. This chapter describes and discusses the interplay between observations at these dramatically different scales and presents an argument for the potential of retaining high-heat producing material in the deep crust.

Chapter 3 *Thorium zoning in monazite: a case study from the Ivrea–Verbano Zone, NW Italy*

Chapter 3 builds on the previous chapter by presenting a second case study, from the Ivrea–Verbano Zone in Italy. The Ivrea–Verbano Zone has a distinctly different tectonic and thermal history to Mt Stafford, as well as more calcic metasedimentary rock compositions, and therefore presents an opportunity to extend the discussion from chapter 2 into other tectonic settings and other metasedimentary rock compositions. This second case study presents a similar dataset to that presented in chapter 2, investigating both outcrop and micro scales, and compares the interplay of these observations with those in chapter 2. The Ivrea–Verbano Zone reaches higher temperatures and pressures than Mt Stafford, resulting in the near complete dissolution of monazite at the highest grades in the former. The results obtained from this chapter enable discussion of the chemical composition of monazite at or near its stability limit, and cover a crucial interval of interaction between monazite and silicate melt that has rarely been documented in nature.

Chapter 4 *Temperature dependence of thorium substitution mechanisms in monazite*

Chapter 4 builds on from the previous two chapters by integrating the monazite data in this thesis with published data from metamorphosed metasedimentary rocks from around the world. This large dataset further illustrates the finding from chapters 2 and 3 – that Th-in-monazite is controlled primarily by temperature and secondarily by whole rock composition – but moves this finding from the site-specific analysis of the first two chapters and into a more in-depth discussion of the mechanisms behind these observations. In particular, this chapter has a focus on the relative proportions of the two thorium-bearing mineral endmembers of monazite as a function of metamorphic grade. This focus allows a preliminary analysis of the extent to which monazite displays thermodynamic equilibrium compositions, and hence the appropriateness of interrogating monazite with calculated equilibrium thermodynamics.

Chapter 5 *Theoretical modelling of monazite growth in a Th-bearing system*

Chapter 5 builds on the previous chapters by presenting calculated monazite-bearing metamorphic assemblage diagrams in a Th-bearing system that also includes major monazite forming elements La, Ce, Nd and Y, using an equilibrium thermodynamic framework. These metamorphic assemblage diagrams are used to explore changes in the composition and abundance of monazite with pressure, temperature and bulk rock composition. The metasedimentary rock compositions modelled in this chapter are compared with data from natural rocks (presented in chapter 4) to further explore how monazite composition can be used to more precisely identify the pressure–temperature conditions of its formation. It is further illustrated how the models can be used to monitor the extent of partial melting and other metamorphic reactions. This chapter highlights the powerful potential for this modelling as a technique to integrate monazite's use as a geochronometer with the sensitive *P–T–X* information it records as a new tool in geospeedometry. The thermodynamic models are then applied to specific samples from Mt Stafford (Chapter 2) and the Ivrea-Verbano Zone (Chapter 3).

Chapter 6 *Thesis summary and conclusions*

Chapter 6 concludes the thesis by providing a concise discussion of the changes to the chemistry of monazite with progressive metamorphism, with particular reference to Th and the two Th-bearing endmembers of monazite. It assimilates key results and interpretations of the previous chapters and highlights questions that future research might pursue.

References

Allaz, J., Selleck, B., Williams, M. L., & Jercinovic, M. J. (2013). Microprobe analysis and dating of monazite from the Potsdam Formation, New York: A progressive record of chemical reaction and fluid interaction. American Mineralogist, 98(7), 1106-1119.

Bea, F., & Montero, P. (1999). Behavior of accessory phases and redistribution of Zr, REE, Y, Th, and U during metamorphism and partial melting of metapelites in the lower crust: an example from the Kinzigite Formation of Ivrea-Verbano, NW Italy. Geochimica Et Cosmochimica Acta, 63(7–8), 1133-1153.

Berry, R., Chmielowski, R., Steele, D., & Meffre, S. (2007). Chemical U–Th–Pb monazite dating of the Cambrian Tyennan Orogeny, Tasmania. Australian Journal of Earth Sciences, 54(5), 757-771.

Bial, J., Buettner, S. H., Schenk, V., & Appel, P. (2015). The long-term high-temperature history of the central Namaqua Metamorphic Complex: Evidence for a Mesoproterozoic continental back-arc in southern Africa. Precambrian Research, 268, 243-278.

Bial, J., Büttner, S., & Appel, P. (2016). Timing and conditions of regional metamorphism and crustal shearing in the granulite facies basement of south Namibia: Implications for the crustal evolution of the Namaqualand metamorphic basement in the Mesoproterozoic. Journal of African Earth Sciences, 123, 145-176.

Engi, M. (2017). Petrochronology based on REE-minerals: monazite, allanite, xenotime, apatite. Reviews in Mineralogy and Geochemistry, 83(1), 365-418.

Finger, F., Broska, I., Roberts, M. P., & Schermaier, A. (1998). Replacement of primary monazite by apatite-allanite-epidote coronas in an amphibolite facies granite gneiss from the eastern Alps. American Mineralogist, 83(3-4), 248-258.

Foster, G., Kinny, P., Vance, D., Prince, C., & Harris, N. (2000). The significance of monazite U–Th–Pb age data in metamorphic assemblages; a combined study of monazite and garnet chronometry. Earth and Planetary Science Letters, 181(3), 327-340.

Franz, G., Andrehs, G., & Rhede, D. (1996). Crystal chemistry of monazite and xenotime from Saxothuringian-Moldanubian metapelites, NE Bavaria, Germany. European Journal of Mineralogy, 8(5), 1097-1118.

Harrison, T. M., & Watson, E. B. (1984). The behavior of apatite during crustal anatexis: equilibrium and kinetic considerations. Geochimica Et Cosmochimica Acta, 48(7), 1467-1477.

Kelsey, D. E., Clark, C., & Hand, M. (2008). Thermobarometric modelling of zircon and monazite growth in melt-bearing systems: Examples using model metapelitic and metapsammitic granulites. Journal of Metamorphic Geology, 26(2), 199-212.

Kelsey, D. E., & Powell, R. (2011). Progress in linking accessory mineral growth and breakdown to major mineral evolution in metamorphic rocks: a thermodynamic approach in the Na2O-CaO-K2O-FeO-MgO-Al2O3-SiO2-H2O-TiO2-ZrO2 system. Journal of Metamorphic Geology, 29(1), 151-166.

Kohn, M. J., & Malloy, M. A. (2004). Formation of monazite via prograde metamorphic reactions among common silicates: implications for age determinations. Geochimica Et Cosmochimica Acta, 68(1), 101-113.

Laurent, A. T., Duchene, S., Bingen, B., Bosse, V., & Seydoux-Guillaume, A. M. (2018). Two successive phases of ultrahigh temperature metamorphism in Rogaland, S. Norway: evidence from Y-in-monazite thermometry. Journal of Metamorphic Geology, 36(8), 1009-1037.

Martins, L., Vlach, S. R. F., & de Assis Janasi, V. (2009). Reaction microtextures of monazite: correlation between chemical and age domains in the Nazaré Paulista migmatite, SE Brazil. Chemical Geology, 261(3-4), 271-285.

Overstreet, W.C., 1967. The geologic occurrence of monazite. 530, US Geological Survey Professional Paper 530.

Rasmussen, B., & Muhling, J. R. (2007). Monazite begets monazite: evidence for dissolution of detrital monazite and reprecipitation of syntectonic monazite during low-grade regional metamorphism. Contributions to Mineralogy and Petrology, 154(6), 675-689.

Schulz, B. (2017). Polymetamorphism in garnet micaschists of the Saualpe Eclogite Unit (Eastern Alps, Austria), resolved by automated SEM methods and EMP–Th–U–Pb monazite dating. Journal of Metamorphic Geology, 35(2), 141-163.

Skrzypek, E., Bosse, V., Kawakami, T., Martelat, J.-E., & Štípská, P. (2017). Transient allanite replacement and prograde to retrograde monazite (re) crystallization in medium-grade metasedimentary rocks from the Orlica-Śnieżnik Dome (Czech Republic/Poland): Textural and geochronological arguments. Chemical Geology, 449, 41-57.

Skrzypek, E., Kato, T., Kawakami, T., Sakata, S., Hattori, K., Hirata, T., & Ikeda, T. (2018). Monazite behaviour and time-scale of metamorphic processes along a low-pressure/high-temperature field gradient (Ryoke belt, SW Japan). Journal of Petrology, 59(6), 1109-1144.

Spear, F. S. (2010). Monazite–allanite phase relations in metapelites. Chemical Geology, 279(1–2), 55-62.

Spear, F. S., & Pyle, J. M. (2010). Theoretical modeling of monazite growth in a low-Ca metapelite. Chemical Geology, 273(1), 111-119.

Stepanov, A. S., Hermann, J., Rubatto, D., & Rapp, R. P. (2012). Experimental study of monazite/melt partitioning with implications for the REE, Th and U geochemistry of crustal rocks. Chemical Geology, 300, 200-220.

Taylor, R. J. M., Kirkland, C. L., & Clark, C. (2016). Accessories after the facts: Constraining the timing, duration and conditions of high-temperature metamorphic processes. Lithos, 264, 239-257.

Watson, E. B., & Harrison, T. M. (1983). Zircon saturation revisited: temperature and composition effects in a variety of crustal magma types. Earth and Planetary Science Letters, 64(2), 295-304.

Williams, M. L., Jercinovic, M. J., & Hetherington, C. J. (2007). Microprobe monazite geochronology: understanding geologic processes by integrating composition and chronology. Annual Review of Earth and Planetary Sciences, 35(1), 137.

Wolf, M. B., & London, D. (1994). Apatite dissolution into peraluminous haplogranitic melts: an experimental study of solubilities and mechanisms. Geochimica Et Cosmochimica Acta, 58(19), 4127-4145.

Yakymchuk, C. (2017). Behaviour of apatite during partial melting of metapelites and consequences for prograde suprasolidus monazite growth. Lithos, 274, 412-426.

Yakymchuk, C., & Brown, M. (2014). Behaviour of zircon and monazite during crustal melting. Journal of the Geological Society, 171(4), 465-479.

Yakymchuk, C., & Brown, M. (2019). Divergent behaviour of Th and U during anatexis: Implications for the thermal evolution of orogenic crust. Journal of Metamorphic Geology. 37, 899– 916.

Yakymchuk, C., Brown, M., Clark, C., Korhonen, F., Piccoli, P., Siddoway, C., . . . Vervoort, J. (2015). Decoding polyphase migmatites using geochronology and phase equilibria modelling. Journal of Metamorphic Geology, 33(2), 203-230.

Yakymchuk, C., Kirkland, C. L., & Clark, C. (2018). Th/U ratios in metamorphic zircon. Journal of Metamorphic Geology, 36(6), 715-737.

Chapter 2

This chapter is published as:

Williams, M.A., Kelsey, D.E., Baggs, T., Hand, M. & Alessio, K.L. (2018). Thorium distribution in the crust: Outcrop and grain-scale perspectives. *Lithos*, 320-321, 222-235. doi.org/10.1016/j.lithos.2018.09.016

Statement of Authorship

Title of Paper	Thorium distribution in the crust: outcrop and grain-scale perspectives
Publication Status	☑ Published ☐ Accepted for Publication ☐ Submitted for Publication ☐ Unpublished and Unsubmitted w ork w ritten in manuscript style
Publication Details	Williams, M.A., Kelsey, D.E., Baggs, T., Hand, M., Alessio, K.L., 2018. Thorium distribution in the crust: Outcrop and grain-scale perspectives. *Lithos*. 320: 222-235.

Principal Author

Name of Principal Author (Candidate)	Megan A Williams
Contribution to the Paper	Contributed to field sampling, performed analysis on all samples, interpreted data, prepared manuscript and acted as corresponding author.
Overall percentage (%)	80%
Certification:	This paper reports on original research I conducted during the period of my Higher Degree by Research candidature and is not subject to any obligations or contractual agreements with a third party that would constrain its inclusion in this thesis. I am the primary author of this paper.
Signature	Date 26/11/18.

Co-Author Contributions

By signing the Statement of Authorship, each author certifies that:

i. the candidate's stated contribution to the publication is accurate (as detailed above);

ii. permission is granted for the candidate in include the publication in the thesis; and

iii. the sum of all co-author contributions is equal to 100% less the candidate's stated contribution.

Name of Co-Author	David E Kelsey
Contribution to the Paper	Assisted with study design, supervised development of work, assisted with field sampling and data collection helped with data interpretation and manuscript evaluation.
Signature	Date 28/11/18

Name of Co-Author	Thomas Baggs
Contribution to the Paper	Assisted with sample analysis and data interpretation.
Signature	Date 15/11/19

Name of Co-Author	Martin Hand
Contribution to the Paper	Assisted with study design, field sampling and data collection helped evaluate and edit the manuscript.
Signature	Date 26-11-2018

Name of Co-Author	Kiara L Alessio
Contribution to the Paper	Assisted with field sampling and data collection.
Signature	Date 26/11/18

Thorium distribution in the crust: outcrop and grain-scale perspectives

ABSTRACT

The spatial distribution of heat producing elements (K, U, and Th) in the continental crust has long-term implications for the thermal and physical evolution of orogens. Heat producing elements, in particular Th, are most abundant in metasedimentary rock types. As such, these rock types have a significant control on the spatial distribution of heat production in the crust. The major host of the heat producing element thorium in pelitic metasedimentary rocks is the REE–Th phosphate monazite. We present in-field gamma ray spectrometry (in-field GRS) data integrated with grain-scale electron probe microanalysis data to reveal grain to terrane scale links in thorium distribution. In-field GRS data shows that thorium is not depleted in granulite facies residual rocks that have lost melt with respect to their subsolidus counterparts. Concurrently, the bulk thorium budget of monazite is approximately uniform within samples and if anything increases with increasing metamorphic grade. Monazite average grain size increases with metamorphic grade and prograde cores are largely preserved in granulite facies samples. Thorium is preserved in residual metasediments after melting and melt loss implying that even when melting and melt extraction is efficient it does not strip Th from granulite facies rocks.

1 INTRODUCTION

Monazite is the major Th-bearing mineral in high temperature (>500°C) continental crust. Thus, the controls on monazite growth, dissolution and recrystallization control the spatial distribution of Th in the continental crust. It has been a tacit assumption that melting of continental crust will remove Th – a major heat producing element (HPE) – from the residue and concentrate it in granitic rocks. However, it is now understood that Th will preferentially partition into monazite over silicate melt regardless of the temperature of crustal melting (Rapp, Ryerson, & Miller, 1987; Skora & Blundy, 2010; Stepanov, Hermann, Rubatto, & Rapp, 2012) and that monazite can remain stable well into the granulite facies (Yakymchuk, 2017; Yakymchuk & Brown, 2014). Recently, Alessio et al. (2018) showed that heat production rates, sampled at the outcrop scale, at least remain constant between sub- and supra-solidus rocks of similar bulk compositions. The implication of this is that Th can commonly remain in the residuum during crustal melting and melt extraction from that residuum.

Controls on the behaviour of Th as a function of progressive metamorphism in metasedimentary sequences are poorly quantified. As the major host of Th in crustal rocks, monazite is ideal for studying these controls. Numerous monazite forming reactions have been proposed (e.g. Corrie & Kohn, 2008; Kohn & Malloy, 2004; Pyle & Spear, 2003; Pyle, Spear, Rudnick, & McDonough, 2001; Spear & Pyle, 2010), but these studies do not systematically investigate Th behaviour within monazite. However, disparate empirical data suggests that monazite becomes more Th-rich in granulite facies rocks (e.g. Engi, 2017; Watt, 1995).

The aim of this study is to understand the behaviour of Th by presenting a database which quantifies the spatial distribution and chemistry of monazite for rock compositions that have undergone progressive metamorphism from below to above the solidus, with the expressed purpose of understanding the concentration and behaviour of Th in monazite. We track the textural and chemical evolution of monazite in pelitic and psammitic prograde sequences from Mt Stafford, central Australia and show that metamorphic monazite from mid-amphibolite facies rocks is comparatively low in Th and that upper-amphibolite and granulite facies monazite is elevated in Th. The abundance and overall Th budget of monazite increases with increasing metamorphic grade, in agreement with trends in outcrop-scale gamma ray spectrometer data. Moreover, our dataset lends support to the experimental and thermodynamic modelling findings of Stepanov et al. (2012) and Yakymchuk, Kirkland, and Clark (2018) in which monazite is found or calculated to increase in Th with increasing temperature.

2 GEOLOGICAL BACKGROUND

Mount Stafford, central Australia (Fig. 1) records an uninterrupted prograde metamorphic sequence in rocks of broadly homogeneous

bulk rock composition (Greenfield, Clarke, & White, 1998). Metamorphism ranges from mid amphibolite to granulite facies and the rocks preserve evidence for low accumulated strain (Vernon, Clarke, & Collins, 1990). The metamorphic system is bounded to the north and east by two granite bodies, with the Northern Granite being emplaced syn-post-metamorphism, and the Eastern Granite being emplaced pre-syn-metamorphism (Greenfield et al., 1998; Rubatto, Hermann, & Buick, 2006; White, Powell, & Clarke, 2003). The sequence consists of interlayered pelites and psammites of the Mt Stafford beds and their metamorphosed equivalents. The Mt Stafford beds are interpreted to have been deposited as part of the more extensive Lander Formation (Greenfield et al., 1998; White et al., 2003), which is constrained by detrital zircons and intrusive granites to be between 1820-1802 Ma (Rubatto et al., 2006). Metamorphism in the sequence occurred between 1805-1795Ma (Rubatto et al., 2006).

The sequence at Mt Stafford preserves a near-isobaric section with a temperature increase of ~300 °C from mid amphibolite (~580 °C; historically called greenschist after Greenfield, Clarke, Bland, & Clark, 1996) to granulite facies rocks (~820 °C; Bartoli, 2017; White et al., 2003). The section has been separated into four zones, bound by mineral isograds, described in Table 1 (Greenfield et al., 1998; White et al., 2003). The abundance of biotite decreases with metamorphic grade, linked by White et al. (2003) to the melt-producing reactions (lowest to highest grade) at Mt Stafford (mineral abbreviations after Holland & Powell, 2011):

bi+sill+q cd+ksp+liq (1)

bi+sill cd+sp+ksp+liq (2)

bi+q+cd g+ksp+liq (3)

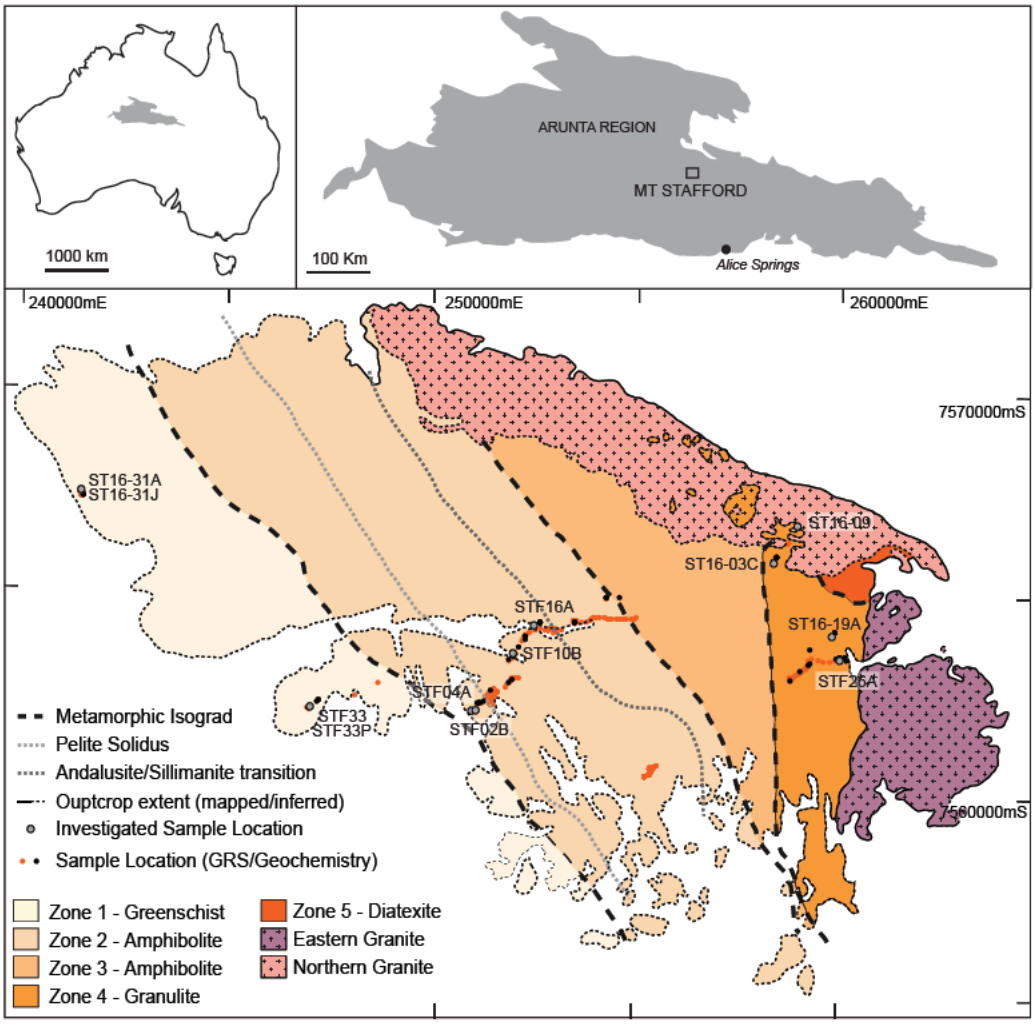

Figure 1. Map of the Mt Stafford area showing major metamorphic zones (see table 1; after Anderson et al., 2013; Greenfield et al., 1996; White et al., 2003) and location of samples in this study. Inset: Location of Mt Stafford within the Arunta Region and within Australia.

Table 1. Metamorphic zones in the Mt Stafford Terrane (after White et al., 2003). Mineral abbreviations after Holland and Powell (1998). Samples from this study are aluminous metapelites and metapsammites. *Pressure Temperature* constraints from White et al. (2003). Andalusite in the sequence is interpreted to be metastable (White et al., 2003).

Rock Type	Mineral Assemblages			
	Zone 1	*Zone 2*	*Zone 3*	*Zone 4*
Aluminous metapelite	mu–bi–a–and	cd–ksp–bi–q–and/sill	cd–ksp–q–sill cd–ksp–sp–bi–sill cd–ksp–sp–sill	cd–ksp–q–sill cd–ksp–sp–sill
Subaluminous metapelite	mu–bi–q mu–bi–q–and	cd–ksp–bi–q–and/sill	cd–ksp–bi–q cd–ksp–sp–bi–sill cd–ksp–sp–bi cd–ksp–bi–q–g	cd–ksp–bi–q cd–ksp–q cd–ksp–sp cd–ksp–bi–sp cd–ksp–q–g
Metapsammite	mu–bi–q	cd–ksp–bi–q–and/sill	cd–ksp–bi–q cd–ksp–bi–q–g	cd–ksp–q–g–opx cd–ksp–q–g cd–ksp–q–opx
Cordierite Granofels	mu–bi–q–cd–and bi–q–cd–ksp bi–q–cd–ksp–and	cd–bi–q–ksp cd–ksp–bi–and/sill cd–ksp–bi–q–and/sill	cd–bi–q–ksp cd–ksp–q–sill cd–ksp–bi–sill–sp cd–ksp–bi–q–sill	cd–q–ksp opx–cd–q–ksp g–cd–q–ks cd–ksp–q–sill cd–ksp–bi–sill–sp
P-T constraints	<2.55±0.25 kbar <620 ºC	2.55±0.25 – 3.05±0.25 kbar 620–665 ±15 ºC	3.05±0.25 – 3.65±0.35 kbar 665±15 – 780±5 ºC	>3.65±0.35 kbar >820 ºC

All of these reactions imply that the decrease in biotite abundance in the samples is linked to the production of melt. The maximum melt productivity of 22-23 wt% was predicted at the peak temperature of 820°C in the Mt Stafford area (Bartoli, 2017) and melt loss in the area has been documented by depletion of melt-mobile elements in granulite facies samples with respect to the protolith compositions (Palya, Buick, & Bebout, 2011; see also White et al., 2003).

3 SAMPLE SELECTION

Samples were selected to be representative of the prograde sequence of metamorphism across the solidus at Mt Stafford (Fig. 1). There is inherent variability in the trace element concentration between samples due to natural variation in their sedimentary protoliths. This was minimized by careful sample selection on the basis of similarity in major element bulk composition. Metapelite and metapsammite lithologies (Table 2) were selected on the basis of their general propensity for forming monazite. At the outcrop and thin section scale, samples in Table 2 contain an even distribution of poikiloblasts of andalusite and/or cordierite. Only peritectic granulite facies migmatites with poikiloblasts of garnet are obviously more heterogeneous.

4 METHODS

4.1 Whole rock geochemistry

Whole-rock geochemical analyses of samples were undertaken to quantify bulk rock budgets of HPE as well as determine similarity of chemical composition between samples. Whole-rock geochemical analyses were undertaken by Wavelength Dispersive X-ray Fluorescence spectrometry at the Department of Earth and Environment, Franklin and Marshall College, Lancaster PA, USA. Major elements were analysed on fused disks prepared using a lithium tetraborate flux, calculated on a volatile-free basis. Element and oxide concentrations from whole-rock geochemistry will be denoted in the form Th_WR and CaO_WR respectively (i.e. trace and major elements).

4.2 In field Gamma ray Spectrometry (in field GRS)

Handheld gamma-ray spectrometers (GRSs) were used in the field to provide a broad scale, bulk sampling of the concentrations of heat producing elements (HPEs; K, U, Th) of outcrops. Analyses were conducted using four Radiation Solutions RS-230 model handheld GRSs. The RS-230 model has a 103 cm^3 bismuth germinate oxide crystal sensor, and the units were calibrated using concrete test pads, constructed by Radiation Solutions. The detectors were placed directly onto the outcrops and analyses were integrated over 120 seconds. The sample volume for the RS-230 model is approximately 0.5 m^3, therefore only fresh outcrops larger than this were analysed. Machine errors are propagated for all analyses, as per the manufacturer's instructions (see Appendix S1 in Alessio et al., 2018). Analyses were collected from transects of Mt Stafford from lowest to highest grade, with multiple analyses

Table 2. Samples and locations. Samples listed in increasing grade order, refer to Fig. 1 (Map). Metamorphic zones after Greenfield et al. (1998); White et al. (2003). Mineral abbreviations after Holland and Powell (1998). Metm., metamorphic. Locations are in UTM coordinates, zone 53K, using the WGS84 datum.

Sample	*Grade*	*Metm. Zone*	*Rock type*	*Mineralogy*	*Location*
ST16–31J	Mid Amphibolite	1	pelite	bi–q–and–mu–ilm apt–mnz–xtm	241394 mE 7567785 mS
STF33P	Mid Amphibolite	1	pelite	mu–bi–q–ksp–mt apt–mnz–xtm	247199 mE 7562360 mS
STF02B	Amphibolite	2	pelite	ksp–bi–and–q–mu–ilm apt–mnz–xtm	251197 mE 7562283 mS
STF16A	Amphibolite	2	pelite	ksp–crd–bi–q–and–sill–ilm apt–mnz–xtm	252677 mE 7564418 mS
ST16–09	Granulite	4	pelite	ksp–sill–crd–bi–pl–q–ilm ± tor apt–mnz–xtm–zrn	259078 mE 7566925 mS
ST16–19A	Granulite	4	pelite	ksp–crd–sill–bi–q–pl–ilm ± grt apt–mnz–xtm–zrn	259976 mE 7564102 mS
ST16–31A	Mid Amphibolite	1	psammite	q–bi–ksp–mu ± tor apt–mnz–xtm–zrn	241394 mE 7567785 mS
STF33	Mid Amphibolite	1	psammite	bi–mu–ilm ± tor apt–mnz–xtm–zrn	247199 mE 7562360 mS
STF04A	Amphibolite	2	psammite	mu–bi–ksp–ilm ± tor apt–mnz–xtm–zrn	251292 mE 7562338 mS
STF10B	Amphibolite	2	psammite	ksp–crd–pl–bi–sill–mt mnz–apt–xtm–zrn	252150 mE 7563754 mS
STF26A	Granulite	4	psammite	ksp–cd–g–bi–sp–q–ilm ± pl apt–mnz–xtm–zrn	260269 mE 7563397 mS
ST16–03C	Granulite	4	psammite	q–ksp–crd–bi–pl–sill–ilm ± tor ± mu mnz–apt–xtm–zrn–aln	258476 mE 7565983 mS

collected at each location to account for the natural heterogeneity of sequences in outcrop. Thorium concentrations obtained from in-field GRS data are denoted Th_GRS.

4.3 Mineral Liberation Analysis (MLA)

Entire thin sections of samples were mapped for monazite using a FEI Quanta600 Scanning Electron Microscope (SEM) with automated mineral liberation analysis (MLA) software at Adelaide Microscopy, The University of Adelaide. Imaging and mapping conditions were an accelerating voltage of 25 kV, beam current of 40 nA, spot size of 6.8, working distance of 10 mm and 250× magnification. Mineral identification was undertaken by x-ray spot analysis with electron dispersive spectrometers and by mineral liberation analysis (MLA) mapping. MLA mapping is based on defining a searchable grey scale interval within the full range of 0 (black) to 255 (white), where the brightness of 255 is defined by the BSE response of an Au standard (for liberation of monazite, xenotime and zircon) and a rutile standard (for liberation of apatite). Wherever a mineral occurs within the map region within the searchable range an x-ray spot analysis is taken. Processing of x-ray data is performed by specifying a mineral list, whereby each mineral in the list has an x-ray spectra to be matched against the collected x-rays, to a matching threshold of 70%. Back scattered electron (BSE) scans of full thin sections were collected simultaneously with MLA maps. MLA maps were analysed using pixel counting techniques in Adobe software to calculate the proportion of monazite, apatite, xenotime and zircon in the samples, as well as abundance and grain size of these minerals.

4.4 Electron Probe Microanalysis (EPMA)

Qualitative mapping and quantitative point analyses of monazite chemistry were performed at Adelaide Microscopy, the University of Adelaide, using a Cameca SXFive electron microprobe. Qualitative compositional mapping used a beam current of 200 nA, accelerating voltage of 20 kV, a dwell time of 100 ms and a step size of 1 µm. For each sample, elements Ca, La, Nd, P, Si and Sm were mapped with wavelength dispersive spectrometers (WDS) and Th, Ce, U, Pb and Y were mapped with energy dispersive spectrometers (EDS). Quantitative point analyses used combined beam conditions, with a beam current of 20 nA and accelerating voltage of 15 kv used for the elements F, Cl, Si, Mg, Al, K, P and Ca, and a beam current of 100nA and accelerating voltage of 15kv used for the elements Th, U, Pb, Gd, Sm, Nd, Pr, La, Ce and Y. Pb was not analysed for samples STF33, STF33P, STF04A and STF16A to reduce individual spot analysis time. Calibration was done on certified synthetic

and natural mineral standards from Astimex Ltd and P&H Associates. Data calibration and reduction was carried out in 'Probe for EPMA', distributed by Probe Software Inc. Monazite weight % oxide and cation data from Electron Probe Microanalysis will be denoted in the form ThO_2_mnz and Th^{4+}_mnz respectively.

Average ThO_2 concentrations for individual grains and compositionally distinct parts of grains (monazite zones) were calculated by manually scaling qualitative maps using quantitative point analyses from the same grains (Fig. 2). For each individual grayscale map, the locations of each EPMA point was located, and a grey value for that point was calculated, averaging over 9 pixels (pixel size = 1x1µm, spot size = 2x2µm). The average point grey values were plotted against point ThO_2_mnz, and a regression line (and equation) was calculated for each grain. Average ThO_2 concentrations for the whole grain and monazite zones within were then calculated using this regression and the average grey values of each area respectively. Where regression equation slope could not be calculated for an individual grain, the average slope from other grains in the sample was used as the slopes were uniform for a given sample. Grain average and Zone average ThO_2 contents calculated by this method are denoted ThO_2_GA and ThO_2_ZA respectively.

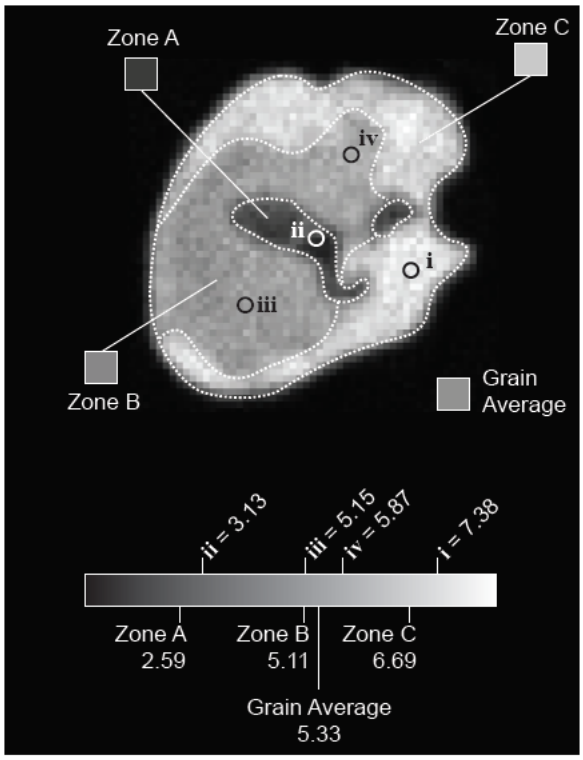

Figure 2. Grain Average ThO_2 wt% Calculations. Example of calculation from STF16 03C, monazite 7. Grey value and corresponding to point analysis ThO_2 wt% concentration are used to scale EPMA maps. Grey values of zones and whole grain are then assigned a ThO_2 wt% concentration based on this calibration. Circles labelled A D represent the locations of spot analyses, with the ThO_2 wt% concentrations from those spots given in the greyscale bar.

5 RESULTS

5.1 Whole rock geochemistry

Whole-rock geochemistry of the 12 samples (6 metapelite, 6 metapsammite) selected for MLA and EPMA are provided in Table 3. A comparison of whole-rock geochemistry of the 12 investigated samples with other samples from the terrane is shown in Figure 3. Th_WR concentrations for all samples taken at Mt Stafford are shown in Figure 4, adjacent to Th_GRS concentrations acquired at the same locations (Alessio et al., 2018). The whole-rock geochemistry for all samples in shown in Figure 3 are provided in Appendix S2.1. The selected metapelite and metapsammite samples cluster in two distinct compositional groups for most indicator elements (Fig. 3 a, c, d); however, there are some elements for which there is cross over between the groups (e.g. Fe, Mg; Fig. 3b).

5.2 In field GRS

In-field GRS data from Mt Stafford shows no change in the average Th_GRS concentrations from subsolidus to suprasolidus amphibolite facies rocks (22.9 ± 2.7 and 23.4 ± 2.7 ppm Th_GRS respectively, Fig. 4). The range of concentrations in sub- and supra-solidus amphibolite facies rocks is similar (14.3–30.1 and 17.7–47.5 ppm Th_GRS respectively). Seven anomalously high analyses (of 259 total analyses) in the suprasolidus amphibolite facies rocks are in the range 33.1–47.5 ppm Th_GRS. When these analyses are considered outliers, the range of Th_GRS concentrations for suprasolidus amphibolite facies rocks is 17.7–31.9 ppm. This range is the same within error as the range of concentrations for subsolidus amphibolite facies rocks. Granulite facies rocks show increased scatter in Th_GRS concentrations (between 17.3 and 41.7 ppm Th_GRS). Clear distinction between Th_GRS concentrations for leucosome-rich and residuum-rich parts of the sequence is generally not seen in the granulite facies samples, except within the highest temperature migmatites ('schlieren migmatites'; Fig. 4; Greenfield et al., 1996; White et al., 2003). For these rocks, residual-rich layers have systematically higher heat

Table 3. Whole rock geochemistry. Fe_2O_3 and FeO determined by titration.

	Mt Stafford metapelites						*Mt Stafford metapsammites*					
	ST16-31J	**STF33P**	**STF02B**	**STF16A**	**ST16-09**	**ST16-19A**	**ST16-31A**	**STF33**	**STF04A**	**STF10B**	**STF26A**	**ST16-03C**
Major elements (wt%)												
SiO_2	56.90	58.92	55.39	55.53	56.38	54.78	82.18	76.73	83.20	75.16	73.69	73.92
TiO_2	0.58	0.54	0.61	0.59	0.52	0.74	0.31	0.37	0.32	0.47	0.55	0.49
Al_2O_3	25.15	21.06	24.43	24.73	25.13	25.18	9.26	11.17	8.84	13.17	12.78	13.74
Fe_2O_3T	7.68	7.13	8.06	7.83	6.90	9.55	2.63	4.20	1.77	4.48	6.61	4.57
MnO	0.07	0.07	0.13	0.06	0.10	0.11	0.05	0.04	0.06	0.13	0.11	0.07
MgO	2.33	1.89	2.60	2.03	2.31	3.20	0.75	1.32	0.48	1.35	1.83	1.48
CaO	0.03	0.10	0.34	0.21	0.36	0.33	0.64	0.44	0.66	0.71	0.47	0.84
Na_2O	0.68	0.44	0.62	1.23	1.37	1.17	1.24	0.98	1.05	0.74	0.59	1.49
K_2O	6.26	6.04	6.64	6.62	6.66	4.58	2.76	2.97	2.41	3.25	2.36	3.63
P_2O_5	0.05	0.10	0.13	0.13	0.15	0.20	0.10	0.09	0.11	0.11	0.10	0.07
Total	**99.73**	**96.29**	**98.95**	**98.96**	**99.88**	**99.84**	**99.92**	**98.31**	**98.90**	**99.57**	**99.09**	**100.30**
LOI	4.42	3.94	2.06	0.72	1.16	0.75	0.70	1.82	1.11	0.89	1.25	0.95
Fe_2O_3	2.19	-	-	-	0.50	0.50	0.46	-	0.27	-	-	0.57
FeO	4.94	-	-	-	5.76	8.14	1.95	-	1.35	-	-	3.60
Trace elements (ppm)												
Rb	448	409	381	408	284	229	128	199	96	162	119	188
Sr	74	61	106	49	134	148	105	85	57	121	57	117
Y	25	14	34	29	32	23	20	22	25	24	24	20
Zr	118	117	118	92	120	166	265	224	335	251	260	273
V	90	81	92	69	135	113	40	43	27	60	64	57
Ni	54	55	42	38	43	66	18	29	16	31	38	27
Cr	86	78	70	60	75	94	56	54	25	59	81	78
Nb	17	16	17	17	15	17	10	12	10	14	14	13
Ga	35	32	34	35	36	35	15	17	13	20	20	21
Cu	34	34	37	41	17	25	13	9	8	16	7	49
Zn	107	118	111	115	93	117	45	73	27	73	134	65
Co	17	19	17	18	17	29	2	9	1	11	21	8
Ba	1011	884	913	1060	1014	956	587	567	487	521	516	852
La	36	26	45	42	41	53	47	43	46	41	40	34
Ce	78	163	108	109	93	132	80	75	80	84	83	74
U	0	1	1	0	0	0	3	1	3	1	0	1
Th	33	34	34	35	25	38	30	27	37	34	25	30
Sc	14	15	14	13	12	2	2	5	2	6	17	4
Pb	11	15	17	23	20	20	12	25	14	13	14	16

production than leucocratic-rich layers (28.7–41.7 and 19.0–24.8 ppm Th_GRS respectively).

5.3 MLA

Representative BSE images of the microstructural settings of monazite are presented in Figure 5. Monazite grain size, abundance and chemical zones are summarised in Table 4 and monazite microstructural location is summarised in Table 5. A comparison of the proportions of accessory minerals is shown in Figure 6.

In amphibolite facies samples (ST16-31J, STF33P, STF02B, STF16A, ST16-31A, STF33, STF04A and STF10B) monazite is predominantly hosted at grain boundaries between K-feldspar, biotite, quartz, apatite ± cordierite, muscovite, ilmenite and andalusite within the matrix (Table 5). Monazite is evenly distributed throughout the samples and frequently occurs as clusters of small grains (<10 µm). Monazite is rarely

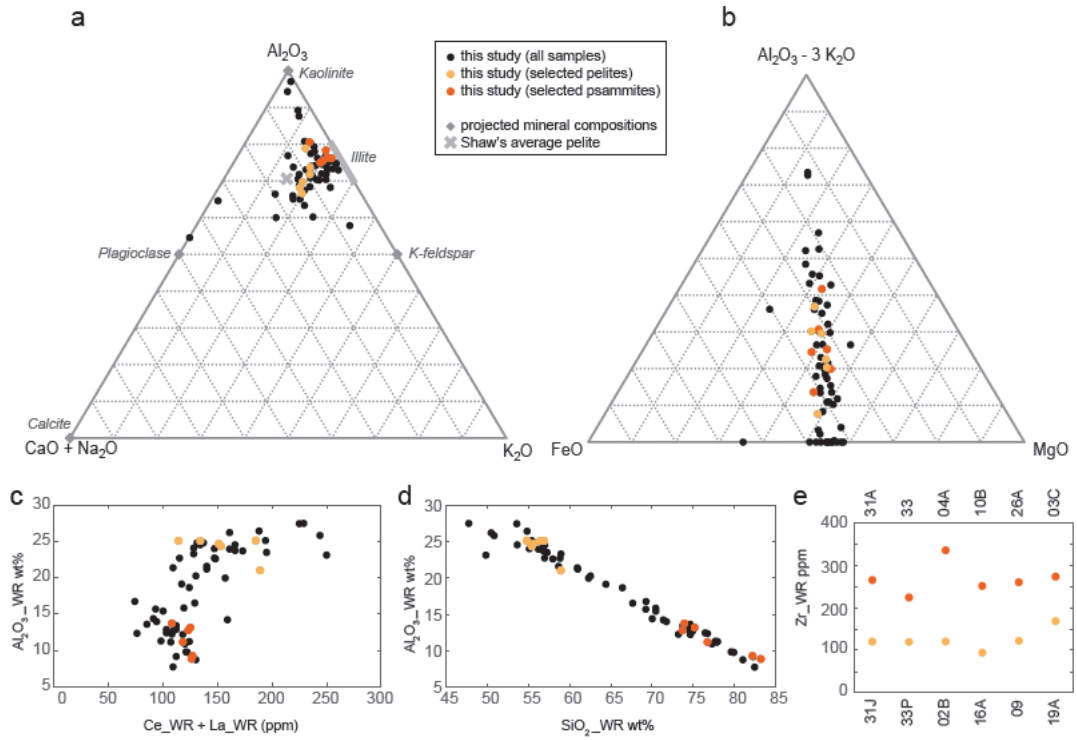

Figure 3. Whole rock geochemistry from Mt Stafford. Investigated metapelites shown in blue, metapsammites in red. All other samples from this study filled black circles. (a) Al2O3 CaO+Na2O K2O diagram after (Janots et al., 2006). Shaw's average pelite shown with grey cross (Shaw, 1956); (b) AFM diagram; (c) Al2O3 WR vs Ce WR + La WR; (d) Al2O3 WR vs SiO2 WR; (e) Zr WR for investigated samples. Samples increase in metamorphic grade from left to right. Metapelite samples (yellow) are labelled below, metapsammite samples (red) above. Sample prefixes (STF and ST16) have been omitted, refer to Table 2 for full sample names.

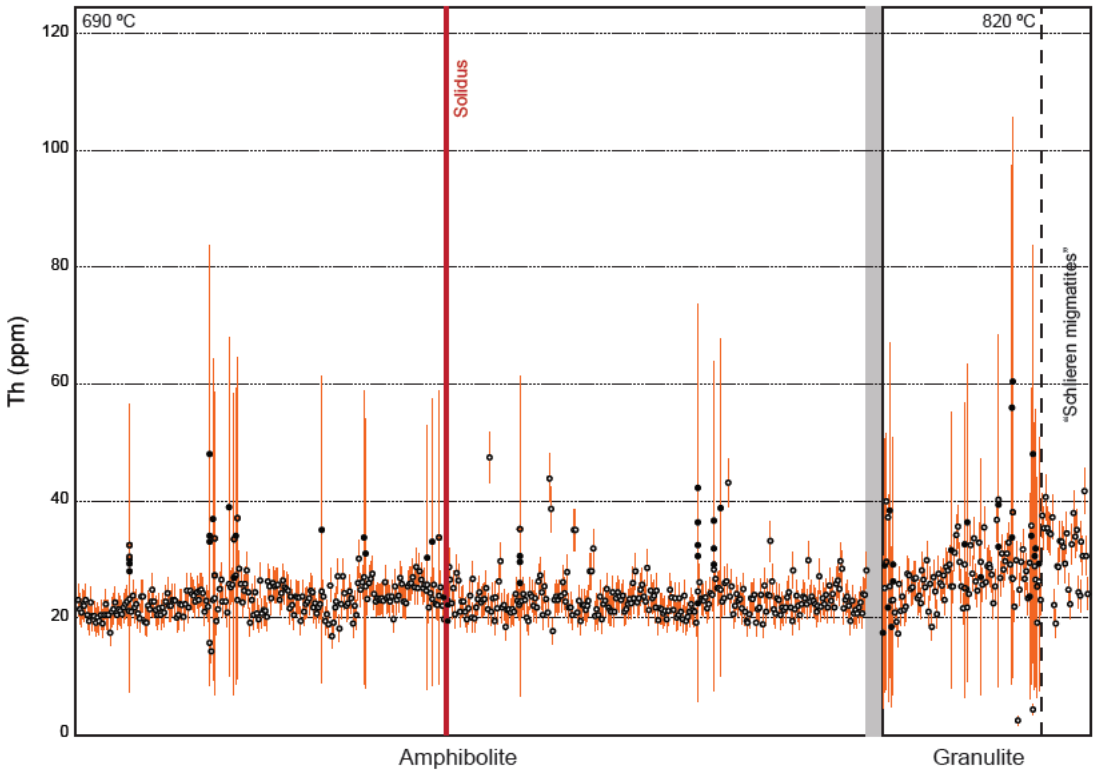

Figure 4. Th GRS (open cirlces) and Th WR (filled circles) concentrations for Mt Stafford as a function of metamorphic grade (Th GRS from Alessio et al., 2018): Solid red line indicates the in field location of the solidus, black solid lines indicate facies transitions, and black dotted lines indicate significant boundaries within facies. Error bars are 2 sigma, Th GRS errors calculated from machine errors and Th WR errors calculated from standard data. Pressure temperature estimates from White et al. (2003). "Schlieren migmatites" refer to samples of segregated leucosome and residuum (see White et al., 2003).

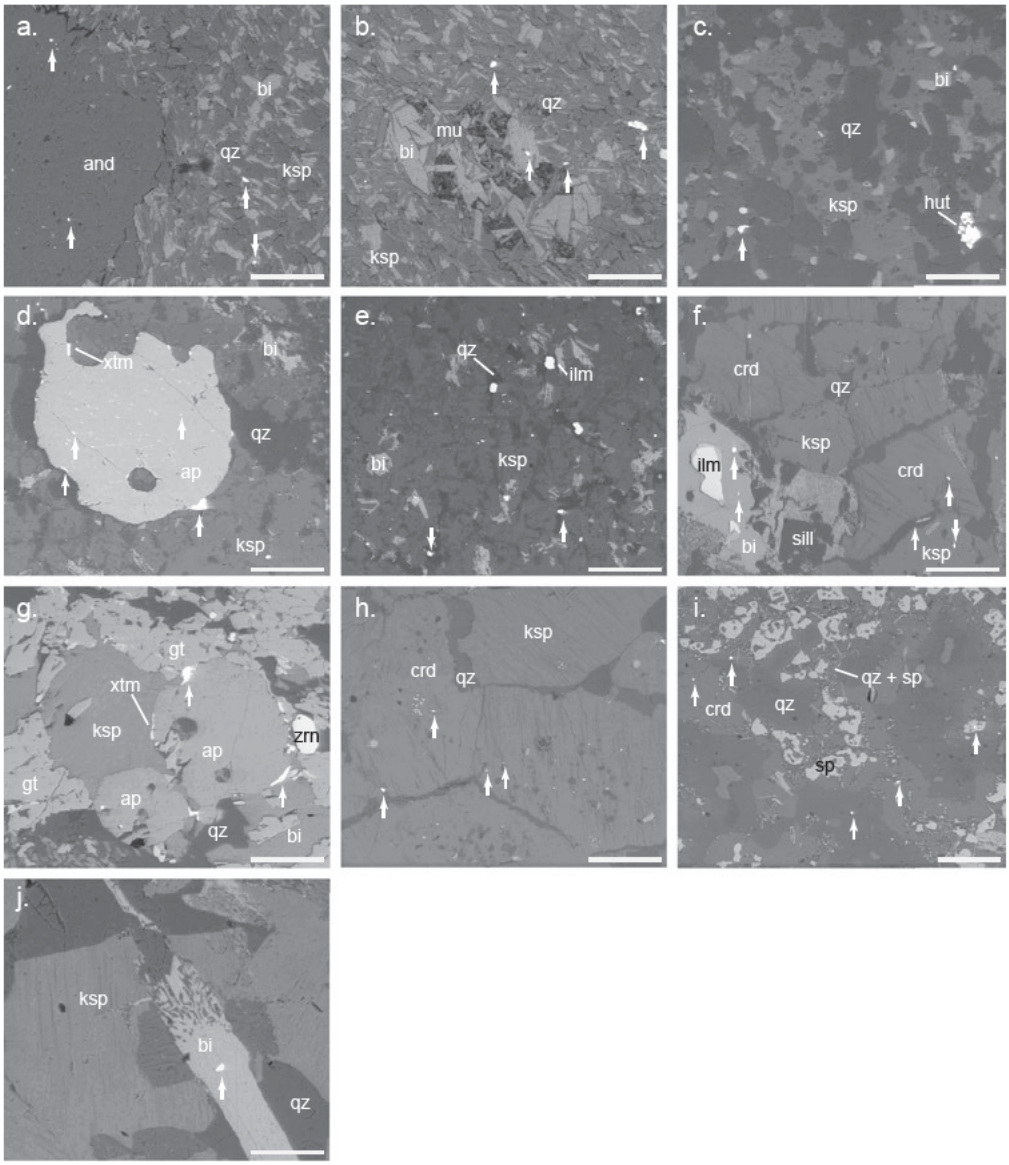

Figure 5. Representative BSE photomicrographs showing microstructural setting of monazite. White arrows indicate monazite grains. (a) ST16 31J, monazite included in porphyroblastic andalusite and within matrix; (b) ST16 31J, monazite included in biotite clusters and within matrix; (c) STF10B, monazite and huttonite within matrix; (d) ST16 09, monazite and xenotime at grain boundaries between coarse grained apatite and matrix. Monazite included within coarse grained apatite; (e) ST16 09, monazite within matrix; (f) ST16 19A, monazite included in biotite, K feldspar, cordierite and interstitial quartz; (g) STF26A, monazite and xenotime at grain boundaries between coarse grained apatite and matrix. (h) STF26A, monazite included in coarse grained cordierite and K feldspar; (i) STF26A, monazite included in cordierite, quartz and spinel and within spinel quartz symplectites; (j) monazite included in coarse grained biotite. Scale bar = 200μm. And, andalusite; ap, apatite; bi, biotite; crd, cordierite; gt, garnet; hut, huttonite; ilm, ilmenite; ksp, K feldspar; mu, muscovite; qz, quartz; sill, sillimanite; sp, spinel; xtm, xenotime; zrn, zircon.

found in contact with or adjacent to xenotime. Monazite is additionally found as inclusions in some porphyroblastic minerals as follows: ST16-31J, inclusion in porphyroblastic andalusite and within coarse-grained patches of biotite; STF02B and STF16A, included in K-feldspar, biotite and quartz; STF04A, rarely found as inclusion in quartz; STF10B, included in cordierite, K-feldspar ±and quartz. Notably, monazite is not included in K-feldspar porphyroblasts in the sample STF33P. Huttonite-rich grains in sample STF10B are found at grain boundaries between quartz, K-feldspar and cordierite.

In granulite facies samples (ST16-09, ST16-19A, ST16-03C and STF26A), monazite occurs as inclusions in coarse-grained minerals, at grain boundaries between matrix minerals and as elongate grains along the edges of larger apatite grains. Monazite is rarely found in contact with or adjacent to xenotime. In ST16-09, monazite grains are evenly distributed throughout the sample, and occur at grain boundaries between

Table 4. Monazite grain characteristics. Number of monazite grains and average grainsize from MLA maps of thin sections, ThO_2 GA and mnz zones from EPMA determined from map and point analysis data (see text for details). Mnz, monazite; total incl. mnz, volume % of monazite included in all minerals.

Sample	Grade	*n* mnz grains	Average grainsize (μm^2)	ThO_2 GA	mnz zones	total incl mnz
Mt Stafford metapelites						
ST16–31J	Mid Amphibolite	628	87	1 70–3 81	A	0 122
STF33P	Mid Amphibolite	56	95	2 10–3 58	A	0 044
STF02B	Amphibolite	84	201	2 70–3 77	A, B	0 335
STF16A	Amphibolite	48	415	5 10–5 70	A, B	0 411
ST16–09	Granulite	152	346	3 35–4 98	C*, D	0 451
ST16–19A	Granulite	9	4418	4 23–5 01	A, B, C	0 860
Mt Stafford metapsammites						
ST16–31A	Mid Amphibolite	902	20	0 21-4 73	A	0 015
STF33	Mid Amphibolite	254	79	1 65-5 98	A	0 052
STF04A	Amphibolite	117	177	2 45-3 45	A, B	0 072
STF10B	Amphibolite	97	314	2 18-5 8	A, B, B*	0 185
STF26A	Granulite	22	1257	4 83-9 44	A, B, C, D	0 431
ST16–03C	Granulite	75	707	2 02-22 76	A, B, C	0 193

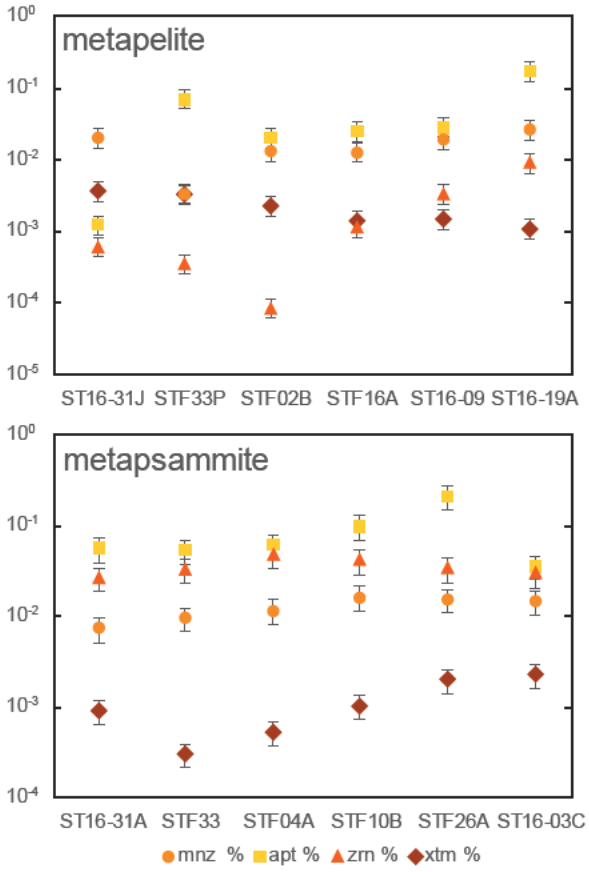

Figure 6. Accessory mineral volume (as %), calculated by point counting of MLA maps of entire thin sections (approximately 25x50mm). Pixel size of maps is 1.03 µm. Samples increase in metamorphic grade from left to right. Mnz = monazite, apt = apatite, zrn = zircon, xtm = xenotime.

K-feldspar, biotite, quartz, spinel, cordierite ± ilmenite. In addition to monazite grains found on the edges of coarser grained apatite, micro-inclusions (<1 µm) of monazite are found within these coarse grained apatites. In sample ST16-19A, monazite occurs at grain boundaries between K-feldspar, cordierite, quartz, spinel and ilmenite, and additionally as inclusions in coarse grained K-feldspar, cordierite, biotite, ilmenite and spinel. In sample STF26A— which is a heterogeneous peritectic-mineral bearing migmatite— monazite occurs in a broad range of microstructural locations, but is notably absent from within peritetic garnet grains. In this sample monazite occur at grain boundaries between K-feldspar, cordierite, quartz, spinel, biotite, ilmenite ± sillimanite and garnet. They are also included in coarse grained K-feldspar, apatite, ilmenite, spinel and biotite, as well as within fine grained aggregates of cordierite, and within fine grained spinel–quartz symplectites (adjacent to cordierite). Sample ST16-03A contains monazite hosted at grain boundaries between cordierite, K-feldspar, biotite and quartz, and as inclusions in biotite, K-feldspar, cordierite, quartz and ilmenite.

Xenotime is predominantly hosted at grain

Table 5. Summary of monazite microstructural locations. Microstrutural locations and proportions determined by point counting of MLA maps (see text for details). Mineral abbreviations after Holland and Powell (2011). Cg, coarse grained.

Sample	Grain boundary			Stable phases						Reactant phases				Product phases						
	matrix	apt	total	and	bi (cg)	mu	Ksp core	ilm	total	bi	qz	crd	total	ksp rim	sill	pl	crd	sp	gt	total
Metapelites																				
ST16-31J	94 05		94 05	3 49	2 46				5 95				0 00							0 00
STF33P	87 24		87 24	8 16		2 04	1 53		11 73		1 02		1 02							0 00
STF02B	75 26		75 26		0 61		1 69		2 30	3 91	6 47		10 38	12 06						12 06
STF16A	68 61		68 61		0 89		7 59		8 48	0 71	4 88		5 60	17 32						17 32
ST16-09	76 42	0 39	76 81				1 17		1 17	2 09			2 09	19 16	0 78					19 94
ST16-19A	67 64		67 64		5 04		4 81		9 85	4 84		1 69	6 53	10 59	0 11	0 15	5 14			15 98
Metapsammites																				
ST16-31A	97 89		97 89						0 00		2 11		2 11							0 00
STF33	94 58		94 58		0 61	1 06			1 68		3 74		3 74							0 00
STF04A	93 75		93 75		2 12	1 06	3 07		6 25				0 00							0 00
STF10B	88 65		88 65				0 97		0 97		7 68	0 92	8 60	1 30			0 47			1 77
STF26A	65 78	6 15	71 93		1 26		8 83	0 15	10 24	0 87	5 88		6 74	6 67	0 27		1 34	1 53	1 27	11 08
ST16-03C	86 86		86 86		1 01		0 47		1 48		11 66		11 66							0 00

boundaries (>89.77% of xenotime) in the subsolidus samples and the two granulite facies psammite samples (ST16-31J, STF33P, STF02B, ST16-31A, STF33, STF04A, STF26A and ST16-03C), with the remainder being hosted as inclusions in K-feldspar. In the suprasolidus pelite samples (STF16A, ST16-09 and ST16-19A) approximately half of the xenotime is hosted at grain boundaries (59.70%, 49.14% and 43.13% respectively). The remainder of the xenotime in these samples is hosted as inclusions in K-feldspar (40.30%, 50.86% and 18.75% respectively) and, in ST16-19A, cordierite (34.38%) and coarse grained biotite (3.75%). The lowest proportion of grain boundary xenotime is found in sample STF10B (17.46%) with the remainder of the xenotime hosted as inclusions in K-feldspar. In the two samples that contain zone D (apatite grain boundary) monazite (ST16-09 and STF26A), xenotime found at grain boundaries of coarse grained apatite account for 3.09% and 49.26% respectively of all grain boundary xenotime.

Monazite volume proportions at Mt Stafford, calculated from point counting, are in the range 0.003–0.027% for pelite samples and 0.007–0.016% for metapsammite samples (Fig. 6). Monazite is present in all samples and, if anything, the proportion of monazite increases with metamorphic grade.

Monazite volume increase is accompanied by an increase in apatite volume at higher grades in both metapelite and metapsammite samples (Fig. 6). Zircon proportion in the metapelite samples decreases from mid to upper amphibolite, then increases to the granulite facies. In the metapsammite samples, zircon proportion is similar in all samples, but slightly higher in the upper amphibolite facies samples (STF04A, STF10B). Xenotime abundance decreases with metamorphic grade in the metapelite samples, and increases with metamorphic grade in the metapsammite samples. Allanite was not detected in the samples except as rare intergrowths with apatite on monazite rims in sample ST16-03C (see Fig. 7).

Table 6. Representative EPMA analyses of monazite. Hut, Huttonite/cheralite; N/A, not analysed.

mnz zone	A	B	B*	C	C*	D	Hut
Sample	ST16-31J	STF04A	STF10B	ST16-19A	ST16-09	STF26A	STF10B
Grain	mnz 19	mnz 4	mnz 4	mnz 8	mnz 17	mnz24	mnz 3
Analysis	59-1	48-1	7-5	29-2	119-3	82-1	6-4
SiO_2	0 32	0 37	1 52	0 43	0 32	0 17	3 20
CaO	1 26	0 50	2 42	1 00	1 07	0 62	2 68
Y_2O_3	1 20	1 28	2 34	1 37	4 04	3 06	1 74
La_2O_3	14 49	15 06	10 78	14 42	14 08	13 65	7 90
Ce_2O_3	28 31	30 04	22 55	28 77	26 40	30 42	16 96
Pr_2O_3	2 83	3 27	2 29	2 99	2 69	3 21	1 76
Nd_2O_3	10 22	11 14	8 48	11 06	9 72	12 44	6 69
Sm_2O_3	1 76	1 69	1 44	1 73	1 73	2 01	1 24
Gd_2O_3	1 26	1 17	1 23	1 40	1 67	1 69	1 13
ThO_2	5 21	3 24	14 84	5 12	4 08	0 38	27 18
UO_2	0 55	0 12	0 47	0 13	1 00	0 42	0 41
PbO	0 54	N/A	1 28	0 40	0 61	0 11	2 10
P_2O_5	32 27	30 43	29 55	31 33	31 78	32 06	26 51
Total	100 21	98 32	99 19	100 15	99 19	100 23	99 50
Si^4	0 012	0 014	0 059	0 016	0 012	0 007	0 129
Ca^2	0 051	0 021	0 101	0 041	0 044	0 025	0 116
Y^3	0 024	0 027	0 048	0 028	0 082	0 061	0 037
La^3	0 202	0 217	0 155	0 203	0 197	0 190	0 117
Ce^3	0 391	0 430	0 321	0 402	0 367	0 419	0 250
Pr^3	0 039	0 047	0 032	0 042	0 037	0 044	0 026
Nd^3	0 138	0 156	0 118	0 151	0 132	0 167	0 096
Sm^3	0 023	0 023	0 019	0 023	0 023	0 026	0 017
Gd^3	0 016	0 015	0 016	0 018	0 021	0 021	0 015
Th^4	0 045	0 029	0 131	0 044	0 035	0 003	0 249
U^4	0 005	0 001	0 004	0 001	0 008	0 004	0 004
Pb^2	0 005	N/A	0 013	0 004	0 006	0 001	0 023
P^5	1 030	1 008	0 973	1 013	1 021	1 022	0 904
Total Cations (S)	1 979	1 987	1 99	1 986	1 984	1 99	1 983

5.4 EPMA

Representative analyses of monazite composition are given in Table 6 and compositional ranges are summarised in Table 7. Representative EPMA maps of monazite and trends in ThO2_mnz with

Table 7. Ranges of compositional variables for monazite zones. Th ZA wt% concentrations calculated from EPMA point analyses and compositional maps. All other variables calculated from EPMA point analyses.

	Zone A	**Zone B**	**Zone B***	**Zone C**	**Zone C***	**Zone D**	**huttonite**
ThO_2_ZA wt%							
range	0.21–6.58	0.50–8.76	9.06–21.14	3.71–6.99	3.35–5.57	0.38–0.44	25.43–42.58
mean	2.76	5.49	16.54	5.54	4.17	0.41	32.20
point analyses							
ThO_2 wt%	0.40–10.32	3.02–9.74	13.93–27.18	4.50–7.58	3.27–5.80	0.22–1.69	7.92–25.20
Ce_2O_3 wt%	23.89–31.70	25.66–30.04	16.96–22.88	25.23–29.03	24.56–27.61	29.13–30.77	16.73–25.82
Y_2O_3 wt%	0.75–2.84	0.93–3.77	1.71–2.30	1.85–3.61	2.04–5.10	2.37–3.06	1.64–2.80
Th wt%	0.00–9.07	2.65–8.56	12.25–23.89	3.95–6.66	2.87–5.10	0.19–1.49	6.96–22.14
Ce wt%	10.20–13.53	10.96–12.83	7.24–9.77	10.77–12.39	10.48–11.79	12.43–13.14	7.14–11.02
Y wt%	0.30–1.12	0.37–1.48	0.67–0.91	0.73–1.42	0.80–2.01	0.93–1.21	0.65–1.10
p(mnz)	0.81–1.01	0.85–0.95	0.04–0.15	0.87–0.93	0.89–0.93	0.97–1.00	0.01–0.09
p(cher)	0.01–0.19	0.04–0.14	0.18–0.29	0.06–0.13	0.07–0.11	0.01–0.03	0.12–0.29
p(hut)	-0.02–0.04	-0.03–0.05	0.60–0.78	-0.01–0.01	-0.01–0.01	-0.02–0.00	0.62–0.87

Th_ZA = zone average Th, p(mnz)= proportion of monazite end-member (∑REE), p(cher)= proportion of cheralite end-member ($2Ca^{2+}$), p(hut)= proportion of huttonite end-member ($Th^{4+}+U^{4+}-Ca^{2+}$).

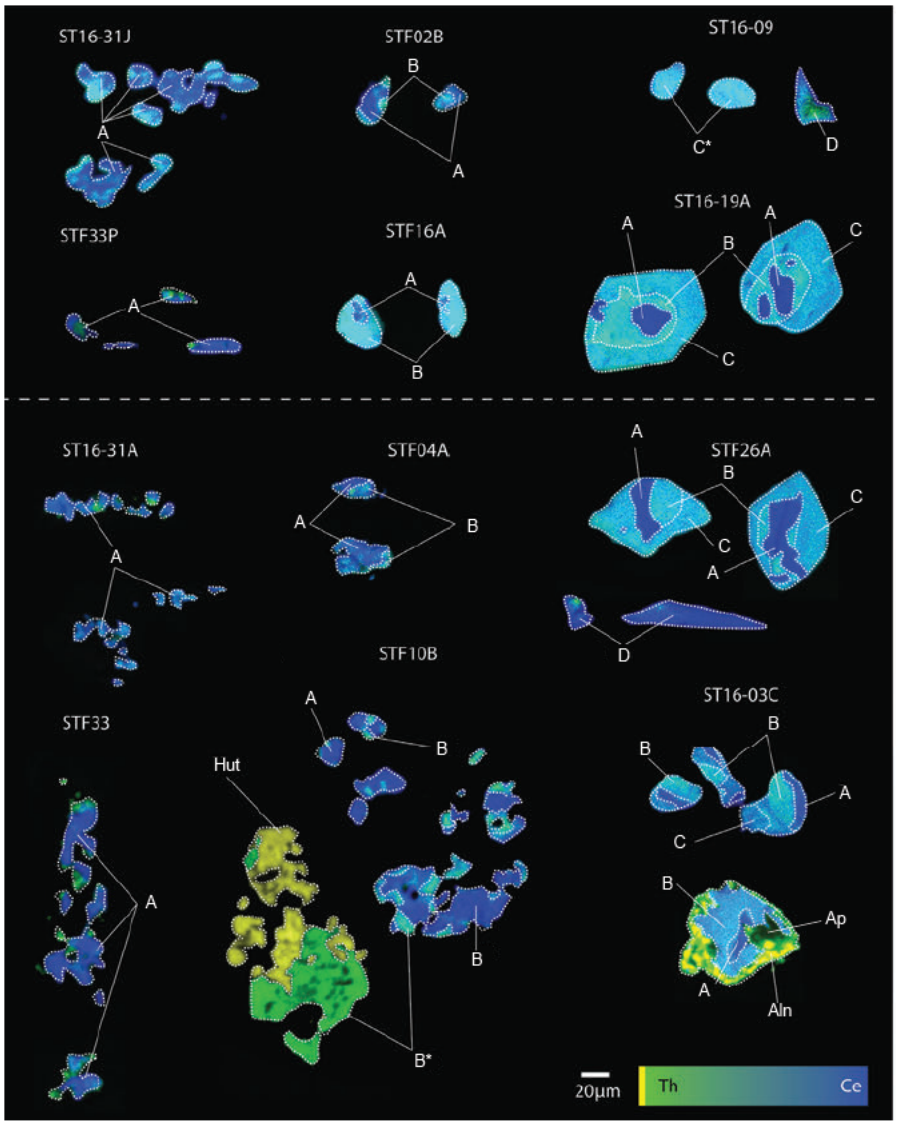

Figure 7. Representative EPMA maps of monazite from Mt Stafford. Images are composite qualitative maps of thorium and cerium with the two element maps overlain (thorium in green and cerium in blue). A D, B*, C* refer to monazite zones described in text. Yellow areas represent thorium rich minerals allanite and huttonite (labelled Aln and Hut respectively).

metamorphic grade are shown in Figures 7 and 8 respectively. On the basis of EPMA map and point data as well as the spatial distribution of compositional zones within monazite, monazite grains and parts of grains in the samples have been separated into six chemical zones as follows:

Zone A monazite occurs in all samples except ST16-09, as either whole grains or as cores of grains. Zone A monazite commonly occurs as clusters of small grains (<10 µm each, Fig. 7), particularly in the amphibolite facies samples. In upper amphibolite and granulite facies samples, zone A monazite forms the cores of larger grains, with typically embayed zone edges (Fig. 7). This zone is rich in the Ce-monazite endmember, but shows a range of ThO_2_ZA contents (0.21–6.58 wt%; mean 2.76 wt%; Table 6), which define a sublinear negative correlation with Ce_2O_3_mnz contents. These grains have low Y_2O_3_mnz concentrations (0.75–2.84 wt%; Table 6).

Zone B monazite occurs in upper amphibolite and granulite facies samples. This zone occurs rim-ward of zone A and has higher Th_ZA (0.50–8.76 wt%; mean 5.49 wt%; Table 6) and lower Ce_2O_3_mnz (25.66–30.04 wt%; Table 6) than Zone A.

Zone B* monazite is found exclusively within sample STF10B, occasionally adjacent to grains of huttonite. Zone B* monazite has very high Th_ZA contents in the range 9.06–21.14 wt% (Table 6). Zone B* monazite also occurs as grains with cores containing Zone A and B monazite (Fig. 7). Grains of zone B* monazite show no core-rim relationship with adjacent huttonite.

Zone C monazite occurs in granulite facies samples, rim-ward of zone B. Zone C monazite

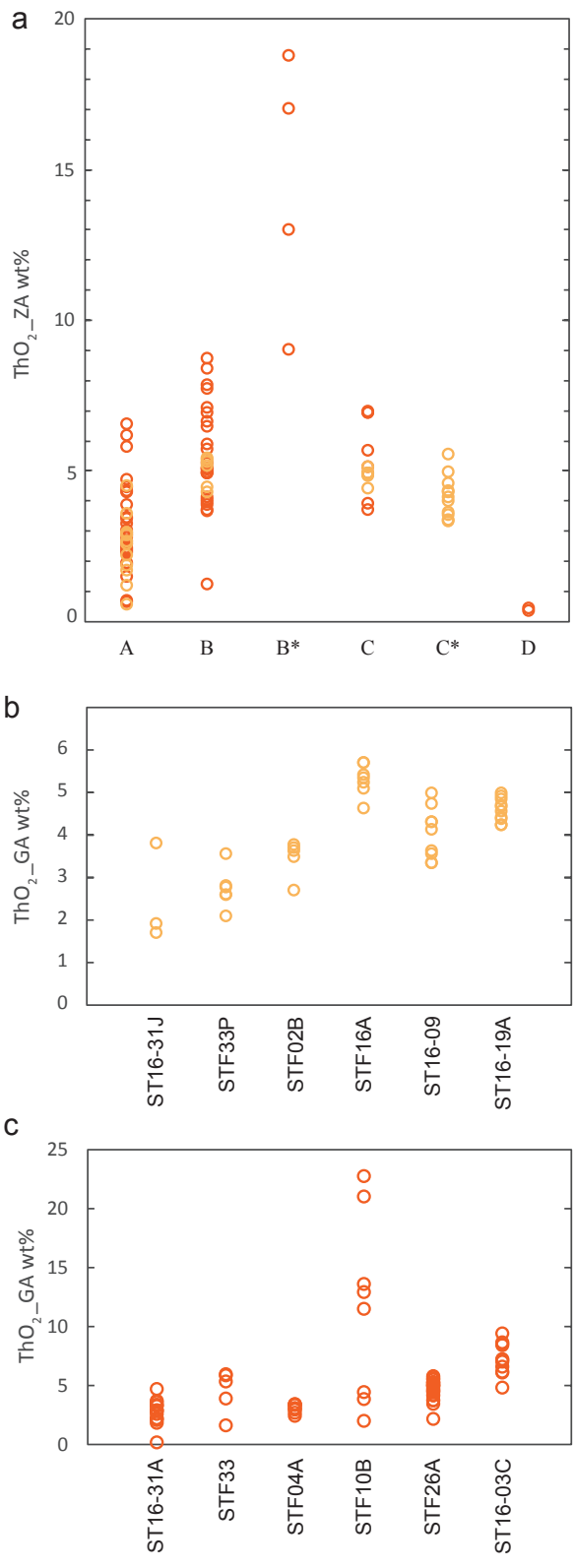

Figure 8. Zone average and grain average thorium concentrations from Mt Stafford. (a) Zone average ThO_2 wt% concentrations vs monazite zone. Monazite zones B* and C* are found exclusively within samples STF10B and ST16 09 respectively, see text for details; (b) Grain average ThO_2 wt% concentrations for metapelite samples; (c) Grain average ThO_2 wt% concentrations for metapsammite samples.

commonly surrounds cores with components of both zones A and B. Zone C monazite has high Th_ZA (3.71–6.99 wt%; mean 5.54 wt%) and comparable Ce_2O_3_mnz (25.23–29.03; Table 6) to Zone B.

Zone C* monazite is found exclusively in sample ST16-09 and has the highest Y_2O_3_mnz concentrations of the zones (2.04–5.10 wt%). It has lower Ce_2O_3_mnz concentrations (24.56–27.61 wt%) and Th_ZA concentrations in the range 3.35–5.57 wt % (mean 4.17 wt%; Table 6). Zone C* monazite typically has higher HREE concentrations (Table 6).

Zone D monazite occurs as small, elongate grains at the grain boundaries of apatite (Fig. 5) in samples ST16-09 and STF26A. This zone has characteristically low Th_ZA contents (0.38–0.44), high Ce_2O_3_mnz (29.13–30.77) and (relatively) high Y_2O_3_mnz (2.37–3.06; Table 6). Zone D monazite typically has very low Si and Ca concentrations (Table 6).

Not all EPMA point analyses could be uniquely assigned to a monazite zone either due to mixing or zones being unresolvable at the scale of the EPMA maps. The zones A–D are described on the basis of analyses that could be unambiguously assigned to one zone. In both metapelitic and metapsammitic samples, ThO_2_GA concentrations (weighed average Th concentrations from individual grains) are higher in granulite facies rocks than subsolidus samples with similar bulk compositions (Fig. 8b,c).

Monazite grains for every unique microstructural location were analysed (EPMA points and EPMA maps) to allow textural analysis of monazite composition. This analysis revealed limited microstructural control on the distribution of all monazite zones except zone D, which is limited to the grain boundaries of large apatite grains (see above). In samples ST16–31J, STF33P, STF16A, ST16–09, ST16-31A, STF33, STF04A, STF10B and STF26A there is no correlation between microstructural location and composition for zones A, B, B*, C and C*, such that monazite found at grain boundaries and as inclusions show the same type of zonation. In sample STF02B, rare grains of monazite composed wholly of zone A occur as inclusions in K-feldspar, with monazites in all other microstructural locations composed of both zones A and B monazite. In sample ST16-03C, there is one monazite grain wholly composed of monazite zone B, which

is found in contact with xenotime. There are two grains which show breakdown (interpreted as retrogression) to a mixture of finer-grained allanite and apatite, one of which is included in biotite and the other of which is at a grain boundary between quartz and K-feldspar. Sample ST16-19A contains one instance of monazite with only zones A and B included in K-feldspar. All other monazite grains included in K-feldspar also contain zone C. In this sample, the only grain found to be wholly composed of zone C monazite occurs at the grain boundary between ilmenite, biotite and quartz, but other grains found in similar microstructural locations also contain monazite zone B.

6 DISCUSSION

6.1 Melt loss and the preservation of monazite

Previous studies of the Mt Stafford terrane have established that up to 23% melt was produced at the highest metamorphic grade (Bartoli, 2017) and that a portion of this melt was subsequently extracted from the sequence (Palya et al., 2011; White et al., 2003) consistent with the decrease in biotite abundance across the terrane represented by the samples in this study. Monazite is present in all of the samples in this study and grains from the highest grade rocks preserve interpreted prograde zoning features (Fig.7). This indicates that monazite was stable up to the highest grades of metamorphism in the terrane.

Zr_WR from the studied samples (Fig. 3) increases with metamorphic grade in both metapelitic and metapsammitic lithologies, with this increase more pronounced in the metapelite samples. Typically Zr is highly compatible and partitions into zircon rather than melt (e.g. Rubatto & Hermann, 2007), and with increasing temperature, the mode of relatively Zr-rich minerals (e.g. garnet) also increases (Kohn, Corrie, & Markley, 2015). The concurrent increase in zircon proportion with metamorphic grade, particularly in the metapelite samples, suggests that in the Mt Stafford rocks zircon did not participate in melting reactions to a large degree and that the Zr_WR concentration is a proxy for increasing melt loss from the residue. This trend supports the findings of Bartoli (2017) and Palya et al. (2011) that melt was progressively lost for the Mt Stafford terrane along the prograde path. Given the role of bulk rock Zr content on relative changes to zircon abundance between the rock types we have studied (Kelsey, Clark, & Hand, 2008; Yakymchuk & Brown, 2014), it is not possible to determine the relative abundance of melt loss in the pelite and psammite sequences uniquely from this dataset. That is, rocks with higher bulk Zr will record a proportionally smaller increase to zircon abundance with increasing temperature as a function of melt production and loss (Kelsey et al., 2008; Yakymchuk & Brown, 2014), as seen for the metapsammites in Figure 3, that is not uniquely a function of more or less melt loss than the metapelites.

6.2 Bulk rock trends in thorium distribution

GRS data from Mt Stafford shows that there is an overall increase in Th_GRS concentration from amphibolite to granulite facies rocks (Fig. 4; Alessio et al., 2018). In the granulite facies, the scatter in Th_GRS and Th_WR data is larger than in the amphibolite facies rocks (Fig. 4). This probably suggests small-scale differentiation in the granulite facies, consistent with greater heterogeneity of grain size and mineralogy in these samples due to the presence of coarse peritectic mineral-bearing leucosomes. Residual rocks segregated from leucosomes ("schlieren migmatites"; Fig. 4; White et al., 2003) show an increase in Th_GRS concentrations relative to subsolidus rocks with similar compositions, as well as an increase compared to Th_GRS concentrations in the leucosome-rich rocks in the same part of the sequence. Together these observations suggest that during melting Th preferentially partitioned into the residuum, which in turn suggests that with increasing melt fraction the residuum becomes more enriched in Th. This finding supports experimental data of Stepanov et al. (2012) in which Th strongly partitioned into monazite rather than silicate melt, with monazite commonly being retained in the residuum (Watt, 1995; Watt & Harley, 1993).

Th_WR concentrations for all investigated samples from Mt Stafford are the same within error, however $2\boldsymbol{\sigma}$ errors on these analyses are very large (~20 ppm) and thus analytical error masks any systematic trend that may be present in the whole rock budget of thorium for these samples. Mass balance approximations of the abundance and chemistry of monazite and other Th-bearing minerals (apatite, xenotime and huttonite) in the samples suggest that the whole rock concentration of thorium should increase

with metamorphic grade. This is consistent with trends in Th_GRS which show that thorium concentration (albeit from larger sample volumes than whole rock XRF chemistry) is preserved through the prograde sequence at Mt Stafford, and enriched in the residue with respect to the melt fraction (Fig. 4).

6.3 Monazite distribution at Mt Stafford

Monazite volume proportions in metapelitic samples broadly increase with increasing metamorphic grade (Fig. 6). The two lower amphibolite facies metapelitic samples, ST16-31J and STF33, have significantly different proportions of monazite (0.020 and 0.003 vol% respectively). These samples also have markedly different proportions of apatite, with 0.001 and 0.072 vol% respectively, correlated with Ce_WR of 78 and 163 ppm, La_WR 36 ppm and 26 ppm and Ca_WR of 0.03 and 0.10 wt%, all respectively. This is interpreted to be a relic of source heterogeneity in the abundance of the phosphates or bulk-rock composition, with ST16-31J being a monazite-rich layer, and STF33P being a relatively monazite-poor and LREE–calcium-rich layer. Elevated calcium content of a rock has been reported to increase the stability of apatite and/or allanite at the expense of REE-monazite (discussed further below; Spear & Pyle, 2010; Yakymchuk, 2017). Monazite volume proportions increase consistently in the metapelitic samples from the upper amphibolite facies into the granulite faces, accompanied by a decrease in biotite abundance.

In the metapsammitic samples, monazite volume proportions increase through the amphibolite facies and then decrease slightly in the granulite facies rocks (Fig. 6), suggesting that monazite is less stable in metapsammitic compositions than metapelitic compositions in the granulite facies. This may be a function of lower total LREE whole rock concentration in metapsammites compared to metapelites, a known control on monazite stability (e.g. Kelsey et al., 2008; Rapp et al., 1987; Rapp & Watson, 1986; Yakymchuk, 2017). Furthermore, in granulite facies sample ST16-03C allanite occurs as rims on monazite in some cases (Fig. 7). Allanite is known to form by the breakdown of monazite in (sub-) greenschist facies rocks (e.g. Budzyń, Harlov, Kozub-Budzyń, & Majka, 2017; Gieré & Sorensen, 2004; Janots et al., 2007; Smith & Barreiro, 1990; Wing, Ferry, & Harrison, 2003), so these allanite rims likely represent breakdown of monazite on the retrograde path, and account for some of the decrease in monazite abundance in the granulite facies samples. The allanite in these rare cases is intergrown with apatite, and from raw EPMA map data the intergrowth has similar Th content to zone B monazite from the same grain.

In both lithologies, monazite grain size broadly increases with increasing metamorphic grade (Table 4). This is linked with decreasing numbers of monazite grains (Table 4), which suggests sample scale recrystallization of monazite and movement of thorium occurred, with increasing efficiency at higher grades, as monazite is the only major Th-bearing mineral in the samples. This may be a result of Ostwald ripening, where smaller grains are preferentially dissolved which facilitates the growth of new monazite on the crystal faces of larger grains (cf. Rapp & Watson, 1986; Yakymchuk & Brown, 2014). Wholesale recrystallization of all monazite grains is unlikely as monazite grains from granulite facies rocks preserve compositional zones (A and B), predominantly within cores of grains, (Fig. 7; see Taylor, Kirkland, & Clark, 2016), which have consistent chemistry with monazite found in lower grade samples, interpreted as preservation of prograde zoning in these grains.

Monazite in all samples is evenly (but not entirely homogeneously) distributed at the thin section scale, occurring at grain boundaries and within porphyroblasts in all mineralogical domains in the granulite facies samples. The total amount of monazite hosted as inclusions is higher in the granulite facies samples than the subsolidus amphibolite facies samples (total incl. mnz, Table 4). This represents an important mechanism for retaining monazite in granulite facies rocks (e.g. Bea, 1996; Watson, Vicenzi, & Rapp, 1989). In all samples the majority of monazite is hosted at grain boundaries (67.64–94.05% in pelite samples, 71.93–97.89% in psammite samples, table 5), with slightly more monazite hosted at grain boundaries in the psammitic samples. The grainsize of monazite hosted at grain boundaries is also larger in the granulite facies samples relative to amphibolite facies samples, suggesting that monazite dissolution and reprecipitation was assisted by the mobility of monazite forming elements (REEs and Th) along grain boundaries. The grainsize of included monazite is typically <10μm and thus the internal variation of many included grains was irresolvable at the scale of the maps. Those grains for which internal zones

were resolvable record both prograde and peak monazite compositions.

Monazite throughout each thin section has ThO_2–GA concentrations that show no systematic variation with microstructural setting, except for where grains are wholly composed of zone D, discussed further below. This suggests that dissolution/reprecipitation processes occurred in a somewhat efficient manner, as grains become more systematically zoned with increasing metamorphic grade. Zones A–D are found in multiple samples and suggest that similar reactions and/or diffusion processes were in operation within the samples during the growth of monazite. Zones B* and C* are only found in samples STF10B and ST16-09 respectively, suggesting that these samples have distinct chemistries that allowed alternative reactions/ exchange mechanisms to dominate monazite growth.

6.4 Monazite forming reactions

In the following we explore possible reaction mechanisms by which monazite may have grown, taking into account (a) volume proportion changes; (b) microstructural location of monazite; (c) chemistry of monazite zones A–D; and (d) possible sources of LREE and Th.

Most studies linking monazite growth to silicate mineral reactions have focussed on garnet-bearing rocks or sequences (e.g. Corrie & Kohn, 2008; Kohn & Malloy, 2004; Pyle & Spear, 2003; Pyle et al., 2001) and have linked the Y concentration of monazite to Y-in-garnet and Y-in-xenotime (e.g. Pyle et al., 2001; Spear & Pyle, 2010). However, almost all the Mt Stafford rocks are garnet- and plagioclase-absent (REE hosts), except in the leucosome (melt)-bearing granulite facies rocks (Greenfield et al., 1996; Rubatto et al., 2006). Therefore it is more difficult to link monazite/ accessory mineral growth to major silicate mineral reactions for the Mt Stafford samples, but K-feldspar is likely to play an important role as a LREE host/source (e.g. Rubatto et al., 2006), as is apatite (e.g.Yakymchuk, 2017).

Previously proposed monazite-forming reactions at amphibolite facies (e.g. Gasser, Bruand, Rubatto, & Stüwe, 2012; Janots et al., 2008; Tomkins & Pattison, 2007; Wing et al., 2003) generally contain allanite as a reactant and plagioclase as a product, neither of which is common in the Mt Stafford samples. *P–T* equilibrium modelling of monazite and allanite (Spear, 2010; Spear & Pyle, 2010) shows that the bulk rock CaO composition is one factor which has a dramatic effect on the stability of allanite and monazite (cf. Yakymchuk, Clark, & White, 2017). For a bulk rock CaO content of 1.08 wt%, the allanite-monazite phase transition occurs at ~450 ºC at 3 kbar, whereas in a composition with double the CaO content, the same transition occurs at ~700 ºC at the same pressure. This suggests that for the Mt Stafford samples (all with CaO <1.08 wt%), any prograde/ detrital allanite would have been removed from the rocks a temperatures below 450 ºC, well below the minimum temperature estimate for the lowest grade samples (580 ºC). However, as there is no direct evidence for the presence of allanite below the amphibolite facies at Mt Stafford, we cannot prove that it existed during prograde metamorphism. If allanite was not the Ca source for apatite (and monazite) then the source may have been pre-existing/ detrital apatite, or small amounts liberated from silicate minerals such as feldspar. The potential role for xenotime in this reaction is not clear.

The concentration of Th in monazite is known to increase up temperature from both natural examples (e.g. Engi, 2017)and predictions from phase equilibria forward modelling (Yakymchuk et al., 2018). Zone A monazite is interpreted to have grown at temperature conditions lower than the recorded conditions in the lowest grade rocks exposed at Mt Stafford (i.e. on the prograde path), since it has the lowest Th concentration of the three major zones (A–C) and is present in all samples except ST16-09. The heterogeneity of Th_ZA concentrations (and individual EPMA point analyses) in zone A monazite is large compared with other zones, and this may reflect a larger proportion of detrital monazite with highly variable composition. Much of the monazite in the mid-amphibolite facies rocks where zone A monazite is most prevalent was too small to be analysed, and thus the full extent of this heterogeneity cannot be assessed. Zone A monazite may have been grown according to a reaction that involved the breakdown of allanite at lower temperatures (i.e. greenschist or lower amphibolite) than those previously proposed (e.g. Gasser et al., 2012; Janots et al., 2007; Rasmussen, Muhling, Fletcher, & Wingate, 2006; Tomkins & Pattison, 2007; Wing et al., 2003), although this cannot be assessed in these samples.

Growth of monazite zones B and C are similarly

difficult to link to precise mineral reactions. The progression of low Th cores (zone A) to higher Th rims (zones B and C) is contrary to the findings of (Kohn & Malloy, 2004), where monazite evolved from high Th to low Th with prograde metamorphism. This was proposed to be due to stoichiometric constraints, with earlier monazite sequestering the majority of Th in the rock. Thus, later monazite (rims) were enriched in LREE because less thorium was available. This mechanism may explain the slight reduction in ThO_2_ZA between zones B and C (see also Engi, 2017). The increase in ThO_2_ZA between zones A and B is concurrent with an increase in apatite volume proportion from the mid to the upper amphibolite facies. Both these trends are more apparent in the metapsammite samples and may have a causal relationship, where the increase in the stability (and therefore growth) of apatite makes the LREEs less available for the growth of monazite, and thus zone B monazite is more Th-rich than zone A monazite. Simultaneously, melt has been lost from the system with metamorphic grade which likely results in an apparent increase in the volume of monazite with metamorphic grade, but limited extraction of thorium from the residue (see below). The slight decrease in Th between zone B and C monazite may reflect the Rayleigh-like stoichiometric mechanism proposed by Kohn and Malloy (2004), or that some Th is lost to melt as a consequence of partial monazite dissolution (e.g. Stepanov et al., 2012).

Zone D monazite occurs exclusively around the margins of larger metamorphic apatite grains in the granulite facies samples (ST16-09, STF26A), and is interpreted to have formed by breakdown of apatite during the retrograde metamorphic history (Fig. 5; e.g. Harlov, Förster, & Nijland, 2002; Harlov, Wirth, & Förster, 2005). These same apatite grains have micro-inclusions of monazite (Fig. 5) which were too small to be analysed, but are interpreted to have formed during recrystallization of the apatite. Similarly, these large apatite grains also have grain margin xenotime associated with them, interpreted to have formed by the same breakdown process.

6.5 Grain scale trends in thorium distribution

In the metapelites, there is an upward trend in ThO_2_GA until the upper amphibolite facies (sample STF16A), and the trend plateaus in the granulite facies (Fig. 8b). This coincides with the appearance of zones C and C* monazite in the granulite facies samples (ST16-09A and ST16-19A), both of which are lower in ThO_2_ZA than zone B monazite, which predominates amphibolite facies samples (e.g. STF02B). In the metapsammite samples a similar trend is seen, however the granulite facies samples (ST1F26A and ST16-03C) continue the upward trend of the lower grade samples, with STF10B the outlier (Fig. 8c). The ThO_2_GA concentrations in a given sample typically span ≤ 5 wt%, except in sample STF10B where it spans ~20 wt% (Fig. 8b). STF10B has several grains with systematically higher ThO_2_GA contents than any other sample in the study. This sample contains a small population of monazites with compositions equivalent to zones A and B; however, the majority of the monazite analysed in the sample has significant proportions of the huttonite end-member (zone B* monazite) and coexists with huttonite (Fig. 7). The whole rock chemistry of STF10B is similar to that of other samples (Fig. 3). The sample fits within the metapsammitic trends of both monazite abundance and the abundance of the other phosphates (Fig. 6). Furthermore, the Th_WR of the sample is the same as the other metapsammite samples within error (albeit with large analytical uncertainty). It is therefore unclear why this sample contains monazites with such high Th_mnz concentrations. The P_2O_5_WR content of sample STF10B is amongst the highest of all the metapsammite samples, so a deficiency in P_2O_5 cannot explain why monazite in STF10B has such high huttonite component, or why huttonite is stable as a separate phase. A similar relationship between monazite and huttonite/thorite was reported by Bingen, Demaiffe, and Hertogen (1996), which suggested that composite monazite/thorite grains were produced by the prograde breakdown of allanite. This may indicate that the protolith of STF10B contained allanite. However as there is no occurrence of allanite in the low grade samples in this study, and STF10B contains no relict allanite, this cannot be confirmed. Alternatively, the protolith of STF10B may have contained more Th and P due to the sedimentary concentration of heavy minerals in this layer.

In all other metapsammite samples the range of ThO_2_GA increases with metamorphic grade (Fig. 8b), but notably the spread of compositions within each monazite zone gets smaller (Fig. 8a). Thus the spread of ThO_2_GA in the mid

amphibolite facies samples is representative of low grade and pre-metamorphic monazite of zone A, whereas the granulite facies samples represent within-grain averaging of zones A–C of various proportions, as well as zone C* grains.

By sampling monazites across metamorphic grade, we can identify that a considerable proportion of monazite present in granulite facies rocks in the Mt Stafford system was grown on the prograde path (Fig. 7). This is demonstrated by the increase in the total amount of monazite found as inclusions in both the pelitic and psammitic granulite facies samples relative to chemically similar subsolidus samples (total incl. mnz, Table 4).The ThO_2_ZA concentrations of zone C monazite, interpreted by its presence exclusively within granulite facies rocks to have grown at granulite facies conditions, shows considerable overlap with monazite compositions from zones A and B. Combined with the large proportion of zone A and B monazite in granulite facies samples, this helps explain that Th is not depleted in the residual rocks in this study (as shown by trends in Th_GRS) due to the retention of considerable proportions of high-Th monazite from lower metamorphic grades in high grade (granulite facies) rocks.

Monazite-melt partitioning coefficients for Th (Stepanov et al., 2012) show that Th is approximately 30% more compatible in monazite than the LREE, resulting in an increasing Th/La ratio in monazite with increasing temperature in their melting experiments. The implication in melt-bearing systems is that monazite compositions with become increasingly Th-rich up to the point of total dissolution. Additionally, monazite has been shown to be stable to higher temperatures in open systems where melt extraction is efficient (Yakymchuk & Brown, 2014). When the relative proportions of monazite and melt are taken into account (typically 0.001–0.05% and 1–25% respectively), $D_{mnz/liq}$ dictates that Th in the residue (i.e. monazite) is equal to or greater than Th in melt for typical pelitic compositions (ThO_2–in–mnz = 1–6%, Th_WR = 20–40 ppm), which provides a mechanism for the retention of Th in residual rocks.

6.6 Retention of thorium in granulite facies terranes

The Mt Stafford sequence can be considered an endmember in terms of metasedimentary composition (low Ca) and geothermal gradient. However, as shown by Alessio et al. (2018) thorium is retained in the residuum well into the granulite facies in several terranes worldwide. Additionally, retention of monazite and thus thorium into the granulite facies was previously reported for several terranes (e.g. Bea & Montero, 1999; Bingen et al., 1996; Gasser et al., 2012; Rubatto, Williams, & Buick, 2001) suggesting that the results presented here represent common mid-deep crustal processes. However, there are terranes that potentially have lower Th concentrations in granulite facies rocks with respect to their amphibolite facies counter parts (e.g. the Superior Province, Canadian Shield; Ashwal, Morgan, Kelley, & Percival, 1987) which cannot be explained by the same partial melting processes that occurred at Mt Stafford.

The destabilisation of monazite in granulite facies rocks may be caused by a range of factors including bulk-rock composition, P–T history, melting and melt extraction history, and fluid influx. Monazite is known to be most stable in rocks of metapelitic composition. High bulk-rock calcium contents can result in the destabilisation of monazite at lower temperatures, as can low bulk rock silica contents (e.g. Kelsey et al., 2008; Spear & Pyle, 2002). However, we show in this study that monazite and Th can be retained in rock of both pelitic and psammitic composition along steep geothermal gradients, both as inclusions within major phases and at grain boundaries. Modelling studies by Kelsey et al. (2008), Yakymchuk (2017) and Yakymchuk and Brown (2014) suggest that monazite solubility in silicate melt has limited pressure dependence. Therefore, despite the high geothermal gradient of the Mt Stafford terrane it is likely that the results presented here are applicable to other low-Ca metapelites which attained higher pressure conditions.

The results presented here, in combination with experimental studies (e.g. Stepanov et al., 2012) suggest that partitioning of Th into monazite over melt sequesters the majority of bulk rock Th from the original source rocks while monazite remains stable. Modelling in Yakymchuk (2017) indicates that in an open system (with incremental melt loss) monazite may be stable well into UHT granulite facies conditions (>900°C). The Mt Stafford granulite facies rocks reached temperatures of 820°C (Bartoli, 2017), which is below the predicted monazite 100% dissolution contours of Yakymchuk (2017) for rocks of pelitic composition with similar LREE and P budgets.

Therefore, for the pelitic residue to be depleted in Th, the wholesale dissolution of monazite may be required and thus temperatures in excess of 900°C.

Monazite is also known to be unstable in fluids of particular compositions (e.g. brines, aluminous melts; Budzyń, Harlov, Williams, & Jercinovic, 2011; Hetherington, Harlov, & Budzyń, 2010). However, the deep continental crust is widely considered to be largely fluid absent (White, Pomroy, & Powell, 2005; White & Powell, 2002). Additionally, fluid absent partial melting is interpreted to be the main process of melt generation, both in the examples of Th rich granulite facies above and in the mid–lower crust as a whole (Brown & Korhonen, 2009). Therefore regional depletion of Th in residual rocks by fluids would require pervasive fluid influx at a terrane scale.

7 CONCLUSIONS

Mt Stafford is a low pressure, low-strain terrane with significant field and microtextural evidence of partial melting and some evidence for melt extraction. Whole-rock thorium concentration is preserved at even the highest grades of metamorphism both at the outcrop and micro-scales. This suggests that the process of partial melting of mid-lower crustal metapelites does not result in the broad-scale destabilisation of monazite, and thus bulk movement of thorium into silicate melt and out of residual crust (see also Alessio et al., 2018). Therefore, in terranes that contain thorium-depleted residual rocks, other factors must be involved, potentially including: differences in composition, resulting in the destabilisation of monazite at lower temperatures; attainment of higher peak temperature conditions; or influx of fluid and/or different melting styles.

ACKNOWLEDGEMENTS

The authors thank C. Yakymchuk and T. Zack for helpful and insightful reviews that greatly improved the quality of this manuscript. M. Scambelluri is thanked for swift editorial handling. B. Liley and C. Kemp are thanked for assistance with fieldwork. Thanks are due to B. Wade and S. Gilbert at Adelaide Microscopy for their assistance with analytical work and S. Mertzman at Franklin and Marshall College for geochemical analysis. This work is supported Australian Research Council project by DP160101006 to DEK. MAW and KLA are supported by Australian Government Research Training Program Scholarships.

SUPPORTING INFORMATION

Appendix S2.1: Whole rock geochemistry for Mt Stafford samples.

REFERENCES

Alessio, K. L., Hand, M., Kelsey, D. E., Williams, M. A., Morrissey, L. J., & Barovich, K. (2018). Conservation of deep crustal heat production. Geology, 46(4), 335 338.

Anderson, J., Kelsey, D., Hand, M., & Collins, W. (2013). Conductively driven, high-thermal gradient metamorphism in the Anmatjira Range, Arunta region, central Australia. Journal of Metamorphic Geology, 31(9), 1003 1026.

Ashwal, L. D., Morgan, P., Kelley, S. A., & Percival, J. A. (1987). Heat production in an Archean crustal profile and implications for heat flow and mobilization of heat producing elements. Earth and Planetary Science Letters, 85(4), 439 450.

Bartoli, O. (2017). Phase equilibria modelling of residual migmatites and granulites: an evaluation of the melt reintegration approach. Journal of Metamorphic Geology, 35(8), 919 942.

Bea, F. (1996). Residence of REE, Y, Th and U in granites and crustal protoliths; implications for the chemistry of crustal melts. Journal of Petrology, 37(3), 521 552.

Bea, F., & Montero, P. (1999). Behavior of accessory phases and redistribution of Zr, REE, Y, Th, and U during metamorphism and partial melting of metapelites in the lower crust: an example from the Kinzigite Formation of Ivrea Verbano, NW Italy. Geochimica Et Cosmochimica Acta, 63(7 8), 1133 1153.

Bingen, B., Demaiffe, D., & Hertogen, J. (1996). Redistribution of rare earth elements, thorium, and uranium over accessory minerals in the course of amphibolite to granulite facies metamorphism: the role of apatite and monazite in orthogneisses from southwestern Norway. Geochimica Et Cosmochimica Acta, 60(8), 1341 1354.

Brown, M., & Korhonen, F. (2009). Some remarks on melting and extreme metamorphism of crustal rocks Physics and Chemistry of the Earth's Interior (pp. 67 87): Springer.

Budzyń, B., Harlov, D. E., Kozub Budzyń, G. A., & Majka, J. (2017). Experimental constraints on the relative stabilities of the two systems monazite (Ce) allanite (Ce) fluorapatite and xenotime (Y) (Y, HREE) rich epidote (Y, HREE) rich fluorapatite, in high Ca and Na Ca environments under PT conditions of 200 1000 MPa and 450 750 C. Mineralogy and Petrology, 111(2), 183 217.

Budzyń, B., Harlov, D. E., Williams, M. L., & Jercinovic, M. J. (2011). Experimental determination of stability relations between monazite, fluorapatite, allanite, and REE epidote as a function of pressure, temperature, and fluid composition. American Mineralogist, 96(10), 1547 1567.

Corrie, S. L., & Kohn, M. J. (2008). Trace element distributions in silicates during prograde metamorphic reactions: Implications for monazite formation. Journal of Metamorphic Geology, 26(4), 451 464.

Engi, M. (2017). Petrochronology based on REE minerals: monazite, allanite, xenotime, apatite. Reviews in Mineralogy and Geochemistry, 83(1), 365 418.

Gasser, D., Bruand, E., Rubatto, D., & Stüwe, K. (2012). The behaviour of monazite from greenschist facies phyllites to anatectic gneisses: an example from the Chugach

Metamorphic Complex, southern Alaska. Lithos, 134, 108 122.

Gieré, R., & Sorensen, S. S. (2004). Allanite and other REE rich epidote group minerals. Reviews in Mineralogy and Geochemistry, 56(1), 431 493.

Greenfield, J., Clarke, G., Bland, M., & Clark, D. (1996). In situ migmatite and hybrid diatexite at Mt Stafford, central Australia. Journal of Metamorphic Geology, 14(4), 413 426.

Greenfield, J. E., Clarke, G. L., & White, R. W. (1998). A sequence of partial melting reactions at Mt Stafford, central Australia. Journal of Metamorphic Geology, 16(3), 363 378.

Harlov, D. E., Förster, H. J. r., & Nijland, T. G. (2002). Fluid induced nucleation of (Y+ REE) phosphate minerals within apatite: Nature and experiment. Part I. Chlorapatite. American Mineralogist, 87(2 3), 245 261.

Harlov, D. E., Wirth, R., & Förster, H. J. (2005). An experimental study of dissolution reprecipitation in fluorapatite: fluid infiltration and the formation of monazite. Contributions to Mineralogy and Petrology, 150(3), 268 286.

Hetherington, C. J., Harlov, D. E., & Budzyń, B. (2010). Experimental metasomatism of monazite and xenotime: mineral stability, REE mobility and fluid composition. Mineralogy and Petrology, 99(3), 165 184.

Holland, T., & Powell, R. (2011). An improved and extended internally consistent thermodynamic dataset for phases of petrological interest, involving a new equation of state for solids. Journal of Metamorphic Geology, 29(3), 333 383.

Janots, E., Brunet, F., Goffé, B., Poinssot, C., Burchard, M., & Cemič, L. (2007). Thermochemistry of monazite (La) and dissakisite (La): implications for monazite and allanite stability in metapelites. Contributions to Mineralogy and Petrology, 154(1), 1 14.

Janots, E., Engi, M., Berger, A., Allaz, J., Schwarz, J. O., & Spandler, C. (2008). Prograde metamorphic sequence of REE minerals in pelitic rocks of the Central Alps: implications for allanite monazite xenotime phase relations from 250 to 610 C. Journal of Metamorphic Geology, 26(5), 509 526.

Kelsey, D. E., Clark, C., & Hand, M. (2008). Thermobarometric modelling of zircon and monazite growth in melt bearing systems: Examples using model metapelitic and metapsammitic granulites. Journal of Metamorphic Geology, 26(2), 199 212.

Kohn, M. J., Corrie, S. L., & Markley, C. (2015). The fall and rise of metamorphic zircon. American Mineralogist, 100(4), 897 908.

Kohn, M. J., & Malloy, M. A. (2004). Formation of monazite via prograde metamorphic reactions among common silicates: implications for age determinations. Geochimica Et Cosmochimica Acta, 68(1), 101 113.

Palya, A. P., Buick, I. S., & Bebout, G. E. (2011). Storage and mobility of nitrogen in the continental crust: Evidence from partially melted metasedimentary rocks, Mt. Stafford, Australia. Chemical Geology, 281(3), 211 226.

Pyle, J. M., & Spear, F. S. (2003). Four generations of accessory phase growth in low pressure migmatites from SW New Hampshire. American Mineralogist, 88(2 3), 338 351.

Pyle, J. M., Spear, F. S., Rudnick, R. L., & McDonough, W. F. (2001). Monazite xenotime garnet equilibrium in metapelites and a new monazite garnet thermometer. Journal of Petrology, 42(11), 2083 2107.

Rapp, R. P., Ryerson, F., & Miller, C. F. (1987). Experimental evidence bearing on the stability of monazite during crustal anatexis. Geophysical Research Letters, 14(3), 307 310.

Rapp, R. P., & Watson, E. B. (1986). Monazite solubility and dissolution kinetics: implications for the thorium and light rare earth chemistry of felsic magmas. Contributions to Mineralogy and Petrology, 94(3), 304 316.

Rasmussen, B., Muhling, J. R., Fletcher, I. R., & Wingate, M. T. (2006). In situ SHRIMP U Pb dating of monazite integrated with petrology and textures: does bulk composition control whether monazite forms in low Ca pelitic rocks during amphibolite facies metamorphism? Geochimica Et Cosmochimica Acta, 70(12), 3040 3058.

Rubatto, D., & Hermann, J. (2007). Experimental zircon/melt and zircon/garnet trace element partitioning and implications for the geochronology of crustal rocks. Chemical Geology, 241(1), 38 61.

Rubatto, D., Hermann, J., & Buick, I. S. (2006). Temperature and bulk composition control on the growth of monazite and zircon during low pressure anatexis (Mount Stafford, central Australia). Journal of Petrology, 47(10), 1973 1996.

Rubatto, D., Williams, I. S., & Buick, I. S. (2001). Zircon and monazite response to prograde metamorphism in the Reynolds Range, central Australia. Contributions to Mineralogy and Petrology, 140(4), 458 468.

Shaw, D. M. (1956). Geochemistry of pelitic rocks. Part III: Major elements and general geochemistry. Geological Society of America Bulletin, 67(7), 919 934.

Skora, S., & Blundy, J. (2010). High pressure hydrous phase relations of radiolarian clay and implications for the involvement of subducted sediment in arc magmatism. Journal of Petrology, 51(11), 2211 2243.

Smith, H. A., & Barreiro, B. (1990). Monazite U Pb dating of staurolite grade metamorphism in pelitic schists. Contributions to Mineralogy and Petrology, 105(5), 602 615.

Spear, F. S. (2010). Monazite allanite phase relations in metapelites. Chemical Geology, 279(1 2), 55 62.

Spear, F. S., & Pyle, J. M. (2002). Apatite, Monazite, and Xenotime in Metamorphic Rocks. Reviews in Mineralogy and Geochemistry, 48(1), 293 335.

Spear, F. S., & Pyle, J. M. (2010). Theoretical modeling of monazite growth in a low Ca metapelite. Chemical Geology, 273(1), 111 119.

Stepanov, A. S., Hermann, J., Rubatto, D., & Rapp, R. P. (2012). Experimental study of monazite/melt partitioning with implications for the REE, Th and U geochemistry of crustal rocks. Chemical Geology, 300, 200 220.

Taylor, R. J. M., Kirkland, C. L., & Clark, C. (2016). Accessories after the facts: Constraining the timing, duration and conditions of high temperature metamorphic processes. Lithos, 264, 239 257.

Tomkins, H., & Pattison, D. (2007). Accessory phase petrogenesis in relation to major phase assemblages in pelites from the Nelson contact aureole, southern British Columbia. Journal of Metamorphic Geology, 25(4), 401 421.

Vernon, R., Clarke, G., & Collins, W. (1990). Local, mid crustal granulite facies metamorphism and melting: an example in the Mount Stafford area, central Australia High temperature metamorphism and crustal anatexis (pp. 272 319): Springer.

Watson, E. B., Vicenzi, E. P., & Rapp, R. P. (1989). Inclusion/host relations involving accessory minerals in high grade metamorphic and anatectic rocks. Contributions to Mineralogy and Petrology, 101(2), 220 231.

Watt, G. R. (1995). High thorium monazite (Ce) formed during disequilibrium melting of metapelites under granulite facies conditions: De Gruyter.

Watt, G. R., & Harley, S. (1993). Accessory phase controls on the geochemistry of crustal melts and restites produced during water undersaturated partial melting. Contributions

to Mineralogy and Petrology, 114(4), 550 566.

White, R., Pomroy, N., & Powell, R. (2005). An in situ metatexite diatexite transition in upper amphibolite facies rocks from Broken Hill, Australia. Journal of Metamorphic Geology, 23(7), 579 602.

White, R., & Powell, R. (2002). Melt loss and the preservation of granulite facies mineral assemblages. Journal of Metamorphic Geology, 20(7), 621 632.

White, R. W., Powell, R., & Clarke, G. L. (2003). Prograde metamorphic assemblage evolution during partial melting of metasedimentary rocks at low pressures: migmatites from Mt Stafford, Central Australia. Journal of Petrology, 44(11), 1937 1960.

Wing, B. A., Ferry, J. M., & Harrison, T. M. (2003). Prograde destruction and formation of monazite and allanite during contact and regional metamorphism of pelites: petrology and geochronology. Contributions to Mineralogy and Petrology, 145(2), 228 250.

Yakymchuk, C. (2017). Behaviour of apatite during partial melting of metapelites and consequences for prograde suprasolidus monazite growth. Lithos, 274, 412 426.

Yakymchuk, C., & Brown, M. (2014). Behaviour of zircon and monazite during crustal melting. Journal of the Geological Society, 171(4), 465 479.

Yakymchuk, C., Clark, C., & White, R. W. (2017). Phase relations, reaction sequences and petrochronology. Reviews in Mineralogy and Geochemistry, 83(1), 13 53.

Yakymchuk, C., Kirkland, C. L., & Clark, C. (2018). Th/U ratios in metamorphic zircon. Journal of Metamorphic Geology, 36(6), 715 737.

Supporting information

APPENDIX S2.1: WHOLE ROCK GEOCHEMISTRY FOR MT STAFFORD SAMPLES.

Supplementary Table S2.1.1. Whole rock geochemistry for Mt Stafford samples. Sample locations are in UTM coordinates using WGS84 datum, zone 53K. n/a, not analysed.

Sample	STF01	STF02a	STF02b	STF03	STF04a	STF05	STF06	STF07	STF08	STF09	STF10B
Easting (mE)	251144	251197	251197	251220	251292	251489	251909	252005	251917	252042	252150
Southing (mS)	7562280	7562283	7562283	7562292	7562338	7562609	7562824	7562914	7563411	7563491	7563754
Major elements (%)											
SiO_2	56.95	62.52	55.39	74.91	83.2	57.95	56.21	62.28	77.94	54.83	75.16
TiO_2	0.58	0.59	0.61	0.46	0.32	0.6	0.66	0.61	0.39	0.64	0.47
Al_2O_3	22.77	20.3	24.43	12.67	8.84	22.65	24	19.99	11.23	26.49	13.17
Fe_2O_3T	9	6.59	8.06	4.35	1.77	7.92	7.59	6.05	3.79	6.32	4.48
MnO	0.11	0.19	0.13	0.06	0.06	0.09	0.12	0.08	0.11	0.09	0.13
MgO	2.72	2.13	2.6	1.25	0.48	2.38	2.39	1.97	1.05	2.11	1.35
CaO	0.48	0.29	0.34	0.63	0.66	0.25	0.32	0.3	0.78	0.37	0.71
Na_2O	0.4	0.38	0.62	0.86	1.05	0.81	0.98	1.2	0.72	1.44	0.74
K_2O	5.98	5.92	6.64	3.84	2.41	6.15	6.49	6.34	3.12	6.46	3.25
P_2O_5	0.14	0.09	0.13	0.11	0.11	0.14	0.13	0.14	0.10	0.16	0.11
Total	100.87	100.75	101.01	99.85	100.01	99.6	100.34	99.75	100.08	99.8	100.46
LOI	1.74	1.75	2.06	0.71	1.11	0.66	1.45	0.79	0.85	0.89	0.89
Fe_2O_3	1.04	n/a	n/a	0.37	0.27	n/a	n/a	n/a	n/a	n/a	n/a
FeO	7.16	n/a	n/a	3.58	1.35	n/a	n/a	n/a	n/a	n/a	n/a
Trace elements (ppm)											
Rb	342.1	340.3	380.7	235.3	96.4	339.1	368.2	280.2	172.2	366.1	161.8
Sr	28	185	106	35	57	49	95	60	192	42	121
Y	23.4	26.6	34.2	23.1	24.7	28.2	29.3	28.6	20.1	37	24.1
Zr	85	156	118	200	335	102	119	151	245	101	251
V	76	84	92	47	27	77	89	65	44	86	60
Ni	46	40	42	28	16	45	53	38	25	47	31
Cr	52	73	70	38	25	64	78	61	48	72	59
Nb	17.6	16.1	16.6	14.5	10	16.1	17	15.6	12	18.3	13.5
Ga	32.2	30.7	34.2	19.9	12.6	32.7	34.5	29.1	16.9	41.2	20.2
Cu	38	18	37	12	8	21	16	18	14	17	16
Zn	144	100	111	65	27	123	119	97	63	89	73
Co	27	18	17	11	1	23	22	16	7	17	11
Ba	804	829	913	535	487	911	1002	1326	719	1415	521
La	41	40	45	39	46	42	42	45	37	48	41
Ce	106	90	108	70	80	106	119	112	87	140	84
U	0.25	0.7	0.5	1.8	3.2	0.25	1.1	1.5	0.9	5	1.2
Th	39	26.8	33.5	34	37	35.1	33.7	30.3	31	33	33.7
Sc	15	12	14	7	2	15	16	12	4	18	6
Pb	11	16	17	9	14	19	1	22	15	13	13

Sample	STF11	STF12	STF13	STF16a	STF16b	STF17a	STF17b	STF18a	STF18b	STF18c dark	STF18c light
Easting (mE)	252321	252343	252343	252677	252677	252677	252677	253577	253577	253577	253577
Southing (mS)	7563936	7564021	7564021	7564418	7564418	7564418	7564418	7564417	7564417	7564417	7564417
Major elements (%)											
SiO_2	71.74	58.64	70.01	55.53	64 38	74.46	70.45	60.92	56.69	66.39	56.96
TiO_2	0.56	0 57	0.58	0.59	0.58	0.47	0.6	0.52	0.58	0.62	0.45
Al_2O_3	13 98	21.63	14.39	24.73	19 16	13.46	15.44	21.42	24.13	18.68	24.59
Fe_2O_3T	5.25	6.63	5.71	7.83	6.22	4.42	5.85	4.72	6.5	8 15	6.86
MnO	0.08	0.07	0.06	0.06	0.09	0.06	0.07	0.07	0.07	0.08	0.08
MgO	1.58	1 95	1.6	2.03	1.93	1 13	1.67	1.46	2.06	2 54	2.06
CaO	0.53	0 31	0.74	0.21	0.22	0 11	0.19	0.36	0.19	0 25	0.21
Na_2O	1.03	1 58	1.54	1.23	0.90	0.46	0.51	1.59	1.27	0 54	1.12
K_2O	4.37	7 22	4.38	6.62	5.57	4 33	4.38	8.02	7.42	1.85	6.52
P_2O_5	0.11	0 13	0.1	0.13	0.13	0.09	0.12	0.14	0.12	0 10	0.13
Total	100.24	100.3	100.18	99.68	100.48	100.07	100.35	99.69	99.62	100.62	100.19
LOI	1.01	1 57	1.07	0.72	1.30	1.08	1.07	0.47	0.59	1.42	1.21
Fe_2O_3	n/a	n/a	n/a	n/a	n/a	n/a	n/a	n/a	n/a	n/a	n/a
FeO	n/a	n/a	n/a	n/a	n/a	n/a	n/a	n/a	n/a	n/a	n/a
Trace elements (ppm)											
Rb	232.7	432	273.9	407.7	349.5	250.2	273.7	443.3	408.4	109	379.2
Sr	167	158	201	49	94	90	80	68	44	49	75
Y	12.8	19.1	14.1	28.5	19.6	15.9	16.7	16.5	28.6	57	33.9
Zr	184	119	187	92	169	235	200	95	99	221	125
V	67	81	72	69	76	53	69	54	65	79	79
Ni	32	41	35	38	38	27	41	35	43	62	54
Cr	76	89	79	60	68	64	81	67	67	88	86
Nb	16 5	14.9	15.7	16.7	17.7	12.1	18.6	14.6	13.8	14.9	16.5
Ga	22	28.9	21	34.5	28.2	20.7	24.7	28.2	33.7	32.8	36.8
Cu	19	24	18	41	7	15	16	6	19	78	33
Zn	89	105	86	115	93	69	80	102	114	92	138
Co	14	17	14	18	14	9	18	8	17	29	20
Ba	735	1382	926	1060	706	665	677	1029	926	236	923
La	28	38	29	42	35	37	31	33	39	37	39
Ce	66	102	62	109	82	73	69	76	89	87	95
U	0.25	0 25	0.25	0.25	0.25	0.6	0.5	0.25	1.8	0 5	0.25
Th	23 5	22.2	19.5	35.2	29.6	30.5	26	22.5	32.4	36.4	30.6
Sc	9	12	8	13	8	5	10	8	10	13	13
Pb	19	24	20	23	19	28	16	36	34	10	33

Sample	STF18d	STF20	STF21a	STF21b	STF21c	STF22	STF24	STF25	STF26a	STF26b	STF27
Easting (mE)	253577	254680	254335	254335	254335	262960	264386	262889	260269	260269	260230
Southing (mS)	7564417	7565053	7565037	7565037	7565037	7559749	7562415	7565775	7563397	7563397	7563459
Major elements (%)											
SiO_2	70.43	79.59	74.95	76.43	58.82	74.64	73.2	77.86	73.69	74.34	74.63
TiO_2	0.59	0.44	0.51	0.43	0.71	0 31	0.38	0.25	0.55	0 57	0.54
Al_2O_3	15.86	9.81	12.89	12.43	22.74	13.62	12.25	11.15	12.78	12.91	12.2
Fe_2O_3T	6.17	3.61	4.28	4.22	6.79	2.49	4.1	2.18	6.61	6.02	4.23
MnO	0.07	0.06	0.06	0.05	0.09	0.05	0.08	0.04	0.11	0.09	0.08
MgO	1.83	1 13	1.19	1.19	2.07	0.71	1.41	0.30	1.83	1.64	1.25
CaO	0.22	0 96	1.00	0.39	0.33	1 15	2.59	0.86	0.47	1.01	0.93
Na_2O	0.66	1.41	1.08	0.75	1.22	1 94	2.06	1.77	0.59	0 94	1.39
K_2O	3.26	2.69	2.98	3.2	6.23	4 23	3.52	4.74	2.36	1 93	3.22
P_2O_5	0.13	0 11	0.11	0.11	0.12	0 13	0.10	0.11	0.10	0 10	0.11
Total	99.71	100.54	99.55	99.72	99.72	100.08	100.55	100.05	100.34	99.64	100.21
LOI	0.49	0.73	0.5	0.52	0.6	0.81	0.86	0.79	1.25	0.09	1.63
Fe_2O_3	n/a	n/a	n/a	n/a	n/a	n/a	n/a	n/a	n/a	n/a	n/a
FeO	n/a	n/a	n/a	n/a	n/a	n/a	n/a	n/a	n/a	n/a	n/a
Trace elements (ppm)											
Rb	167.8	140.3	159.9	154.3	343	258.9	208.3	550.3	119.4	91.5	137.1
Sr	32	96	67	42	75	102	107	42	57	32	210
Y	28 5	18.7	20.4	20	24 1	9 5	18.3	60.1	23.5	25.3	19.1
Zr	198	349	234	213	128	196	277	248	260	206	340
V	53	45	45	39	72	30	46	17	64	54	57
Ni	40	26	26	27	46	16	24	9	38	33	29
Cr	39	56	50	34	68	32	40	11	81	49	69
Nb	16.8	13.3	15.2	11.4	19 2	10.8	9.8	12.6	13.8	12.1	12.7
Ga	24 9	17.1	19.2	18.6	33 5	20.8	17.4	17.9	20.1	20.5	18.3
Cu	12	8	6	12	10	12	11	11	7	6	8
Zn	75	47	64	63	111	37	45	33	134	117	64
Co	19	6	9	8	17	1	8	0.5	21	18	9
Ba	603	517	504	521	798	462	412	201	516	472	903
La	39	38	39	34	37	29	32	36	40	39	39
Ce	80	83	64	69	78	56	76	71	83	73	79
U	1.7	1 3	1.3	2.6	1.6	0 25	0.25	1.8	0.25	1 3	1.6
Th	42 2	38.8	29.1	36.6	31.8	25.3	25.2	65.1	25.3	29.2	31.9
Sc	8	4	8	6	11	3	7	3	17	12	5
Pb	17	14	18	8	19	17	6	21	14	17	11

Sample	STF28 dark	STF28 light	STF29	STF30	STF31a	STF31b	STF31af	STF32	STF33	STF33P	ST16-31G
Easting (mE)	260116	260116	260031	260031	246946	246946	246946	247181	247199	247199	241394
Southing (mS)	7563459	7563459	7563436	7563436	7562150	7562150	7562150	7562335	7562360	7562360	7567785
Major elements (%)											
SiO_2	50.47	56.79	79.91	55.1	77.69	71.37	77 28	81.02	76.73	58.92	56.76
TiO_2	1.31	0.6	0.43	0.59	0.38	0.56	0.38	0 34	0.37	0.54	0.62
Al_2O_3	26.27	23.8	9.75	24.06	11.3	14.23	10 9	8.72	11.17	21.06	24.87
Fe_2O_3T	13.34	7.48	3.21	7.3	3.06	5.03	3.21	1.86	4.2	7.13	6.7
MnO	0.09	0.05	0.08	0.62	0.06	0.06	0.24	0.03	0.04	0.07	0.08
MgO	4.12	2.26	0.84	2.36	0.92	1.64	0.95	0 51	1.32	1.89	2.42
CaO	0.11	0.26	1.44	1.06	0.62	0.15	0.89	0 27	0.44	0.10	0.07
Na_2O	0.12	1.05	1.46	2.83	1.48	0.24	1.84	0.78	0.98	0.44	0.48
K_2O	0.57	6.94	2.03	4.67	3.36	4.88	3.12	5 31	2.97	6.04	7.88
P_2O_5	0.06	0.12	0.09	0.13	0.10	0.11	0.11	0 11	0.09	0.10	0.05
Total	98.39	100.73	99.89	100.95	100.31	100.71	100.09	99.77	100.13	100 23	103.45
LOI	1.93	1.38	0.65	2.23	1.34	2.44	1.17	0.82	1.82	3.94	3.52
Fe_2O_3	n/a	n/a	n/a	0.62	0.52	1.10	0.38	n/a	n/a	n/a	2.78
FeO	n/a	n/a	n/a	6.01	2.29	3.54	2.55	n/a	n/a	n/a	3.53
Trace elements (ppm)											
Rb	58.7	322.8	75.5	224.1	182.4	330.2	166.7	279.8	199	409	480.5
Sr	19	138	196	216	93	17	141	65	85	61	32
Y	31.7	20.3	18.9	38.3	21.5	37.5	27 2	9 9	22.2	13.6	21.6
Zr	178	126	326	84	222	273	229	340	224	117	179
V	178	88	39	76	44	62	42	30	43	81	55
Ni	71	55	20	49	20	31	19	15	29	55	53
Cr	147	95	61	60	43	43	35	46	54	78	96
Nb	32.2	14.1	10.2	16.7	13	15.7	12	11.8	12.4	15.7	18.6
Ga	42	30.8	15.3	32.7	17.6	23.9	17 5	10.2	17.2	32.2	36 3
Cu	13	8	7	7	14	17	13	10	9	34	23
Zn	137	115	41	160	51	87	51	15	73	118	101
Co	53	21	4	23	4	8	3	0 5	9	19	13
Ba	62	1378	648	987	774	700	1118	849	567	884	1268
La	50	46	43	46	35	55	38	30	43	26	42
Ce	111	120	79	101	63	104	82	100	75	163	95
U	1.2	0.25	0.5	1.1	4.9	2.4	5.2	0 9	0.7	0.8	0.25
Th	48	30.6	23.7	34	34	48	33	36.9	27.2	33.6	28
Sc	23	11	4	10	6	9	5	2	5	15	14
Pb	0.5	27	15	32	17	14	16	3	25	15	18

Sample	ST16-31G	ST16-01	ST16-02A	ST16-02B	ST16-03A	ST16-03B	ST16-03C	ST16-04	ST16-05	ST16-07B	ST16-09
Easting (mE)	241394	258537	258537	258537	258476	258476	258476	258479	258534	259078	259078
Southing (mS)	7567785	7566097	7566097	7566097	7565983	7565983	7565983	7565972	7566127	7566925	7566925
Major elements (%)											
SiO_2	56.76	82.45	60.97	73.73	76.73	69.24	73.92	69.26	53.58	55.4	56.38
TiO_2	0.61	0.26	0.69	0.54	0.3	0.61	0.49	0 51	0.77	0.68	0.52
Al_2O_3	24.85	7.72	21.24	13.43	12.35	15.71	13.74	16.77	27.51	25.18	25.13
Fe_2O_3T	6.8	2.1	6.56	4.76	2.65	5.91	4.57	5.07	6.97	6.03	6.9
MnO	0.08	0.33	0.09	0.07	0.05	0.1	0.07	0.06	0.09	0.08	0.1
MgO	2.4	0.56	2.37	1.44	0.82	1.99	1.48	1.75	2.69	2.74	2.31
CaO	0.07	6.26	0.43	1.05	0.92	0.74	0.84	0.61	0.59	0.80	0.36
Na_2O	0.48	0.15	1.45	1.32	1.93	1.19	1.49	1 53	1.57	2.3	1.37
K_2O	7.83	0.02	6.41	3.24	4.3	4.34	3.63	4.04	5.85	6.55	6.66
P_2O_5	0.06	0.08	0.13	0.14	0.14	0.08	0.07	0.09	0.16	0.14	0.15
Total	103.61	100.28	101.67	100 9	100.8	101.01	101.25	100.84	100.9	101.53	101.04
LOI	3.67	0.35	1.33	1.18	0.61	1.1	0.95	1 15	1.12	1.63	1.16
Fe_2O_3	2.88	0.06	0.55	0.45	0.15	0.10	0.57	0 35	0.62	0.75	0.50
FeO	3.53	1.84	5.41	3.88	2.25	5.23	3.6	4 25	5.71	4.75	5.76
Trace elements (ppm)											
Rb	488.1	1.4	271	154.4	212.5	242.5	187.6	202.6	341.1	278.1	284.4
Sr	31	215	198	168	151	138	117	121	135	192	134
Y	22	45.5	20.5	21.1	17	11.8	19.6	12.1	29.7	35	32.1
Zr	178	328	171	275	225	239	273	203	166	151	120
V	57	23	95	71	40	79	57	58	120	143	135
Ni	52	12	29	28	16	35	27	26	57	38	43
Cr	103	65	88	85	56	80	78	81	91	87	75
Nb	18.4	7.3	16	14.7	10	15	13.4	15.2	19.2	21.1	15.4
Ga	36.6	12.3	30.2	20	16.9	23	20.5	25	39.2	36.9	35.9
Cu	27	65	13	18	18	44	49	18	8	15	17
Zn	100	32	117	72	51	85	65	69	86	87	93
Co	11	1	17	9	1	15	8	12	15	15	17
Ba	1282	104	1250	751	591	942	852	974	1708	1730	1014
La	40	44	40	37	27	29	34	26	61	55	41
Ce	91	65	100	75	49	64	74	48	164	139	93
U	0.25	3	0.25	1.9	0.25	0.25	1.2	0 25	0.25	2.5	0.25
Th	29.2	18.4	29.1	26.3	17.5	29	29.6	21.8	38.4	32.6	25.1
Sc	14	4	8	8	4	9	4	5	16	13	12
Pb	10	15	28	17	20	16	16	24	29	37	20

Sample	ST16-13A	ST16-13B	ST16-14	ST16-15	ST16-16A	ST16-17	ST16-18	ST16-19A	ST16-19B	ST16-31A	ST16-31D	ST16-31J
Easting (mE)	259976	259976	259362	259369	259320	258861	259139	259976	259976	241394	241394	241394
Southing (mS)	7564102	7564102	7563665	7563298	7563275	7562864	7563105	7564102	7564102	7567785	7567785	7567785
Major elements (%)												
SiO_2	50 82	57 25	49 83	82 25	67 65	53 63	54 78	47 73	82 18	58 94	56 9	50 82
TiO_2	1 21	0 76	0 56	0 34	0 7	0 98	0 74	1 15	0 31	0 55	0 58	1 21
Al_2O_3	25 88	23 55	23 18	9 16	16 54	24 6	25 18	27 55	9 26	23 34	25 15	25 88
Fe_2O_3T	14 84	7 09	17 64	2 4	6 92	10 86	9 55	16 91	2 63	7 13	7 68	14 84
MnO	0 2	0 08	0 2	0 13	0 07	0 25	0 11	0 31	0 05	0 06	0 07	0 2
MgO	3 9	2 5	2 75	0 64	2 22	3 29	3 2	4 5	0 75	2 4	2 33	3 9
CaO	0 23	0 64	0 51	3 37	0 24	0 25	0 33	0 44	0 64	0 02	0 03	0 23
Na_2O	0 68	1 82	1 17	1 42	0 85	1 2	1 17	0 43	1 24	0 65	0 68	0 68
K_2O	2 22	5 82	3 84	0 23	4 39	4 57	4 58	0 79	2 76	6 67	6 26	2 22
P_2O_5	0 10	0 12	0 11	0 14	0 10	0 10	0 20	0 20	0 1	0 04	0 05	0 10
Total	102 14	102 78	102 15	100 36	100 14	101 16	100 59	100 43	100 62	103 09	104 15	102 14
LOI	2 06	3 15	2 36	0 28	0 46	1 43	0 75	0 42	0 7	3 29	4 42	2 06
Fe_2O_3	1 78	1 23	3 58	0 10	0 59	0 81	0 50	1 78	0 46	2 33	2 19	1 78
FeO	11 75	5 27	12 65	2 07	5 7	9 04	8 14	13 61	1 95	4 32	4 94	11 75
Trace elements (ppm)												
Rb	253 8	133 5	241 9	140 5	8 4	178 6	180 4	228 9	60 7	128 4	452 4	448
Sr	150	72	155	152	151	173	123	148	60	105	79	74
Y	18 1	212	25 4	283 3	33 1	18 3	77 4	22 7	156 1	19 8	23 5	24 7
Zr	192	298	151	147	291	267	188	166	283	265	115	118
V	123	157	91	193	46	82	130	113	160	40	90	90
Ni	56	74	55	55	16	49	66	66	72	18	45	54
Cr	108	120	80	162	41	93	105	94	135	56	84	86
Nb	17 5	18	15 5	5 9	8 7	16	20	16 6	19 6	10 2	15 8	16 6
Ga	31 8	34 7	33 3	25 5	13 2	24 4	33 4	35 3	37 2	14 5	33 9	35
Cu	22	67	16	82	14	19	19	25	37	13	21	34
Zn	97	141	116	191	37	100	128	117	174	45	108	107
Co	23	49	17	46	1	20	32	29	56	2	16	17
Ba	1673	616	1462	723	216	1138	1311	956	164	587	941	1011
La	47	71	66	74	41	43	48	53	70	47	40	36
Ce	126	173	129	176	71	86	118	132	159	80	88	78
U	0 25	0 9	0 25	0 25	4 8	0 25	0 25	0 25	2 7	2 5	0 25	0 25
Th	33 7	55 9	32 2	39 3	27	31 6	36 3	38 1	60 5	30 4	30	32 5
Sc	13	53	2	81	2	5	19	2	41	2	13	14
Pb	24	10	30	22	1	26	27	20	8	12	23	11

Chapter 3

This chapter is submitted and reviewed as:

Williams, M. A., Kelsey, D. E., & Rubatto, D. Thorium zoning in monazite: a case study from the Ivrea–Verbano Zone, NW Italy. *Journal of Metamorphic Geology.*

Statement of Authorship

Title of Paper	Phase equilibria modelling of monazite in a Th-bearing system
Publication Status	☐ Published ☐ Accepted for Publication ☑ Submitted for Publication ☐ Unpublished and Unsubmitted work written in manuscript style
Publication Details	Williams, M.A., Kelsey, D.E. & Rubatto, D. Thorium zoning in monazite: a case study from the Ivrea–Verbano Zone, NW Italy. *Submitted to Journal of Metamorphic Geology*

Principal Author

Name of Principal Author (Candidate)	Megan A Williams
Contribution to the Paper	Contributed to field sampling, performed analysis on all samples, interpreted data, prepared manuscript and acted as corresponding author.
Overall percentage (%)	85%
Certification:	This paper reports on original research I conducted during the period of my Higher Degree by Research candidature and is not subject to any obligations or contractual agreements with a third party that would constrain its inclusion in this thesis. I am the primary author of this paper.
Signature	Date 15/11/19

Co-Author Contributions

By signing the Statement of Authorship, each author certifies that:

i. the candidate's stated contribution to the publication is accurate (as detailed above);

ii. permission is granted for the candidate in include the publication in the thesis; and

iii. the sum of all co-author contributions is equal to 100% less the candidate's stated contribution.

Name of Co-Author	David E Kelsey
Contribution to the Paper	Assisted with study design, supervised development of work, assisted with field sampling, helped with data interpretation and manuscript evaluation.
Signature	Date 13/11/19

Name of Co-Author	Daniela Rubatto
Contribution to the Paper	Assisted with geochronology processing and interpretation, supervised development of work, assisted with field sampling and data collection, helped with data interpretation and manuscript evaluation.
Signature	Date 13/11/2019

Thorium zoning in monazite: a case study from the Ivrea–Verbano Zone, NW Italy

ABSTRACT

Metamorphism and partial melting of the lower crust is commonly assumed to cause depletion in heat producing elements (HPEs; K, U, Th). In the deep crust, volumetrically subordinate metasedimentary layers, which are source to crustal granites (sensu lato), host the majority of Th ± U, primarily within the REE+Th+U+Y phosphate mineral monazite. We examine the spatial and temporal distribution of Th within monazite grains in metasedimentary rocks from the lower crustal section of the Ivrea–Verbano Zone (Italy), using textural, compositional and geochronological data. We link this to outcrop and regional scale trends described by in-field gamma-ray spectrometry (in-field GRS) data for the purpose of understanding how Th distribution is controlled by progressive metamorphism and partial melting. In-field GRS data shows that the whole rock budget of Th does not change between granulite-facies rocks and their unmelted equivalents, but is significantly lower in rocks that have undergone more significant melt loss at ultra-high temperature (UHT) conditions. Concurrently, the bulk Th budget of monazite increases with metamorphic grade to granulite-facies conditions, and is greatly reduced in UHT samples. Monazite U-Pb geochronology shows regionally elevated temperatures facilitating monazite growth spanning >60 Ma, in particular recording timing of pre-peak to peak metamorphic conditions. Monazite is preserved at all metamorphic grades and presents a mineralogical mechanism for retaining Th in residual deep crust during partial melting and after melt loss.

1 INTRODUCTION

Monazite is a common accessory mineral in clastic metasediments across a wide range of pressure and temperature conditions and tectonic settings in the crust (e.g. Engi, 2017; Parrish, 1990). Its utility and significance far outweighs its low modal abundance: monazite is an important geochronometer for high temperature crustal processes and the major host of Th—a major heat producing element—in the crust. Despite extensive study of the chemical behaviour of the rare earth elements (REEs) and Y in monazite (e.g. Bea & Montero, 1999; Kelly, Harley, & Möller, 2012; Pyle & Spear, 2003; Taylor, Kirkland, & Clark, 2016; Yang & Pattison, 2006) and experimental studies including Th in the monazite–melt system (e.g. Rapp, Ryerson, & Miller, 1987; Rapp & Watson, 1986; Stepanov, Hermann, Rubatto, & Rapp, 2012), the behaviour of Th-in-monazite with progressive metamorphism is under-explored. Thus, the changing chemical concentration and zoning of Th and bulk Th content of monazite grains as a function of pressure, temperature and bulk rock composition remains unclear.

Previous studies have successfully linked chemical zoning of Ce or Y in metamorphic monazite to mineral reactions involving garnet, apatite, xenotime and melt (Corrie & Kohn, 2008; Dumond, Goncalves, Williams, & Jercinovic, 2015; Kohn & Malloy, 2004; Pyle & Spear, 1999, 2003; Rubatto, Hermann, & Buick, 2006; Smith & Barreiro, 1990; Wing, Ferry, & Harrison, 2003). However, to date, studies that have focused on Th behaviour in particular are few (Chapter 2; Bea & Montero, 1999; Bingen, Demaiffe, & Hertogen, 1996; Skrzypek et al., 2018; Watt, 1995) and studies reporting Th zoning in monazite have produced seemingly contradictory results (e.g. decreasing Th from core to rim; Kohn & Malloy, 2004; Th-in-monazite is constant or increases with metamorphic grade; Chapter 2; Skrzypek et al., 2018). Chapter 2 and recent work by Skrzypek et al. (2018), both on low pressure terranes, identified monazite chemical zones in prograde metamorphic sequences. These monazite zones showed a systematic progression of increasing Th from the lowest to highest grade rocks. In Mt Stafford this retention of Th in monazite resulted in the retention of Th in granulite-facies rocks despite significant partial melting and interpreted melt loss (Chapter 2; Bartoli, 2017; Palya, Buick, & Bebout, 2011). In this study, we explore bulk Th and monazite chemistry in the higher pressure Ivrea–Verbano Zone to explore similarities and differences in the record of monazite formation in these terranes.

Sections of metasedimentary sequences that expose a continuous and well constrained metamorphic gradient are the best targets to investigate monazite composition over a *P–T* range. The Ivrea–Verbano Zone (IVZ) in northern

Italy exposes such a sequence along the Val Strona di Omegna. This is an ideal natural laboratory as it: (a) provides a continuous metamorphic field gradient from the mid-amphibolite through to granulite facies; (b) the exposed metamorphic gradient is nearly perpendicular to the steeply dipping schistose and gneissic foliation; (c) contains an abundance of metapelite layers throughout the transect that have arguably consistent chemistry across the solidus (Bea & Montero, 1999; Redler, Johnson, White, & Kunz, 2012), and thus presents the opportunity to study monazite behaviour without the complexity of significant changes to bulk rock chemistry; and (d) has a well-constrained regional *P–T* framework (Ewing, Hermann, & Rubatto, 2013; Kunz, Johnson, White, & Redler, 2014; Redler et al., 2012; Redler, White, & Johnson, 2013).

The behaviour of accessory minerals and their trace element compositions in the IVZ was previously studied in the landmark paper by Bea and Montero (1999), details of which are outlined below. However, as informative and revolutionary as the Bea and Montero (1999) study was, it was limited by the resolution of analytical techniques (i.e. whole rock geochemistry and EPMA) available at the time. To this end, we revisit the same section of Val Strona di Omegna to add several hundred more data points to the regional bulk rock Th trends reported in Bea and Montero (1999) and examine the micro-scale compositional variations within monazite grains, interpreted within a *P–T*–time framework. The extended dataset and greater breadth of interpretation gives greater insight into (a) the preservation (or not) of pre-peak and peak monazite; (b) the relative and changing importance of the two Th substitution mechanisms within natural monazite; and (c) the part of the *P–T* path to which monazite geochronology relates.

2 GEOLOGICAL SETTING

The Ivrea–Verbano Zone (also known as the Ivrea Zone, IVZ) in the southern Alps, north-west Italy, represents a tilted mid to lower crustal section of the pre-alpine basement (e.g. Bea & Montero, 1999; Brodie & Rutter, 1987; Fountain, 1976; Peressini, Quick, Sinigoi, Hofmann, & Fanning, 2007; Redler et al., 2012; Redler et al., 2013; Rivalenti, Garuti, Rossi, Siena, & Sinigoi, 1981; Zingg, Handy, Hunziker, & Schmid, 1990). The sequence consists of interlayered metabasites and metapelites with subordinate meta-carbonate and calc-silicate layers which together form the Kinzigite Formation (Fig. 1). The sequence has a metamorphic field gradient from mid-amphibolite-facies rocks (locally known as Kinzigites) in the SE, adjacent to the Cossato–Mergozzo–Brissago (CMB) tectonic line, to granulite-facies rocks (locally known as Stronalites) at the base of the section, adjacent to the Insubric line in the west (Fig. 1; e.g. Henk, Franz, Teufel, & Oncken, 1997; Quick et al., 2003; Redler et al., 2013; Schmid & Wood, 1976; Sills

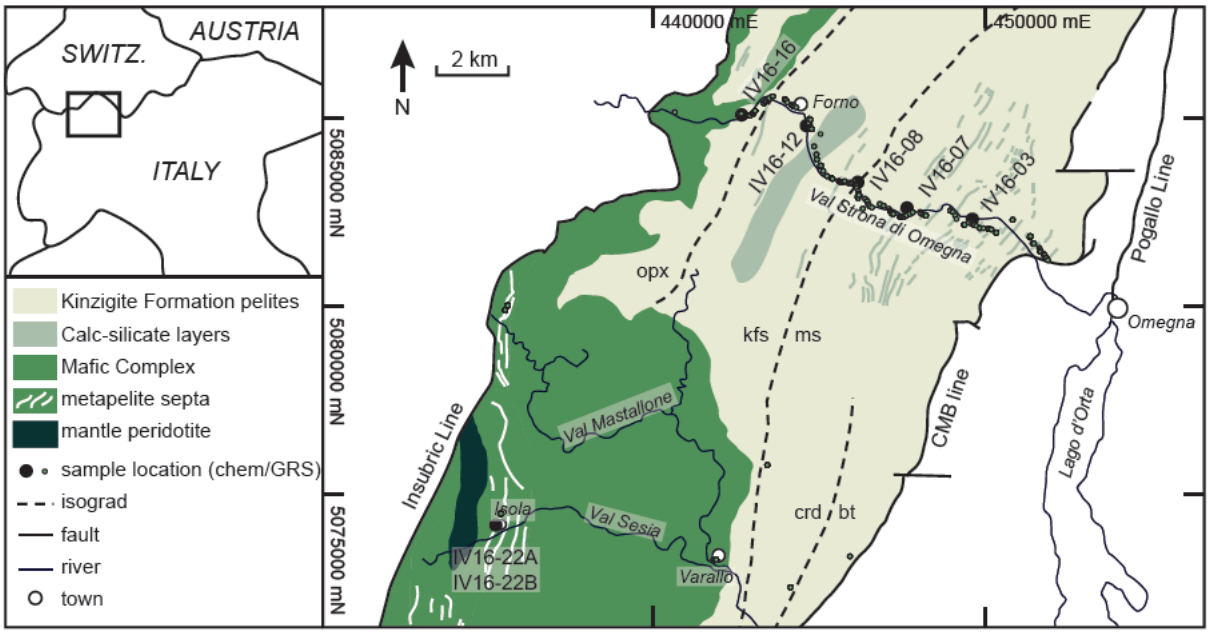

Figure 1. Simplified map of the Ivrea Verbano Zone showing major stratigraphic units (after Bea & Montero, 1999; Ewing et al., 2013; Redler et al., 2012) and locations of samples in this study (see Table 1). Inset: location of the Ivrea Verbano Zone. Mineral abbreviations after Kretz (1983).

& Tarney, 1984). The sequence is intruded to the SW by a large mafic body ('Mafic Complex', Fig. 1), the upper part of which has a narrow contact aureole (~1 km wide) that overprints the regional metamorphic field gradient (Barboza & Bergantz, 2000; Barboza, Bergantz, & Brown, 1999). The minimum *P–T* conditions adjacent to the CMB line, as constrained by thermodynamic forward modelling, are <3.5–7.9 kbar and <640–710 °C (Redler et al., 2012). The maximum *P–T* conditions in the continuous metasedimentary sequence, as determined by thermodynamic forward modelling, are >9.5 kbar and >870 °C (Kunz & White, 2019; Redler et al., 2012)NW Italy, but higher temperatures up to 1100 °C are recorded by Zr-in-rutile thermometry in the slivers of metapelites ("septa") within the Mafic Complex (Ewing, Rubatto, & Hermann, 2014; Pape, Mezger, & Robyr, 2016). The metamorphic field (thermal) gradient in Val Strona di Omegna is approximately 70 °C/kbar based on the published *P–T* results (Kunz & White, 2019; Redler et al., 2012).

Remnants of regional metamorphism related to the Variscan Orogeny in the IVZ have been dated to ca. 320–300 Ma (Ewing et al., 2013; Kunz, Regis, & Engi, 2018; Vavra, Schmid, & Gebauer, 1999). The Mafic Complex intruded the sequence shortly afterwards. The main pulse of the Mafic Complex was dated at 288 ± 4 Ma by Peressini et al. (2007), and a recent ID–TIMS study constrains the main felsic and mafic magmatism to a short period between 286–282 Ma (Karakas et al., 2019). Minor magmatic activity occured from c. 300 to 270 Ma (Klötzli et al., 2014; Peressini et al., 2007). The majority of U–Pb ages (zircon and monazite) in the pelitic rocks constrain regional heating to amphibolite-and granulite-facies conditions to the Permian, i.e. 290–270 Ma (Ewing et al., 2013; Guergouz, Martin, Vanderhaeghe, Thébaud, & Fiorentini, 2018; Henk et al., 1997; Kunz et al., 2018; Vavra et al., 1999). Geochronology from the IVZ suggests that the Mafic Complex formed during a sequential emplacement, providing significant thermal energy required for the granulite-facies metamorphism of the Kinzigite Formation (Ahrendt, Hoefs, Strackenbrock, & Weber, 1989; Baker, 1990; Barboza et al., 1999; Peressini et al., 2007). Relatively high temperatures may have been maintained until cooling below ~ 550 °C in the Jurassic (175–160 Ma), as constrained by rutile geochronology (Ewing, Rubatto, Beltrando, & Hermann, 2015). Rifting to the west of the IVZ during the late Permian to Jurassic may have resulted in some fluid influx within the Mafic Complex (Vavra & Schaltegger, 1999; Vavra et al., 1999). Tilting of the IVZ into its current steeply inclined orientation is suggested to have begun during the Jurassic (Wolff, Dunkl, Kiesselbach, Wemmer, & Siegesmund, 2012) and continued during the Oligocene as part of the Alpine Orogeny (e.g. Handy, Franz, Heller, Janott, & Zurbriggen, 1999).

The behaviour of accessory minerals in the IVZ was previously studied by Bea and Montero (1999), who documented the chemistry of metapelites, metabasites and leucosomes in Val Strona di Omegna, as well as the abundance, habit, microstructural location and chemistry of the four common accessory minerals in these rocks: monazite, xenotime, apatite and zircon. Progressive changes to accessory mineral composition documented in that study demonstrate that reactions between accessory, major minerals and, where present, melt were continuous throughout the metamorphic sequence (see also Corrie & Kohn, 2008; Kohn & Malloy, 2004). Monazite in the sequence was not consumed by major mineral-forming reactions, retaining a similar modal abundance with increasing metamorphic grade, and did not completely dissolve into melt even at high temperatures, as evidenced by its presence in the residual granulites at the highest metamorphic grade. Bea and Montero (1999) reported that the proportion of high-Th/U monazite increases with metamorphic grade, and its predominant location at grain boundaries suggested growth in the presence of melt. Bea and Montero (1999) observed that metapelitic rocks throughout the sequence have approximately the same average concentration of LREE and Th regardless of metamorphic grade. Similarly, the metabasites do not show any perceptible change in Th concentration with increasing metamorphic grade. The study concluded that chemical changes associated with metamorphism and partial melting did not significantly change heat production in the lower crust. The heat production of the Val Strona metapelites was recently investigated by Alessio et al. (2018), who showed empirically that the heat production in the Ivrea–Verbano Zone was equivalent in sub- and supra-solidus rocks.

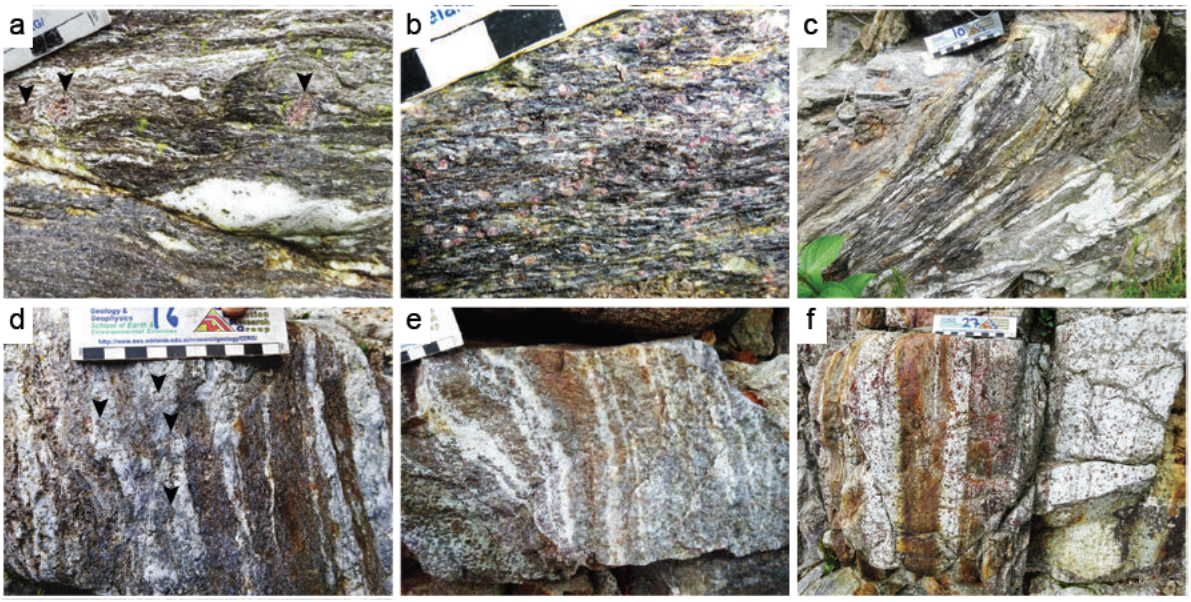

Figure 2. Field relations from Val Strona di Omegna (a) (e) and Val Sesia (f), in order of increasing metamorphic grade. Scale bar graduations 10mm. (a) Micaschist with garnet porphyroblasts and muscovite rich leucosome (lower amphibolite; IV16 03A). Arrows indicate garnet porphyroblasts. (b) Micaschist with abundant garnet (lower amphibolite; IV16 07). (c) Folded micaschist with muscovite poor leucosome (upper amphibolite; IV16 08). (d) Garnet sillimanite biotite gneiss (granulite; IV16 12). Arrows indicate peritectic garnet. (e) Garnet sillimanite gneiss (biotite absent, granulite; IV16 16). (f) Layered residual metapelite in UHT septa. Light bands are mainly plagioclase garnet, dark bands are rich in garnet and sillimanite (UHT granulite; IV16 22A/B).

3 MINERAL ASSEMBLAGES AND TEXTURES IN METAPELITES

The IVZ is split into three zones based on metamorphic assemblages: the Kinzigite zone, a transition zone and the Stronalite zone, which broadly correspond to mid- and upper-amphibolite and granulite facies, respectively (Bea & Montero, 1999; Redler et al., 2012; Schnetger, 1994). Amphibolite-facies metapelites in the Kinzigite zone are folded micaschists with variable proportions of biotite, muscovite, fibrolitic sillimanite, garnet, plagioclase and quartz (Fig. 2a, b). At the lowest grade, micaschists contain leucocratic patches with a high proportion of muscovite and plagioclase that are almost completely devoid of biotite (Fig. 2a; e.g. Bea & Montero, 1999). These leucocratic patches were described by Bea & Montero (1999) as hydrothermal mobilizates. Garnet at the lowest metamorphic grade occurs as rare isolated porphyroblasts, wrapped in a fabric of biotite and muscovite (Fig. 2a). With increasing metamorphic grade, garnet becomes more abundant and generally smaller in size (Fig. 2b). The transition zone represents the change from amphibolite- to granulite-facies assemblages, and extends from the K-feldspar-in isograd in the metapelites to the orthopyroxene-in isograd in the metabasites (Bea & Montero, 1999; Redler et al., 2012). In this zone, the metapelitic rocks change from micaschists to gneisses, accompanied by an overall decrease in the modal proportion of biotite and increase in the modal proportion of garnet, sillimanite and leucosome (Fig. 2c). In the granulite-facies zone (Stronalite) the metapelites consist primarily of garnet, plagioclase, K-feldspar, prismatic sillimanite, biotite and quartz, with accessory rutile, ilmenite and graphite. The modal proportion of biotite decreases with metamorphic grade, in an inverse relationship with the increase in the number and volume of leucosomes preserved in the rocks and modal abundance of peritectic garnet (Fig. 2 d). Whole rock geochemistry and phase equilibria modelling by Redler et al. (2013) shows that the unmelted mid-amphibolite-facies rocks in the IVZ can be considered as protolith compositions for the rocks at higher metamorphic grades and that melt production in the granulite-facies rocks reached a maximum of approximately 25–30 mol. %. Within the Mafic Complex exist several septa of metapelitic rocks that were metamorphosed to ultra-high temperature granulite (UHT; >900 °C) conditions and have mineral assemblages containing abundant garnet, sillimanite, plagioclase (sometimes perthitic), rutile and virtually no biotite (Figs. 1, 2f; e.g. Ewing 2013).

4 SAMPLE SELECTION

Representative metapelite samples of the IVZ

Table 1. Samples and locations. Samples listed in increasing grade order, refer to Fig. 1. Metamorphic grade after Redler et al. (2012). Locations are in UTM coordinates, zone 32T, using the WGS84 datum. Mineral abbreviations after Kretz (1983). Metm., metamorphic; UHT, Ultra high temperature granulite. Vein in IV16 03A comprises 10% of thin section.

Sample	*Metm. grade*	*Rock type*	*Mineralogy*	*Location*
IV16–03A	Amphibolite	pelite with	bt–ms–pl–grt–qtz	
		vein	mnz–apt–xtm–zrn	0450804mE 5083388mN
IV16–07	Amphibolite	pelite	bt–sil–pl–grt–ms–qtz	
			mnz–apt–xtm–zrn–gr	0448640mE 5083912mN
IV16–08	Amphibolite	pelite	bt–ms–pl–grt–qz–sil	
			mnz–apt–xtm–zrn–gr	0446706mE 5084125mN
IV16–12	Granulite	pelite	bt–ms–pl–grt–sil–ru–qz	
			mnz–apt–xtm–zrn–gr	0445135mE 5086576mN
IV16–16	Granulite	pelite	bt–pl–kfs–grt–sil–ru–qz–gr	
		restite	mnz–apt–xtm–zrn	0442972mE 5087044mN
IV16-22A	UHT	pelite	sil–pl–grt–qtz–rt–ilm	
		leucosome	mnz–apt–xtm–zrn–aln–chl	0435591mE 5074755mN
IV16-22B	UHT	pelite	grt–sil–pl–qtz–rt–ilm	
		restite	mnz–apt–xtm–zrn–aln–chl	0435591mE 5074755mN

were collected along the well exposed traverse in Val Strona Di Omegna (Val Strona; Figs. 1, 2). This part of the sequence is the best exposed, most continuous, easily accessible and the furthest removed from the overprinting effects of the Mafic Complex in the SW, thus is the best place to study the regional metamorphic trend. The Val Strona sequence has been extensively investigated in terms of petrology and geochronology (e.g. Bea & Montero, 1999; Ewing et al., 2013; Ewing et al., 2014; Kunz et al., 2018; Kunz & White, 2019; Peressini et al., 2007; Redler et al., 2012; Redler et al., 2013 and references therein), allowing direct comparison of the new results with previous studies. Of the 31 samples collected and investigated for bulk rock composition in this study, seven were selected for detailed textural and mineral analysis (Table 1). Three amphibolite-facies and two granulite-facies metapelites are from Val Strona; two samples are UHT metapelite from septa within the Mafic Complex from the locality of Isola in Val Sesia (Figs. 1, 2f). Thin sections were cut in the same orientation for all samples, perpendicular to foliation and parallel to lineation.

5 METHODS

5.1 Whole rock geochemistry

Whole-rock geochemical analyses of all collected samples were undertaken to determine similarity of chemical composition between samples as well as quantify bulk rock concentrations of heat producing elements. Whole-rock geochemical analyses were undertaken by Wavelength Dispersive X-ray Fluorescence spectrometry at the Department of Earth and Environment, Franklin and Marshall College, Lancaster PA, USA. Major elements were analysed on fused disks prepared using a lithium tetraborate flux. Element (ppm) and oxide (wt %) concentrations from whole-rock geochemistry are herein denoted in the form Th_WR and CaO_WR, respectively (e.g. trace and major elements).

5.2 In field gamma ray spectrometry

Handheld gamma ray spectrometry (GRS) data for the Ivrea–Verbano Zone were published in Alessio et al. (2018), which contains the full dataset and methods for this technique. Analyses were collected from transects of the IVZ, predominantly in Val Strona Di Omegna, from lowest to highest metamorphic grade, with multiple analyses collected at each location to account for the natural heterogeneity of sequences in outcrop (Fig. 3). Thorium concentrations obtained from in-field GRS data are denoted Th_GRS and are cast as ppm.

5.3 Mineral Liberation Analysis (MLA)

Entire thin sections were mapped for monazite, xenotime, zircon, allanite and apatite at Adelaide Microscopy, the University of Adelaide, using a FEI Quanta600 Scanning Electron Microscope (SEM) with automated mineral liberation analysis (MLA) software. Full detail of the MLA procedure is detailed in Chapter 2.

5.4 Electron Probe Microanalysis (EPMA)

Qualitative mapping and quantitative analyses of monazite chemistry were performed at Adelaide Microscopy, the University of Adelaide, using a Cameca SXFive electron microprobe following the method described in Chapter 2. Pb was not analysed for any samples herein to reduce individual spot analysis time. Average detection

limits for each element (Table 4) were calculated from the individual detection limits on all point analyses in the study. Monazite wt % oxide and cation data for 4-oxygen monazite from Electron Probe Microanalysis will be denoted in the form ThO_2_mnz and Th^{4+}_mnz, respectively.

5.5 Laser Ablation Inductively coupled plasma Mass Spectrometry (LA ICP MS)

In-situ U–Pb dating and trace element concentrations of monazite were quantified by Laser Ablation ICP–MS at Adelaide Microscopy, the University of Adelaide. Analysis spot locations were selected based on zoning identified in EPMA maps of grains, with spots located within specific chemical zones where possible adjacent to EPMA point analyses. Ablation of monazites was performed in situ with a beam diameter of 13 µm. A common Pb correction was applied using the "VizualAge_UcomPbine" Data Reduction Scheme (Chew, Petrus, & Kamber, 2014) in the program Iolite (Paton, Hellstrom, Paul, Woodhead, & Hergt, 2011) which applies a common Pb correction following the ^{207}Pb method. Detailed LA–ICP–MS methods are described in Appendix S3.1 and uncorrected data are provided in Appendix S3.2.

6 RESULTS

6.1 Bulk rock composition

Whole rock Th concentrations measured by X-ray Florescence (Th_WR) for all samples are in the range 5–43 ppm, within the range of whole rock Th measured by in-field GRS and other published analyses from Val Strona (Fig. 3, Appendix S3.3). The chemistry of the amphibolite- and granulite-facies samples (Table 2) is equally spread in the AFM and Al_2O_3–(CaO+Na_2O)–K_2O diagrams (Fig. 4a, b) regardless of metamorphic grade. Amphibolite- and granulite-facies samples with similar (high Al, low Ca) compositions were selected for further analysis. This composition was chosen due to its propensity to form and

Table 2. Whole rock geochemistry for studied samples from the Ivrea Verbano Zone. FeO and Fe_2O_3 determined by titration.

	Amphibolite			Granulite		UHT	
	IV16-03A	**IV16-07**	**IV16-08**	**IV16-12**	**IV16-16**	**IV16-22A**	**IV16-22B**
Major elements (wt%)							
SiO_2	49.18	51.88	56.96	57.00	54.75	57.75	46.53
TiO_2	1.34	1.16	1.16	1.19	1.56	1.31	1.83
Al_2O_3	28.66	28.54	22.88	22.86	24.58	18.16	23.18
Fe_2O_3T	12.18	12.57	9.79	10.57	12.71	11.33	16.16
MnO	0.14	0.13	0.19	0.26	0.13	0.17	0.26
MgO	3.48	1.69	2.91	2.69	3.87	4.64	5.47
CaO	0.15	0.56	0.47	1.22	0.46	2.66	2.82
Na_2O	0.46	0.74	1.21	0.73	0.57	2.27	2.22
K_2O	4.29	2.87	3.93	3.19	1.39	1.51	1.23
P_2O_5	0.05	0.06	0.17	0.15	0.05	0.09	0.06
Total	99.93	100.20	99.67	99.86	100.07	99.89	99.76
LOI	1.62	1.88	2.41	2.80	2.00	1.38	1.85
Fe_2O_3	10.37	8.53	7.96	6.68	10.13	6.32	10.74
FeO	0.66	3.09	0.94	3.15	1.45	4.31	4.22
Trace elements (ppm)							
Rb	283	228	233	147	48	13	14
Sr	62	205	125	133	132	365	333
Y	16	45	28	39	58	89	127
Zr	161	203	189	185	195	242	311
V	203	173	179	238	226	187	281
Ni	72	69	76	104	65	72	51
Cr	160	165	166	209	178	192	199
Nb	26	37	25	18	24	20	41
Ga	40	45	32	32	38	20	27
Cu	96	26	36	60	41	65	59
Zn	191	205	143	165	149	189	171
Co	42	37	31	38	45	38	55
Ba	610	399	475	706	558	863	642
La	30	43	26	40	36	40	26
Ce	62	76	56	83	72	73	55
U	n/d	n/d	n/d	n/d	n/d	n/d	n/d
Th	31	37	25	28	29	7	5
Sc	22	18	17	14	19	18	34
Pb	1	9	7	13	1	6	11

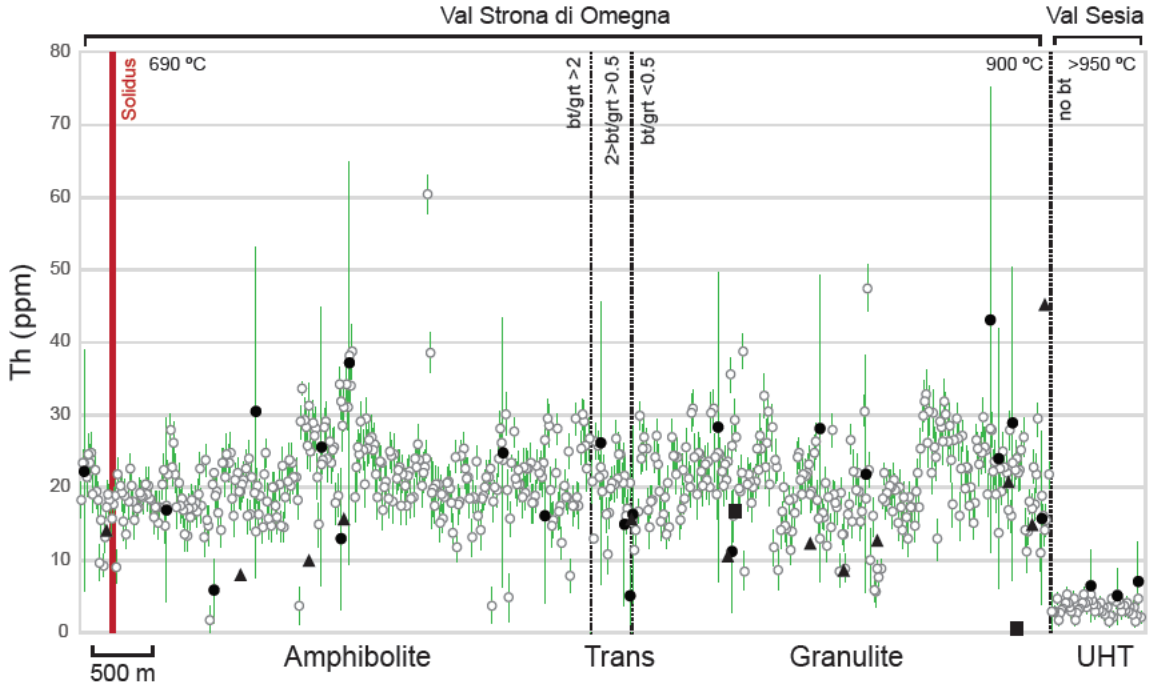

Figure 3. Th GRS (open circles) and Th WR (filled circles) concentrations in the Ivrea Verbano Zone as a function of metamorphic grade. Th GRS concentrations are from Alessio et al. (2018). Th WR concentrations are presented in table S2. Solid red line indicates the in field location of the solidus, black dotted lines indicate facies transitions, as defined by Bea and Montero (1999) on the basis of modal biotite/garnet (bt/grt). Error bars are 2 sigma: Th GRS errors calculated from machine errors, Th WR errors calculated from standard data. Pressure temperature estimates from Redler et al. (2013) and Ewing et al. (2013). Whole rock Th concentrations from Bea and Montero (1999) and Guergouz et al. (2018) indicated by black triangles and squares respectively. Trans, Transition zone; UHT, ultra high temperature granulite (septa).

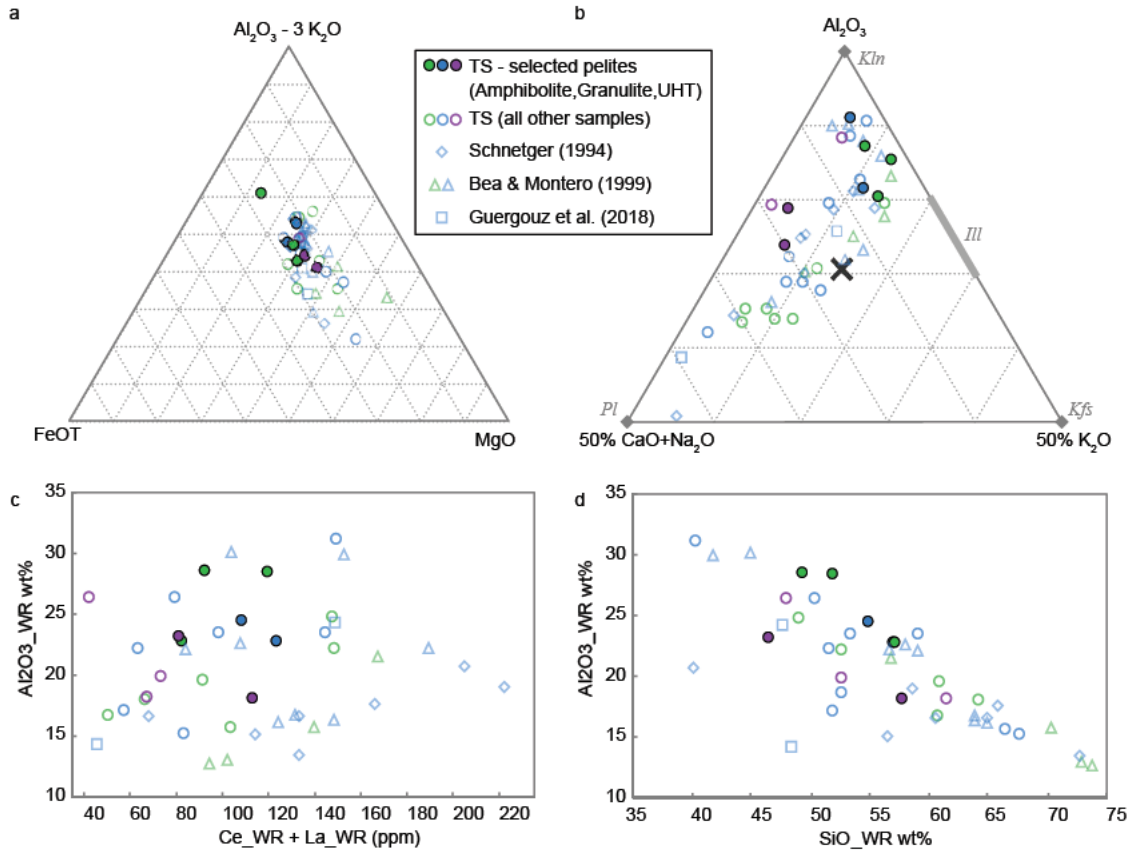

Figure 4. Whole rock geochemistry from the Ivrea Verbano Zone metapelites of this study. (a) Al_2O_3 FeO(total) MgO (AFM) diagram. (b) Al_2O_3 CaO+Na_2O K_2O diagram after Janots et al. (2006). Shaw's average pelite shown with grey cross (Shaw, 1956). Ill, Illite, Kln, Kaolinite, Kfs, K feldspar, Pl, plagioclase. (c) Al_2O_3 WR vs Ce WR + La WR. (d) Al_2O_3 WR vs SiO_2 WR. See Table S2 for whole rock geochemical analyses.

retain monazite, enabling the largest *P–T* range over which to study monazite chemistry (e.g. Spear, 2010; Spear & Pyle, 2010). In particular, monazite in these rock compositions exists well above the solidus, enabling study of monazite–melt interactions. The UHT samples have distinctly lower K_2O (Fig. 4b) than amphibolite- and granulite-facies samples. Samples IV16-22A and IV16-22B were selected for further analysis as they are the least weathered of the UHT samples. In addition to having lower K_2O than other samples selected for analysis, these samples also have significantly higher CaO and Na_2O (Fig. 4b). Whether the UHT rock chemistry reflects the primary chemistry of the metasediments is unclear. However, CaO- and Na_2O-rich metasediments are reported from within the Ivrea section (Fig. 4b; Bea & Montero, 1999; Guergouz et al., 2018; Schnetger, 1994).

In-field GRS data (Th_GRS) from IVZ metapelites (Fig. 3, data from Alessio et al., 2018) shows no change in the range of Th ppm concentrations between amphibolite- and granulite-facies rocks with peak temperatures up to approximately 900 °C. Analyses from the UHT septa at Isola (peak temperatures >950 °C) have significantly lower Th_GRS than lower-temperature granulite-facies metapelites (Fig. 3). The average Th_GRS ppm for the amphibolite, granulite and UHT samples are 21 ± 5 (*n*=306), 20 ± 6 (*n*=249) and 3 ± 1 (*n*=54), respectively (errors are 1 s.d.). Analyses for each facies fall in the ranges 3–34 ppm, 3–31 ppm and 1–5 ppm, respectively (see Alessio et al., 2018).

6.2 Accessory mineral petrography and vol ume proportions

Monazite occurs in all seven samples investigated, encompassing amphibolite-facies to UHT conditions. In the three amphibolite-facies samples, monazite occurs in various textural positions, in contact with or included in all major minerals. Monazite grains are predominantly within the matrix, included within or at the grain boundaries of biotite (Fig. 5a) and K–feldspar (Fig. 5a, b), and aligned with the fabric. Monazite rarely occurs as very small grains included in garnet porphyroblasts (e.g. Fig. 5b). In granulite-facies sample IV16-12, monazite occurs within the matrix adjacent to sillimanite (Fig. 5c), plagioclase (Fig. 5d) and biotite (Fig. 5d), and rarely at sillimanite–ilmenite/rutile grain boundaries. Monazite also occurs at the grain boundaries of garnet and sillimanite (Fig. 5c, d). In granulite-facies sample IV16-16, monazite most commonly occurs within leucosomes, with varying degrees of spatial association with apatite and allanite (Fig. 5e, f) or as inclusions in garnet (Fig. 5f). In the UHT samples, monazite occurs adjacent to quartz, K-feldspar, plagioclase and sillimanite (Fig. 5g, h), and rarely as inclusions in or adjacent to garnet (Fig. 5g).

Monazite maximum grain size increases from amphibolite-facies to granulite-facies, then decreases sharply in the UHT samples (Table 3). Monazite volume proportions ('modes') are in the range 0.001–0.074 vol.%. Monazite modes increase through the amphibolite-facies (0.037, 0.045 and 0.047 vol.%, Table 3). The two granulite-facies samples (IV16-12 and IV16-16) have significantly different monazite volume proportion (0.039 and 0.074 vol.% respectively). The UHT samples (IV16-22A, IV16-22B) have the lowest proportion of monazite of all samples (0.004 and 0.001 vol.% respectively).

Based our estimates from this section (Val Strona di Omegna), the zircon volume proportion generally increases with metamorphic grade from 0.013 to 0.030 vol.% (Fig. 6a, Table 3). However, the whole rock geochemistry data show constant Zr concentrations. Xenotime proportion is variable within the amphibolite-facies samples (0.0016–0.0078 vol.%) and decreases sharply

Table 3. Modal proportions of accessory minerals (vol. %) and grain characteristics in IVZ samples determined from point counting of MLA maps. Volume proportion detection limit is 10^{-6} vol.%.

	Volume proportion (vol. %)							*grain size (μm)*		
Sample	**mnz**	**ap**	**zrn**	**xtm**	**grt**	**aln**	***n***	**Ave**	**SD**	**Max**
IV16-03A	0.0367	0.0238	0.0128	0.0078	2.9955	0.0022	114	308	497	2613
IV16-07	0.0449	0.0184	0.0182	0.0016	8.2067	n.d.	137	362	564	3184
IV16-08	0.0472	0.2413	0.0195	0.0034	0.9999	2.10×10^{-6}	129	426	595	3890
IV16-12	0.0389	0.1097	0.0375	3.87×10^{-5}	17.3668	0.0147	174	264	431	2646
IV16-16	0.0745	0.0149	0.0300	n.d.	17.2629	0.0739	113	595	1520	12504
IV16-22A	0.0045	0.0005	0.0217	n.d.	22.6242	0.0265	133	18	42	438
IV16-22B	0.0010	0.0041	0.0297	3.86×10^{-5}	24.6371	0.0159	71	21	32	197

n.d. not detected; mnz, monazite; ap, apatite; zrn, zircon; xtm, xenotime; grt, garnet; aln, allanite; *n*, number of monazite grains.

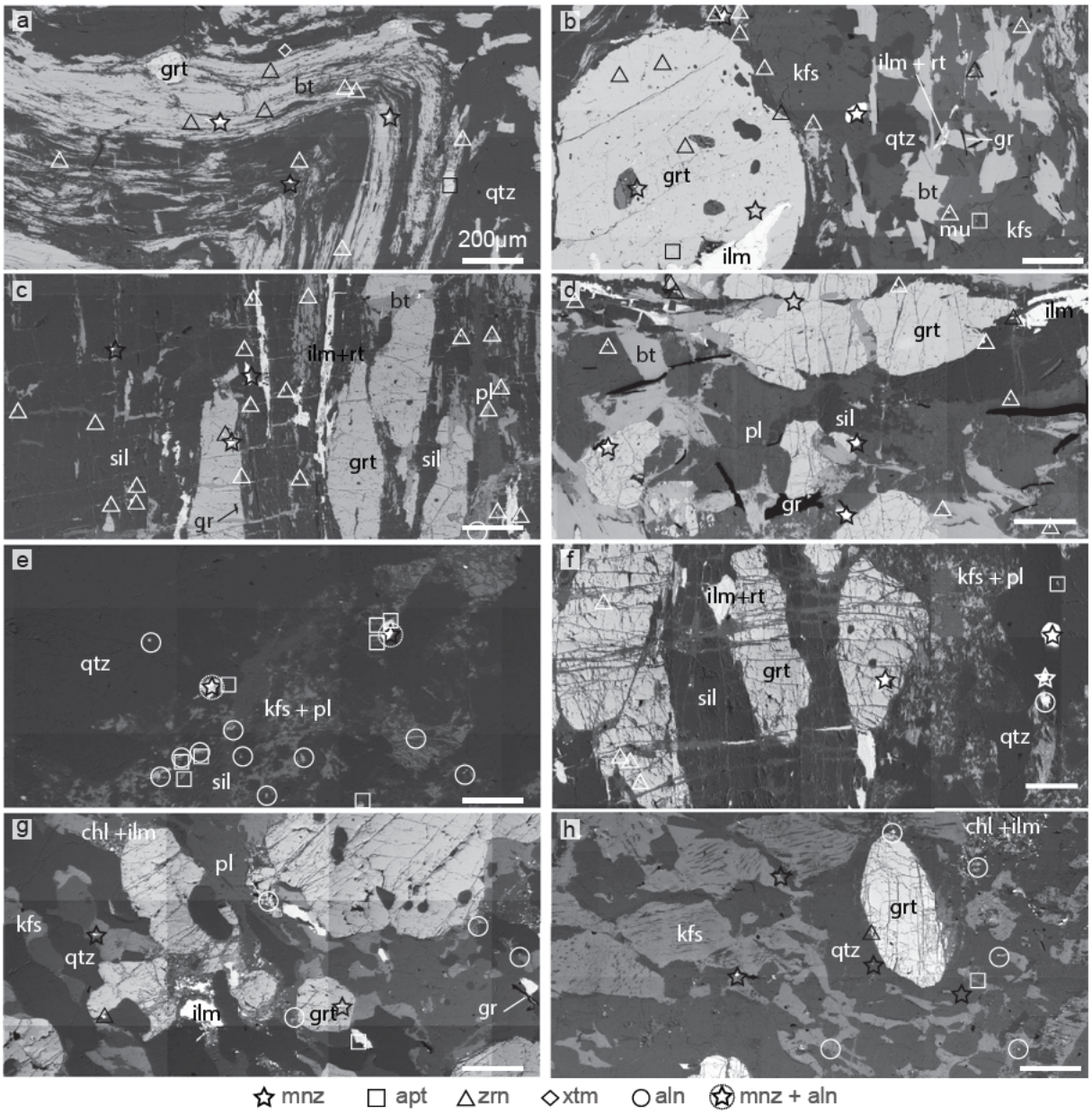

Figure 5. Representative backscattered electron photomicrographs indicating microstructural setting of monazite and other accessory minerals. (a) IV16 08; monazite preferentially distributed along the biotite fabric. (b) IV16 07; monazite within matrix and included in garnet. (c) IV16 12; mnz at sillimanite garnet grain boundary and aligned with sillimanite biotite fabric. (d) IV16 12; monazite included in garnet and plagioclase, and at garnet plagioclase and garnet biotite grain boundaries. (e) IV16 16; monazite with allanite rims in leucosome. (f) IV16 16; monazite included in quartz and garnet. (g) IV16 22A; monazite included in K feldspar and garnet. (h) IV16 22B; monazite in K feldspar and quartz in leucosome. (a) (h) Mineral abbreviations after Kretz (1983).

in the granulite-facies and UHT samples (less than 0.0001 vol.%; Fig. 6, Table 3). Apatite proportion is the most variable, in the range 0.0005–0.24 vol.%, and has maximum volume proportion in the upper amphibolite-facies (Fig. 6a). Allanite occurs in cracks in garnet in sample IV16-03A (0.0022 vol.%) and occurs in negligible volume proportion (<0.000002 vol.%) in the other amphibolite-facies samples (Fig. 6a). Allanite occurs as fine grained aggregates on monazite grain boundaries in leucocratic parts of all granulite and UHT samples, with greatest volume proportion in IV16-16. Volume estimates based on MLA maps confirm that garnet volume proportion broadly increases with metamorphic grade (Fig. 6b). There is a step change in garnet volume proportion between the amphibolite- (<10 vol.%) and granulite-facies (~18 vol.%) rocks, and similarly between granulite-facies and UHT samples (>22 vol.%; Fig. 6b).

6.3 Monazite composition

Monazite has been separated into nine distinct chemical zones based on EPMA map and point

Table 4. Representative EPMA analyses of monazite. Z1–9 refer to monazite zones described in text.

Mnz Zone		**Z1**	**Z2**	**Z3**	**Z4**	**Z5**	**Z6**	**Z7**	**Z8**	**Z9**
Sample		03A	07	08	03A	12	12	16	22B	22A
Grain		mnz 6	mnz 2	mnz 9	mnz 4	mnz 5	mnz 9	mnz 1	mnz 5	mnz 8
Analysis	**d l.**	23-6	40-6	31-3	22-4	54-2	58-2	104-6	66-3	120-1
SiO_2	0.02	0.21	0.38	0.12	0.14	0.33	0.22	0.82	1.98	0.26
CaO	0.01	0.25	0.97	1.09	0.71	0.90	1.02	0.37	2.56	0.13
Y_2O_3	0.04	0.60	b.d.l.	1.89	3.32	0.62	0.12	b.d.l.	0.12	0.06
La_2O_3	0.04	13.42	15.55	14.64	14.64	14.87	14.72	12.85	11.64	16.23
Ce_2O_3	0.04	32.18	29.22	28.63	28.19	29.56	30.09	32.79	23.23	33.30
Pr_2O_3	0.15	3.81	3.23	3.07	3.15	3.22	3.25	4.00	2.62	3.65
Nd_2O_3	0.15	13.87	11.67	10.65	11.06	11.40	12.32	13.61	9.63	13.42
Sm_2O_3	0.16	2.18	2.05	1.68	1.84	1.76	1.67	0.92	1.09	1.12
Gd_2O_3	0.17	1.62	1.16	1.23	1.71	0.92	0.65	0.23	0.38	0.33
ThO_2	0.03	0.75	4.35	4.50	2.12	4.28	4.53	4.37	17.63	b.d.l.
UO_2	0.01	0.07	0.48	0.56	0.68	0.27	0.23	0.05	0.04	0.06
P_2O_5	0.05	31.38	30.59	31.85	31.51	31.21	31.10	29.59	28.40	31.00
Total		**100.35**	**99.67**	**99.93**	**99.07**	**99.35**	**99.94**	**99.60**	**99.33**	**99.55**
Si^{4+}		0.008	0.015	0.005	0.005	0.013	0.009	0.032	0.078	0.010
Ca^{2+}		0.010	0.040	0.045	0.029	0.037	0.042	0.016	0.108	0.005
Y^{3+}		0.012	b.d.l.	0.038	0.068	0.013	0.002	b.d.l.	0.003	0.001
La^{3+}		0.189	0.223	0.205	0.206	0.211	0.209	0.186	0.169	0.231
Ce^{3+}		0.451	0.415	0.398	0.394	0.416	0.424	0.471	0.335	0.471
Pr^{3+}		0.053	0.046	0.043	0.044	0.045	0.046	0.057	0.038	0.051
Nd^{3+}		0.190	0.162	0.144	0.151	0.157	0.169	0.191	0.136	0.185
Sm^{3+}		0.029	0.027	0.022	0.024	0.023	0.022	0.012	0.015	0.015
Gd^{3+}		0.021	0.015	0.015	0.022	0.012	0.008	0.003	0.005	0.004
Th^{4+}		0.007	0.038	0.039	0.018	0.038	0.040	0.039	0.158	b.d.l.
U^{4+}		0.001	0.004	0.005	0.006	0.002	0.002	0.000	0.000	0.000
P^{5+}		1.017	1.005	1.024	1.019	1.017	1.014	0.984	0.947	1.014
Total Cations (S)		1.987	1.991	1.983	1.987	1.984	1.988	1.992	1.992	1.989
p(REEmnz)		0.976	0.927	0.867	0.874	0.906	0.911	0.943	0.721	0.994
p(cher)		0.010	0.071	0.088	0.050	0.067	0.079	0.023	0.195	0.000
p(hut)		0.001	0.002	0.005	0.006	0.013	0.009	0.033	0.081	0.005
p(xtm)		0.013	<0.001	0.040	0.070	0.013	0.003	<0.001	0.003	0.001

Prefix for all samples is IV16-XX. Oxide values are wt %. Detection limit (d.l.) quoted at 99% confidence level. Cations calculated for 4 oxygens. p(REEmnz)= proportion of monazite end-member (∑REE), p(cher)= proportion of cheralite end-member (1-((∑REE+Y+Si)), p(hut)= proportion of huttonite end-member (Si^{4+}), p(xtm) = proportion of YPO4 end-member in monazite (Y^{3+}). B.d.l., below detection limit.

Table 5. Summary of monazite compositional zones and microstructural locations. Z1–9 are monazite zones defined in text. The chemistry of zones is summarised in Figs. 7 and 8.

Zone	Samples	Location	Th^{4+} APFU	*p(REEmnz)*	*p(cher)*	*p(hut)*	*p(xtm)*	*n*
Z1	03A, 08	c, m	0.0003–0.0153	0.956–0.981	0.001–0.029	0.006–0.018	0.007–0.013	8
Z2	03A, 07, 08	c, m	0.0111–0.0566	0.890–0.954	0.036–0.105	0.006–0.022	bdl–0.015	55
Z3	03A, 07, 08	r, m	0.0165–0.0757	0.840–0.887	0.064–0.125	0.002–0.017	0.024–0.060	139
Z4	03A	i, l	0.0181–0.0283	0.853–0.886	0.035–0.075	0.005–0.019	0.060–0.072	5
Z5	12	r, m	0.0279–0.0457	0.881–0.914	0.056–0.082	0.010–0.023	0.008–0.029	22
Z6	12, 16	c, r, m	0.0238–0.0577	0.858–0.968	0.010–0.113	0.007–0.035	bdl–0.025	85
Z7	16	r*, m	0.0192–0.0591	0.913–0.960	0.003–0.054	0.012–0.055	bdl–0.001	15
Z8	22A, 22B	i, g, m	0.0621–0.1879	0.681–0.861	0.111–0.227	0.024–0.091	0.002–0.004	10
Z9	22A, 22B	i, m	bdl–0.0141	0.946–0.994	bdl–0.038	0.003–0.042	bdl–0.013	73

Prefix for all samples is IV16-XX; c, core; r, rim; r*, rims (discontinuous); m, matrix; i, isolated grains; l, leucosome; g, garnet inclusion; bdl; below detection limit. p(REEmnz)= proportion of monazite end-member (∑REE), p(cher)= proportion of cheralite end-member (1-((∑REE+Y+Si)), p(hut)= proportion of huttonite end-member (Si^{4+}), p(xtm) = proportion of YPO4 end-member in monazite (Y^{3+}). *n* = number of monazite grains. Detection limits: Th^{4+} = 0.0003 APFU; *p(REEmnz)* = 0.0045; *p(cher)* = 0.0004; *p(hut)* = 0.0008; *p(xtm)* = 0.008.

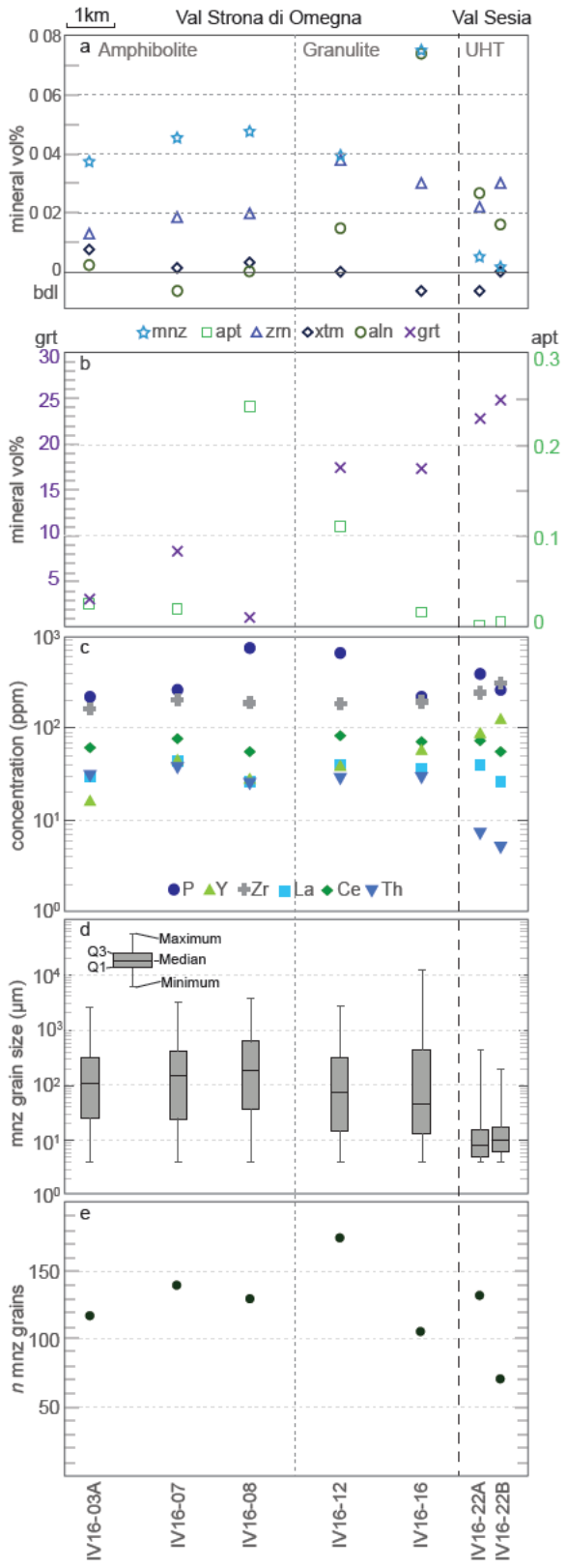

Figure 6. Mineralogical and chemical variation across metamorphic grade. Distance scale (x axis) shows distance between projected location of samples onto a linear transect of Val Strona di Omegna, increasing in metamorphic grade from left to right. Dashed line indicates break in section. IV16 22A and IV16 22B were collected approximately 1 m apart in the outcrop of Val Sesia. Note logarithmic scale for (c) and (d). Uncertainty in measurements represented by the size of markers. (a) Volume proportions of accessory minerals (as vol. %), calculated from point counting of MLA maps. bdl, below detection limit (10 6 vol. %) (b) Volume proportions of garnet and apatite (as vol. %) calculated from point counting of MLA maps. Garnet scale on left of diagram, apatite scale on right. (c) Whole rock concentrations of P and selected trace elements, as element ppm. (d) Boxplots of monazite grain size determined from MLA mapping. Boxplots show dispersion of data, the interquartile range and median values for each element. Q1, quartile 1; Q3, quartile 3. (e) Number of monazite grains in each sample (thin section) demined from MLA maps. (a) (e) aln, allanite; apt, apatite; gt, garnet; mnz, monazite; xtm, xenotime; zrn, zircon.

analysis data, summarised in Tables 4 and 5. Zones were correlated between grains in the same sample, and also between samples, according to texture and chemical composition and in particular: (a) the regular and recurring spatial organisation of distinct zones in EPMA maps (Fig. 7); and (b) the identification of distinct populations in divariant scatter (Harker) plots of EPMA point data (Th, Ce, Y, Ca Fig. 8a). Monazite zones 1–4 (Z1–Z4) occur in the amphibolite-facies samples, zones 5–7 (Z5–Z7) occur in the granulite-facies samples and zones 8 and 9 (Z8, Z9) occur in the UHT samples. Three of the nine zones (Z4, Z5, Z7) occur solely within single samples, with the remaining six zones occurring in two or more samples.

Monazite Z1 is a Th-poor and REE-rich zone with moderate Y (Fig. 8). Monazite Z1 occurs within the cores of monazite grains in samples IV16–03A and IV16-08, and is surrounded by Z2 and Z3 monazite (Fig. 7). Monazite Z2 is a moderate Th, Y-poor zone and Z3 is a moderate Th, Y-rich zone (Fig. 8). Zones 2 and 3, found in samples IV16-03A, IV16-07 and IV16-08, consistently show a core–mantle relationship, with Z2 internal to Z3. The width of Z3 rims increases with metamorphic grade (Fig. 7). Zone 4 is a very Y-rich zone with moderate Th and low LREE (Fig. 8). Zone 4 occurs only in sample IV16-03A as isolate grains with embayed edges within a leucocratic vein (see also Bea & Montero, 1999). Zone 5 is a moderate Th, moderate Y, and moderate REE zone (Fig. 8). Zone 5 occurs as cores of grains and rarely as isolate grains in granulite-facies sample IV16-12. Zone 5 has Y between that of Z2 and Z3 (Fig. 8a) and is therefore defined as a distinct monazite zone. Zone 6 is a moderate Th, low–moderate Y, and moderate REE zone (Fig. 8). Zone 6 occurs in samples IV16-12 and IV16-16, in the former as rims around Z5 and in the latter as cores of grains. Zone 7 is a moderate Th, Y- and HREE-poor and LREE-rich zone (Fig. 8). Zone 7 occurs in sample

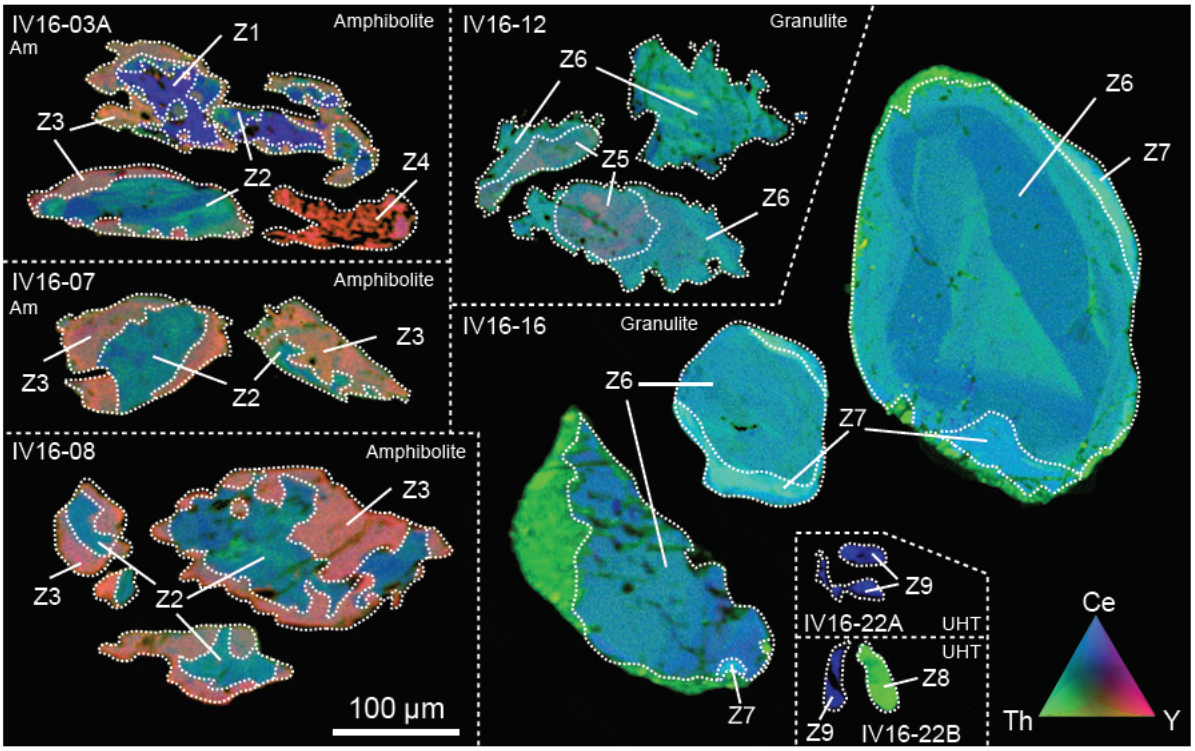

Figure 7. Representative composite EPMA maps of element concentrations in monazite from the Ivrea Verbano Zone metapelites. Images are composite qualitative maps of thorium, cerium and yttrium with the three element maps overlain. Green channel represents ThO_2 in the range 0 20.3 wt%, blue represents Ce_2O_3 in the range 0 33.9 wt% and red represents Y_2O_3 in the range 0 3.4 wt%. Colour scale shows the relative proportions of the elements Th, Ce and Y in each grain, scaled to highlight differences in chemistry between monazite zones. Z1 Z9 refer to monazite zones described in text. Bright green areas in IV16 16 represent intergrowths of allanite and Th orthosilicate.

IV16–16 as narrow, discontinuous rims around Z6. Monazite Z8 is a very Th-rich, Y- and REE-poor zone and Z9 is a very LREE-rich, Th- and Y-poor zone (Fig. 8). Monazite Z8 occurs within and adjacent to garnet grains in both UHT samples and Z9 occurs in the matrix of the UHT samples. Monazite zone 9 also occurs within garnet grains along fractures connected to the matrix. These are no additional microstructural controls on the appearance of other monazite zones (Z1–Z3, Z5–Z8) other than described above.

Th varies from <0.0003 to 0.19 atoms per formula unit (APFU; Table 5, Fig. 8a, b). It increases from monazite Z1 to Z2, then it is effectively constant in the remaining amphibolite-facies zones and in granulite-facies samples (Z5–Z7). Monazite Z8 in UHT samples has the highest Th concentration of all zones and Z9 the lowest. Y data show a peak in the amphibolite-facies samples (maximum of 0.07 APFU Y in Z4), intermediate Y concentration in the core of the granulite-facies monazite Z5 (0.01–0.03 APFU), and low Y concentrations (<0.0008 – 0.02 APFU) through the granulite-facies and UHT samples (Fig.s 7, 8). There is a similar, although more subtle, trend in Gd and U concentrations: higher contents are found in the rims of monazite grains of amphibolite-facies samples or cores of monazite grains of granulite-facies samples (Z1–5). ΣLREE and Ca have anti-correlated trends (ΣLREE = La+Ce+Pr+Nd+Sm). The lowest ΣLREE concentrations (0.7–0.8 APFU) occur in Z8, corresponding to proportional increases in Th, Ca and to a lesser extent Si.

In all compositional plots (Fig. 8b), Zone 8 is significantly distinct from other zones; this monazite zone has high Th and Ca and low ΣLREE (Table 5, Fig. 9a), indicating that grains from this zone have significantly higher fractions of huttonite [$ThSiO_4$] and cheralite [$Ca_{1/2}Th_{1/2}PO_4$] end-members than all other monazite zones. Zones 8 and 9 have been defined such that analyses with Th^{4+}_mnz > 0.02 APFU are Z8, and <0.02 APFU are Z9. In reality, Z8 and Z9 analyses are fairly evenly spread from the highest Th^{4+}_mnz (~ 0.19 APFU; Z8) to the lowest (<0.0003 APFU; Z9, Fig. 8), but with a distinct data gap in Th^{4+}_mnz between 0.014 APFU and 0.062 APFU (Table 3). Z9 has very low Th, with only 11 of 57 analyses above the detection limit. The difference between grains that preserve high rather than low Th compositions in these two UHT samples is a combination of grain size and microstructural

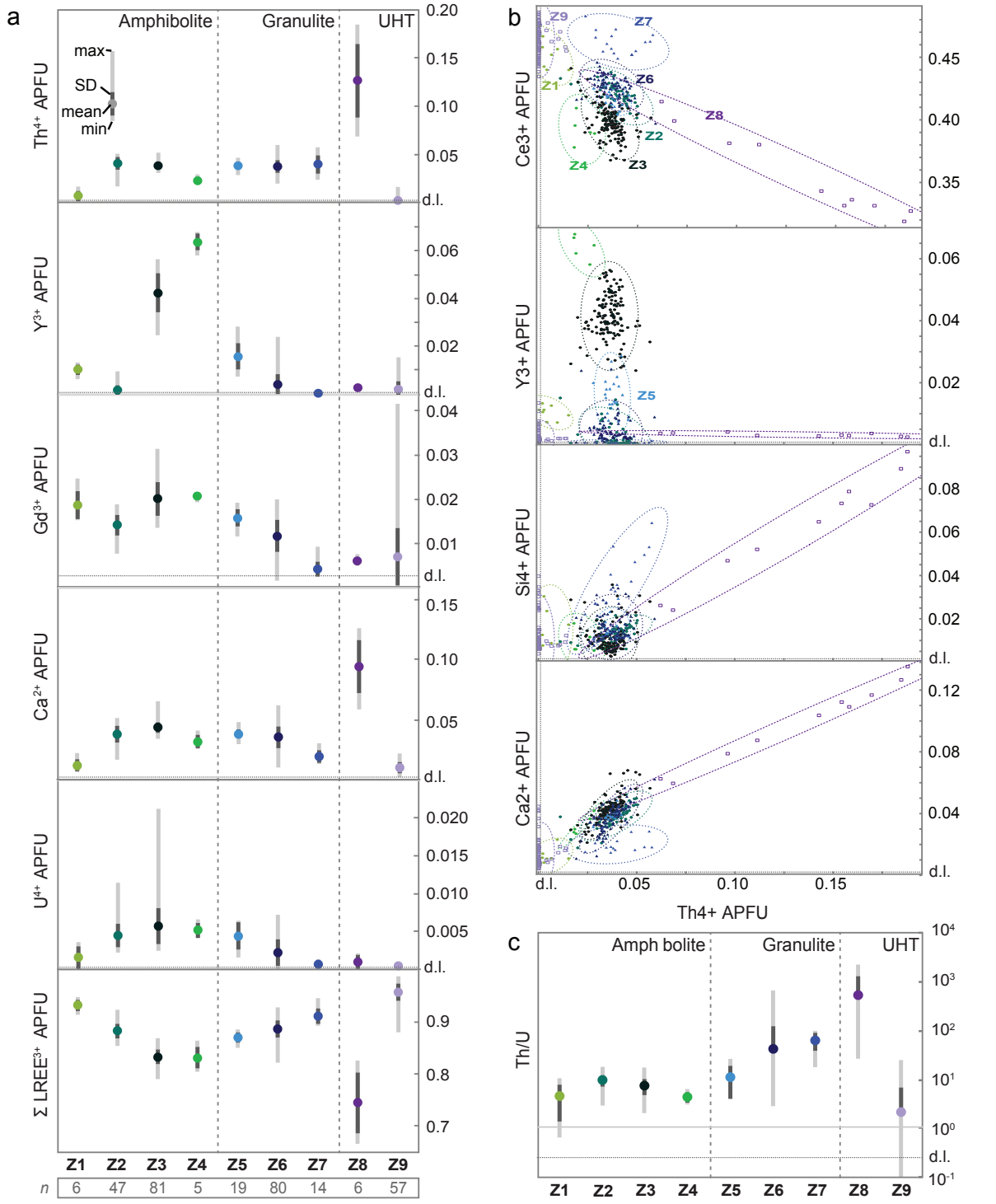

Figure 8. Harker and boxplots of EPMA point analyses of monazite from zones 1 9 (labelled Z1 Z9 respectively). Z1 Z4 occur in amphibolite facies samples, Z5 Z7 in granulite facies samples and Z8 Z9 in UHT samples. Number of analyses for each zone are given at the base of part (a). (a) Boxplots of chemical compositions of monazite (atoms per formula unit, APFU, normalised to 4 oxygen atoms) from zones Z1 Z9. Boxplots show dispersion of data, the interquartile range (IQR; Q1, quartile 1, Q3, quartile 3) and median values for each element. Dotted lines indicate metamorphic facies changes within the sequence. (b) Harker plots of monazite EPMA point analyses showing the range of compositions within each monazite zone, and the overlap between zones. Mahalanobis ellipses show range of compositions for each monazite zone (2σ). (c) Boxplots of Th/U ratios of monazite for compositional zones Z1 Z9. Boxplots show dispersion of data, the interquartile range (IQR) and median values for each element (as in (a)). Dotted lines indicate facies changes of the host rock. Note logarithmic scale.

location. Larger grains and those included in garnet preserve higher Th compositions than smaller grains located interstitially.

The Th/U ratio in monazite is relatively constant in amphibolite-facies zones (Z1–Z4) and granulite-facies Z5 (means of 4.3–11.3, Fig. 8c). Th/U then increases from Z6 to Z8 (means of 42, 64 and 531 for Z6, Z7 and Z8, respectively). Of the

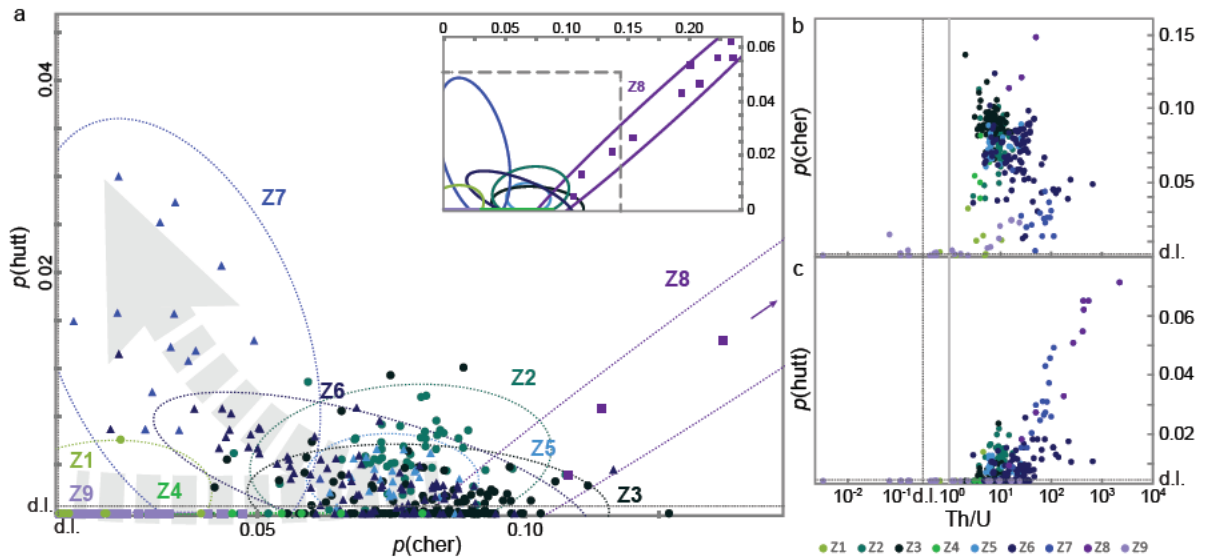

Figure 9. Fractions of Th end members of monazite cast from EPMA point data and normalised to p(cher) + p(hutt) + p(mnz) = 1, the proportions of the cheralite (Th Ca P), huttonite (Th Si) and Y+REE monazite respectively. Z1 Z9 refer to monazite zones Z1 Z9 described in text. (a) Relative proportion of Th end members cheralite and huttonite. Mahalanobis ellipses show range of compositions for each monazite zone (2σ). Dashed arrow represents interpreted changes to the cheralite/huttonite ratio with metamorphic grade. (b) Proportion of cheralite vs Th/U ratio. (c) Proportion of huttonite vs Th/U ratio.

Z9 analyses with Th above the detection limit, Th/U ratios are variable but the lowest in the sequence (0.5–24.3, Fig. 8c).

6.4 Monazite U Pb geochronology

The different chemical zones identified by EPMA mapping were targeted (size permitting) for U–Pb geochronology. All samples in the study have complex spectra of Pb-corrected $^{206}Pb/^{238}U$ dates, with a total spread between 347 ± 20 and 154 ± 16 Ma, (Fig. 10 and Appendix S3.2). Date ranges for all amphibolite- and granulite-facies monazite zones (Z1–Z7) overlap and mostly fall in the range 240–320 Ma. Analyses on monazite from the UHT samples are fewer due to these monazite grains being small and yield more scattered dates in the range c. 150–300 Ma (Z8 and Z9). There is no systematic age difference between grains in different microstructural locations either within or between samples. Additionally, the range of dates for all monazite zones overlap, and for the zones that yield a significant number of analyses in statistically homogeneous populations (Z2, Z3, Z4, Z5 and Z6) the main cluster is between 275 and 290 Ma. The main cluster for Z2 is 290 ± 2.5 Ma, for Z3 is 280 ± 2.5 Ma, for Z4 is 279 ± 6.9 Ma, for Z5 is 276 ± 6.7 Ma and for Z6 is 275 ± 2.9 Ma. Notably, the youngest, although scattered, dates to 150 Ma are all from Z9 monazite in UHT samples. The overall data show two major age peaks at 290 ± 1.7 Ma and 271 ± 1.7 Ma and one minor peak at 173 ± 16 Ma (Fig. 10).

7 DISCUSSION

7.1 Whole rock Th budget

The extensive data set of Th concentrations acquired with the two methods (XRF and GRS; Fig. 3; Alessio et al., 2018) show that Th is retained in the metapelitic rocks up to the highest grade of regional metamorphism (~900 °C; Redler et al., 2012), consistent with the findings of Schnetger (1994), Bea and Montero (1999) and Bea (2012). The retention of whole rock (WR) Th during pre-peak to peak metamorphism of pelites to granulite-facies conditions is consistent with the trends found in several other terranes worldwide (e.g. Chapter 2; Alessio et al., 2018; Andreoli, Hart, Ashwal, & Coetzee, 2006; Horton, Hacker, Kylander–Clark, Holder, & Jöns, 2016; Skrzypek et al., 2018).

By contrast, the UHT samples have significantly lower Th content than other samples in this study. This observation is in agreement with the whole rock geochemistry data of Ewing et al. (2014), which show a decrease in WR Th concentration in the septa of an order of magnitude with respect to amphibolite- and granulite-facies samples. As this depletion of WR Th is only observed in the UHT septa and the monazite in these samples has small grain size and low volume proportion, the process that causes the efficient extraction of Th from the residual rocks must only occur at very high crustal temperatures (i.e. > ~900 °C) or in samples with chemistry similar to the

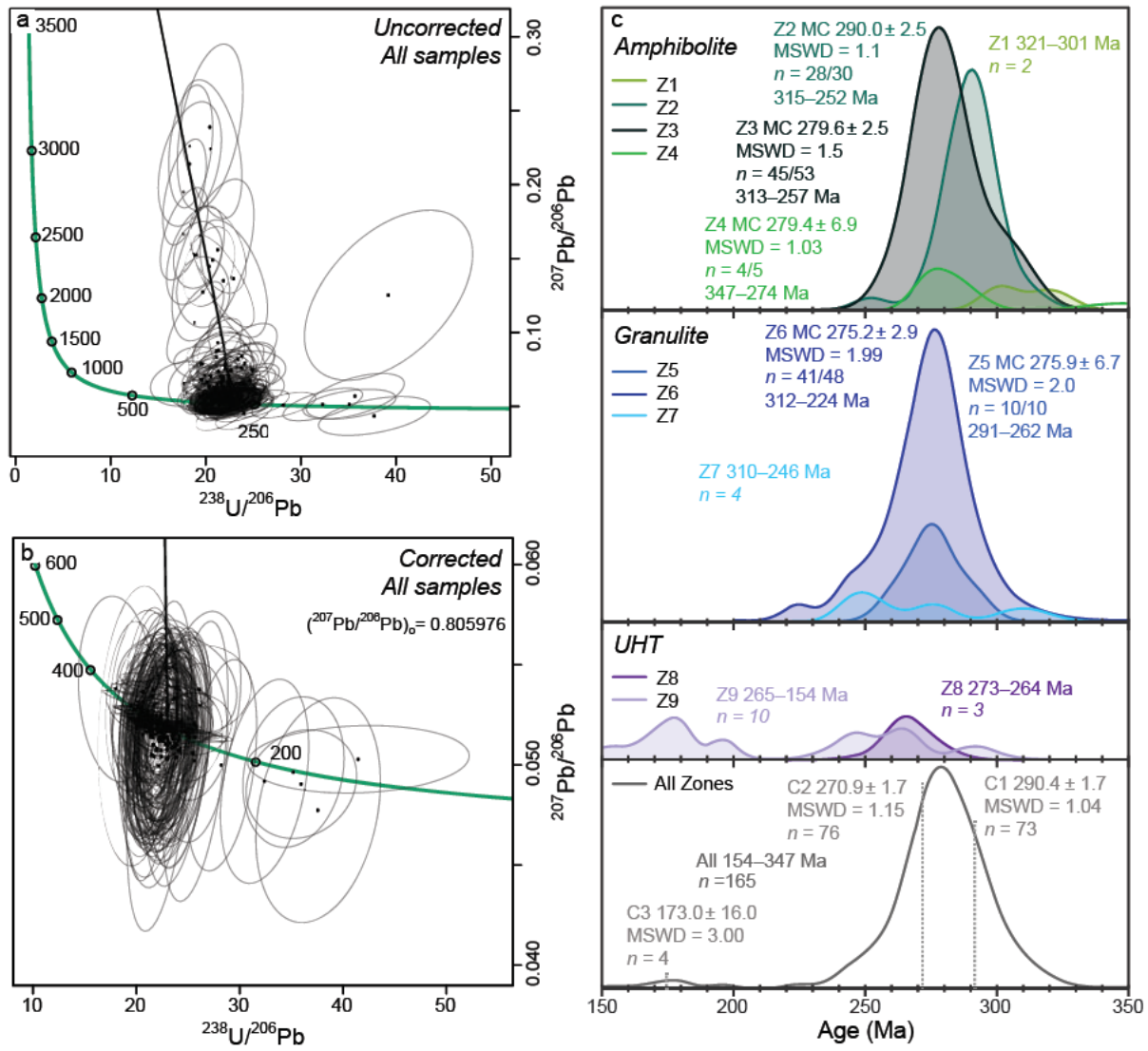

Figure 10. LA ICP MS monazite geochronology from the Ivrea Verbano Zone. (a) Tera Wasserburg plot of uncorrected monazite data; (b) Tera Wasserburg plot of ^{207}Pb corrected monazite data. Bold black line in parts (a) and (b) is the regression line for the initial $^{207}Pb/^{206}Pb$ ratio ($^{207}Pb/^{206}Pb_0$) used in the ^{207}Pb correction; (c) Probability density plot of LA ICP MS monazite Pb corrected $^{206}Pb/^{238}U$ dates. Ranges of $^{206}Pb/^{238}U$ ages are shown for all zones and weighted average $^{206}Pb/^{238}U$ ages are shown for compositional zones Z2, Z3, Z4, Z5 and Z6. Statistically meaningful ages could not be calculated for Z1, Z7 Z8 and Z9. In each legend the samples are listed in order of increasing metamorphic grade. Pb correction was performed using 207 method. MC, main cluster; C1 3, Cluster 1 3 determined by radial plot.

UHT granulites in this study. In agreement with previous studies of UHT samples (Ewing et al., 2014; Stepanov, Hermann, Korsakov, & Rubatto, 2014) and modelling (Yakymchuk & Brown, 2014a; Yakymchuk, Kirkland, & Clark, 2018) we interpret metamorphism to UHT conditions at Ivrea to have involved significant dissolution of monazite into (extracted) melts, and that the solubility of monazite was most advanced in the UHT metapelitic septa. The presence of monazite in the UHT rocks (Fig. 10; Ewing et al., 2013) suggests either that the temperature for total monazite dissolution is higher than previously reported (Kelsey, Clark, & Hand, 2008; at least in the rocks we have studied; e.g. Spear & Pyle, 2010; see also Yakymchuk & Brown, 2019) and/or that monazite dissolution was kinetically or physically inhibited (see also Yakymchuk & Brown, 2019). The marked decrease in average grain size, low volume proportion of monazite and the location of monazite primarily at grain boundaries within the matrix of the two UHT samples (Table 3, Figs. 6, 7) supports that significant monazite dissolution has occurred at UHT conditions. This monazite dissolution may have been further facilitated by interaction with mafic melt surrounding the septa as the UHT samples have higher CaO than other pelite samples in this study.

Th_WR ppm concentrations of samples collected from the same outcrops as Th_GRS measurements broadly lie within the spread of Th_GRS data (Fig. 3; Alessio et al., 2018). Values from XRF analyses

that fall outside the spread of GRS data from the same outcrops most likely reflect the decimetre to metre scale of heterogeneous layering, and the variable proportion of mafic and calc–silicate rocks in the sequence that contribute to the GRS outcrop-scale data.

7.2 Monazite stability

Monazite occurs in all samples in this study. Monazite volume proportions increase with metamorphic grade in the Val Strona section (mid-amphibolite to granulite facies), consistent with other studies (e.g. Chapter 2; Foster et al., 2002; Franz, Andrehs, & Rhede, 1996; Rubatto, Williams, & Buick, 2001; Schulz, 2017; Skrzypek et al., 2018; Williams, 2001). These data indicate that monazite was stable up to the peak of regional metamorphism (~9.5 kbar, 900 °C; Redler et al., 2012; Kunz et al., 2018). The increase in monazite volume proportions can partially be explained by a decrease in the rock volume due to the extraction of melt, estimated to be up to 40% in the IVZ (Redler et al., 2013). However some monazite (or monazite components) is expected to have been extracted with the melt (Stepanov et al., 2012).

The maximum grain size of monazite increases with metamorphic grade (Fig. 6, Table 3); however, as large(r) monazite grains are few in each sample they do not greatly affect the sample average grain size. The grain size increase may be the result of processes which favour the growth of large grains of monazite, such as the REE-saturated melt infiltration model proposed by (Yakymchuk & Brown, 2019), decompression melting (e.g. Johnson, Clark, Taylor, Santosh, & Collins, 2015), or Ostwald ripening (dissolution of smaller grains and precipitation onto larger grains; e.g. Nemchin, Giannini, Bodorkos, & Oliver, 2001). However, Ostwald ripening would typically preserve lower temperature cores, which are not observed in the granulite facies samples and so cannot explain the full range of textures observed here. It is also possible, but unlikely, that it is an artefact of the orientation of the thin section cuts, whereby processes such as dissolution-precipitation creep could elongate grains in the fabric orientation and lead to an overestimation of monazite volume proportion at higher grades. Regardless, a general increase in monazite grain size and mode with metamorphic grade has been reported for other metapelitic sequences (e.g. Chapter 2; Foster et al., 2002; Franz et al., 1996; Rubatto et al., 2001; Schulz, 2017; Williams, 2001). Monazite volume proportions and average and maximum grain sizes decrease sharply in the UHT septa relative to the amphibolite- and granulite-facies samples. This is related to dissolution in the extracted melt (see above). Allanite volume proportion in the granulite-facies samples (IV16-12 and IV16-16) is non-negligible (Fig. 6); however all of the allanite in these samples is hosted in allanite–Th-orthosilicate aggregates on monazite grain boundaries. These aggregates were interpreted by Bea and Montero (1999) to be products of the retrograde breakdown of monazite (see also Chapter 4).

7.3 Grain scale variation of Th

The monazite geochronology presented in Figure 10 shows that all monazite in the investigated samples is metamorphic, and records a protracted growth (and dissolution) history (see section 7.4). In that context monazite composition can be evaluated to give insights on the origin and behaviour of this mineral. As outlined below, we interpret the main sequence of prograde-to-peak monazite formation in the order: Z1–Z3 then Z5–Z8 (Fig. 11). Zones Z4 and Z9 are interpreted to have formed on the retrograde path (see below) and thus are not strictly part of the pre-peak to peak sequence of monazite formation. Monazite zones Z1–Z3 and Z5–Z8 preserve a temporal series of chemical zones, the compositions and order of which are consistent with the recorded and modelled progression of major and accessory mineral growth along the metamorphic field gradient in the IVZ (Fig. 6; Redler et al., 2012). Y-in monazite is a suitable tool to link monazite growth with that of garnet and xenotime and to calculate *P–T* conditions when it coexists with these two minerals (e.g. Pyle & Spear, 2003). Monazite forming in a xenotime bearing assemblage is Y-buffered, whereas monazite formed in equilibrium with garnet is Y- (and HREE-) poor (e.g. Pyle & Spear, 1999; Pyle, Spear, Rudnick, & McDonough, 2001). Additionally, high REE monazite has been observed in several studies at low temperatures (<300 °C; e.g.Allaz, Selleck, Williams, & Jercinovic, 2013; Cabella, Lucchetti, & Marescotti, 2001; Rasmussen & Muhling, 2007) where there are fewer competing hosts for REE that are released from the breakdown of lower *T* minerals such as allanite. We use these observations in combination with the microstructural location of zones to assess

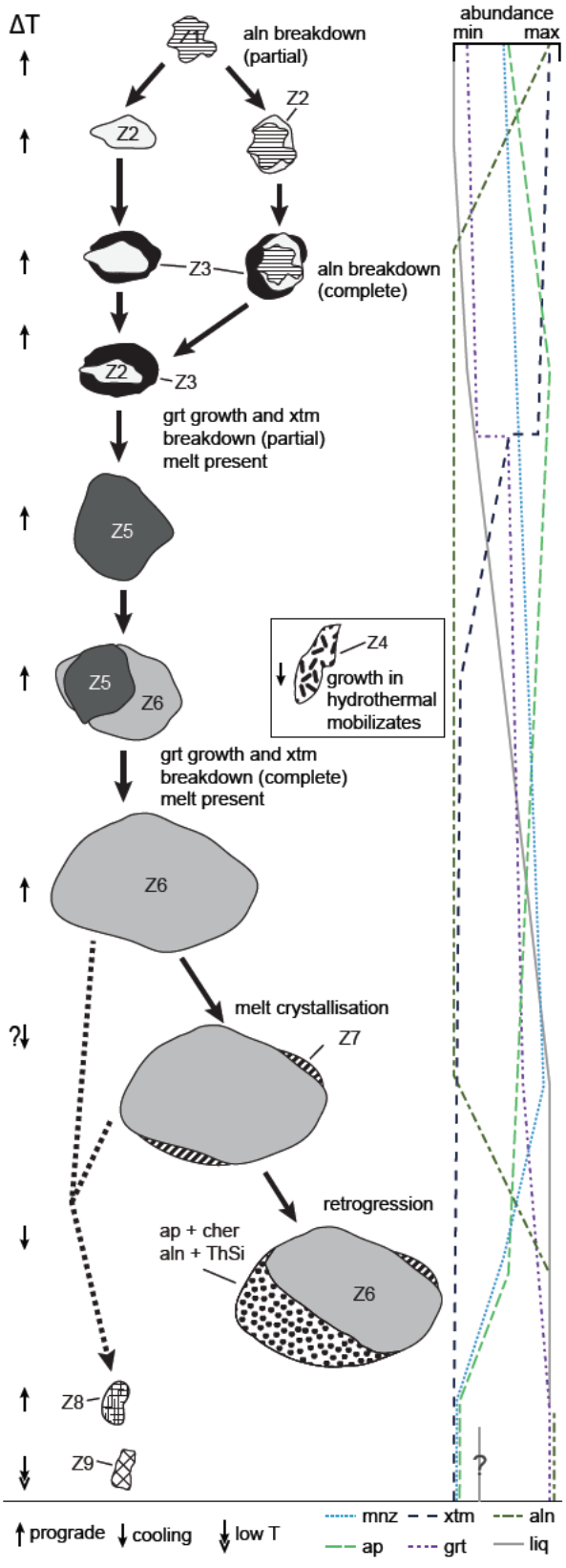

Figure 11. Interpretative monazite formation summary from the IVZ. Z1–Z9 are monazite zones described in text. Schematic abundance plot shows changes in mineral and melt abundance relative to the growth of monazite zones. Refer to Figure 6 for absolute volume proportions of minerals. Melt abundance from Redler et al. (2013). Ap, apatite; aln, allanite; gt, garnet; liq, melt; mnz, monazite; xtm, xenotime.

the *P–T* history of monazite formation in the IVZ metapelites.

High LREE Z1 monazite is found in the cores of grains, only in amphibolite-facies samples IV16-03A and IV16-08. Similar patchy core textures have been reported from other terranes (Chapter 2; Skrzypek et al., 2018). In both of these published examples, the high LREE zones can be traced through metamorphic grade changes, originating as aggregates of small monazite grains in lower-amphibolite-facies rock, pseudomorphed after (probable) allanite (Chapter 2; Skrzypek et al., 2018). In low Ca compositions such as IV16-03A and IV16-08 (0.15 and 0.47 CaO_WR respectively), the stability of allanite is reduced and this first monazite zone is inferred to form at lower amphibolite-facies conditions, close to where the transition from metamorphic allanite to metamorphic monazite first occurs (e.g. Spear, 2010). Z1 monazite is also particularly low in Th and this is likely due to low solubility of cheralite and huttonite in monazite at low temperatures and/or the persistence of allanite, thorite or some other Th-bearing orthosilicate as a Th-bearing phase.

The transition between Z1 and Z2 monazite, characterised by a change to higher Th and lower REEs, indicates the progressive incorporation of Th, predominantly via the cheralite substitution, within monazite at inferred lower-to-mid amphibolite-facies conditions. We interpret this as a continuation of the allanite-consuming reaction that forms Z1 monazite. In this scenario, the increase in Th from Z1 and Z2 is due to the higher temperature at which the continuous reaction is occurring, rather than a difference in the minerals reacting (i.e. no new reactants). We propose that as the continuous allanite breakdown reaction progresses to higher temperature, monazite accommodates more Th that is released from high(er)-Th allanite (see also Skrzypek et al., 2018), primarily via the cheralite coupled substitution mechanism.

Zone 3 monazite is characterised by a higher Y content than Z1–2 and likely formed in a xenotime-bearing (i.e. Y buffered) assemblage (as there is xenotime in amphibolite-facies samples), as such assemblages correspond with high Y monazite (e.g. Pyle & Spear, 2003). On the basis of previous studies of Y in garnet, monazite and xenotime, Y-in-monazite is thought to be a monitor of temperature (e.g. Pyle & Spear, 2003). If this is the case, all subsolidus monazite

(Z1, Z2 and Z3) in the IVZ is grown during pre-peak to peak metamorphism. The disappearance of Z3 monazite in the granulite-facies rocks is concurrent with a decrease in xenotime volume proportion by two orders of magnitude (Fig. 6, Table 3) and increase in garnet volume proportion with metamorphic grade (Fig. 6, Table 3).

Zone 4 monazite occurs only in muscovite-rich leucocratic veins in the lowest grade sample studied, IV16-03A. These leucocratic veins were interpreted by Bea and Montero (1999) to have been hydrothermal mobilizates, rather than partial melts. It is for this reason that we do not consider Z4 monazite as part of the pre-peak monazite reaction sequence, but rather formed during the retrograde evolution.

Notably, no monazite compositional zone found in amphibolite-facies samples is preserved in the granulite-facies samples, showing that all amphibolite-facies monazite is lost at higher *T* in the studied samples. Monazite included in garnet and that located interstitially in the matrix were identified in granulite IV16-12 and investigated in detail. All of the monazite grains located inside garnet were located within fractures and thus in likely chemical communication with the matrix. It is possible that our textural analysis may have missed rare monazite grains included in garnet that may preserve amphibolite-facies zoning. However, this is unlikely as the full thin section was mapped (by MLA) and no such grains were found. The processes which resulted in the lack of amphibolite facies cores preserved in granulite facies samples are unclear and such a feature is not observed in other recent studies of the chemical response of monazite in response to progressive metamorphism (e.g. Chapter 2; Skrzypek et al., 2018). These processes could involve fully consuming earlier generations of monazite by dissolution–precipitation creep (e.g. Wawrzenitz, Krohe, Rhede, & Romer, 2012) facilitated by elevated strain and the presence of melt in the granulite facies samples. It could also be a result of a reaction sequence in the granulite facies samples where the first appearance of monazite (from allanite) closely coincides with, or occurs above, the solidus due to the positive slopes of the allanite to monazite reactions (Spear, 2010). This would probably limit the formation and preservation potential of (subsolidus) prograde or pre-peak monazite. Such a scenario could be further influenced by changing melt composition characteristic of an open melting system (e.g. Yakymchuk & Brown, 2019).

Monazite Z5 is relatively similar in composition to Z3, but with significantly lower Y (Fig. 8a, b). A clear step change in garnet (increase) and xenotime (decrease) volume proportion between the upper amphibolite- and granulite-facies samples exists (Fig. 6). These combined observations suggest the formation of Z5 monazite in the presence of increasing garnet and decreasing (to zero) xenotime volume proportion at granulite-facies conditions. In this scenario, the increasingly larger volume of garnet sequesters the Y and HREE (e.g. Gd, Fig. 8a) and as the reactive bulk composition becomes undersaturated in Y due to disappearance of xenotime the Y available to monazite decreases (e.g. Pyle et al., 2001). As a consequence, Z5–Z7 monazite formed at granulite facies is depleted in Y and HREE compared with the last amphibolite-facies monazite, Z3, which grew in the presence of xenotime and lower volume proportion of garnet. It is inferred that the LREE and P for monazite growth in granulite-facies rocks come from the cannibalisation of amphibolite-facies monazite (absent in the granulite-facies samples) or that LREE came from allanite and P from apatite and xenotime as discussed above (Fig. 6).

Zone 6 monazite has very low Y and Gd concentrations that are consistent with near total absence of xenotime in sample IV16-16 (and lack of Z5 monazite in this sample), suggesting that Z6 represents near-completion of the reaction that removed xenotime. We interpret that Z5 and Z6 monazite formed on the pre-peak to peak part of the granulite-facies *P–T* path (Fig. 11) since this is consistent with garnet mode increasing from lower to higher grade samples and thus increased sequestering of Y and Gd by garnet. Figure 8c shows that Z6 is distinct from Z2 in having significantly higher Th/U ratios. Additionally, Z6 monazite occurs as rims on Z5 monazite in IV16-12. If Z2 and Z6 were in fact the same monazite zone, we would expect to see some record of monazite in the amphibolite facies with compositions similar to Z5. Despite very low Gd and Y in Z6 relative to Z5 monazite, these two zones (as well as Z7) have similar Th concentrations (Fig. 8). This confirms that Y-in-monazite and Th-in-monazite are controlled by two different processes, the former by xenotime and garnet (e.g. Pyle et al., 2001) and the latter most likely by silicate melt and temperature (Stepanov et al., 2012; Yakymchuk et al., 2018)

and monazite volume proportion (see chapter 4).

The microstructural locations of large monazite grains in sample IV16-16 containing Z6 and Z7 are predominantly within or adjacent to leucocratic layers (Fig. 5), suggesting that these monazite grew in the presence of silicate melt. Forward thermodynamic modelling of granulite-facies samples from the same crustal section by Redler et al. (2013) shows that the granulite-facies metapelite produced up to 25–30% melt which was progressively extracted. It has been proposed that such large volumes of melt do not 'pool' in high grade rocks (e.g. Rosenberg & Handy, 2005; Yakymchuk & Brown, 2014b). Rather, the melt is extracted in pulsed batches once it becomes interconnected (~7 vol.% melt; Rosenberg & Handy, 2005) and able to flow, leaving behind films of melt at the grain boundaries in amounts that are below that of linked interconnectivity (~1 vol% melt; e.g. Yakymchuk & Brown, 2014a). Further temperature increases produce more melt and lead to renewed interconnectivity of melt pockets, melt flow and ultimately extraction of a new batch of melt. It is unclear how such melt-extraction processes could facilitate the formation/preservation of large monazite grains but this may be the result of melt compositions which are not conducive to monazite dissolution (e.g. 'dry' melts) or kinetically inhibited dissolution of monazite (see also Yakymchuk & Brown, 2019).

Zone 7 appears as thin, discontinuous rims on large, predominantly Z6 grains in sample IV16-16. Zone 7 has higher U, Ca and ΣHREE and lower ΣLREE than Z6, and comparable Th to Z6 (Fig. 8). The increase in HREE suggests growth during modal decrease of garnet, a major source for HREE, which would occur as a result of a down-pressure and retrograde trajectory along a clockwise path (see also Redler et al., 2012). An alternative source of HREE could be zircon, but this option can be excluded as the mode of zircon is constant across the sequence (Fig. 6).

The UHT samples have a distinct monazite population in composition, texture, mode and partially age. Analogous to the amphibolite to granulite change, the UHT samples contain no remnants of monazite zones observed in the lower *T* granulite samples of the regional sequence. In the UHT samples monazite volume proportion is very low (0.001–0.0045 vol. %) and monazite compositions show a range between high (Z8) and low Th (Z9). The high Th content in monazite at UHT can be explained by a high $D^{Th}_{mnz/liq}$ (see also Stepanov et al., 2012) in samples with a low monazite volume proportion that have undergone signifi cant partial melting and melt extraction. The very low monazite Y content is consistent with a high volume proportion of garnet in the UHT samples.

High LREE compositions, typical of low temperature monazite (e.g. Allaz et al., 2013; Cabella et al., 2001; Rasmussen & Muhling, 2007) and recorded by Z9 monazite, could be the result of episodic formation of monazite on the retrograde path, for example during late fl uid circulation in the Mafi c Complex (Vavra & Schaltegger, 1999).

7.4 Monazite ages

The purpose of collecting age data in the context of this study is primarily to decipher whether monazite is metamorphic or detrital. Overall our monazite data conform with the range and complexity of zircon and monazite ages reported in previous studies and attributed to metamorphism (e.g. Ewing et al., 2013; Guergouz et al., 2018; Kunz et al., 2018; Vavra et al., 1999). Figure 10a shows a clear discordant trend in the U–Pb unknown data across all samples in this study. This trend was attributed to common Pb and was corrected for using a ^{207}Pb correction (Fig. 10b, see appendix S3.1 for details). In general, the ^{207}Pb correction produces age distributions with less scatter and slightly younger ages (ca. 5 Ma) for probability density plot peaks than uncorrected data (Fig. 10). In addition to the common Pb trend, there is a spread in the ^{238}U/^{206}Pb ratios for unknown data in this study. This type of spread is typically attributed as either Pb loss during retrogression or periodic or protracted growth of monazite (e.g. Gasser et al., 2015; Kirkland et al., 2016; Rubatto et al., 2001). The progression of monazite chemical zones identified in this study would suggest that this scatter has some geological significance, perhaps such as periodic or protracted growth, rather than be the result of Pb loss. Indeed, this is the same conclusion drawn by Guergouz et al. (2018) and Peressini et al. (2007) in reference to similar distributions within their monazite and zircon age data from the metapelites of the IVZ and Mafi c Complex, respectively. If Pb loss has aff ected the data it must have occured with the perious of high temperature metamorphism as there is no other Pb loss trend observed in the data (See Fig. S3.1.1).

Monazite in the cores of amphibolite facies grains, Z1, yields the oldest dates (321 ± 16.6 and 301 ± 14.4 Ma; both from IV16-03A). The lack of a clear and distinct age peak relating to the Variscan regional metamorphism (ca. 320–300 Ma; Ewing et al., 2013; Kunz, Regis, & Engi, 2018; Vavra, Schmid, & Gebauer, 1999) likely reflects the fact that the moderate *P,* moderate *T* conditions of the Variscan regional metamorphism (Ewing et al., 2013; Kunz et al., 2018; Vavra et al., 1999) were generally not conducive to the formation of monazite (i.e. were within the allanite stability field; Spear, 2010).

Ages from Z3, Z4, Z5 and Z6 monazite from the Val Strona samples (280 ± 2.5 , 279 ± 6.9, 276 ± 6.7 and 275 ± 2.9 Ma, respectively; Fig.10c) are in agreement with previously reported monazite ages (283 ± 6 and 279 ± 6 Ma; Guergouz et al., 2018) from the same sequence and with zircon ages from amphibolite-facies rocks in Val Strona (280 ± 2 and 272 ± 1 Ma; Kunz et al., 2018). All these published age constraints are interpreted as dating metamorphism and partial melting in the metapelites and are within uncertainty of or shortly postdate the ca. 292–282 Ma intrusion of the upper Mafic Complex (Peressini et al., 2007). The texturally older monazite zone (Z2) that could be dated with confidence records an age of 290 ± 2.5 Ma which is within the range of the published zircon age spectra, but has not been clearly identified in monazite before. 'Main clusters' (Fig. 10c) were defined on statistically homogenous populations (see Spencer, Kirkland, & Taylor, 2016). This was done to derive geologically meaningful ages from the scatter of the natural data to order to compare between zones and to previous geochronology. However, as the U–Th–Pb system likely records processes occurring during progressive (protracted) metamorphism, it is therefore reasonable that similar chemical zones could show a range of monazite dates.

In the UHT samples, larger monazite grains (>50 µm Ø) and those included in garnet (Z8) yield scattered dates in the range 273–264 Ma, whereas smaller grains (<50 µm Ø) located interstitially (Z9) yield scattered dates in the range 265–154 Ma. The young dates, although scattering in the range 181–154 Ma (n = 4), are unique to the UHT samples, and in particular to Z9 monazite.

Our age data are consistent with chemical evidence that monazite in the IVZ predominantly records the immediately pre-peak and peak (Permian) history of the terrane. As all the monazite dates from this study fall within the expected age range of prograde-to-peak metamorphism, we conclude that the samples contain no detrital monazite and that all the monazite investigated formed during metamorphism. Further dissection of the geological significance of dates from individual monazite zones is treated with caution as the timescale of metamorphism is similar to the uncertainty associated with the LA–ICP–MS ages obtained.

7.5 Changes to monazite Th end member fractions with metamorphic grade

The fractions of the two Th-end-members of monazite, cheralite and huttonite, change with metamorphic grade in the IVZ (Fig. 9a). Amphibolite-facies monazite zones (Z1–Z3) favour cheralite rather than huttonite in terms of Th. This is consistent with other studies of monazite chemistry over metamorphic grade changes (Chapter 2; Skrzypek et al., 2018). Above the solidus, monazite increasingly favours huttonite at the expense of cheralite which is particularly evident from Z5 to Z6, a trend which is also reported by Skrzypek et al. (2018) in the Ryoke Belt (see also chapter 4). We interpret this as the probable result of: (a) unfavourable thermodynamic properties of huttonite to allow its presence in significant proportion at subsolidus temperatures and pressures (e.g. Mazeina, Ushakov, Navrotsky, & Boatner, 2005; Robie & Hemingway, 1995); (b) cheralite being more soluble in melt than huttonite, as silicate melt produced from melting of metapelites is typically saturated in Si but not Ca; and (c) buffering of P (and possibly Ca) in monazite by the presence of apatite in amphibolite-facies samples, with apatite volume proportion decreasing by dissolution into melt through the granulite facies (Fig. 6). At very high temperatures apatite (and plagioclase) is likely to have dissolved completely in melt (e.g. Yakymchuk, 2017), leaving the residual rock under-saturated with respect to P (and possibly Ca) and driving further exchange of the cheralite component of monazite with/into melt. The preference for higher huttonite (Si) fractions in monazite with increasing temperature could provide an important mechanism by which monazite remains stable to extremely high temperatures (>900 °C, see also Yakymchuk, 2017) as the stability of the huttonite component of monazite does not require P or Ca saturation.

Monazite grains in the UHT rocks show a different Th solid-solution trend to the granulite-facies samples, having huttonite-rich compositions which also have a high proportion of cheralite (Z8; Fig. 9a inset), as well as a population with low fractions of cheralite and near zero huttonite (Z9; Fig. 9a). Zone Z8 is enriched in both cheralite and huttonite due to melt-driven enrichment in total Th (see above).

There is also a marked increase in the Th/U ratio of monazite from the lower granulite facies (Z5) to the UHT conditions (Z8; Fig. 8). This is consistent with previous findings from the IVZ (Bea & Montero, 1999) and also more generally (Taylor et al., 2014; Taylor et al., 2016; Yakymchuk et al., 2018), in that monazite has a weaker preference for U than Th with increasing temperature. The increase in Th/U above the solidus is not correlated with the fraction of cheralite (*p*(cher); Fig. 9b), but is correlated with the increase in huttonite fraction (*p*(hutt), Fig. 9c), showing that huttonite has a stronger influence on controlling Th/U in monazite, at least in melt-bearing rocks. A similar positive correlation between huttonite fraction and Th/U in monazite was observed at Mt Stafford (Williams, Kelsey, Baggs, Hand, & Alessio, 2018).

7.6 Mechanisms of monazite formation

The internal structure, compositional zoning and ages of monazite in the investigated anatectic metapelites shows evidence for monazite having grown mostly during pre-peak to peak metamorphism, with limited Variscan and retrograde signature. It is possible to infer that garnet mode was either increasing or remaining unchanged during the formation of zones Z5, Z6 and Z8, on the basis of the relatively low concentration of Y and Gd (which have a strong affinity for garnet) in these zones. This is consistent with a *P–T* path involving heating and pressure increase. On the basis of the investigation of monazite composition presented herein, we contend that retrograde or cooling related monazite makes up only a small proportion of the total monazite in the IVZ metapelites (only the volumetrically minor zones Z4, Z9 and possibly Z7).

In contrast to the evidence from natural samples, forward thermodynamic models (Kelsey et al., 2008; Spear & Pyle, 2010; Yakymchuk, 2017) are unable to account for progressive, up temperature growth of monazite (nor zircon) above the solidus as the components that comprise monazite are not regarded as being present in high enough concentrations in major minerals to allow growth of monazite by major mineral breakdown. Rather, silicate melt is the only major phase that has appreciable concentrations of monazite-forming (and zircon) components. As the volume proportion of melt increases with increasing temperature, equilibrium models predict that monazite mode progressively decreases. Studies based on natural samples have suggested an Ostwald ripening mechanism (e.g. Nemchin et al., 2001; Rubatto et al., 2001; Vavra, Gebauer, Schmid, & Compston, 1996; Williams, 2001) by which prograde accessory mineral growth could occur in the anatectic realm. However, these processes are not grounded in equilibrium thermodynamics and thus cannot be modelled as part of the typical calculated pseudosection approach of modern metamorphic studies. As such, explaining prograde suprasolidus growth of monazite (and zircon) remains an ongoing issue. While the mechanism of Ostwald ripening is consistent with observations from amphibolite facies monazite, it cannot explain the lack of amphibolite facies zones in cores of granulite facies monazite. Therefore, other processes (e.g. dissolution–precipitation creep; Wawrzenitz et al., 2012) may be responsible for at least part of the monazite record here.

Lower grade (Z1–Z3) monazite has reasonably variable compositions whereas granulite-facies monazite has a smaller range of compositions, showing that the granulite-facies grains are more chemically equilibrated. This is in line with results from other terranes which showed that (effective) chemical equilibrium for Th and LREE was reached by ~600 °C (Chapter 2; Skrzypek et al., 2018). At temperatures below 600 °C, variable monazite compositions and Th/U ratios likely reflect variable local availability of Th due to the grain size and composition of prograde allanite (which breaks down to form monazite).

Recently, Yakymchuk and Brown (2019) suggested that prograde suprasolidus accessory mineral growth could occur via infiltration of melt generated at deeper crustal levels into shallower anatectic crustal rocks. By this logic, hotter melts generated at deeper crustal levels have higher LREE, Th and Zr concentrations than shallower melts due to more advanced dissolution of the accessory minerals, which when mixed together causes oversaturation of melt with respect to

LREE and Th (and Zr), leading to (prograde) monazite precipitation on existing grains. The highest grade rocks in Val Strona (sample IV16-16 in the present case) are closely (~2 km) underlain by metabasic granulites of the Mafic Complex, meaning that only a thin pelitic section exists in between IV16-16 and the Mafic Complex in which melts with more LREE and Th could be generated. Although we do not discount this possibility, the systematic trends in Th and trace element behaviour that we document suggests that open system behaviour pertaining to the trace elements was not the major controlling factor. Given the high bulk Ca in the UHT samples relative to other pelites in this study (Table 2) and their location within the mafic complex, it is likely that the UHT granulite samples were contaminated by mafic melt. While the bulk compositional change which the septa have seemingly undergone is unlikely to be a significant factor in other samples in this study, it may have played a role which stabilised monazite in these already melt depleted rocks. The presence of monazite with high Th contents in the UHT septa shows that monazite can in some cases resist high temperature dissolution processes.

7.7 Differentiation of continental crust through partial melting

The IVZ lower crustal section contains abundant mafic and calc-silicate rocks throughout (e.g. Bertolani, 1968; Rutter, Brodie, James, & Burlini, 2007) and the extensive Mafic Complex is located at the base of the section (e.g. Peressini et al., 2007; Quick et al., 2003; Sinigoi et al., 1994). The monazite record reported here supports the idea that the Mafic Complex was a major heat source for high pressure, high temperature metamorphism and that it was emplaced at or near the peak of metamorphism. The total volume of metabasic crust in the Val Strona section (excluding the Mafic Complex) is 10–30%, with a further 8–14% metacarbonate lithologies (estimated from Bertolani, 1968; Rutter et al., 2007). However, much of the Th in the section is hosted by metapelite layers (although some of the subordinate metabasic layers contain huttonite; see also Förster & Harlov, 1999) that have an average Th content 70 times greater than associated subordinate metabasic layers within the pelite (metapelite layers 21.0 ± 2.5 ppm, metabasic layers 0.3 ± 0.3 ppm; from Alessio et al. (2018) and Bea and Montero (1999), respectively). These metapelitic layers comprise ~50% of the metamorphic sequence in Val Strona (Bertolani, 1968; Rutter et al., 2007). As shown here and also in Alessio et al. (2018), the process of partial melting of pelitic rock types does not result in a net loss of Th from residual rocks except in the case of extreme metamorphism, at temperatures in excess of 900 °C (see also Ewing et al., 2014; Yakymchuk & Brown, 2019). This is consistent with Bea and Montero (1999) and Bea (2012) who argued that segregated melts had equal or lower Th and overall heat production than their sources, as well as observations of both Th concentrations and radiogenic heat production in numerous other metasediment-dominated terranes (e.g. Chapter 2; Alessio et al., 2018; Skrzypek et al., 2018). The conservation of high heat production in granulite facies rocks is thought to be strongly influenced by the behaviour of the accessory minerals, particularly monazite, in partially melted metasedimentary rocks (see also Alessio et al., 2018; Yakymchuk & Brown, 2019).

The conservation of relatively high heat production (2.29 ± 0.05 μWm^{-3}; Alessio et al., 2018) in the IVZ lower crustal (granulite) metapelites may have assisted the attainment of peak temperature conditions (e.g. Jamieson, Beaumont, Fullsack, & Lee, 1998; Nandakumar & Harley, 2019; Yakymchuk & Brown, 2019), helped to sustain elevated thermal conditions for a prolonged (> 30 Myr; this study) period (e.g. Clark, Fitzsimons, Healy, & Harley, 2011; Holder, Hacker, Horton, & Rakotondrazafy, 2018; Horton et al., 2016; Kelsey & Hand, 2015) and resulted in slow cooling of the terrane relative to the conductive geotherm (Ewing et al., 2015; Yakymchuk & Brown, 2019).

The IVZ example shows that partial melting of metasedimentary-dominated crust can conserve its thermal potential energy (in the form of heat producing elements; Fig. 3, see also Alessio et al., 2018; and Yakymchuk and Brown, 2019). Therefore, if the lower crust is depleted in heat producing elements, as has been proposed (e.g. Rudnick & Gao, 2003; Rudnick & Fountain, 1995), it is due to other processes and/or a dominance of rock types with low Th and U. However, according to the calculations of Hacker, Kelemen, and Behn (2011), a minimum of 27% of samples from granulite terranes and 43% of rocks from ultra-high pressure terranes are peraluminous, pelitic metasediments. This suggests that the exposed distribution of felsic and mafic rock types in the

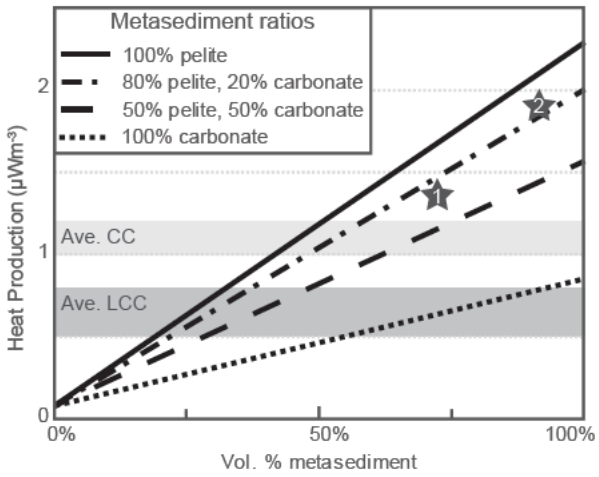

Figure 12. Total heat production rate for the IVZ for different ratios of rock types with different (but fixed) radiogenic heat production rates. Heat production rates for lithologies are metapelite = 2.29 μWm 3 (Alessio et al., 2018), metacarbonate = 0.85 μWm 3 (Abart et al., 2001) and metabasite = 0.08 μWm 3 (Bea & Montero, 1999). Stars represent IVZ heat production rates based on the proportion of pelitic, carbonate and metabasite lithologies given by (1) Bertolani (1968) and (2) Rutter et al. (2007). Oblique solid and dashed mixing lines show heat production for the terrane given different proportions of the three rock types (metapelite, metacarbonate and metabasite), from 100% metabasites at the left to 100% metasediment at the right. Heat production rate estimates for average continental crust (Ave. CC) and average lower continental crust (Ave. LCC) are shown for comparison (Bea, 2012) and are independent of vol.% metasediment calculations.

IVZ can be considered representative of the lower crust. However, estimations of the average heat production of the IVZ (Val Strona section) are significantly higher than reported heat production for both the average lower continental crust and the average continental crust as a whole (Fig. 12; Bea, 2012). The marked difference in heat production between metasedimentary and other (in this case mafic) rocks suggests that even if the proportion of metasedimentary rocks in granulite terranes is minor, the heat producing element budget, and thus radiogenic thermal energy budget, is strongly determined and controlled by the residual metasedimentary rocks (e.g. Fig. 12). Average lower continental crustal heat production (0.5–0.8 μWm^{-3}; Bea, 2012) can be replicated with 20–30% metapelite (2.29 μWm^{-3}; Alessio et al, 2018) and 70–80% metabasite (0.08 μWm^{-3}; Bea & Montero, 1999), with the metapelite layers contributing circa 90% of the heat production (Fig. 12). This is well below the estimates for the proportion of metapelitic crust in Val Strona (52–78 vol.%; Bertolani, 1968; Rutter et al., 2007).

8 CONCLUSIONS

The IVZ is a tilted cross section considered to be representative of the orogenic lower crust, with pelitic rocks showing evidence for partial melting and melt extraction. Monazite in the IVZ preserves recognisable and systematic chemical composition zones that can be linked to the growth/consumption of other accessory and major minerals. This allows monazite formation to be placed within an existing *P–T* framework. The pre-peak to peak ages recorded by monazite compositional zones in the IVZ are within the range of existing zircon age data for the same section. Monazite volume proportion increases to and through the granulite facies and only decreases sharply in UHT septa, showing that extreme temperatures (>900 °C) or a change in the sample chemistry need to be reached before monazite is no longer present in metasedimentary granulites. On the basis of our detailed investigation of monazite we contend that monazite formed during retrograde cooling comprises only a small proportion of the total monazite. Th contents in the lowest temperature prograde monazite are low (0.0003–0.0153 APFU), then increase to 0.0165–0.0757 APFU by the mid amphibolite facies (~650 °C) and remain relatively constant to the granulite facies (~ 900 °C, 0.0238–0.0591 APFU). Th contents of monazite grains that are large (>50 μm Ø) and in garnet in the UHT samples are the highest in the sequence (0.0621–0.1879 APFU). These observations show that monazite is a primary control on the retention of Th in metasedimentary lower crust and indeed the deep crust. As a consequence, whole rock Th concentration is conserved from amphibolite-(~650 °C) to granulite-facies conditions (~ 900 °C), and only decreases in UHT rocks where monazite volume proportion is significantly reduced due to the approach of full monazite solubility into melt.

SUPPORTING INFORMATION

Appendix S3.1: detailed analytical technique for LA–ICP–MS monazite geochronology and trace element analysis

Appendix S3.2: Uncorrected LA–ICP–MS monazite geochronology data (electronic appendix only)

Appendix S3.3: Whole rock geochemistry for Ivrea–Verbano metapelite samples.

REFERENCES

Abart, R., Schmud, R., & Harlov, D. (2001). Metasomatic coronas around hornblendite

xenoliths in granulitefacies marble, Ivrea zone, N Italy, I: constraints on componentmobility. *Contributions to Mineralogy and Petrology,* 141(4), 473-493.

Ahrendt, H., Hoefs, J., Strackenbrock, I., & Weber, K. (1989). A geothermal gradient of the lower crustal section of the Ivrea-Zone during Hercynian time deduced from carbon isotopes. Paper presented at the Varallo Conference on the Lower Continental Crust, Varallo, Italy, Spec. Pub. Consiglio Nazionale delle Ricerche, Varallo.

Alessio, K. L., Hand, M., Kelsey, D. E., Williams, M. A., Morrissey, L. J., & Barovich, K. (2018). Conservation of deep crustal heat production. *Geology,* 46(4), 335-338.

Allaz, J., Selleck, B., Williams, M. L., & Jercinovic, M. J. (2013). Microprobe analysis and dating of monazite from the Potsdam Formation, New York: A progressive record of chemical reaction and fluid interaction. *American Mineralogist,* 98(7), 1106-1119.

Andreoli, M. A., Hart, R. J., Ashwal, L. D., & Coetzee, H. (2006). Correlations between U, Th content and metamorphic grade in the western Namaqualand Belt, South Africa, with implications for radioactive heating of the crust. *Journal of Petrology,* 47(6), 1095-1118.

Baker, A. (1990). Stable isotopic evidence for fluid-rock interactions in the Ivrea Zone, Italy. *Journal of Petrology,* 31(1), 243-260.

Barboza, S. A., & Bergantz, G. W. (2000). Metamorphism and anatexis in the mafic complex contact aureole, Ivrea Zone, Northern Italy. *Journal of Petrology,* 41(8), 1307-1327.

Barboza, S. A., Bergantz, G. W., & Brown, M. (1999). Regional granulite facies metamorphism in the Ivrea zone: Is the Mafic Complex the smoking gun or a red herring? *Geology,* 27(5), 447-450.

Bartoli, O. (2017). Phase equilibria modelling of residual migmatites and granulites: an evaluation of the melt-reintegration approach. *Journal of Metamorphic Geology,* 35(8), 919-942.

Bea, F. (2012). The sources of energy for crustal melting and the geochemistry of heat-producing elements. *Lithos,* 153, 278-291.

Bea, F., & Montero, P. (1999). Behavior of accessory phases and redistribution of Zr, REE, Y, Th, and U during metamorphism and partial melting of metapelites in the lower crust: an example from the Kinzigite Formation of Ivrea-Verbano, NW Italy. *Geochimica Et Cosmochimica Acta,* 63(7–8), 1133-1153.

Bertolani, M. (1968). La petrografia della Valle Strona (Alpi occidentali Italiane). *Schweiz. mineral. petrogr. Mitt,* 48(3), 695-732.

Bingen, B., Demaiffe, D., & Hertogen, J. (1996). Redistribution of rare earth elements, thorium, and uranium over accessory minerals in the course of amphibolite to granulite facies metamorphism: the role of apatite and monazite in orthogneisses from southwestern Norway. *Geochimica Et Cosmochimica Acta,* 60(8), 1341-1354.

Brodie, K., & Rutter, E. (1987). Deep crustal extensional faulting in the Ivrea Zone of northern Italy. *Tectonophysics,* 140(2-4), 193-212.

Cabella, R., Lucchetti, G., & Marescotti, P. (2001). Authigenic monazite and xenotime from pelitic metacherts in pumpellyite–actinolite-facies conditions, Sestri–Voltaggio Zone, central Liguria, Italy. *The Canadian Mineralogist,* 39(3), 717-727.

Chew, D., Petrus, J., & Kamber, B. (2014). U–Pb LA–ICPMS dating using accessory mineral standards with variable common Pb. *Chemical Geology,* 363, 185-199.

Clark, C., Fitzsimons, I. C., Healy, D., & Harley, S. L. (2011). How does the continental crust get really hot? *Elements,* 7(4), 235-240.

Corrie, S. L., & Kohn, M. J. (2008). Trace-element distributions in silicates during prograde metamorphic reactions: Implications for monazite formation. *Journal of Metamorphic Geology,* 26(4), 451-464.

Dumond, G., Goncalves, P., Williams, M., & Jercinovic, M. (2015). Monazite as a monitor of melting, garnet growth and feldspar recrystallization in continental lower crust. *Journal of Metamorphic Geology,* 33(7), 735-762.

Engi, M. (2017). Petrochronology based on REE-minerals: monazite, allanite, xenotime, apatite. *Reviews in Mineralogy and Geochemistry,* 83(1), 365-418.

Ewing, T. A., Hermann, J., & Rubatto, D. (2013). The robustness of the Zr-in-rutile and Ti-in-zircon thermometers during high-temperature metamorphism (Ivrea-Verbano Zone, northern Italy). *Contributions to Mineralogy and Petrology,* 165(4), 757-779.

Ewing, T. A., Rubatto, D., Beltrando, M., & Hermann, J. (2015). Constraints on the thermal evolution of the Adriatic margin during Jurassic continental break-up: U–Pb dating of rutile from the Ivrea–Verbano Zone, Italy. *Contributions to Mineralogy and Petrology,* 169(4), 44.

Ewing, T. A., Rubatto, D., & Hermann, J. (2014). Hafnium isotopes and Zr/Hf of rutile and zircon from lower crustal metapelites (Ivrea–Verbano Zone, Italy): implications for chemical differentiation of the crust. *Earth and Planetary Science Letters,* 389, 106-118.

Förster, H.-J., & Harlov, D. (1999). Monazite-(Ce)–huttonite solid solutions in granulite-facies metabasites from the Ivrea-Verbano Zone, Italy. *Mineralogical Magazine,* 63(4), 587-594.

Foster, G., Gibson, H., Parrish, R., Horstwood, M., Fraser, J., & Tindle, A. (2002). Textural, chemical and isotopic insights into the nature and behaviour of metamorphic monazite. *Chemical Geology,* 191(1-3), 183-207.

Fountain, D. M. (1976). The Ivrea—Verbano and Strona-Ceneri Zones, Northern Italy: A cross-section of the continental crust—New evidence from seismic velocities of rock samples. *Tectonophysics,* 33(1), 145-165.

Franz, G., Andrehs, G., & Rhede, D. (1996). Crystal chemistry of monazite and xenotime from Saxothuringian-Moldanubian metapelites, NE Bavaria, Germany. *European Journal of Mineralogy,* 8(5), 1097-1118.

Gasser, D., Jeřábek, P., Faber, C., Stünitz, H., Menegon, L., Corfu, F., . . . Whitehouse, M. J. (2015). Behaviour of geochronometers and timing of metamorphic reactions during deformation at lower crustal conditions: phase equilibrium modelling and U–Pb dating of zircon, monazite, rutile and titanite from the Kalak Nappe Complex, northern Norway. Journal of Metamorphic Geology, 33(5), 513-534.

Guergouz, C., Martin, L., Vanderhaeghe, O., Thébaud, N., & Fiorentini, M. (2018). Zircon and monazite petrochronologic record of prolonged amphibolite to granulite facies metamorphism in the Ivrea-Verbano and Strona-Ceneri Zones, NW Italy. *Lithos,* 308-309, 1-18.

Hacker, B. R., Kelemen, P. B., & Behn, M. D. (2011). Differentiation of the continental crust by relamination. *Earth and Planetary Science Letters,* 307(3), 501-516.

Handy, M., Franz, L., Heller, F., Janott, B., & Zurbriggen, R. (1999). Multistage accretion and exhumation of the continental crust (Ivrea crustal section, Italy and Switzerland). *Tectonics,* 18(6), 1154-1177.

Henk, A., Franz, L., Teufel, S., & Oncken, O. (1997). Magmatic Underplating, Extension, and Crustal Reequilibration: Insights From A Cross-Section Through the Ivrea Zone and Strona-Ceneri Zone, Northern Italy. *The Journal of Geology,* 105(3), 367-378.

Holder, R. M., Hacker, B. R., Horton, F., & Rakotondrazafy, A. M. (2018). Ultrahigh-temperature osumilite gneisses in southern Madagascar record combined heat advection and high rates of radiogenic heat production in a long-lived high-T orogen. *Journal of Metamorphic Geology,* 36(7), 855-880.

Horton, F., Hacker, B., Kylander-Clark, A., Holder, R., & Jöns, N. (2016). Focused radiogenic heating of middle crust caused ultrahigh temperatures in southern Madagascar. *Tectonics,* 35(2), 293-314.

Jamieson, R. A., Beaumont, C., Fullsack, P., & Lee, B. (1998). Barrovian regional metamorphism: Where's the heat? *Geological Society, London, Special Publications,* 138(1), 23-51.

Johnson, T. E., Clark, C., Taylor, R. J. M., Santosh, M., & Collins, A. S. (2015). Prograde and retrograde growth of monazite in migmatites: An example from the Nagercoil Block, southern India. *Geoscience Frontiers,* 6(3), 373-387.

Karakas, O., Wotzlaw, J.-F., Guillong, M., Ulmer, P., Brack, P., Economos, R., . . . Bachmann, O. (2019). The pace of crustal-scale magma accretion and differentiation beneath silicic caldera volcanoes. *Geology*.

Kelly, N. M., Harley, S. L., & Möller, A. (2012). Complexity in the behavior and recrystallization of monazite during high-T metamorphism and fluid infiltration. *Chemical Geology,* 322, 192-208.

Kelsey, D. E., Clark, C., & Hand, M. (2008). Thermobarometric modelling of zircon and monazite growth in melt-bearing systems: Examples using model metapelitic and metapsammitic granulites. *Journal of Metamorphic Geology,* 26(2), 199-212.

Kelsey, D. E., & Hand, M. (2015). On ultrahigh temperature crustal metamorphism: Phase equilibria, trace element thermometry, bulk composition, heat sources, timescales and

tectonic settings. *Geoscience Frontiers,* 6(3), 311-356.

Kirkland, C., Erickson, T., Johnson, T., Danišík, M., Evans, N., Bourdet, J., & McDonald, B. (2016). Discriminating prolonged, episodic or disturbed monazite age spectra: An example from the Kalak Nappe Complex, Arctic Norway. Chemical Geology, 424, 96-110.

Klötzli, U. S., Sinigoi, S., Quick, J. E., Demarchi, G., Tassinari, C. C., Sato, K., & Günes, Z. (2014). Duration of igneous activity in the Sesia Magmatic System and implications for high-temperature metamorphism in the Ivrea–Verbano deep crust. *Lithos,* 206, 19-33.

Kohn, M. J., & Malloy, M. A. (2004). Formation of monazite via prograde metamorphic reactions among common silicates: implications for age determinations. *Geochimica Et Cosmochimica Acta,* 68(1), 101-113.

Kunz, B. E., Johnson, T. E., White, R. W., & Redler, C. (2014). Partial melting of metabasic rocks in Val Strona di Omegna, Ivrea Zone, northern Italy. *Lithos,* 190, 1-12.

Kunz, B. E., Regis, D., & Engi, M. (2018). Zircon ages in granulite facies rocks: decoupling from geochemistry above 850 °C? *Contributions to Mineralogy and Petrology,* 173(3), 26.

Kunz, B. E., & White, R. W. (2019). Phase equilibrium modelling of the amphibolite to granulite facies transition in metabasic rocks (Ivrea Zone, NW Italy). *Journal of Metamorphic Geology*.

Mazeina, L., Ushakov, S. V., Navrotsky, A., & Boatner, L. A. (2005). Formation enthalpy of ThSiO4 and enthalpy of the thorite-huttonite phase transition. *Geochimica Et Cosmochimica Acta,* 69(19), 4675-4683.

Nandakumar, V., & Harley, S. L. (2019). Geochemical signatures of mid-crustal melting processes and heat production in a hot orogen: The Kerala Khondalite Belt, Southern India. *Lithos*, 324, 479-500.

Nemchin, A. A., Giannini, L. M., Bodorkos, S., & Oliver, N. H. S. (2001). Ostwald ripening as a possible mechanism for zircon overgrowth formation during anatexis: theoretical constraints, a numerical model, and its application to pelitic migmatites of the Tickalara Metamorphics, northwestern Australia. *Geochimica Et Cosmochimica Acta,* 65(16), 2771-2788.

Palya, A. P., Buick, I. S., & Bebout, G. E. (2011). Storage and mobility of nitrogen in the continental crust: Evidence from partially melted metasedimentary rocks, Mt. Stafford, Australia. *Chemical Geology*, 281(3), 211-226.

Pape, J., Mezger, K., & Robyr, M. (2016). A systematic evaluation of the Zr-in-rutile thermometer in ultra-high temperature (UHT) rocks. *Contributions to Mineralogy and Petrology,* 171(5), 44.

Parrish, R. R. (1990). U-Pb dating of monazite and its application to geological problems. *Canadian Journal of Earth Sciences,* 27(11), 1431-1450.

Paton, C., Hellstrom, J., Paul, B., Woodhead, J., & Hergt, J. (2011). Iolite: Freeware for the visualisation and processing of mass spectrometric data. *Journal of Analytical Atomic Spectrometry,* 26(12), 2508-2518.

Peressini, G., Quick, J., Sinigoi, S., Hofmann, A. W., & Fanning, M. (2007). Duration of a large mafic intrusion and heat transfer in the lower crust: a SHRIMP U–Pb zircon study in the Ivrea–Verbano Zone (Western Alps, Italy). *Journal of Petrology,* 48(6), 1185-1218.

Pyle, J. M., & Spear, F. S. (1999). Yttrium zoning in garnet: coupling of major and accessory phases during metamorphic reactions. *Geological Materials Research,* 1(6), 1-49.

Pyle, J. M., & Spear, F. S. (2003). Four generations of accessory-phase growth in low-pressure migmatites from SW New Hampshire. American Mineralogist, 88(2-3), 338-351.

Pyle, J. M., Spear, F. S., Rudnick, R. L., & McDonough, W. F. (2001). Monazite–xenotime–garnet equilibrium in metapelites and a new monazite–garnet thermometer. Journal of Petrology, 42(11), 2083-2107.

Quick, J. E., Sinigoi, S., Snoke, A. W., Kalakay, T. J., Mayer, A., & Peressini, G. (2003). Geologic map of the southern Ivrea-Verbano Zone, northwestern Italy. US Geological Survey.

Rapp, R. P., Ryerson, F., & Miller, C. F. (1987). Experimental evidence bearing on the stability of monazite during crustal anatexis. Geophysical Research Letters, 14(3), 307-310.

Rapp, R. P., & Watson, E. B. (1986). Monazite solubility and dissolution kinetics: implications for the thorium and light rare earth chemistry of felsic magmas. Contributions to Mineralogy and Petrology, 94(3), 304-316.

Rasmussen, B., & Muhling, J. R. (2007). Monazite begets monazite: evidence for dissolution of detrital monazite and reprecipitation of syntectonic monazite during low-grade regional metamorphism. Contributions to Mineralogy and Petrology, 154(6), 675-689.

Redler, C., Johnson, T., White, R. W., & Kunz, B. (2012). Phase equilibrium constraints on a deep crustal metamorphic field gradient: metapelitic rocks from the Ivrea Zone (NW Italy). Journal of Metamorphic Geology, 30(3), 235-254.

Redler, C., White, R. W., & Johnson, T. E. (2013). Migmatites in the Ivrea Zone (NW Italy): Constraints on partial melting and melt loss in metasedimentary rocks from Val Strona di Omegna. Lithos, 175, 40-53.

Rivalenti, G., Garuti, G., Rossi, A., Siena, F., & Sinigoi, S. (1981). Existence of Different Peridotite Types and of a Layered Igneous Complex in the Ivrea Zone of the Western Alps. Journal of Petrology, 22(1), 127-153.

Robie, R., & Hemingway, B. (1995). Thermodynamic properties of minerals and related substances at 298.15 K and 1 bar (105 Pascals) pressure and at higher temperatures (Vol. 2131): US Government Printing Office. pp.

Rosenberg, C., & Handy, M. (2005). Experimental deformation of partially melted granite revisited: implications for the continental crust. Journal of Metamorphic Geology, 23(1), 19-28.

Rubatto, D., Hermann, J., & Buick, I. S. (2006). Temperature and bulk composition control on the growth of monazite and zircon during low-pressure anatexis (Mount Stafford, central Australia). Journal of Petrology, 47(10), 1973-1996.

Rubatto, D., Williams, I. S., & Buick, I. S. (2001). Zircon and monazite response to prograde metamorphism in the Reynolds Range, central Australia. Contributions to Mineralogy and Petrology, 140(4), 458-468.

Rudnick, R., & Gao, S. (2003). Composition of the continental crust. Treatise on geochemistry, 3, 659.

Rudnick, R. L., & Fountain, D. M. (1995). Nature and composition of the continental crust: a lower crustal perspective. Reviews of geophysics, 33(3), 267-309.

Rutter, E., Brodie, K., James, T., & Burlini, L. (2007). Large-scale folding in the upper part of the Ivrea-Verbano zone, NW Italy. Journal of Structural Geology, 29(1), 1-17.

Schmid, R., & Wood, B. J. (1976). Phase relationships in granulitic metapelites from the Ivrea-Verbano zone (Northern Italy). Contributions to Mineralogy and Petrology, 54(4), 255-279.

Schnetger, B. (1994). Partial melting during the evolution of the amphibolite-to granulite-facies gneisses of the Ivrea Zone, northern Italy. Chemical Geology, 113(1-2), 71-101.

Schulz, B. (2017). Polymetamorphism in garnet micaschists of the Saualpe Eclogite Unit (Eastern Alps, Austria), resolved by automated SEM methods and EMP–Th–U–Pb monazite dating. Journal of Metamorphic Geology, 35(2), 141-163.

Sills, J. D., & Tarney, J. (1984). Petrogenesis and tectonic significance of amphibolites interlayered with metasedimentary gneisses in the Ivrea Zone, Southern Alps, Northwest Italy. Tectonophysics, 107(3-4), 187-206.

Sinigoi, S., Quick, J. E., Clemens-Knott, D., Mayer, A., Demarchi, G., Mazzucchelli, M., . . . Rivalenti, G. (1994). Chemical evolution of a large mafic intrusion in the lower crust, Ivrea-Verbano Zone, northern Italy. Journal of Geophysical Research: Solid Earth, 99(B11), 21575-21590.

Skrzypek, E., Kato, T., Kawakami, T., Sakata, S., Hattori, K., Hirata, T., & Ikeda, T. (2018). Monazite behaviour and time-scale of metamorphic processes along a low-pressure/high-temperature field gradient (Ryoke belt, SW Japan). Journal of Petrology, 59(6), 1109-1144.

Smith, H. A., & Barreiro, B. (1990). Monazite U-Pb dating of staurolite grade metamorphism in pelitic schists. Contributions to Mineralogy and Petrology, 105(5), 602-615.

Spear, F. S. (2010). Monazite–allanite phase relations in metapelites. Chemical Geology, 279(1–2), 55-62.

Spear, F. S., & Pyle, J. M. (2010). Theoretical modeling of monazite growth in a low-Ca metapelite. Chemical Geology, 273(1), 111-119.

Spencer, C. J., Kirkland, C. L., & Taylor, R. J. (2016). Strategies towards statistically robust interpretations of in situ U–Pb zircon geochronology. Geoscience Frontiers, 7(4), 581-589.

Stepanov, A. S., Hermann, J., Korsakov, A. V., &

Rubatto, D. (2014). Geochemistry of ultrahigh-pressure anatexis: fractionation of elements in the Kokchetav gneisses during melting at diamond-facies conditions. Contributions to Mineralogy and Petrology, 167(5), 1002.

Stepanov, A. S., Hermann, J., Rubatto, D., & Rapp, R. P. (2012). Experimental study of monazite/melt partitioning with implications for the REE, Th and U geochemistry of crustal rocks. Chemical Geology, 300, 200-220.

Taylor, R. J. M., Clark, C., Fitzsimons, I. C., Santosh, M., Hand, M., Evans, N., & McDonald, B. (2014). Post-peak, fluid-mediated modification of granulite facies zircon and monazite in the Trivandrum Block, southern India. Contributions to Mineralogy and Petrology, 168(2), 1044.

Taylor, R. J. M., Kirkland, C. L., & Clark, C. (2016). Accessories after the facts: Constraining the timing, duration and conditions of high-temperature metamorphic processes. Lithos, 264, 239-257.

Vavra, G., Gebauer, D., Schmid, R., & Compston, W. (1996). Multiple zircon growth and recrystallization during polyphase Late Carboniferous to Triassic metamorphism in granulites of the Ivrea Zone (Southern Alps): an ion microprobe (SHRIMP) study. Contributions to Mineralogy and Petrology, 122(4), 337-358.

Vavra, G., & Schaltegger, U. (1999). Post-granulite facies monazite growth and rejuvenation during Permian to Lower Jurassic thermal and fluid events in the Ivrea Zone (Southern Alps). Contributions to Mineralogy and Petrology, 134(4), 405-414.

Vavra, G., Schmid, R., & Gebauer, D. (1999). Internal morphology, habit and U-Th-Pb microanalysis of amphibolite-to-granulite facies zircons: geochronology of the Ivrea Zone (Southern Alps). Contributions to Mineralogy and Petrology, 134(4), 380-404.

Watt, G. R. (1995). High-thorium monazite-(Ce) formed during disequilibrium melting of metapelites under granulite-facies conditions: De Gruyter.

Wawrzenitz, N., Krohe, A., Rhede, D., & Romer, R. L. (2012). Dating rock deformation with monazite: The impact of dissolution precipitation creep. Lithos, 134, 52-74.

Williams, I. (2001). Response of detrital zircon and monazite, and their U–Pb isotopic systems, to regional metamorphism and host-rock partial melting, Cooma Complex, southeastern Australia. Australian Journal of Earth Sciences, 48(4), 557-580.

Williams, M. A., Kelsey, D. E., Baggs, T., Hand, M., & Alessio, K. L. (2018). Thorium distribution in the crust: Outcrop and grain-scale perspectives. Lithos, 320-321, 222-235.

Wing, B. A., Ferry, J. M., & Harrison, T. M. (2003). Prograde destruction and formation of monazite and allanite during contact and regional metamorphism of pelites: petrology and geochronology. Contributions to Mineralogy and Petrology, 145(2), 228-250.

Wolff, R., Dunkl, I., Kiesselbach, G., Wemmer, K., & Siegesmund, S. (2012). Thermochronological constraints on the multiphase exhumation history of the Ivrea-Verbano Zone of the Southern Alps. Tectonophysics, 579, 104-117.

Yakymchuk, C. (2017). Behaviour of apatite during partial melting of metapelites and consequences for prograde suprasolidus monazite growth. Lithos, 274, 412-426.

Yakymchuk, C., & Brown, M. (2014a). Behaviour of zircon and monazite during crustal melting. Journal of the Geological Society, 171(4), 465-479.

Yakymchuk, C., & Brown, M. (2014b). Consequences of open-system melting in tectonics. Journal of the Geological Society, 171(1), 21-40.

Yakymchuk, C., & Brown, M. (2019). Divergent behaviour of Th and U during anatexis: Implications for the thermal evolution of orogenic crust. Journal of Metamorphic Geology. 37, 899 916.

Yakymchuk, C., Kirkland, C. L., & Clark, C. (2018). Th/U ratios in metamorphic zircon. Journal of Metamorphic Geology, 36(6), 715-737.

Yang, P., & Pattison, D. (2006). Genesis of monazite and Y zoning in garnet from the Black Hills, South Dakota. Lithos, 88(1-4), 233-253.

Zingg, A., Handy, M., Hunziker, J., & Schmid, S. (1990). Tectonometamorphic history of the Ivrea Zone and its relationship to the crustal evolution of the Southern Alps. Tectonophysics, 182(1-2), 169-192.

Supporting information

APPENDIX S3.1: DETAILED ANALYTICAL TECHNIQUE FOR LA–ICP–MS MONAZITE GEOCHRONOLOGY AND TRACE ELEMENT ANALYSIS

U–Pb monazite geochronology was obtained by LA–ICP–MS and was performed at Adelaide Microscopy, the University of Adelaide, using an Australian Scientific Instruments (ASI) Resolution M-50-LR 193 nm excimer laser in a He ablation atmosphere, coupled to an Agilent 7900 ICP-MS. Monazites were analysed simultaneously for U–Pb geochronology and trace elements. Ablation of monazites was performed in situ with a beam diameter of 13 µm. A repetition rate of 5 Hz was used, with a total acquisition time of 60 s, comprising 30 s of background measurement and 30 s of sample ablation. Ablation sites were cleaned prior to analysis to remove contamination using five single pulses of the laser before measurement of the background. Measured isotopes and dwell times for geochemistry and trace elements are given in Table S3.1.1.

Iolite (v. 3.0; Paton, Hellstrom, Paul, Woodhead, & Hergt, 2011) was used to reduce raw LA–ICP–MS data including corrections for baseline, instrumental drift, mass bias and down-hole fractionation using a primary reference material interleaved with the unknowns. The primary reference material for U–Pb ratios was MAdel monazite standard (TIMS normalisation data: $^{207}Pb/^{206}Pb$ age = 492.01 ± 0.77; $^{206}Pb/^{238}U$ age = 517.9 ± 2.6 Ma; $^{207}Pb/^{235}U$ age = 513.13 ± 0.20 Ma; De Vries Van Leeuwen, Morrissey, Kelsey, & Raimondo, 2019) with an overestimated absolute uncertainty of 1% assigned to each normalisation age, and the NIST610 trace element glass (Standard reference material, National institute of Standards and Technology) for trace elements. Data accuracy was also monitored by repeat analyses of the in-house internal standard, 94-222/Bruna-NW monazite (SHRIMP data: $^{206}Pb/^{238}U$ = 450.2 ± 3.4 Ma; Maidment, 2005). Over the duration of this study, the reproducibility (external precision) of the MAdel standard was 491.0 ± 6.83 Ma for $^{207}Pb/^{206}Pb$, 518.4 ± 1.0 Ma for $^{206}Pb/^{238}U$, and 512.7 ± 1.2 Ma for $^{207}Pb/^{235}U$ (2σ *propagated errors*; *n* = 56). The weighted average ages for 94-222/Bruna-NW were 467.3 ± 11.1 Ma for $^{207}Pb/^{206}Pb$, 446.1 ± 2.1 Ma for $^{206}Pb/^{238}U$, and 448.1 ± 2.9 Ma for $^{207}Pb/^{235}U$ (2σ *propagated errors*; *n* = 27). An additional 1.5% error was propagated in quadratic to the final weighted average ages to account for systematic errors (see also Horstwood et al., 2016).

Common Pb could not be explicitly measured due to the unresolvable interference of ^{204}Hg on ^{204}Pb. A common Pb correction was applied to the unknowns using the "VizualAge_UcomPbine" data reduction scheme (DRS) in the Iolite software (Chew, Petrus, & Kamber, 2014; Paton et al., 2011; Petrus & Kamber, 2012). This DRS was used to apply an automated common Pb correction to all unknowns using the ^{207}Pb method and an initial $^{207}Pb/^{206}Pb$ ratio of 0.805976, determined by regression of all unknown data in the study.

The unknown data in this study show a clear discordant trend attributed to common Pb as

Table S3.1.1. Measured isotopes and dwell times for LA ICP MS analysis.

Isotope	Dwell time (ms)
Geochemistry	
^{202}Hg	20
^{204}Pb	20
^{206}Pb	30
^{207}Pb	60
^{208}Pb	10
^{232}Th	5
^{238}U	10
Trace elements	
^{29}Si	5
^{31}P	5
^{43}Ca	5
^{89}Y	5
^{90}Zr	10
^{139}La	5
^{140}Ce	5
^{141}Pr	5
^{146}Nd	5
^{147}Sm	5
^{153}Eu	10
^{157}Gd	5
^{159}Tb	10
^{163}Dy	10
^{165}Ho	10
^{166}Er	10
^{169}Tm	10
^{172}Yb	10
^{175}Lu	10

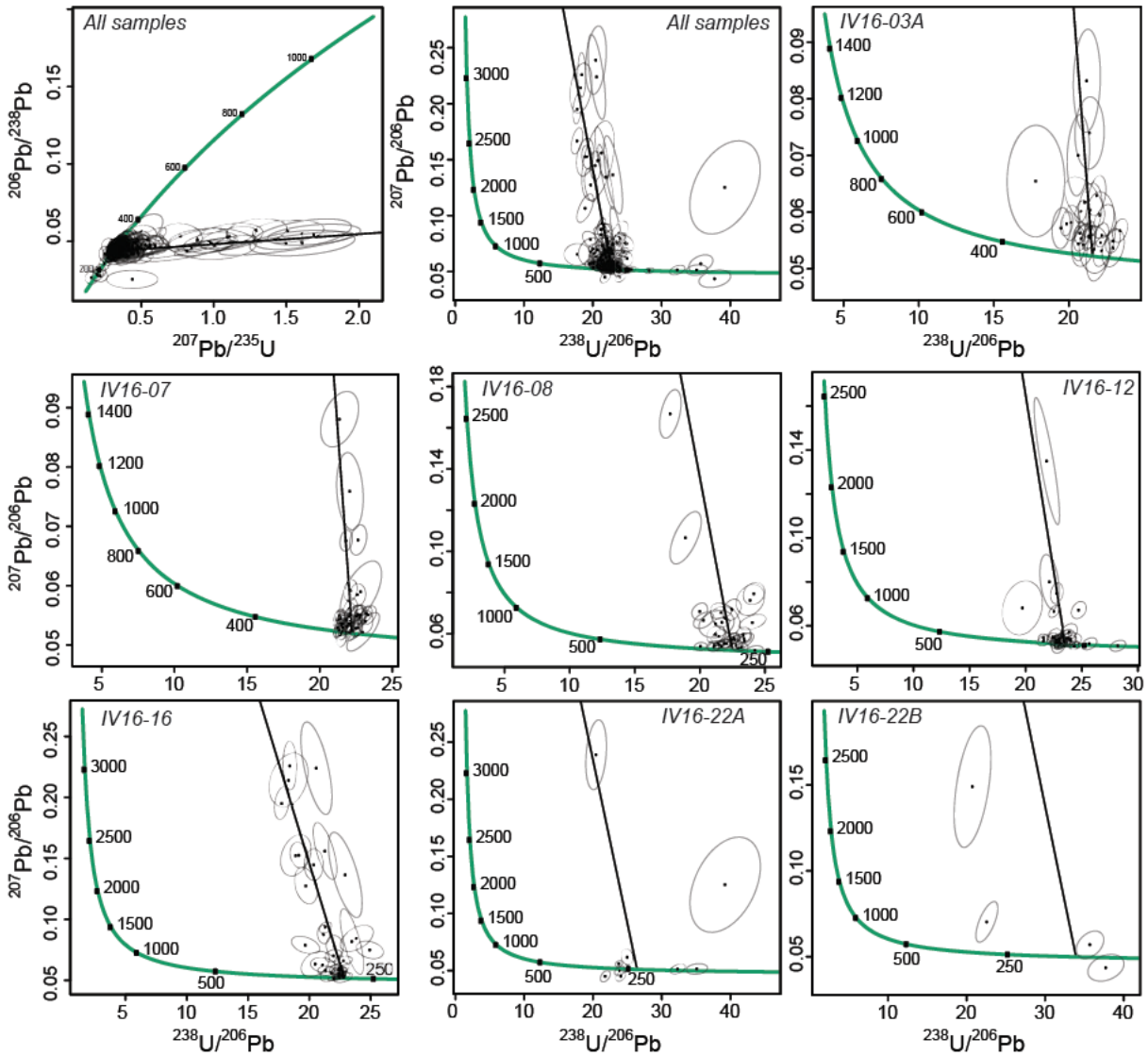

Figure 3.1.1. Tera Wasserburg plot of uncorrected monazite U Pb geochronology with data arranged by sample. Bold black line is the regression line for the initial $^{207}Pb/^{206}Pb$ ratio ($^{207}Pb/^{206}Pb_0$) used in the ^{207}Pb correction, $^{207}Pb/^{206}Pb_0$ = 0.805976.

described in section 7.4 of the main text (Fig. 10, Fig. 3.3.1). This trend is observed to different extents in the samples. The strongest trend is observed in IV16-16 with the majority of samples containing one or more discordant data points which lie along or parallel to the discordia used in the common Pb correction (Fig. 3.3.1). As discussed in section 7.4, there is additionally a spread of $^{238}U/^{206}Pb$ dates (see also Pb corrected data in Fig. 10b) which complicates and compromises the common Pb trend. The discordant trend is recorded to different extents by monazite zones Z1–Z9 (Fig. 3.3.2). The greatest amount of discordant data is in Z6, which predominantly comes from sample IV16-16 (therefore the two trends are related). Whereas the common Pb trend is more clearly identified in some samples than others, all samples contain some discordant data. In addition, the interpretation of the monazite U–Pb geochronology is largely conducted in the context of the monazite zones, most of which span several samples. For these two reasons, the same common Pb correction was applied to all samples to ensure consistency of data processing within the sample set, and particularly within the zones.

Trace elements were reduced using the "Trace element_IS" DRS, which allows for the input of internal standard values for each analysis. In this case, Ce concentrations were taken from probe analyses from the same location as the LA–ICP–MS point analyses and used as the internal standard input for monazite trace element data reduction. This method reduces error associated with the assumption that all monazite analyses have a constant Ce concentration.

LA–ICP–MS analyses of unknowns were attributed to monazite 'zones' (Z1–Z9) determined by EPMA map and point data by correlation of spot

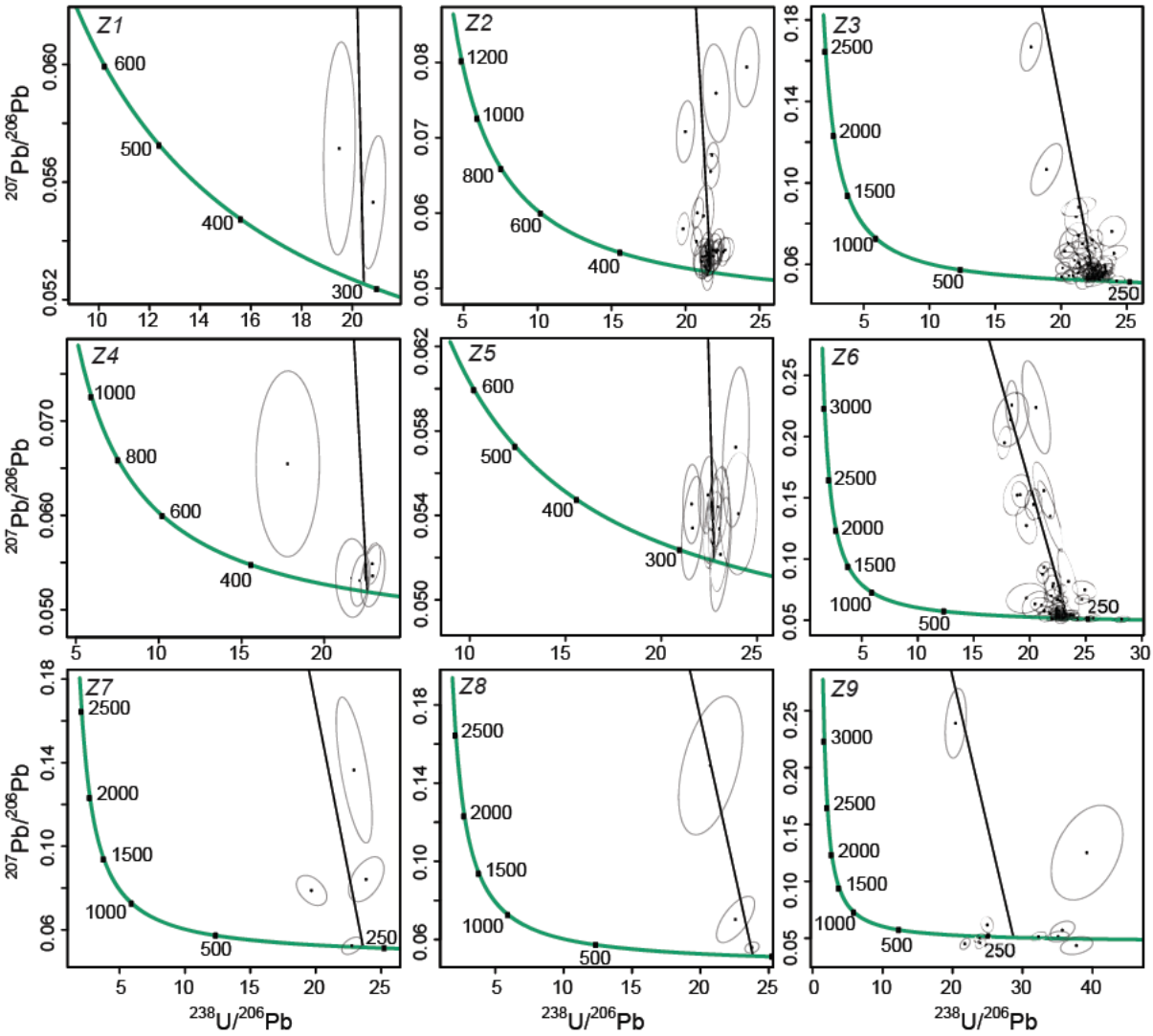

Figure 3.1.2. Tera Wasserburg plot of uncorrected monazite U Pb geochronology with data arranged by monazite zone (Z1 Z9). Zones are described in main text. Bold black line is the regression line for the initial $^{207}Pb/^{206}Pb$ ratio ($^{207}Pb/^{206}Pb_0$) used in the ^{207}Pb correction, $^{207}Pb/^{206}Pb_0 = 0.805976$.

location with EPMA maps of monazite grains and correlation of trace element compositions of monazite between EPMA and LA–ICP–MS data.

REFERENCES

Chew, D., Petrus, J., & Kamber, B. (2014). U Pb LA ICPMS dating using accessory mineral standards with variable common Pb. Chemical Geology, 363, 185 199.

De Vries Van Leeuwen, A. T., Morrissey, L. J., Kelsey, D. E., & Raimondo, T. (2019). Recognition of Pan African aged metamorphism in the Fisher Terrane, central Prince Charles Mountains, East Antarctica. Journal of the Geological Society, jgs2018 2146.

Horstwood, M. S., Košler, J., Gehrels, G., Jackson, S. E., McLean, N. M., Paton, C., . . . Vermeesch, P. (2016). Community derived standards for LA ICP MS U (Th) Pb geochronology Uncertainty propagation, age interpretation and data reporting. Geostandards and Geoanalytical Research, 40(3), 311 332.

Maidment, D. W. (2005). Palaeozoic high grade metamorphism within the Centralian Superbasin, Harts Range region, central Australia.

Paton, C., Hellstrom, J., Paul, B., Woodhead, J., & Hergt, J. (2011). Iolite: Freeware for the visualisation and processing of mass spectrometric data. Journal of Analytical Atomic Spectrometry, 26(12), 2508 2518.

Petrus, J. A., & Kamber, B. S. (2012). VizualAge: A novel approach to laser ablation ICP MS U Pb geochronology data reduction. Geostandards and Geoanalytical Research, 36(3), 247 270.

APPENDIX S3.3: WHOLE ROCK GEOCHEMISTRY FOR IVREA–VERBANO METAPELITE SAMPLES.

Supplementary Table S3.3.1. Whole rock geochemistry for Ivrea Verbano metapelite samples Major elements are pressetned as oxide wt%, trace elements as ppm. % errors calculated from standard data. Sample locations are in UTM coordinates using WGS84 datum, zone 32T.

Sample	*%error (2σ)*	IV16-01	IV16-02	IV16-03A	IV16-04	IV16-05	IV16-06	IV16-07	IV16-08	IV16-09A
Easting (mE)		449390	449812	450804	451834	452131	452387	448640	446706	446472
Northing (mN)		5084067	5083630	5083388	5083247	5082826	5082544	5083912	5084125	5084856
Major elements (%)										
SiO_2	*0.19*	48.93	52.51	49.18	60.65	64.19	62.62	51.88	56.96	66.39
TiO_2	*0.36*	0.75	0.9	1.34	1.3	0.79	0.93	1.16	1.16	0.79
Al_2O_3	*0.26*	24.87	22.31	28.66	16.79	18.12	17.09	28.54	22.88	15.75
Fe_2O_3T	*0.21*	7.44	9.14	12.18	7.47	6.48	7.09	12.57	9.79	6.41
MnO	*0.54*	0.06	0.15	0.14	0.13	0.09	0.09	0.13	0.19	0.11
MgO	*0.19*	3.25	2.34	3.48	4.03	2.8	2.93	1.69	2.91	2.05
CaO	*0.16*	8.94	5.03	0.15	6.07	1.73	2.41	0.56	0.47	6.46
Na_2O	*0.38*	2.86	3.38	0.46	0.84	2.8	4.5	0.74	1.21	0.49
K_2O	*0.54*	2.56	4.26	4.29	2.65	2.98	2.2	2.87	3.93	1.43
P_2O_5	*0.69*	0.12	0.17	0.05	0.33	0.18	0.13	0.06	0.17	0.19
Total		99.78	100.19	99.93	100.26	100.16	99.99	100.2	99.67	100.07
LOI	-	2.84	2.74	1.62	1.26	1.76	1.85	1.88	2.41	0.95
Fe_2O_3	*0.21*	5.23	6.44	10.37	6.85	5.66	5.48	8.53	7.96	4.49
FeO	*0.21*	1.63	1.98	0.66	-0.14	0.19	1.00	3.09	0.94	1.42
Trace elements (ppm)										
Rb	*11.55*	161.3	210.4	283.2	129.6	134.1	86.3	228	232.5	96.1
Sr	*1.94*	1554	660	62	325	308	249	205	125	337
Y	*2.29*	32.5	34.1	16.2	21.4	28.1	35.8	45.3	28	33.2
Zr	*2.33*	122	178	161	225	189	241	203	189	304
V	*1.40*	178	146	203	152	140	136	173	179	103
Ni	*1.15*	51	57	72	48	60	69	69	76	35
Cr	*5.98*	124	106	160	125	110	128	165	166	96
Nb	*4.98*	15.5	23.4	25.9	10.8	14.5	19.6	36.5	24.8	20.2
Ga	*1.51*	36.4	27.2	39.8	20.4	24.9	23.4	44.7	32.1	22.3
Cu	*5.54*	40	47	96	27	59	38	26	36	26
Zn	*1.09*	136	155	191	78	114	88	205	143	92
Co	*4.88*	14	20	42	22	23	24	37	31	11
Ba	*12.43*	278	776	610	357	720	428	399	475	428
La	*15.81*	54	50	30	18	21	34	43	26	37
Ce	*5.97*	93	98	62	32	45	63	76	56	66
U	*74.50*	2.7	0.25	0.25	0.25	0.25	1.8	0.25	0.25	0.9
Th	*75.47*	13	25.7	30.5	5.9	17	22.3	37.2	24.9	16.2
Sc	*3.80*	20	19	22	17	15	13	18	17	10
Pb	*69.28*	13	34	0.5	0.5	9	7	9	7	0.5

Supplementary Table S3.3.1. (cont.)

Sample	IV16-10	IV16-11	IV16-12	IV16-13A	IV16-14	IV16-15	IV16-16	IV16-17A	IV16-17B	IV16-18	IV16-21	IV16-22A	IV16-22B	IV16-24	IV16-25	IV16-26
Easting (mE)	445772	445135	445135	445420	445420	444335	442972	443171	443171	444315	442203	435591	435591	435814	435724	444484
Northing (mN)	5085044	5086576	5086576	5085449	5085449	5087460	5087044	5086996	5086996	5087488	5073338	5074755	5074755	5081125	5081011	5072489
Major elements (%)																
SiO_2	59.05	67.61	57.00	52.56	51.44	51.8	54.75	40.28	53.31	50.23	61.45	57.75	46.53	47.89	52.6	60.81
TiO_2	1.14	0.56	1.19	1.47	1.17	1.77	1.56	2.03	1.32	2.01	0.97	1.31	1.83	1.78	1.87	1.32
Al_2O_3	23.55	15.29	22.86	18.72	22.32	17.2	24.58	31.27	23.61	26.48	18.24	18.16	23.18	26.51	19.94	19.64
Fe_2O_3T	8.17	8.5	10.57	11.21	11.18	11.01	12.71	16.52	11.55	13.9	7.45	11.33	16.16	15.45	14.96	10.15
MnO	0.18	0.28	0.26	0.13	0.26	0.16	0.13	0.3	0.2	0.13	0.07	0.17	0.26	0.17	0.23	0.08
MgO	2.45	2.02	2.69	6.68	3.55	6.72	3.87	5.67	4.04	4.54	3.47	4.64	5.47	4.81	5.09	2.95
CaO	0.96	2.56	1.22	3.35	3.52	7.92	0.46	1.18	1.45	0.37	2.29	2.66	2.82	0.69	2.89	0.37
Na_2O	0.98	1.73	0.73	1.88	3.67	1.69	0.57	0.6	2.09	0.25	3.14	2.27	2.22	1.1	1.86	1.01
K_2O	3.03	1.58	3.19	3.68	2.88	0.9	1.39	2.22	2.52	2.11	2.85	1.51	1.23	1.69	0.49	3.7
P_2O_5	0.11	0.20	0.15	0.12	0.09	0.45	0.05	0.08	0.06	0.04	0.16	0.09	0.06	0.05	0.05	0.07
Total	99.62	100.33	99.86	99.8	100.08	99.62	100.07	100.15	100.15	100.06	100.09	99.89	99.76	100.14	99.98	100.1
LOI	1.17	1.22	2.8	1.47	1.42	1.15	2	3.15	2.48	2.42	1.52	1.38	1.85	1.25	1.51	2.35
Fe_2O_3	5.77	4.7	6.68	7.38	8.05	7.86	10.13	12.27	9.27	10.97	5.84	6.32	10.74	9.16	8.25	8.57
FeO	1.76	3.28	3.15	3.01	2.23	2.27	1.45	2.88	1.25	1.71	0.96	4.31	4.22	5.27	5.79	0.63
Trace elements (ppm)																
Rb	175.9	53.6	146.7	207.4	123.9	46.2	48.2	64.6	62.9	101.9	107.6	13	14	52.4	4.8	173
Sr	123	185	133	120	207	336	132	128	218	107	216	365	333	129	285	124
Y	21.1	44.3	39	4.5	43.2	19.1	58	82.1	65.9	55.3	33.5	88.5	126.7	71.6	70	36.8
Zr	207	98	185	94	171	119	195	247	172	337	192	242	311	238	304	298
V	213	129	238	275	228	244	226	302	207	249	159	187	281	270	271	195
Ni	90	35	104	191	94	97	65	111	65	122	69	72	51	62	92	70
Cr	187	83	209	434	157	247	178	244	138	210	118	192	199	201	219	145
Nb	24.3	8.1	18.4	20.7	20.1	17.4	23.6	44.9	15.6	33	15.8	20.4	40.6	31.8	35	23.6
Ga	35.9	18.7	32.4	25.5	27.1	25	38.1	52.4	36.5	41	24.7	20.3	26.6	42	21.3	28.5
Cu	17	21	60	11	63	52	41	85	46	76	20	65	59	41	89	39
Zn	151	83	165	160	158	153	149	228	141	302	168	189	171	117	133	142
Co	33	21	38	50	36	43	45	57	39	52	25	38	55	53	56	32
Ba	554	428	706	267	431	404	558	877	923	617	545	863	642	666	293	649
La	35	30	40	8	23	18	36	44	46	28	24	40	26	16	26	30
Ce	63	53	83	12	40	39	72	105	98	51	43	73	55	26	47	61
U	0.6	0.25	0.25	0.25	0.25	0.25	0.25	0.25	0.25	0.25	0.25	0.25	0.25	1.9	0.25	0.25
Th	26.2	11.2	28.4	5.2	15	0.25	28.9	43.1	24	21.9	15.9	7.2	5.1	25.4	6.6	28.2
Sc	8	12	14	17	20	23	19	33	22	19	12	18	34	23	25	18
Pb	20	14	13	7	14	3	1	6	13	9	4	6	11	8	5	14

Chapter 4

This chapter is prepared for submission as:

Williams, M. A. & Kelsey, D. E. Temperature dependence of thorium substitution mechanisms in monazite.

Statement of Authorship

Title of Paper	Temperature dependence of thorium substitution mechanisms in monazite
Publication Status	☐ Published ☐ Accepted for Publication ☐ Submitted for Publication ☑ Unpublished and Unsubmitted w ork w ritten in manuscript style
Publication Details	

Principal Author

Name of Principal Author (Candidate)	Megan A Williams
Contribution to the Paper	Study design, dataset colla ion and interpreta ion, all draf ing of figures, manuscript/chapter writing
Overall percentage (%)	95%
Cer ification:	This paper reports on original research I conducted during the period of my Higher Degree by Research candidature and is not subject to any obligations or contractual agreements with a third ¸ art¸ that would constrain its inclusion in this thesis. I am the primary author of this paper.
Signature	Date 8/12/19

Co-Author Contributions

By signing he Statement of Authorship, each author certifies that:

i. the candidate's stated contribution to the publication is accurate (as detailed above);

ii. permission is granted for the candidate in include the publication in the thesis; and

iii. the sum of all co-author contribu ions is equal to 100% less the candidate's stated contribu ion.

Name of Co-Au hor	David E Kelsey
Contribution to the Paper	Manuscript editing, assistance wi h dataset interpretation, project design
Signature	Date 9/12/19

Temperature dependence of thorium substitution mechanisms in monazite

ABSTRACT

Recent studies have provided evidence that the formation temperature of monazite directly controls its Th concentration as well as the ratio of the two Th-endmembers of monazite. To find out if this could be observed more broadly, we compiled the largest database to date of full chemical analyses of monazite, linked to pressures and temperatures of formation. We use this dataset to investigate the trends in Th-in-monazite and Th-endmember fractions as a function of pressure and temperature. With this dataset, we show that Th-in-monazite increases with temperature, with little effect from pressure. We cast the data in terms of the two thorium-bearing monazite endmembers – huttonite and cheralite – and show that, of the two, cheralite is the more dominant endmember. Huttonite becomes significant in partially melted rocks, showing an antithetic relationship with cheralite, but is otherwise of low fraction. These mechanisms within monazite fundamentally control the Th contribution to the heat producing element budget within common crustal rocks. Our findings provide potential for added utility of monazite in decoding crustal processes to complement wide and growing usage of monazite in geoscience research.

1 INTRODUCTION

The rare earth element (REE)+Y+Th+U phosphate mineral monazite only makes up <0.1 vol% of common peraluminous crustal rock types, but commonly has high ThO_2 concentrations (1–10 wt%). It therefore typically hosts more than half the Th in these rocks. Monazite can display a wide variety of morphologies and internal chemical and isotopic zoning patterns (see Fig. 3 in Taylor et al., 2016 and references therein). These zones can be retained within grains through multiple cycles of metamorphism and partial melting (e.g. Yakymchuk et al., 2015). In addition, monazite is stable in rocks recording a wide range of pressure and temperature conditions (Fig. 1; see also appendix S4.1). This suggests monazite has the potential to record considerable information about the conditions in which it formed.

The full detail of the processes that cause each of the wide variety of internal zoning patterns in monazite is yet to be revealed. Nevertheless, patterns within the scatter of natural compositional point and map datasets are somewhat evident. For example, when monazite grows in equilibrium with garnet and/or xenotime it records sensitive, temperature dependent, compositional information which can be extracted to decode the heating path of the rock (e.g. Gratz and Heinrich, 1997; Pyle et al., 2001; Seydoux-Guillaume et al., 2002). With regard to Thorium, we have shown in chapters 2 and 3 that there are systematic patterns to its behaviour in monazite with changing metamorphic grade (see also Skrzypek et al., 2018), and numerous other studies have proposed this with smaller datasets (e.g. Bea and Montero, 1999; Foster et al., 2000; Kohn and Malloy, 2004; Overstreet, 1967). Fully understanding Th behaviour in monazite is complicated due to Th substituting into monazite via two different coupled exchange end-members. It is not yet explicitly understood whether the ratio of the two Th-endmembers (cheralite, $Ca_{0.5}Th_{0.5}PO_4$, and huttonite, $ThSiO_4$) in natural monazite changes systematically with metamorphic grade or mineral assemblage. If we are to more fully understand the behaviour of Th in monazite and in peraluminous rocks, we need to understand the interplay between the two Th-end-members of monazite as a function of pressure, temperature and rock composition (*P–T–X*). Ultimately, a better understanding of Th behaviour in monazite will improve our understanding of monazite's control on radiogenic heat production in the crust as well as our ability to forward model monazite stability and composition (Chapter 5).

For individual studies, measured monazite composition can show apparently contradictory compositional trends between terranes or even between grains in a single sample. For example, previous work has demonstrated inconsistency within Th patterns in monazite grains (e.g. decreasing Th from core to rim; Kohn & Malloy, 2004; Th-in-monazite is constant or increases with metamorphic grade; Chapter 2; Skrzypek et al, 2018; monazite rims enriched in cheralite component over huttonite component relative to monazite cores and vice versa; e.g. Franz et

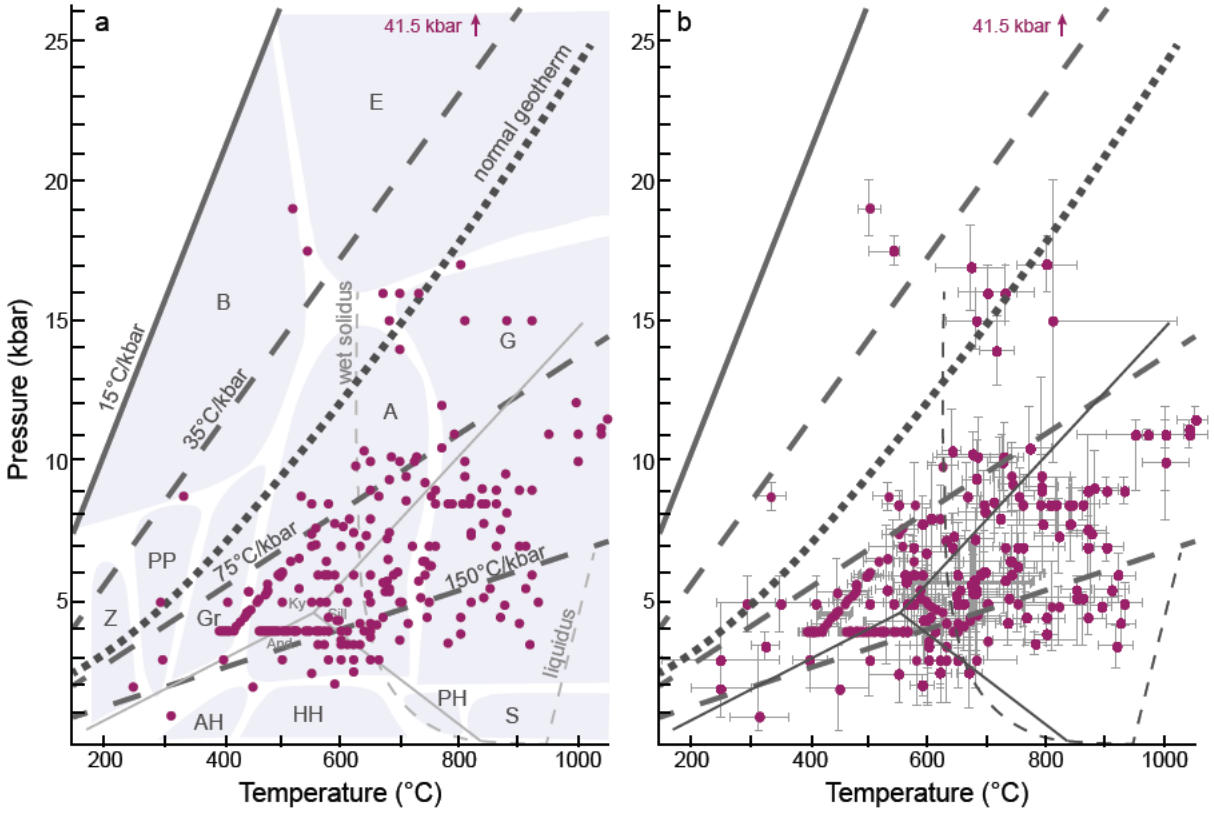

Figure 1. Pressure temperature estimates for analyses in our dataset. See Appendix S4.1 for data sources. (a) P T conditions of analyses relative to metamorphic facies and geothermal gradients. Circles indicate the pressure temperature conditions of one or more samples. (b) uncertainties on *P T* conditions of analyses. Shaded metamorphic facies: A, amphibolite; AH, albite epidote horfels; And, andalusite; B, blueschist; E, eclogite; G, granulite; Gr, greenschist; HH, hornblende hornfels; Ky, Kyanite; PH, pyroxene hornfels; PP, prehnite pumpellyite; S, sanidinite; Sill, sillimanite; Z, zeolite.

al., 1996). Many, particularly older, studies only analysed or reported a relatively small number of monazite compositional analyses. This has changed in recent years with the rise of electronic supplementary datasets. However, the ambiguity about what monazite composition does with metamorphic grade is somewhat understandable given the considerable investment in time and money required to complete highly detailed monazite analytical programs. Nevertheless, the paucity of detailed studies serves to blur whether or not there are systematic changes to monazite chemistry because only a subset of all monazite compositions is presented or few total analyses are actually undertaken. However, detailed studies of monazite chemistry exist (e.g. Chapters 2 and 3; Dumond et al., 2015; Kohn et al., 2005; Pyle and Spear, 2003; Skrzypek et al., 2017; Skrzypek et al., 2018; Williams et al., 2017; see also Appendix S4.1), but the effects of temperature, pressure, *P–T* path and whole rock chemistry mean that each of these studies can each only tell part of the monazite story. By considering all of these studies together we can constrain the contributions to monazite composition from each of these variables and understand whether the trends observed in individual studies are universal.

A further challenge for understanding monazite chemistry is the difficulty in specifically ascribing monazite compositional zone chemistries to particular *P–T* conditions across changes in metamorphic grade and thus parts of a *P–T* path. This is especially challenging if only a few monazite grains were mapped and/or analysed and if there were large changes in whole rock geochemistry from one sample to the next with increasing metamorphic grade. We have tools to link monazite chemistry with *P–T* (e.g. Y-in-monazite thermometer), but these require quite specific conditions to be met (e.g. xenotime, garnet and monazite which have grown in equilibrium), which can be difficult to assess in a small or isolated dataset. Due to this complexity, it is perhaps unwise to make universal statements about monazite compositional behaviour based on any individual study that doesn't involve detailed linking to *P–T–X*, even though such studies may well be showing what are actually universal trends.

To address these issues and identify whether

there are in fact systematic, universal trends in monazite chemistry as a function of metamorphic grade, we have collated a dataset from existing literature containing over 5000 monazite compositional analyses. This is the largest dataset of its kind to date, and contains monazite compositions including REE, Th, U, Ca, Si, Y and P, peak pressure and temperature estimates for the monazite analyses as well as whole rock composition, where possible. Using this dataset, we aim to address the following questions: (a) How do monazite compositional observations compare between studies and terranes?; (b) What are the universal trends and range of concentrations of Th-in-monazite and Th endmembers?; (c) Can apparently contradictory observations of monazite chemistry trends from different studies be reconciled?; (d) Does Th-in-monazite display equilibrium- or trace element-type behaviour?; and (e) Can we explicitly define how cheralite and huttonite vary across *P–T* space? We recognise that there are limitations with this approach (discussed below), but we believe that the approach enables us to gain valuable insight into global trends in monazite behaviour. We supplement this integrated data approach by assessing and comparing with the best constrained studies. This gives us a basis for hypothesis testing within the larger database.

1.1 Thorium substitution mechanisms in monazite

Thorium is incorporated into monazite through two coupled substitutions: the cheralite substitution (1) and the huttonite exchange (2) (see Williams et al., 2007 and references therein).

$$2REE^{3+} \leftrightarrow Th^{4+} + Ca^{2+} \quad (1)$$

$$P^{5+} + REE^{3+} \leftrightarrow Th^{4+} + Si^{4+} \quad (2)$$

Cheralite is typically observed to be the more abundant of these two endmembers in natural monazite (Bial et al., 2015; Bial et al., 2016; Finger et al., 1998; Finger and Helmy, 1998; Franz et al., 1996; Kelly et al., 2006; Kelly et al., 2012; Laurent et al., 2018; Manzotti et al., 2018; Martins et al., 2009; Nagy et al., 2002). Huttonite fraction is commonly observed to decrease in monazite grains from core to rim (Finger et al., 1998; Finger and Helmy, 1998; Kelly et al., 2006; Laurent et al., 2018), even accounting for Si coupled to U, but the opposite trend is also observed (Bial et al., 2016; Franz et al., 1996; Kelly et al., 2012). In isolation is not (yet) possible to resolve these discrepancies. It remains unclear how the ratio of cheralite and huttonite changes as a function of pressure, temperature and bulk rock composition and what the controlling factors are on the incorporation of Th into monazite by each of these substitution mechanisms. It is also unclear what role, if any, melt plays in the observed variability in cheralite and huttonite proportions.

2 DATASET COLLATION

The dataset used in this study contains 5414 monazite chemical analyses, linked with pressure and temperature conditions which span a range of metamorphic facies, thermal gradients, ages and tectonic settings (Fig. 1, Appendix S4.2). In the analysis below, we identify compositional trends based on the moving mean of data and then seek clarification of specific element exchange mechanisms based on the best constrained data. We consider this to be a reasonable interpretation of the data that allows for global, systematic trends to be identified with limited influence from outlying data points. This method produces similar trends to those defined by the highest density of data (see Appendix S4.3).

Temperatures are defined based on the following available hierarchy of information from the original publications: (1) point analysis temperature from Y-in-monazite thermometry; (2) grain temperature from Y-in-monazite thermometry; (3) sample temperature from conventional or phase equilibria thermobarometry; or (4) temperature interpolated or extrapolated from other samples within the terrane. Where possible we used temperatures associated with individual analyses provided by the original authors. We used a similar hierarchy to define pressures, but in most cases pressure estimates were only available for the whole rock (rather than individual grains or analyses). Where samples had undergone multiple phases of metamorphism, care was taken to try to associate monazite analyses with the conditions of interpreted formation of that grain. These were correlated using either age data or microstructural location from the original publications. Pressure and temperature errors were obtained from the original source data. Where possible these errors relate to the specific sample, otherwise the maximum method error from that study is used (e.g. when pressures and temperatures are extrapolated). Quoted *P–T* values are the middle of the *P–T* range in the original data source unless specifically described

otherwise in the literature. As such, the quoted method errors relate to the full *P–T* range described in the source publication.

Whole rock compositions, where available, are coupled to monazite compositions in the dataset to establish any whole rock geochemical influence on monazite composition. The data set contains 1145 such coupled monazite compositions from 102 rocks which is insufficient to establish a trend, and so is not discussed further in this chapter (see chapter 5).

Data were filtered for quality, in particular Si and Ca contamination of analyses and stoichiometry. Due to the substitution mechanisms of Th into monazite, ideal monazite has equal cations of (Th+U) and (Ca+Si). For the purposes of this study, we consider poor analyses to be those with (Th + U) – (Ca + Si) <–0.05, i.e. an excess of Ca and/or Si which cannot be accommodated by the available (measured) Th and U. Additionally, ideal monazite has equal cations of (P+Si+S) and (REE+Y+Th+U+Ca) due to substitution of these elements into the tetrahedral and A-sites, respectively. For the purposes of this study, we consider poor analyses to be those with |(P+Si+S) – (REE+Y+Th+U+Ca)| > 0.15, i.e. an excess in the tetrahedral site which cannot be balanced by the A-site and vice versa. A total of 143 data points were discarded on the basis of this criterion from an original total of 5698. A further 219 monazite chemical analyses could not be linked with *P–T* conditions and are therefore not included in our analysis (see Appendix S4.2), leaving 5414 analyses on which the interpretation below is based.

Cations were calculated on a 4-oxygen basis from oxide wt% values given in original studies. Monazite endmember proportions were calculated from the normalised P, Ca and Y atoms per formula unit (APFU) from raw data after the data quality checks (see above) were made. The endmember fractions are calculated as follows: REEmnz, *p*(mnz) = P- (Y + 2Ca); cheralite, *p*(cher) = 2Ca; huttonite, *p*(hut) = 1- P-U; coffinite ($USiO_4$) = U; and 'xenotime' (Y-monazite) = Y; where P, Y, Ca and U are the APFU values normalised to their respective crystal sites (P+Si=1, REE+Th+U+Ca+Si+Y=1). Uranium was assumed to occur as coffinite only in line with the vast bulk of studies on monazite. Alternative methods of casting and visualising the data to identify compositional trends produced similar outcomes (see Section 4.4 and Appendix S4.3).

3 RESULTS

The dataset contains monazite analyses in the pressure range 1.0–41.5 kbar, with the majority of the data in the range 1.0–18.0 kbar (Fig. 1). Over the full pressure range there is no trend in the amount of Th^{4+} contained in monazite or the proportions of the cheralite and huttonite endmembers with pressure (Fig. 2a–c).

Monazite analyses span the temperature range 250–1080 °C (Fig. 1). Th^{4+} in monazite increases from the lowest to highest temperature analyses (Fig. 2d). Within this overall increase are three trend segments: (1) Th^{4+} increases from 0.005 at 250 °C to 0.041 APFU at 550 °C (values here and below averaged over 10 °C window; Fig. 2d); (2) between 550 and 850 °C, Th^{4+} plateaus at ~ 0.048 APFU; and (3) at temperatures >850°C Th^{4+} increases again to 0.062 APFU, though data density is low. *P*(cher) follows the Th^{4+} trend to c. 800 °C, increasing from 0.024 to 0.086, after which it decreases to 0.028 (Fig. 2e). *P*(hutt) remains constant at c. 0.014 until c. 900 °C, after which it increases to 0.055 (Fig. 2f).

Within the full dataset, Th^{4+} is in the range 0–0.324 APFU (Fig. 2) with an interquartile range of 0.024 APFU. *P*(cher) is in the range 0–0.455 (equating to Th^{4+} of 0–0.223 APFU) with an interquartile range of 0.042 and *p*(hutt) is in the range 0–0.280 (equating to Th^{4+} of 0–0.140 APFU) with an interquartile range of 0.020.

4 DISCUSSION

4.1 P T *dependence of Th in monazite*

Th-in monazite is largely controlled by temperature, with a limited influence from pressure (Fig. 2a, d). This is consistent with the use of Y-in-monazite as a thermometer and the published positive slopes of reactions involving monazite growth (Janots et al., 2007; Spear, 2010; Spear and Pyle, 2010) and suggests that, of the two, total monazite composition is largely controlled by changes in temperature. There are two pressure regions where Th-in-monazite trends show variation: at pressures <2kbar; and in the interval 11–13 kbar (Fig. 2a–c). In both instances, these data are limited to a small temperature window from a single terrane and study (Fig. 1) and do not correlate with the pressure trends from the remaining data. It is therefore unreasonable to interpret these perturbations as a function of pressure, but rather more strongly controlled by temperature as in both cases they fit within the

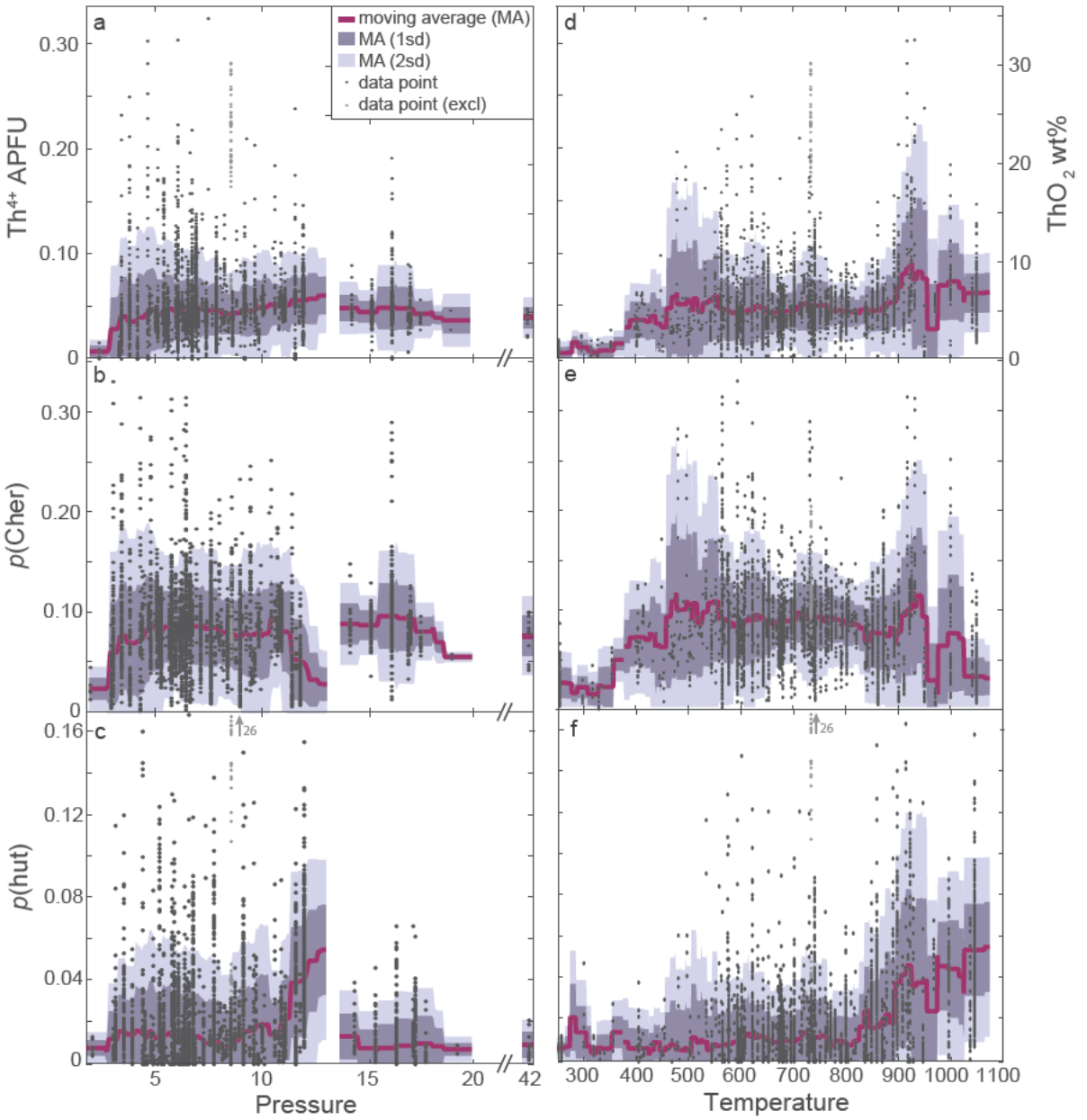

Figure 2. Moving mean of monazite compositional parameters showing the changes in monazite composition with pressure and temperature. See Appendix S4.1 for data sources. Parts a c show compositional trends with pressure and parts d f show compositional trends with temperature from the dataset. For pressure, the moving mean is calculated for every 0.1 kbar between 0 and 40 kbar, averaging over a moving 2 kbar window. For temperature, the moving mean is calculated for every 1 degree between 250°C and 1100°C, averaging over a moving 50°C window. (a)&(d) Th4+ APFU, (b)&(e) proportion of cheralite endmember, Tho.5Cao.5PO4, (c)&(f), proportion of huttonite endmember, ThSiO4. The remaining compositional parameters for monazite are (REE+Y)PO4 and USiO4. p(REE+YPO4)[not shown] + p(USiO4) [not shown] + p(cher) + p(hutt) =1. Light grey data points were determined to be signifi cant outliers and were not used in determination of data density, see text for details. Note scale break in parts (a) (c).

temperature-controlled trends defined in Fig. 2 d–f.

At low temperature (<550 °C), the gradual increase of Th-in-monazite suggests that thorium reservoirs other than monazite are in play. The major Th reservoir at low temperature is likely to be allanite, a known precursor to monazite growth (e.g. Engi, 2017; Janots et al., 2008; Spear, 2010), with possible additional contribution from thorite, the low *P–T* polymorph of $ThSiO_4$ (Seydoux-Guillaume et al., 2002; Seydoux and Montel, 1997). The temperature of the allanite to monazite transition depends on whole rock composition, particularly Ca and Al, and has a positive slope (Spear, 2010; Chapter 5). As allanite breakdown is the major monazite-forming reaction known in the temperature interval 200–550 °C (e.g. Budzyń et al., 2011; Engi, 2017; Janots et al., 2008; Spear, 2010), the increase in Th-in-

monazite over this temperature interval suggests that The temperature at which this reaction occurs is a strong control on the Th concentration of the first generation of metamorphic monazite. That is, the lower the temperature at which the allanite to monazite reaction occurs, the lower in Th the first generation of metamorphic monazite will be. The variability of Th-in-monazite over this interval in the dataset is likely due to the progressive liberation of Th from allanite during the allanite to monazite transition. Th concentrations from monazites within the same sample can vary greatly at low temperatures, particularly where grain size is small (see Chapters 2and 3; Skrzypek et al., 2018). Monazite in such cases likely records formation from prograde allanite (as described above) over a temperature interval on the order of 10°C (Spear, 2010), but such small changes in temperature are not resolvable within the current dataset.

At moderate to high temperatures (550–850 °C), the plateau in Th-in-monazite indicates that monazite is the main Th reservoir in these rocks. Allanite is typically not stable in (low-Ca) peraluminous rocks at the higher end of this temperature interval and REE and P are typically present in enough abundance to saturate the rock in monazite. Therefore, monazite incorporates Th up to a maximum imposed by the whole rock Th concentration of the sample. This maximum appears to be reached by most rocks at moderate temperatures (~550°C, Fig. 2d). Over the interval 550–850 °C, monazite compositions also become more consistent within individual samples and terranes (Fig. 2d; Chapters 2 and 3; Skrzypek et al., 2018). The exact mechanism by which this process occurs is not certain, but Ostwald ripening and dissolution-precipitation creep have been proposed (e.g. Nemchin et al., 2001; Rubatto et al., 2001; Vavra et al., 1996; Wawrzenitz et al., 2012; Williams, 2001). Regardless of the exact mechanism(s), the plateau in Th-in-monazite suggests that monazite mode does not change greatly over this interval.

The consistently high Th^{4+} concentrations in monazite grown at amphibolite facies conditions indicates that reported monazite grains which show higher Th cores grading to lower Th rims are probably formed by one of two processes: (a) equilibrium, whereby high Th cores are formed at higher temperatures than low thorium rims, recording retrograde growth of monazite; or (b) disequilibrium, whereby the local effective bulk composition of Th is sufficiently low once Th has been sequestered in monazite cores that the system transitions from equilibrium behaviour to trace element behaviour. The latter would present problems for interpreting monazite compositions in an equilibrium framework (particularly in low-Th rocks), but may occur only below some measurable threshold of bulk rock Th. However, the temperature dependence of the two Th-endmembers (Fig. 2e, f) shows that monazite arguably displays equilibrium rather than trace element behaviour (see also Goswami-Banerjee and Robyr, 2015). This is supported by the calibrated Y-in-monazite thermometers (YAG–xenotime, YAG–monazite and monazite–xenotime; Gratz and Heinrich, 1997; Pyle et al., 2001; Seydoux-Guillaume et al., 2002).

At high temperatures (>850 °C), Th^{4+} and p(hutt) increase at the expense of p(cher). Whereas Th-in-monazite can be elevated in UHT samples (Fig. 2), the volume proportion of monazite in these samples is not typically reported. The volume of monazite is expected to be lower than at lower (i.e. amphibolite–granulite-facies) temperatures due to the prediction of more advanced dissolution of monazite into silicate melt with increasing temperature (e.g. Chapter 3). The result of this combined with melt loss is that the total (bulk) amount of Th in such rocks may be reduced (e.g. IVZ UHT monazite; Chapter 3; see also Alessio et al., 2018).

P(cher) shows a gradual decline with temperature in the interval 750–850 °C and declines abruptly above 850°C (Fig. 2e). There are two exceptions in the database to this general decline in p(cher). In the samples from Laurent et al. (2018) both cheralite and huttonite are enriched in their highest grade samples ~5 kbar and 900 °C. A similar trend is observed in some UHT monazite in the Ivrea–Verbano Zone (Chapter 3) at higher pressures and temperatures (~ 12 kbar and 1000 °C). The samples are some of the highest temperature analyses within their given pressure window (<5 kbar and >10 kbar; Laurent et al., 2018 and Chapter 3 respectively). This suggests that at extreme high temperatures Th can become enriched in monazite for both Th endmembers, perhaps is mode is low, but it is unclear whether this process is ubiquitous since observations of monazite chemistry from such thermally extreme rocks are rare (see Appendix S4.2).

The Th-in-monazite trend in the dataset can also allow for the appraisal of specific features

observed in some studies. The trends shown in Figure 2 suggest that higher-Th rims on grains should form at higher temperatures than more REE-rich cores. This organisation of monazite zones has been observed in grains in several individual studies (e.g. Chapter 3; Franz et al., 1996; Gasser et al., 2012; Skrzypek et al., 2018) and we would interpret that monazite records a prograde to peak P–T path trajectory in these cases. Conversely, Kohn and Malloy (2004) show the opposite trend, of Th-rich cores trending to Th-poor rims. This was explained as a result of stoichiometric constraints. Whereas the dataset does not give insight into the regions of *P–T* space where monazite grows rapidly, we would interpret (based on the data included here) that such grains record the peak to retrograde history of the rocks rather than being the result of limited availability of Th on a prograde path (see Kohn and Malloy, 2004).

4.2 Possible cheralite huttonite solvus?

Figure 3 shows the dataset on a binary plot of cheralite and huttonite fractions (x(cher) = p(cher)/[p(cher)+p(hut)]) as a function of temperature. More huttonite-rich compositions are rare until temperatures reach ~ 600 °C. No one has yet explored or demonstrated the degree to which solid solution occurs between the cheralite and huttonite endmembers. However, the spread of data in Fig. 3 may provide an argument for the existence of an asymmetric $ThSiO_4$–$(Th,Ca)PO_4$ solvus as approximated by the dashed line.

If this is true, the apex of the solvus occurs at ~600 °C, with complete solid solution above this temperature. The proposed presence of a solvus is consistent with observations that thorite is a common product of retrograde breakdown of peak monazite (e.g. Bea and Montero, 1999). In this scenario, high temperature monazite with

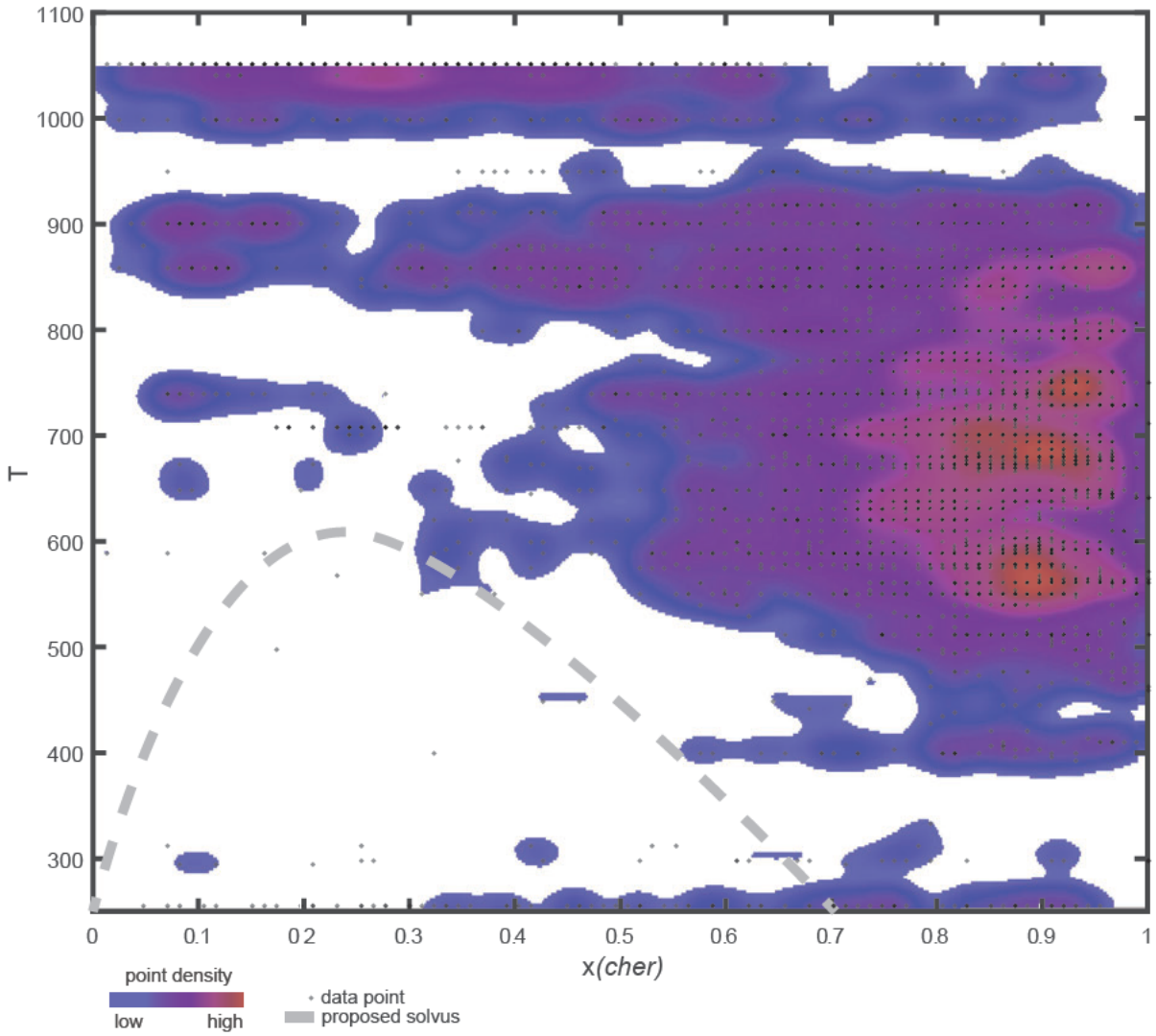

Figure 3. Heat map (data density) of relative proportions of huttonite versus cheralite (x(cher)) with temperature. Low data density in bottom left of plot may indicate the existence of a (previously unreported) solvus between cheralite and huttonite, represented by the grey dashed line. x(cher) = p(cher)/(p(cher)+p(hutt)).

a low cheralite:huttonite ratio (x(cher)) breaks down to form thorite (+ allanite) and monazite with a higher (x(cher)). If the proposed solvus exists, one should expect to also find prograde textures of thorite and cheralite aggregates (e.g. Skrzypek et al., 2017), but identification of the presence of pure thorite in such textures may be hampered by the small grain size typical of low temperature monazite (e.g. Rasmussen and Muhling, 2007; see also chapter 2). As allanite is commonly the major LREE+Th-bearing accessory mineral at low temperatures (see Janots et al., 2008; Spear, 2010; Chapter 5), this may also be manifest as aggregates of thorite + allanite or a thorite–allanite–monazite mix in many rock compositions (e.g. Kim et al., 2009; Kingsbury et al., 1993; Skrzypek et al., 2017).

In addition to the proposed solvus closing with increasing temperature, the shift towards more huttonite-rich compositions at high temperatures (>950 °C; Fig. 3) may indicate preferential dissolution of cheralite-rich monazite into melt at ultra-high temperatures. If this is true, this change to monazite composition could be linked to the undersaturation of Ca in melt, related to the absence of plagioclase (and perhaps apatite) from such high T rocks. If by ~950 °C plagioclase has all been consumed by melting reactions, then with further temperature increases melt will become progressively more undersaturated in Ca. This could drive the breakdown of Ca-bearing accessory minerals, such as monazite and apatite. However, as long as plagioclase and/or apatite remain present (stable) in a rock, monazite should remain cheralitic and the huttonite fraction should not become the dominant Th fraction of monazite. This is suggested by the dataset, where cheralite dominates until temperatures of ~950°C, and huttonite above that. This finding demonstrates an example of what may be possible to understand about monazite with the availability of 'big data'.

4.3 Monazite composition in crustal sections

In terms of specific studies, monazite compositions from three obliquely exposed crustal sections: the Ivrea–Verbano Zone (IVZ; Chapter 3); the Ryoke Belt, SW Japan (RB; Skrzypek et al., 2018); and Mt Stafford, central Australia (STF; Chapter 2) have recently been described and present an opportunity to compare the response of monazite along different thermal gradients to the trends in the dataset. In all three studies, bulk composition as a potential controlling factor on monazite composition was specifically addressed to be as minimal as possible. Whereas there are nearly 50 studies included in the dataset (Appendices S4.1 and S4.2), these three have a specific focus on Th-in-monazite in a *P–T* framework, so provide the opportunity to compare the authors' original interpretations.

All three terranes show evidence of several monazite compositional zones of prograde to peak growth within individual grains and the preservation of prograde cores in higher temperature samples. In the lower pressure RB and STF, prograde monazite cores are preserved to peak metamorphic temperatures, well into the granulite facies (800–880 °C; Chapter 2; Skrzypek et al., 2018). In the IVZ, along a steeper *P–T* gradient, prograde monazite cores are present in amphibolite facies rocks but not in the granulite facies rocks (Chapter 3). This difference is possibly due to the higher strain recorded by the IVZ samples, which may have facilitated dissolution–precipitation creep in the IVZ over other processes such as Ostwald ripening (Chapter 3).

There are similarities in the trends in Th-in-monazite with metamorphic grade in these three terranes. The earliest prograde monazite in IVZ and the RB includes grains with the lowest Th concentration (Chapter 3; Skrzypek et al., 2018) and in the RB and at STF, aggregates of small (~1 µm) monazite grains with highly variable Th are observed in the lowest temperature (< 590 °C) samples (Chapter 2; Skrzypek et al., 2018). Given the small size of these grains, the fact that they occur as aggregates and the difficulty in obtaining uncontaminated analyses, it may be that they are actually aggregates of thorite and more REE-/cheralite-rich monazite (see discussion of solvus, above). Such aggregates are interpreted by Skrzypek et al. (2018) to be pseudomorphs after allanite. By this mechanism, the first monazite formed by the continuous allanite (+ apatite) breakdown reaction (e.g. Goswami-Banerjee and Robyr, 2015) has low Th contents, leaving remaining allanite, and ultimately newly formed monazite, progressively more enriched in Th. This transition occurs over a relatively small temperature window (~ 10°C), evidenced by the rare occurrence of coexisting prograde allanite and monazite preserved in the same sample and replicated by modelling studies (e.g. Spear 2010). This interpretation is consistent with the trends

in the dataset which show low temperature monazite is generally Th-poor but can have highly variable Th contents (Fig. 2d). In the RB and at STF these aggregates become the cores of grains at higher temperature, with amphibolite and granulite facies rims proposed to form through Ostwald Ripening (see also Chapter 2; Skrzypek et al., 2018), although there may be other mechanisms to explain their formation. Similar variable Th cores are observed in amphibolite facies monazite in the IVZ (Chapter 3) and so may have formed by similar processes.

At the sample scale at STF and the RB, chemical equilibrium for Th and the LREE appears to be reached by ~600 °C, indicated by the transition from aggregates of small metamorphic monazite grains with variable Th concentrations (as described above) to more homogeneous monazite compositions (Chapter 2; Skrzypek et al., 2018). This is similar to the trend in the dataset, where chemical equilibrium appears to be reached by ~550 ºC.

Amphibolite to granulite facies monazite have relatively constant Th concentrations in all three terranes (maximum temperatures 820 ºC, 900 ºC and 880 ºC for STF, IVZ and RB, respectively), as reflected by the trends in the global dataset to ~850 ºC. However, in the RB there is also a sub population of peak granulite facies (~ 880 °C) monazite with higher Th concentrations (and also high Y concentrations; Skrzypek et al., 2018). UHT monazite in highly residual rock compositions (IVZ) has very high Th concentrations, facilitated by high proportions of both cheralite and huttonite, similar to the analyses of Laurent et al. (2018) (see discussion above).

IVZ, STF and RB all share some key characteristics in cheralite:huttonite ratios (Chapters 2 and 3; Skrzypek et al., 2018). In all three terranes the cheralite substitution dominates from the lowest temperature monazite through the amphibolite facies and the Th concentration of monazite increases with an approximately constant cheralite:huttonite ratio to the upper amphibolite facies (Chapter 2; Skrzypek et al., 2018). In the IVZ and the RB, monazites formed at the peak of granulite facies metamorphism have higher proportions of the huttonite end-member and commensurately lower cheralite proportions (Chapter 3). This trend is not observed at STF but the cause of this difference remains unclear. Both the IVZ and STF show similar positive correlations between the proportion of huttonite and Th/U ratios of monazite throughout the sections and no correlation between the proportion of cheralite and the Th/U ratio of monazite. It is unclear whether the RB shows the correlation of huttonite proportion and Th/U due to the limited suite of elements reported in monazite analyses (only Ce, La, Th, U, Pb, Ca, Si, S, K were reported, no P, Y or mid to heavy REE).

In both the IVZ and at STF, the modal abundance of monazite increases with metamorphic grade from amphibolite to granulite facies (Chapters 2 and 3), consistent with other studies reporting monazite modal abundance (qualitative or quantitative) increases over metamorphic grade (Foster et al., 2002; Franz et al., 1996; Rubatto et al., 2001; Schulz, 2017; Williams, 2001). In the case of STF, this increase is observed in both pelitic and psammitic rock types (Chapter 2). These increases can be partially explained by a decrease in the rock volume due to the extraction of melt, estimated to be up to 40% in the IVZ and > 25% at STF (Redler et al., 2013; White et al., 2003), with monazite residing largely within the residuum. Even accounting for melt loss, this scenario requires that monazite does not rapidly dissolve in melt (Stepanov et al., 2012), which could be facilitated by a combination of: small volume, rapid, episodic melting and melt extraction; kinetic or physical restriction of monazite dissolution; injection of REE-, P- and Th-saturated melt from deeper crustal levels (see also Yakymchuk and Brown, 2019); and/or sufficiently high whole rock concentrations of Y+REE+Th for monazite terminal stability to greatly exceed the thermal maximum at IVZ and STF (~ 880–1000 °C; Yakymchuk, 2017).

4.4 Dataset limitations

There is considerable potential for smearing within the dataset due to the ambiguity in assigning pressures and temperatures to individual monazite analyses. We have taken care to ascribe reasonable and justifiable pressures and temperatures to formation to monazite grains (see section 2). However, despite our careful approach, there remains potential that prograde and retrograde grains are ascribed higher temperatures due to an absence of the specific *P–T* information in the original publications for monazite grain growth required for our analysis. In addition, many data points have large *P–T* uncertainties (>1 kbar and >50 °C) which may further increase the smearing in the dataset.

Monazite compositions were coupled to whole rock compositions, where possible, but no trend could be established between the two. This is largely for two reasons: (1) for a given study, many monazite compositions are linked to a single whole rock chemistry (sample) and also *P–T–X* point; and (2) a considerable amount of the available bulk rock data is missing the monazite-forming elements P, REE , Y and Th concentrations (with only 60 analyses including all of P, Ce, Y and Th) or other elements known to be significant in monazite formation (e.g. Al and Ca). Therefore, the whole rock compositional data are not sufficiently densely populated to allow for extraction of bulk chemistry trends as distinct from *P–T* trends and significantly more coupled analyses would be required to show these trends explicitly.

The dataset can also potentially be skewed by a small but highly sampled population of monazites from individual studies (e.g. sample R14, 5 grains, 62 analyses; Bhowmik et al., 2010). If such a population has a significantly different chemistry to other analyses from other samples and studies at similar *P–T* conditions (e.g. 30 wt% ThO_2 in population in a single study vs 10 wt% ThO_2 in all other samples in the global dataset; Fig. 2) it can create apparent and skewed changes to the averages which are not reflective of the overall trends. The aim of this study is to understand how changes in pressure, temperature and composition (*P–T–X*) affect monazite composition and stability. In the case of sample R14, these monazite analyses have been excluded from *interpretation* of the dataset because analyses are clear outliers to the general trends (see grey data at 8 kbar and 710 °C in Fig. 2) but there is insufficient information from the sample itself (e.g. whole rock chemistry, mineralogy), or enough of a population from other studies to explore why it is different from the other samples.

The method of casting cheralite and huttonite from Ca and P (see section 2) results in an over-estimation of Th-in-monazite by a median of 0.0067 APFU (see 'ThOverEst', Appendix S4.2), which is similar to the Si excess observed by Pyle et al. (2001). In the ideal case, measured Th should be equivalent to p(hut) +0.5p(cher) and an over estimation of Th points to excess of Si and Ca in the original analyses (after filtering for Th+U = Si+Ca, see section 2). While this is not ideal, the threshold for filtering |Th+U = Si+Ca|<–0.05 was chosen to maximise the available data while removing the most contaminated data and those with an underestimation of Si and Ca (i.e. too much Th+U). Casting cheralite and huttonite from REE and Si is also possible and produces similar results, trends and uncertainties. However, the original studies included in the dataset do not present a consistent set of REEs, with LREEs being ubiquitously reported but M-HREEs only being reported by some studies. The choice was made to cast using Ca and P to avoid the uncertainty introduced by this inconsistency in REE analysis/reporting.

Smearing of x(cher) data at low (<300 °C) temperatures (Fig. 3) is likely due to low Th concentrations (<0.02 APFU), which increases the noise in these data points. This may be exacerbated by the difficulty in obtaining uncontaminated mineral compositional analyses from tiny monazite grains typical of very low metamorphic grade rocks (i.e. Si contamination) and also by the potential for mixed analyses in fine grained aggregates of monazite and thorite common in low-grade rocks as described above. This could be clarified by specific experiments exploring this potential solvus, notwithstanding the issues associated with low temperature experimental petrology.

4.5 Implications of the dataset

4.5.1 Understanding monazite formation and chemistry

By incorporating data from a wide range of sources and locations, this dataset gives a greater contextual understanding of the range that monazite compositions can span and what the tail distributions are (to allow identification of true outliers). This is important for the language used to describe monazite in individual samples or studies. Descriptions such as 'high Th' or 'low Th' are often used for describing monazite but are only contextualised within the range of measured compositions for that study. This dataset collates monazite compositions to provide a more rounded, global understanding of, for example, what 'high' and 'low' Th monazite are. This may assist in identifying significant trends in future studies of monazite chemistry as well as assisting in the identification and explanation of outlying data. This global 'baseline' is critical if we are to understand the complex relationships between the zoning of different elements in monazite.

The challenge of understanding monazite zone morphologies and chemistries was a critical issue raised by Taylor et al. (2016), in part because of the lack of a global dataset showing monazite chemistry in a *P–T* framework. Even though zoning within an individual monazite grain can still be difficult to interpret in isolation, if enough monazite within a single sample are mapped, patterns are likely to emerge that can be understood (with reference to the global dataset) that give information about the *P–T* evolution of a sample (see also Williams 2017). Since the publication of the Taylor et al. (2016) review, several detailed, *P–T* linked monazite studies have been published which are included in the dataset here (Chapters 2 and 3; Klonowska et al., 2017; Laurent et al., 2018; Manzotti et al., 2018; Nicollet et al., 2018; Schulz, 2017; Skrzypek et al., 2017; Skrzypek et al., 2018). These studies, in addition to chapters 2 and 3, contribute invaluable data to the global dataset as they provide a detailed framework for a way to understand complex compositional zoning in monazite for studies where different metamorphic grade rocks (in a *P–T* gradient) are not exposed/preserved and therefore the zoning in monazite has to be studied more in isolation. In particular, these studies show that there are systematic patterns in the compositional zoning preserved in monazite grains, and that these correlate to changes in *P–T* (metamorphic grade). This is where the provision of a global dataset has great utility.

Thorium is not a major contributor to the modal proportion of monazite in the rock, particularly at temperatures <~550 °C (Williams et al., 2007). Therefore, it is not necessary that trends in monazite mode are linked to the availability of Th in the host rock. Changes in monazite mode are predominantly controlled by REE-in-monazite (see also Skora and Blundy, 2010; Williams et al., 2007), and the absolute amount of the Th endmembers remains relatively constant if monazite mode is not changing rapidly. It may be that the trend of increasing Th-in-monazite in samples >900 °C (Fig. 2) is, at least in part, the result of a decreasing mode of monazite without a commensurate decrease in the total amount of the Th-bearing endmembers, i.e. that cheralite and huttonite are increasingly favoured at high temperature. This is supported by laboratory experiments that show increasing $D^{Th}_{mnz/liq}$ with increasing temperature (see also Chapter 3; Stepanov et al., 2012).

4.5.2 Understanding limits to monazite stability

Monazite stability has long been argued to be a function of the bulk LREE content (e.g. Bea, 1996; Janoušek et al., 2016; Montel, 1993; Rapp et al., 1987; Watt and Harley, 1993). This has been demonstrated by modelling studies of monazite (e.g. Kelsey et al., 2008; Spear, 2010; Spear and Pyle, 2010; Yakymchuk and Brown, 2014; Yakymchuk et al., 2017; Yakymchuk et al., 2018). Yakymchuck and Brown (2018) showed that Th has an additional control on stabilising monazite to high (~850 °C for closed systems and >950 °C for open systems) temperature. The data presented here supports the contention by Yakymchuck and Brown (2018) of Th helping to stabilise monazite since there are numerous studies that report monazite in rocks recording temperatures >900–1000 °C, even though bulk Ce in those samples (where available) is 55–73 ppm, which is below the dataset average of 86 ppm (Appendix S4.2). This stabilising effect of thorium on monazite with increasing temperature is supported by the presence of monazite in UHT rocks within the dataset (Chapter 3; Goncalves et al., 2004; Laurent et al., 2018; Nicollet et al., 2018; Pauly et al., 2016; Yakymchuk et al., 2015; Zhu and O'Nions, 1999a, b). This monazite was interpreted in the original contributions to record the timing and conditions of peak (UHT) metamorphism, but the open system model in Yakymchuk and Brown (2018) is the only calculated monazite-bearing model so far which has predicted monazite to remain stable >950°C. Therefore, the available data shows that both Th-in-monazite and melt extraction have major roles to play in retaining monazite (and therefore Th) in mid to lower crustal and thermally extreme rocks.

From the distribution of monazite data in Fig. 1, there is a clear boundary to monazite stability at low temperatures, below which monazite occurrences are rare. This boundary has a positive slope (Fig. 1), starting at approximately 3 kbar, 300 °C and increasing to 600 °C (wet solidus) at 10 kbar. This monazite 'forbidden zone' to higher pressure and lower temperature likely reflects the stability of allanite and/or other LREE- and Th-bearing phases below those *P–T* conditions. Whereas the stability of both allanite and monazite are expected to change with bulk composition (Spear, 2010), this boundary effectively represents the low-temperature extreme of monazite stability. Monazite

occurrence in HP and UHP rocks is likely to be limited by the positive slope of the allanite to monazite reaction, though monazite is reported from UHP terranes (e.g. Klonowska et al., 2017).

4.5.3 Implications for heat production in metamorphic rocks

The decay of four isotopes — ^{40}K, ^{230}Th, ^{235}U and ^{238}U — accounts for the large majority of heat produced by radiogenic decay in the crust. Approximately 20% of this heat production is accounted for by K (Jaupart and Mareschal, 2005). Of the remaining 80%, Uranium contributes nearly 4 times more heat per mass unit than Th due to the fact that there are two isotopes of U which decay at faster rates than the one isotope of Th (see Bea, 2012). However, Th is approximately 4 times more abundant in average crustal rocks than U (e.g. Taylor and McLennan, 1985). The result is that Th and U have roughly equal contributions to crustal heat production in common crustal rock types (~40% each; see Bea, 2012; Jaupart and Mareschal, 2005; Taylor and McLennan, 1985; Vilà et al., 2010). High heat producing element (K, U and Th) rocks in the deep crust thermally prime the crust, making it more susceptible to later and/or long-timescale tectonic reworking (e.g. Fig. 12 in Chapter 3; Holder et al., 2018; Horton et al., 2016). Such rocks may also contribute to, or be a necessary prerequisite for, long-lived UHT events (e.g. Clark et al., 2011; Holder et al., 2018; Horton et al., 2016; Kelsey and Hand, 2015).

The constant or increasing Th-in-monazite with metamorphic grade (Fig. 2) is consistent with terrane scale studies which demonstrate that partially melted rocks retain Th (Chapter 2; Alessio et al., 2018; Andreoli et al., 2006; Bea, 2012; Horton et al., 2016; Yakymchuk and Brown, 2019). This Th retention corresponds to constant or increasing total radiogenic heat production across the amphibolite to granulite facies transition and well into the granulite facies. This change can be explained from a mineralogical point of view considering what is known about Th/U ratios in metamorphic monazite. Th/U ratios are commonly observed to increase with progressive metamorphism, driven by a decrease in U in residual rocks (see Bea and Montero, 1999; Yakymchuk and Brown, 2019). This results in Th becoming increasingly important for heat production in the deep crust, and monazite stability having a major controlling influence on regional scale heat production. (e.g. Chapters 2 and 3; Alessio et al., 2018; Foster et al., 2002; Franz et al., 1996; Rubatto et al., 2001; Schulz, 2017; Williams, 2001; Yakymchuk and Brown, 2019).

Heat producing element depletion, including of Th, in UHT rocks reported by Alessio et al. (2018) can be reconciled with the results presented here by considering monazite modal abundance trends above the solidus. Chapters 2 and 3 reveal that monazite mode increases over the interval ~ 700 to ~ 900°C, supported by available data in the literature (Foster et al., 2002; Franz et al., 1996; Kim et al., 2009; Rubatto et al., 2001; Schulz, 2017; Williams, 2001), then decreases by two orders of magnitude at higher temperatures. However, quantitative monazite modal abundance data is rare and further study of monazite mode in prograde metamorphic terranes, particularly in the granulite facies and UHT terranes would greatly assist in clarifying the relationship between monazite mode, composition, absolute *P–T* and *P–T* trajectory.

4.5.4 Development of phase equilibria models

A detailed understanding of the concentration of Th-in-monazite as a function of *P–T–X* is essential to more fully understand monazite solid solution behaviour. This has flow-on implications for avenues of research such as forward thermodynamic modelling of accessory mineral behaviour. In existing thermodynamic modelling frameworks incorporating monazite, Th is not yet featured. So far, Th is only incorporated in one study (Yakymchuk et al., 2018), external to the phase equilibria calculations via a solubility expression. The dataset herein (see also chapters 2 and 3) provides the global, *P–T* linked monazite chemical data needed to calibrate and test phase equilibrium models of monazite which include Th. In such models, replication of the trends in the fractions of both the Th endmembers, cheralite and huttonite, as well as the bulk Th-in-monazite trends presented here is critical. Thus, the understanding of the relative contributions of cheralite and huttonite discussed above is vital for the reliable calibration of such models. From the dataset, changes to Th^{4+}, p(cher) and p(hutt) have a temperature dependence, but only limited pressure dependence (Fig. 2). This is a key feature that must be replicated by future thermodynamic models. Similarly, the maxima 'saddle' that occurs particularly in p(cher) at amphibolite-facies temperatures should be replicated by such models.

New thermodynamic models for monazite in a chemical system including REEs, Y and Th would provide benefit over existing models and thermometry calculations in several ways: (1) they would allow assessment of the pressures and temperatures of monazite in garnet and/or xenotime absent rocks; (2) they would remove the ambiguity and subjectivity of identifying monazite–xenotime or monazite–garnet pairs which formed in equilibrium; and (3) they would enable better evaluation of solid solution behaviour in monazite, both in subsolidus and suprasolidus rocks. A more realistic chemical system would improve the utility of existing models and encourage their application in metamorphic studies of natural samples. Such models are presented in the following chapter (Chapter 5).

Although the focus of this discussion has been on Th-in-monazite, the dataset presented here could also be used to explore the partitioning of other elements, such as U, into monazite. The dataset collated here is provided in electronic Appendix S4.2 so that other compositional variables in monazite can be explored by the same 'big data' approach used in this study and new data can be added as it becomes available.

5 CONCLUSIONS

Th-in-monazite shows a clear increasing trend with temperature to an average maximum of 0.062 Th^{4+} cations per formula unit, based on a dataset of over 5000 monazite compositional analyses. By including monazite data from a wide range of ages, rock chemistries and *P–T* conditions we are able to view and identity global patterns that occur despite noise inherent in the natural dataset. This increase of Th-in-monazite is facilitated by the changing ratio of the two Th-bearing endmembers of monazite, cheralite and huttonite. The global dataset provides support for the observations reported in recent studies of Th-in-monazite in three prograde metamorphic terranes (Mt Stafford, the Ivrea–Verbano Zone and the Ryoke Belt), indicating that these trends do not just occur in isolated cases. The dataset also provides a framework and a 'baseline' for understanding the (often complex) compositional zoning in natural monazite. In this way we open new avenues for understanding the heat production potential of lower crustal rocks, specifically the impact that metamorphism, partial melting and melt removal has on monazite and therefore the heat production budget of the crust. By establishing a clear framework for temperature driven changes to Th-in-monazite, we pave the way for future integration of Th-in-monazite into thermodynamic models.

SUPPORTING INFORMATION

Appendix S4.1: Summary of literature included in monazite database

Appendix S4.2: monazite database (electronic appendix only)

Appendix S4.3: Alternative dataset visualisations

REFERENCES

Alessio, K.L., Hand, M., Kelsey, D.E., Williams, M.A., Morrissey, L.J., Barovich, K., 2018. Conservation of deep crustal heat production. *Geology* 46, 335 338.

Andreoli, M.A., Hart, R.J., Ashwal, L.D., Coetzee, H., 2006. Correlations between U, Th content and metamorphic grade in the western Namaqualand Belt, South Africa, with implications for radioactive heating of the crust. *Journal of Petrology* 47, 1095 1118.

Bea, F., 1996. Residence of REE, Y, Th and U in granites and crustal protoliths; implications for the chemistry of crustal melts. *Journal of Petrology* 37, 521 552.

Bea, F., 2012. The sources of energy for crustal melting and the geochemistry of heat producing elements. *Lithos* 153, 278 291.

Bea, F., Montero, P., 1999. Behavior of accessory phases and redistribution of Zr, REE, Y, Th, and U during metamorphism and partial melting of metapelites in the lower crust: an example from the Kinzigite Formation of Ivrea Verbano, NW Italy. *Geochimica Et Cosmochimica Acta* 63, 1133 1153.

Bhowmik, S., Bernhardt, H. J., Dasgupta, S., 2010. Grenvillian age high pressure upper amphibolite granulite metamorphism in the Aravalli Delhi Mobile Belt, Northwestern India: New evidence from monazite chemical age and its implication. *Precambrian Research* 178, 168 184.

Bial, J., Buettner, S.H., Schenk, V., Appel, P., 2015. The long term high temperature history of the central Namaqua Metamorphic Complex: Evidence for a Mesoproterozoic continental back arc in southern Africa. *Precambrian Research* 268, 243 278.

Bial, J., Büttner, S., Appel, P., 2016. Timing and conditions of regional metamorphism and crustal shearing in the granulite facies basement of south Namibia: Implications for the crustal evolution of the Namaqualand metamorphic basement in the Mesoproterozoic. *Journal of African Earth Sciences* 123, 145 176.

Budzyń, B., Harlov, D.E., Williams, M.L., Jercinovic, M.J., 2011. Experimental determination of stability relations between monazite, fluorapatite, allanite, and REE epidote as a function of pressure, temperature, and fluid composition. *American Mineralogist* 96, 1547 1567.

Clark, C., Fitzsimons, I.C., Healy, D., Harley, S.L., 2011. How does the continental crust get really hot? *Elements* 7, 235 240.

Dumond, G., Goncalves, P., Williams, M., Jercinovic, M., 2015. Monazite as a monitor of melting, garnet growth and feldspar recrystallization in continental lower crust. *Journal of Metamorphic Geology* 33, 735 762.

Engi, M., 2017. Petrochronology based on REE minerals: monazite, allanite, xenotime, apatite. *Reviews in Mineralogy and Geochemistry* 83, 365 418.

Finger, F., Broska, I., Roberts, M.P., Schermaier, A., 1998. Replacement of primary monazite by apatite allanite epidote coronas in an amphibolite facies granite gneiss from the eastern Alps. *American Mineralogist* 83, 248 258.

Finger, F., Helmy, H.M., 1998. Composition and total Pb model ages of monazite from high grade paragneisses in the Abu Swayel area, southern Eastern Desert, Egypt. *Mineralogy and Petrology* 62, 269 289.

Foster, G., Gibson, H., Parrish, R., Horstwood, M., Fraser, J., Tindle, A., 2002. Textural, chemical and isotopic insights into the nature and behaviour of metamorphic monazite. *Chemical Geology* 191, 183 207.

Foster, G., Kinny, P., Vance, D., Prince, C., Harris, N., 2000. The significance of monazite U Th Pb age data in metamorphic assemblages; a combined study of monazite and garnet chronometry. *Earth and Planetary Science Letters* 181, 327 340.

Franz, G., Andrehs, G., Rhede, D., 1996. Crystal chemistry of monazite and xenotime from Saxothuringian Moldanubian metapelites, NE Bavaria, Germany. *European Journal of Mineralogy* 8, 1097 1118.

Gasser, D., Bruand, E., Rubatto, D., Stüwe, K., 2012. The behaviour of monazite from greenschist facies phyllites to anatectic gneisses: an example from the Chugach Metamorphic Complex, southern Alaska. *Lithos* 134, 108 122.

Goncalves, P., Nicollet, C., Montel, J. M., 2004. Petrology and in situ U Th Pb Monazite Geochronology of Ultrahigh Temperature Metamorphism from the Andriamena Mafic Unit, North Central Madagascar. Significance of a Petrographical P T Path in a Polymetamorphic Context. *Journal of Petrology* 45, 1923 1957.

Goswami Banerjee, S., Robyr, M., 2015. Pressure and temperature conditions for crystallization of metamorphic allanite and monazite in metapelites: a case study from the Miyar Valley (high Himalayan Crystalline of Zanskar, NW India). Journal of Metamorphic *Geology* 33, 535 556.

Gratz, R., Heinrich, W., 1997. Monazite xenotime thermobarometry: Experimental calibration of the miscibility gap in the binary system $CePO_4$ YPO_4. *American Mineralogist* 82, 772 780.

Holder, R.M., Hacker, B.R., Horton, F., Rakotondrazafy, A.M., 2018. Ultrahigh temperature osumilite gneisses in southern Madagascar record combined heat advection and high rates of radiogenic heat production in a long lived high T orogen. *Journal of Metamorphic Geology* 36, 855 880.

Horton, F., Hacker, B., Kylander Clark, A., Holder, R., Jöns, N., 2016. Focused radiogenic heating of middle crust caused ultrahigh temperatures in southern Madagascar. *Tectonics* 35, 293 314.

Janots, E., Brunet, F., Goffé, B., Poinssot, C., Burchard, M., Cemič, L., 2007. Thermochemistry of monazite (La) and dissakisite (La): implications for monazite and allanite stability in metapelites. *Contributions to Mineralogy and Petrology* 154, 1 14.

Janots, E., Engi, M., Berger, A., Allaz, J., Schwarz, J.O., Spandler, C., 2008. Prograde metamorphic sequence of REE minerals in pelitic rocks of the Central Alps: implications for allanite monazite xenotime phase relations from 250 to 610 C. *Journal of Metamorphic Geology* 26, 509 526.

Janoušek, V., Moyen, J. F., Martin, H., Erban, V., Farrow, C., 2016. Trace Elements as Essential Structural Constituents of Accessory Minerals: The Solubility Concept, *Geochemical Modelling of Igneous Processes Principles And Recipes in R Language*. Springer, pp. 129 140.

Jaupart, C., Mareschal, J., 2005. Constraints on heat production from heat flow data, *Treatise on Geochemistry*, vol. 3, 65 84. in: *The Crust*, edited by R. Rudnick. Elsevier Sci., New York.

Kelly, N.M., Clarke, G.L., Harley, S.L., 2006. Monazite behaviour and age significance in poly metamorphic high grade terrains: a case study from the western Musgrave Block, central Australia. *Lithos* 88, 100 134.

Kelly, N.M., Harley, S.L., Möller, A., 2012. Complexity in the behavior and recrystallization of monazite during high T metamorphism and fluid infiltration. *Chemical Geology* 322, 192 208.

Kelsey, D.E., Clark, C., Hand, M., 2008. Thermobarometric modelling of zircon and monazite growth in melt bearing systems: Examples using model metapelitic and metapsammitic granulites. *Journal of Metamorphic Geology* 26, 199 212.

Kelsey, D.E., Hand, M., 2015. On ultrahigh temperature crustal metamorphism: Phase equilibria, trace element thermometry, bulk composition, heat sources, timescales and tectonic settings. *Geoscience Frontiers* 6, 311 356.

Kim, Y., Yi, K., Cho, M., 2009. Parageneses and Th U distributions among allanite, monazite, and xenotime in Barrovian type metapelites, Imjingang belt, central Korea. *American Mineralogist* 94, 430 438.

Kingsbury, J.A., Miller, C.F., Wooden, J.L., Harrison, T.M., 1993. Monazite paragenesis and U Pb systematics in rocks of the eastern Mojave Desert, California, USA: implications for thermochronometry. *Chemical Geology* 110, 147 167.

Klonowska, I., Janák, M., Majka, J., Petrik, I., Froitzheim, N., Gee, D.G., Sasinková, V., 2017. Microdiamond on Åreskutan confirms regional UHP metamorphism in the Seve Nappe Complex of the Scandinavian Caledonides. *Journal of Metamorphic Geology* 35, 541 564.

Kohn, M., Wieland, M., Parkinson, C., Upreti, B., 2005. Five generations of monazite in Langtang gneisses: implications for chronology of the Himalayan metamorphic core. *Journal of Metamorphic Geology* 23, 399 406.

Kohn, M.J., Malloy, M.A., 2004. Formation of monazite via prograde metamorphic reactions among common silicates: implications for age determinations. *Geochimica Et Cosmochimica Acta* 68, 101 113.

Laurent, A.T., Duchene, S., Bingen, B., Bosse, V., Seydoux Guillaume, A.M., 2018. Two successive phases of ultrahigh temperature metamorphism in Rogaland, S. Norway: evidence from Y in monazite thermometry. *Journal of Metamorphic Geology* 36, 1009 1037.

Manzotti, P., Bosse, V., Pitra, P., Robyr, M., Schiavi, F., Ballèvre, M., 2018. Exhumation rates in the Gran Paradiso Massif (Western Alps) constrained by in situ U Th Pb dating of accessory phases (monazite, allanite and xenotime). *Contributions to Mineralogy and Petrology* 173, 24.

Martins, L., Vlach, S.R.F., de Assis Janasi, V., 2009. Reaction microtextures of monazite: correlation between chemical and age domains in the Nazaré Paulista migmatite, SE Brazil. *Chemical Geology* 261, 271 285.

Montel, J. M., 1993. A model for monazite/melt equilibrium and application to the generation of granitic magmas. *Chemical Geology* 110, 127 146.

Nagy, G., Draganits, E., Demény, A., Pantó, G., Arkai, P., 2002. Genesis and transformations of monazite, florencite and rhabdophane during medium grade metamorphism: examples from the Sopron Hills, Eastern Alps. *Chemical Geology* 191, 25 46.

Nemchin, A.A., Giannini, L.M., Bodorkos, S., Oliver,

N.H.S., 2001. Ostwald ripening as a possible mechanism for zircon overgrowth formation during anatexis: theoretical constraints, a numerical model, and its application to pelitic migmatites of the Tickalara Metamorphics, northwestern Australia. *Geochimica Et Cosmochimica Acta* 65, 2771 2788.

Nicollet, C., Bosse, V., Spalla, M.I., Schiavi, F., 2018. Eocene ultra high temperature (UHT) metamorphism in the gruf complex (Central Alps): constraints by LA ICPMS zircon and monazite dating in petrographic context. *Journal of the Geological Society*, jgs2018 2017.

Overstreet, W.C., 1967. The geologic occurrence of monazite. 530, *US Geological Survey Professional Paper 530*.

Pauly, J., Marschall, H.R., Meyer, H. P., Chatterjee, N., Monteleone, B., 2016. Prolonged Ediacaran Cambrian metamorphic history and short lived high pressure granulite facies metamorphism in the HU Sverdrupfjella, Dronning Maud Land (East Antarctica): evidence for continental collision during Gondwana assembly. *Journal of Petrology* 57, 185 228.

Pyle, J.M., Spear, F.S., 2003. Four generations of accessory phase growth in low pressure migmatites from SW New Hampshire. *American Mineralogist* 88, 338 351.

Pyle, J.M., Spear, F.S., Rudnick, R.L., McDonough, W.F., 2001. Monazite xenotime garnet equilibrium in metapelites and a new monazite garnet thermometer. *Journal of Petrology* 42, 2083 2107.

Rapp, R.P., Ryerson, F., Miller, C.F., 1987. Experimental evidence bearing on the stability of monazite during crustal anatexis. *Geophysical Research Letters* 14, 307 310.

Rasmussen, B., Muhling, J.R., 2007. Monazite begets monazite: evidence for dissolution of detrital monazite and reprecipitation of syntectonic monazite during low grade regional metamorphism. *Contributions to Mineralogy and Petrology* 154, 675 689.

Redler, C., White, R.W., Johnson, T.E., 2013. Migmatites in the Ivrea Zone (NW Italy): Constraints on partial melting and melt loss in metasedimentary rocks from Val Strona di Omegna. *Lithos* 175, 40 53.

Rubatto, D., Williams, I.S., Buick, I.S., 2001. Zircon and monazite response to prograde metamorphism in the Reynolds Range, central Australia. *Contributions to Mineralogy and Petrology* 140, 458 468.

Schulz, B., 2017. Polymetamorphism in garnet micaschists of the Saualpe Eclogite Unit (Eastern Alps, Austria), resolved by automated SEM methods and EMP Th U Pb monazite dating. *Journal of Metamorphic Geology* 35, 141 163.

Seydoux Guillaume, A. M., Wirth, R., Heinrich, W., Montel, J. M., 2002. Experimental determination of thorium partitioning between monazite and xenotime using analytical electron microscopy and X ray diffraction Rietveld analysis. *European Journal of Mineralogy* 14, 869 878.

Seydoux, A., Montel, J., 1997. Experimental determination of the thorite huttonite phase transition. *Terra Nova* 9, 421.

Skora, S., Blundy, J., 2010. High pressure hydrous phase relations of radiolarian clay and implications for the involvement of subducted sediment in arc magmatism. *Journal of Petrology* 51, 2211 2243.

Skrzypek, E., Bosse, V., Kawakami, T., Martelat, J. E., Štípská, P., 2017. Transient allanite replacement and prograde to retrograde monazite (re) crystallization in medium grade metasedimentary rocks from the Orlica Śnieżnik Dome (Czech Republic/Poland): Textural and geochronological arguments. *Chemical Geology* 449, 41 57.

Skrzypek, E., Kato, T., Kawakami, T., Sakata, S., Hattori, K., Hirata, T., Ikeda, T., 2018. Monazite behaviour and time scale of metamorphic processes along a low pressure/high temperature field gradient (Ryoke belt, SW Japan). *Journal of Petrology* 59, 1109 1144.

Spear, F.S., 2010. Monazite allanite phase relations in metapelites. *Chemical Geology* 279, 55 62.

Spear, F.S., Pyle, J.M., 2010. Theoretical modeling of monazite growth in a low Ca metapelite. *Chemical Geology* 273, 111 119.

Stepanov, A.S., Hermann, J., Rubatto, D., Rapp, R.P., 2012. Experimental study of monazite/melt partitioning with implications for the REE, Th and U geochemistry of crustal rocks. *Chemical Geology* 300, 200 220.

Taylor, R.J.M., Kirkland, C.L., Clark, C., 2016. Accessories after the facts: Constraining the timing, duration and conditions of high temperature metamorphic processes. *Lithos* 264, 239 257.

Taylor, S.R., McLennan, S.M., 1985. The continental crust: its composition and evolution.

Vavra, G., Gebauer, D., Schmid, R., Compston, W., 1996. Multiple zircon growth and recrystallization during polyphase Late Carboniferous to Triassic metamorphism in granulites of the Ivrea Zone (Southern Alps): an ion microprobe (SHRIMP) study. *Contributions to Mineralogy and Petrology* 122, 337 358.

Vilà, M., Fernández, M., Jiménez Munt, I., 2010. Radiogenic heat production variability of some common lithological groups and its significance to lithospheric thermal modeling. *Tectonophysics* 490, 152 164.

Watt, G.R., Harley, S., 1993. Accessory phase controls on the geochemistry of crustal melts and restites produced during water undersaturated partial melting. *Contributions to Mineralogy and Petrology* 114, 550 566.

Wawrzenitz, N., Krohe, A., Rhede, D., Romer, R.L., 2012. Dating rock deformation with monazite: The impact of dissolution precipitation creep. *Lithos* 134, 52 74.

White, R.W., Powell, R., Clarke, G.L., 2003. Prograde metamorphic assemblage evolution during partial melting of metasedimentary rocks at low pressures: migmatites from Mt Stafford, Central Australia. *Journal of Petrology* 44, 1937 1960.

Williams, I., 2001. Response of detrital zircon and monazite, and their U Pb isotopic systems, to regional metamorphism and host rock partial melting, Cooma Complex, southeastern Australia. *Australian Journal of Earth Sciences* 48, 557 580.

Williams, M.L., Jercinovic, M.J., Hetherington, C.J., 2007. Microprobe monazite geochronology: understanding geologic processes by integrating composition and chronology. *Annual Review of Earth and Planetary Sciences* 35, 137.

Williams, M.L., Jercinovic, M.J., Mahan, K.H., Dumond, G., 2017. Electron microprobe petrochronology. *Reviews in Mineralogy and Geochemistry* 83, 153 182.

Yakymchuk, C., 2017. Behaviour of apatite during partial melting of metapelites and consequences for prograde suprasolidus monazite growth. *Lithos* 274, 412 426.

Yakymchuk, C., Brown, M., 2019. Divergent behaviour of Th and U during anatexis: Implications for the thermal evolution of orogenic crust. *Journal of Metamorphic Geology*. 37, 899 916.

Yakymchuk, C., Brown, M., Clark, C., Korhonen, F., Piccoli, P., Siddoway, C., Taylor, R., Vervoort, J., 2015. Decoding polyphase migmatites using geochronology and phase equilibria modelling. *Journal of Metamorphic Geology* 33, 203 230.

Yakymchuk, C., Kirkland, C.L., Clark, C., 2018. Th/U ratios in metamorphic zircon. *Journal of Metamorphic Geology* 36,

715 737.

Zhu, X., O'Nions, R., 1999a. Monazite chemical composition: some implications for monazite geochronology. *Contributions to Mineralogy and Petrology* 137, 351 363.

Zhu, X., O'Nions, R., 1999b. Zonation of monazite in metamorphic rocks and its implications for high temperature thermochronology: a case study from the Lewisian terrain. *Earth and Planetary Science Letters* 171, 209 220.

Supporting information

APPENDIX S4.1: SUMMARY OF LITERATURE INCLUDED IN MONAZITE DATABASE

Monazite data within the dataset have been obtained from the following data sources. Any whole rock chemistry, mineral proportions and P–T conditions were obtained from the original source unless otherwise specified. # denotes the source number, defined in alphabetical order; Number of monazite analyses (no. mnz analyses) presented as XX/YY, where XX is the number of 'ok' analyses and YY is the total number of analyses. Analyses are judged to be 'poor' if (Th + U) – (Ca + Si) <–0.05 **or** |(P+Si+S) – (REE+Y+Th+U+Ca)| > 0.15; ^ indicates that this information is only included for some analyses.

Table S4.1.1. Monazite data sources.

#	Source reference	Terrane	no. mnz analyses	no. samples	P-T	Chem	TE	Min. prop	Age	P–T source
1	Alessio, K L , pers comm	Reynolds Range, central Australia	310/319	8	x	x^	x^			
2	Allaz, J , Selleck, B , Williams, M L , & Jercinovic, M J (2013) Microprobe analysis and dating of monazite from the Potsdam Formation, New York: A progressive record of chemical reaction and fluid interaction *American Mineralogist,* 98(7), 1106-1119	Potsdam Fm , New York, USA	66/67	9	x				x	
3	Berry, R F , Chmielowski, R M , Steele, D , & Meffre, S (2007) Chemical U–Th–Pb monazite dating of the Cambrian Tyennan Orogeny, Tasmania *Australian Journal of Earth Sciences,* 54(5), 757-771	Vars western Tasmania, Australia	370/372	10	x				x	Chmielowski R M (2009) The Cambrian Metamorphic History of Tasmania, *University of Tasmania PhD Thesis*, supplied by R M Chmielowski; Meffre, S , Berry, R F , and Hall, M (2000) Cambrian metamorphic complexes in Tasmania: tectonic implications *Australian Journal of Earth Sciences,* 47(6), 971-985
4	Bhowmik, S , Bernhardt, H -J , & Dasgupta, S (2010) Grenvillian age high-pressure upper amphibolite-granulite metamorphism in the Aravalli-Delhi Mobile Belt, Northwestern India: New evidence from monazite chemical age and its implication *Precambrian Research,* 178(1-4), 168-184	Aravalli-Delhi Mobile Belt, NW India	81/143	5	x					Bhowamik et al (2010), Saha, L , Bhowmik, S , Fukuoka, M , & Dasgupta, S (2007) Contrasting episodes of regional granulite-facies metamorphism in enclaves and host gneisses from the Aravalli–Delhi mobile belt, NW India *Journal of Petrology,* 49(1), 107-128
5	Bial, J , Buettner, S H , Schenk, V , & Appel, P (2015) The long-term high-temperature history of the central Namaqua Metamorphic Complex: Evidence for a Mesoproterozoic continental back-arc in southern Africa *Precambrian Research,* 268, 243-278	Namaqua Metamorphic Complex, southern Africa	12/12	4	x	x^			x	
6	Bial, J , Büttner, S , & Appel, P (2016) Timing and conditions of regional metamorphism and crustal shearing in the granulite facies basement of south Namibia: Implications for the crustal evolution of the Namaqualand metamorphic basement in the Mesoproterozoic *Journal of African Earth Sciences,* 123, 145-176	Namaqua Metamorphic Complex, Namibia	17/17	5	x	x^	x^ (Ce only)		x	
7	Cabella, R , Lucchetti, G , & Marescotti, P (2001) Authigenic monazite and xenotime from pelitic metacherts in pumpellyite–actinolite-facies conditions, Sestri–Voltaggio Zone, central Liguria, Italy *The Canadian Mineralogist,* 39(3), 717-727	Sestri–Voltaggio Zone, NW Italy	15/15	1	x					

#	Source reference	Terrane	no. mnz analyses	no. samples	P-T	Chem	TE	Min. prop	Age	P–T source
8	Clarke, G., Bhowmik, S., Ireland, T., Aitchison, J., Chapman, S., & Kent, L. (2016). Inverted Oligo miocene metamorphism in the Lesser Himalaya Sequence, Arunachal Pradesh, India; age and grade relationships. *Journal of Metamorphic Geology,* 34(8), 805-820.	Arunachal Pradesh, NW India	8/8	4	x					
9	Corrie, S. L., & Kohn, M. J. (2008). Trace element distributions in silicates during prograde metamorphic reactions: Implications for monazite formation. *Journal of Metamorphic Geology,* 26(4), 451-464.	Great Smoky Mountains National Park, Tennessee, USA	14/15	1	x					
10	Daniel, C. G., & Pyle, J. M. (2005). Monazite–xenotime thermochronometry and Al2SiO5 reaction textures in the Picuris Range, Northern New Mexico, USA: New evidence for a 1450–1400 Ma orogenic event. *Journal of Petrology,* 47(1), 97-118.	Picuris Range, New Mexico, USA	87/87	5	x					
11	Faleiros, F. M , da Cruz Campanha, G. A., Martins, L., Vlach, S. R. F., & Vasconcelos, P. M. (2011). Ediacaran high-pressure collision metamorphism and tectonics of the southern Ribeira Belt (SE Brazil): evidence for terrane accretion and dispersion during Gondwana assembly. *Precambrian Research,* 189(3-4), 263-291.	Ribeira Belt, SE Brazil	57/58	2	x	x	x		x	
12	Finger, F., Broska, I., Roberts, M. P., & Schermaier, A. (1998). Replacement of primary monazite by apatite-allanite-epidote coronas in an amphibolite facies granite gneiss from the eastern Alps. *American Mineralogist,* 83(3-4), 248-258.	Tauern Window, eastern Alps, Austria	6/6	1	x					
13	Finger, F., & Helmy, H. M. (1998). Composition and total-Pb model ages of monazite from high-grade paragneisses in the Abu Swayel area, southern Eastern Desert, Egypt. *Mineralogy and Petrology,* 62(3-4), 269-289.	Abu Swayel Crystalline Complex, Arabian-Nubian shield, Egypt	19/19	2	x					
14	Foster, G., Kinny, P., Vance, D., Prince, C., & Harris, N. (2000). The significance of monazite U–Th–Pb age data in metamorphic assemblages; a combined study of monazite and garnet chronometry. *Earth and Planetary Science Letters,* 181(3), 327-340.	Garhwal region, central Himalaya India; Nanga Parbat Haramosh Massif, Pakistan	206/213	3	x	x (No P)				

#	Source reference	Terrane	no. mnz analyses	no. samples	P-T	Chem	TE	Min. prop	Age	P–T source
15	Foster, G., Gibson, H., Parrish, R., Horstwood, M., Fraser, J., & Tindle, A. (2002). Textural, chemical and isotopic insights into the nature and behaviour of metamorphic monazite. *Chemical Geology,* 191(1-3), 183-207.	southern Canadian Cordillera, Canada; Himalaya, Pakistan	15/16	4	x	x	x^	x		Fraser, James E., et al. (2001).Chronology of deformation, metamorphism, and magmatism in the southern Karakoram Mountains. *Geological Society of America Bulletin* 113(11), 1443-1455.; Gibson, H. Daniel, Richard L. Brown, and Randall R. Parrish. (1999) Deformation-induced inverted metamorphic field gradients: an example from the southeastern Canadian Cordillera. *Journal of Structural Geology* 21(7), 751-767.
16	Foster, G., & Parrish, R.R. (2003). Metamorphic monazite and the generation of P–T–t paths. *Geological Society, London, Special Publications,* 220(1), 25-47.	Himalaya, Pakistan	39/39	3	x	x	x^	x^		Fraser, James E., et al. (2001).Chronology of deformation, metamorphism, and magmatism in the southern Karakoram Mountains. *Geological Society of America Bulletin* 113(11), 1443-1455.
17	Franz, G., Andrehs, G., & Rhede, D. (1996). Crystal chemistry of monazite and xenotime from Saxothuringian-Moldanubian metapelites, NE Bavaria, Germany. *European Journal of Mineralogy,* 8(5), 1097-1118.	Saxothuringian-Moldanubian Zones, Bavaria, Germany	12/12	4	x	x	x (No Th)			
18	Gasser, D., Bruand, E., Rubatto, D , & Stüwe, K. (2012). The behaviour of monazite from greenschist facies phyllites to anatectic gneisses: an example from the Chugach Metamorphic Complex, southern Alaska. *Lithos,* 134, 108-122.	Chugach Metamorphic Complex, Alaska, USA	20/20	2	x	x				
19	Goncalves, P., Pers. comm.	Andriamena, North-Central Madagascar	907/921	12	x				x^	Goncalves, P., Nicollet, C., & Montel, J.-M. (2004). Petrology and in situ U–Th–Pb Monazite Geochronology of Ultrahigh-Temperature Metamorphism from the Andriamena Mafic Unit, North–Central Madagascar. Significance of a Petrographical P–T Path in a Polymetamorphic Context. *Journal of Petrology,* 45(10), 1923-1957 ; Goncalves, P., Nicollet, C., & Lardeaux, J. M. (2003). Finite strain pattern in Andriamena unit (north-central Madagascar): evidence for late Neoproterozoic–Cambrian thrusting during continental convergence. *Precambrian Research*, 123(2-4), 135-157.; Paquette, J. L., Goncalves, P., Devouard, B., & Nicollet, C. (2004). Micro-drilling ID-TIMS U-Pb dating of single monazites: A new method to unravel complex poly-metamorphic evolutions. Application to the UHT granulites of Andriamena (North-Central Madagascar). *Contributions to Mineralogy and Petrology*, 147(1), 110-122.

#	Source reference	Terrane	no. mnz analyses	no. samples	P-T	Chem	TE	Min. prop	Age	P–T source
20	Janots, E , Engi, M , Berger, A , Allaz, J , Schwarz, J O , & Spandler, C (2008) Prograde metamorphic sequence of REE minerals in pelitic rocks of the Central Alps: implications for allanite–monazite–xenotime phase relations from 250 to 610 C *Journal of Metamorphic Geology,* 26(5), 509-526	Lepontine domain, central Alps, Switzerland	28/30	5	x	x	x (no Th)			
21	Kelly, N M , Clarke, G L , & Harley, S L (2006) Monazite behaviour and age significance in poly-metamorphic high-grade terrains: a case study from the western Musgrave Block, central Australia *Lithos,* 88(1), 100-134	Musgrave Block, central Australia	25/25	4	x					
22	Kelly, N M , Harley, S L , & Möller, A (2012) Complexity in the behavior and recrystallization of monazite during high-T metamorphism and fluid infiltration *Chemical Geology,* 322, 192-208	Oygarden Islands, east Antarctica	10/10	4	x					Kelly, N M , & Harley, S L (2004) Orthopyroxene–corundum in Mg–Al-rich granulites from the Oygarden Islands, east Antarctica *Journal of Petrology*, 45(7), 1481-1512
23	Kim, Y , Yi, K , & Cho, M (2009) Parageneses and Th-U distributions among allanite, monazite, and xenotime in Barrovian-type metapelites, Imjingang belt, central Korea *American Mineralogist,* 94(4), 430-438	Imjingang belt, central Korea	7/7	3	x					
24	Kingsbury, J A , Miller, C F , Wooden, J L , & Harrison, T M (1993) Monazite paragenesis and U-Pb systematics in rocks of the eastern Mojave Desert, California, USA: implications for thermochronometry *Chemical Geology,* 110(1), 147-167	Mojave Desert, California, USA	8/9	3	x	x	x			
25	Klonowska, I , Janák, M , Majka, J , Petrik, I , Froitzheim, N , Gee, D G , & Sasinková, V (2017) Microdiamond on Åreskutan confirms regional UHP metamorphism in the Seve Nappe Complex of the Scandinavian Caledonides *Journal of Metamorphic Geology,* 35(5), 541-564 https://doi org/10 1111/jmg 12244	Seve Nappe Complex, Scandinavian Caledonides, Sweden	14/15	3	x	x^ (Al & Ca only)			x	
26	Kohn, M , Wieland, M , Parkinson, C , & Upreti, B (2005) Five generations of monazite in Langtang gneisses: implications for chronology of the Himalayan metamorphic core *Journal of Metamorphic Geology,* 23(5), 399-406 https://doi org/10 1111/j 1525-1314 2005 00584 x	Langtang gneisses, Himalaya, Nepal	54/54	12	x					
27	Laurent, A T , Duchene, S , Bingen, B , Bosse, V , & Seydoux Guillaume, A M (2018) Two successive phases of ultrahigh temperature metamorphism in Rogaland, S Norway: evidence from Y in monazite thermometry *Journal of Metamorphic Geology,* 36(8), 1009-1037 https://doi org/10 1111/jmg 12425	Rogaland, southern Norway	239/241	8	x	x^ (no P)			x^	

#	Source reference	Terrane	no. mnz analyses	no. samples	P-T	Chem	TE	Min. prop	Age	P–T source
28	Lo Pò, D , Braga, R., Massonne, H. J., Molli, G., Montanini, A., & Theye, T. (2016). Fluid induced breakdown of monazite in medium grade metasedimentary rocks of the Pontremoli basement (Northern Apennines, Italy). *Journal of Metamorphic Geology,* 34(1), 63-84. https://doi.org/10 1111/jmg.12171	Pontremoli basement, Northern Apennines, Italy	11/12	1	x	x (no Si, no P)			x^	
29	Manzotti, P., Bosse, V., Pitra, P., Robyr, M., Schiavi, F., & Ballèvre, M. (2018). Exhumation rates in the Gran Paradiso Massif (Western Alps) constrained by in situ U–Th–Pb dating of accessory phases (monazite, allanite and xenotime). *Contributions to Mineralogy and Petrology,* 173(3), 24. https://doi.org/10.1007/s00410-018-1452-7	Gran Paradiso Massif, western Alps, Italy	21/21	3	x	x (No Si)	x			
30	Martins, L., Vlach, S. R. F., & de Assis Janasi, V. (2009). Reaction microtextures of monazite: correlation between chemical and age domains in the Nazaré Paulista migmatite, SE Brazil. *Chemical Geology,* 261(3-4), 271-285. https://doi.org/10 1016/j.chemgeo.2008.09.020	Nazaré Paulista migmatite, SE Brazil	235/235	10	x					
31	Nicollet, C., Bosse, V., Spalla, M. I., & Schiavi, F. (2018). Eocene ultra high temperature (UHT) metamorphism in the gruf complex (Central Alps): constraints by LA-ICPMS zircon and monazite dating in petrographic context. *Journal of the Geological Society*, 175, 774-787. https://doi.org/10.1144/jgs2018-017	Gruf Complex, central Alps, NW Italy	20/20	10	x					
32	Palin, R., Searle, M., St-Onge, M., Waters, D., Roberts, N., Horstwood, M., . . . Yang, J. (2014). Monazite geochronology and petrology of kyanite-and sillimanite-grade migmatites from the northwestern flank of the eastern Himalayan syntaxis. *Gondwana Research,* 26(1), 323-347. http://dx.doi.org/10.1016/j.gr.2013.06.022	Lhasa Block, eastern Himalaya, Tibet	37/37	5	x				x	
33	Palin, R., Searle, M., Waters, D., Horstwood, M., & Parrish, R. (2012). Combined thermobarometry and geochronology of peraluminous metapelites from the Karakoram metamorphic complex, North Pakistan; New insight into the tectonothermal evolution of the Baltoro and Hunza Valley regions. *Journal of Metamorphic Geology,* 30(8), 793-820. https://doi.org/10.1111/j.1525-1314.2012.00999.x	Karakoram metamorphic complex, North Pakistan	22/24	2	x				x	

#	Source reference	Terrane	no. mnz analyses	no. samples	P-T	Chem	TE	Min. prop	Age	P–T source
20	Janots, E., Engi, M., Berger, A., Allaz, J , Schwarz, J. O., & Spandler, C. (2008). Prograde metamorphic sequence of REE minerals in pelitic rocks of the Central Alps: implications for allanite–monazite–xenotime phase relations from 250 to 610 C. *Journal of Metamorphic Geology,* 26(5), 509-526.	Lepontine domain, central Alps, Switzerland	28/30	5	x	x	x (no Th)			
21	Kelly, N. M., Clarke, G. L., & Harley, S. L. (2006). Monazite behaviour and age significance in poly-metamorphic high-grade terrains: a case study from the western Musgrave Block, central Australia. *Lithos,* 88(1), 100-134.	Musgrave Block, central Australia	25/25	4	x					
22	Kelly, N. M., Harley, S. L , & Möller, A. (2012). Complexity in the behavior and recrystallization of monazite during high-T metamorphism and fluid infiltration. *Chemical Geology,* 322, 192-208.	Oygarden Islands, east Antarctica	10/10	4	x					Kelly, N. M., & Harley, S. L. (2004). Orthopyroxene–corundum in Mg–Al-rich granulites from the Oygarden Islands, east Antarctica. *Journal of Petrology*, 45(7), 1481-1512.
23	Kim, Y., Yi, K , & Cho, M. (2009). Parageneses and Th-U distributions among allanite, monazite, and xenotime in Barrovian-type metapelites, Imjingang belt, central Korea. *American Mineralogist,* 94(4), 430-438.	Imjingang belt, central Korea	7/7	3	x					
24	Kingsbury, J. A., Miller, C. F., Wooden, J. L., & Harrison, T. M. (1993). Monazite paragenesis and U-Pb systematics in rocks of the eastern Mojave Desert, California, USA: implications for thermochronometry. *Chemical Geology,* 110(1), 147-167.	Mojave Desert, California, USA	8/9	3	x	x	x			
25	Klonowska, I., Janák, M , Majka, J., Petrik, I., Froitzheim, N , Gee, D. G., & Sasinková, V. (2017). Microdiamond on Åreskutan confirms regional UHP metamorphism in the Seve Nappe Complex of the Scandinavian Caledonides. *Journal of Metamorphic Geology,* 35(5), 541-564. https://doi.org/10.1111/jmg.12244	Seve Nappe Complex, Scandinavian Caledonides, Sweden	14/15	3	x	x^ (Al & Ca only)			x	
26	Kohn, M., Wieland, M , Parkinson, C., & Upreti, B. (2005). Five generations of monazite in Langtang gneisses: implications for chronology of the Himalayan metamorphic core. *Journal of Metamorphic Geology,* 23(5), 399-406. https://doi.org/10.1111/j.1525-1314 2005.00584.x	Langtang gneisses, Himalaya, Nepal	54/54	12	x					
27	Laurent, A. T , Duchene, S., Bingen, B., Bosse, V., & Seydoux Guillaume, A. M. (2018). Two successive phases of ultrahigh temperature metamorphism in Rogaland, S. Norway: evidence from Y in monazite thermometry. *Journal of Metamorphic Geology,* 36(8), 1009-1037. https://doi.org/10.1111/jmg.12425	Rogaland, southern Norway	239/241	8	x	x^ (no P)			x^	

#	Source reference	Terrane	no. mnz analyses	no. samples	P-T	Chem	TE	Min. prop	Age	P–T source
39	Schulz, B (2017) Polymetamorphism in garnet micaschists of the Saualpe Eclogite Unit (Eastern Alps, Austria), resolved by automated SEM methods and EMP–Th–U–Pb monazite dating *Journal of Metamorphic Geology,* 35(2), 141-163 https://doi org/10 1111/jmg 12224	Saualpe Eclogite Unit, eastern Alps, Austria	610/628	11	x			x^ (mnz & xtm only)		
40	Skrzypek, E , Bosse, V , Kawakami, T , Martelat, J -E , & Štípská, P (2017) Transient allanite replacement and prograde to retrograde monazite (re) crystallization in medium-grade metasedimentary rocks from the Orlica-Śnieżnik Dome (Czech Republic/Poland): Textural and geochronological arguments *Chemical Geology,* 449, 41-57 https://doi org/10 1016/j chemgeo 2016 11 033	Orlica-Śnieżnik Dome, Czech Republic/Poland	190/190	3	x				x	
41	F Spear, pers comm	Big Staurolite Nappe, eastern Vermont, USA	139/145	5	x					Spear, F S , Kohn, M J , Cheney, J T , & Florence, F (2002) Metamorphic, Thermal, and Tectonic Evolution of Central New England *Journal of Petrology,* 43(11), 2097-2120 https://doi org/10 1093/petrology/43 11 2097 Spear, F , Cheney, J , Pyle, J , Harrison, T , & Layne, G (2008) Monazite geochronology in central New England: evidence for a fundamental terrane boundary *Journal of Metamorphic Geology,* 26(3), 317-329 https://doi org/10 1111/j 1525-1314 2007 00751 x
42	Suzuki, K , & Adachi, M (1994) Middle Precambrian detrital monazite and zircon from the Hida gneiss on Oki-Dogo Island, Japan: their origin and implications for the correlation of basement gneiss of Southwest Japan and Korea *Tectonophysics,* 235(3), 277-292 https://doi org/10 1016/0040-1951(94)90198-8	Oki-Dogo Island, Japan	7/7	2	x					
43	Tomkins, H , & Pattison, D (2007) Accessory phase petrogenesis in relation to major phase assemblages in pelites from the Nelson contact aureole, southern British Columbia *Journal of Metamorphic Geology,* 25(4), 401-421 https://doi org/10 1111/j 1525-1314 2007 00702 x	Nelson contact aureole, southern British Columbia, Canada	13/15	15	x		x^ (Y only)			
44	**CHAPTER 2** Williams, M A , Kelsey, D E , Baggs, T , Hand, M , & Alessio, K L (2018) Thorium distribution in the crust: Outcrop and grain-scale perspectives *Lithos,* 320-321, 222-235 https://doi org/10 1016/j lithos 2018 09 016	Mt Stafford, Central Australia	208/214	10	x	x	x	x		

#	Source reference	Terrane	no. mnz analyses	no. samples	P-T	Chem	TE	Min. prop	Age	P–T source
45	**CHAPTER 3** Williams, M. A., Kelsey, D. E., & Rubatto, D. (Submitted). Thorium zoning in monazite: a case study from the Ivrea–Verbano Zone, NW Italy.	Ivrea–Verbano Zone	257/257	7	x	x	x	x		
46	Williams, unpublished data	Ivrea–Verbano Zone, NW Italy; Mt Stafford, central Australia	245/250	30	x	x	x	x		**CHAPTER 2** Williams, M. A., Kelsey, D. E., Baggs, T., Hand, M., & Alessio, K. L. (2018). Thorium distribution in the crust: Outcrop and grain-scale perspectives. *Lithos,* 320-321, 222-235. https://doi.org/10.1016/j.lithos.2018.09.016; **CHAPTER 3** Williams, M. A., Kelsey, D. E., & Rubatto, D. (Submitted and reviewed). Thorium zoning in monazite: a case study from the Ivrea–Verbano Zone, NW Italy.
47	Yakymchuk, C., Brown, M., Clark, C., Korhonen, F., Piccoli, P., Siddoway, C , . . . Vervoort, J. (2015). Decoding polyphase migmatites using geochronology and phase equilibria modelling. *Journal of Metamorphic Geology,* 33(2), 203-230. https://doi.org/10.1111/jmg.12117	Fosdick mountains, west Antarctica	212/214	19	x	x^	x^		x	
48	Zhu, X., & O'Nions, R. (1999). Zonation of monazite in metamorphic rocks and its implications for high temperature thermochronology: a case study from the Lewisian terrain. Earth and Planetary Science Letters, 171(2), 209-220. https://doi.org/10.1016/S0012-821X(99)00146-6	Lewisian terrain, Scourie, NW Scotland	8/32	2	x					
49	Zhu, X., & O'Nions, R. (1999). Monazite chemical composition: some implications for monazite geochronology. *Contributions to Mineralogy and Petrology,* 137(4), 351-363. https://doi.org/10.1007/s004100050555	Lewisian terrain, Scourie, NW Scotland	51/53	2	x					^ Boak, J. L., & Dymek, R. F. (1982). Metamorphism of the ca. 3800 Ma supracrustal rocks at Isua, West Greenland: implications for early Archaean crustal evolution. *Earth and Planetary Science Letters,* 59(1), 155-176. https://doi.org/10.1016/0012-821X(82)90123-6

APPENDIX S4.3: ALTERNATIVE DATASET VISUALISATIONS

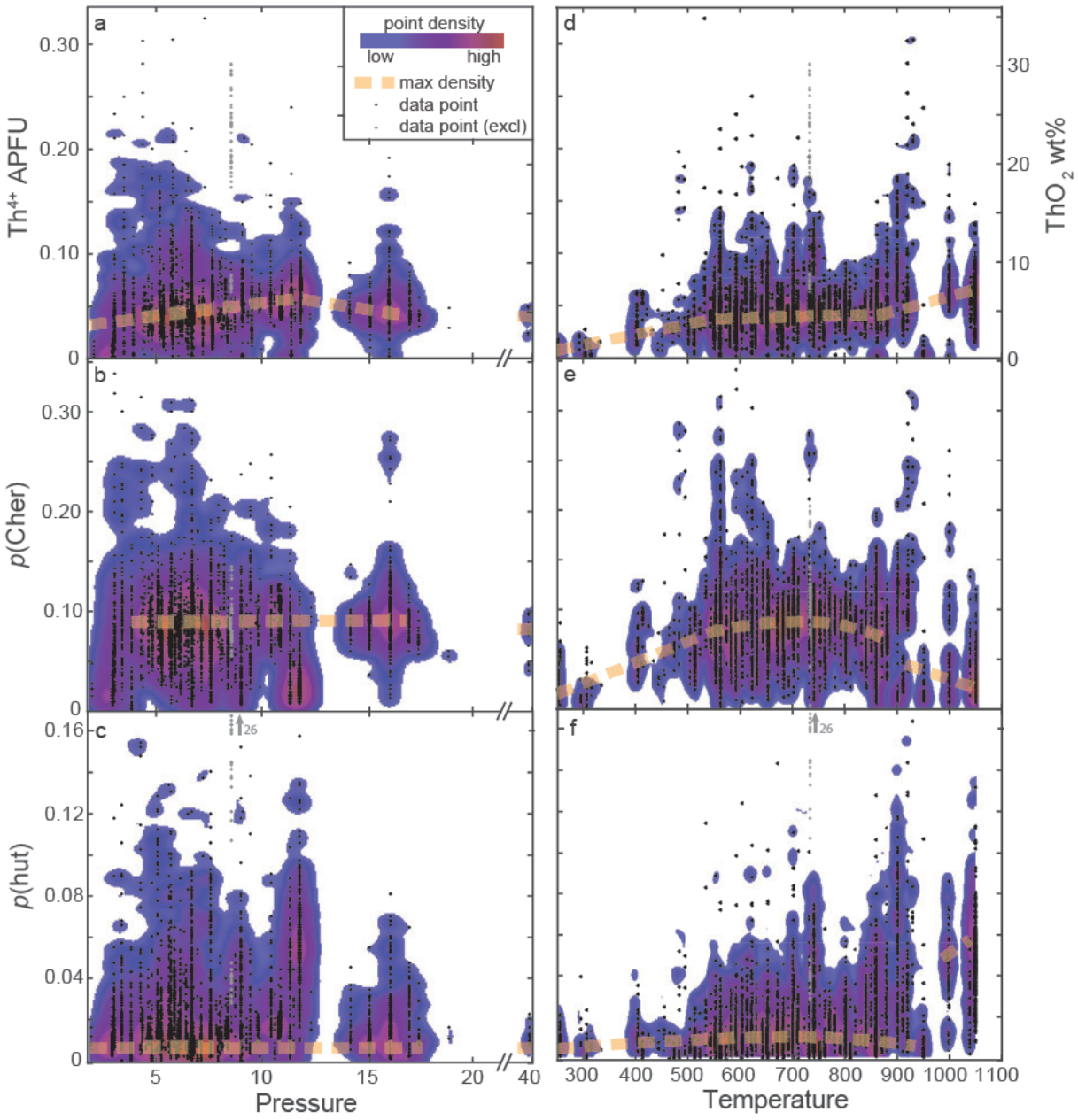

Figure S4.3.1. Data point density plot of compositional changes in monazite with pressure and temperature. See Appendix S4.1 for data sources. Parts a c show compositional trends with pressure and parts d f show compositional trends with temperature from the dataset. (a)&(d) Th^{4+} APFU; (b)&(e) proportion of cheralite endmember, $Th_{0.5}Ca_{0.5}PO_4$; (c) &(f) proportion of huttonite endmember, $ThSiO_4$. The remaining compositional parameters for monazite are $(REE)PO_4$ and USiO4. $p(REEPO_4)$[not shown] + p(USiO4)[not shown] + p(cher) + p(hutt) =1. Colour gradient represents data density. Orange dashed line indicates trend of maximum data density. Light grey data points were determined to be significant outliers and were not used in determination of data density, see main text for details. This method produces the same trends as the moving mean of data (Fig. 2).

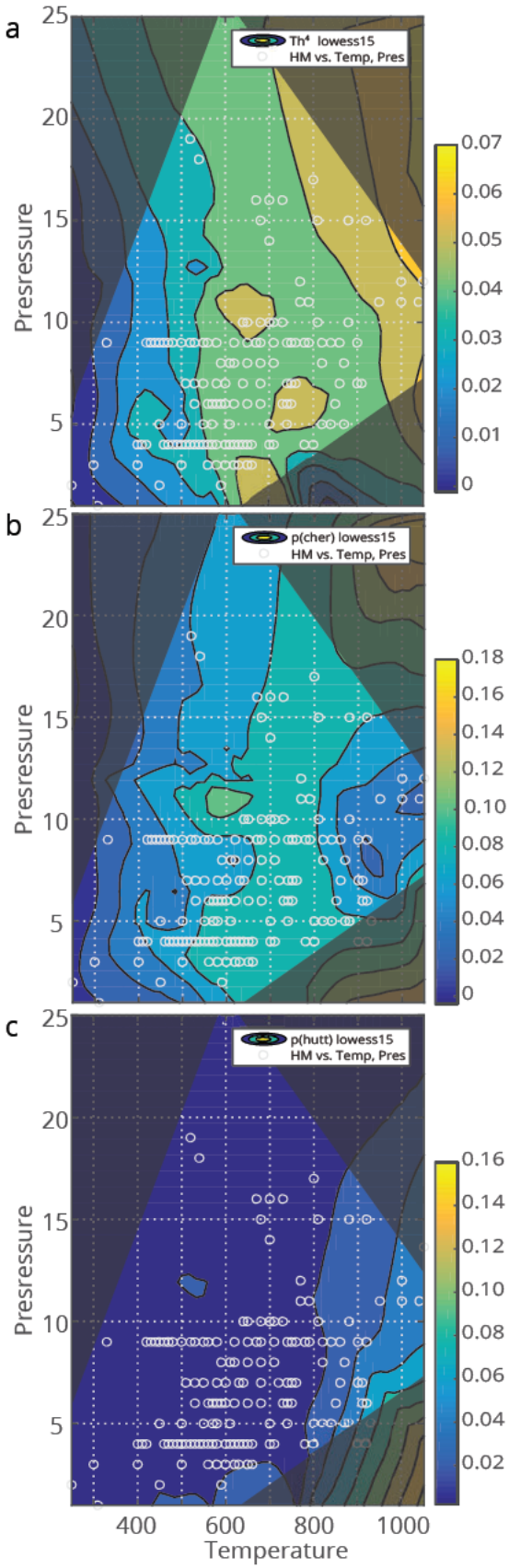

Figure S4.3.2. Contour maps showing the changes in monazite composition with pressure and temperature. (a) Th^{4+} APFU, (b) proportion of cheralite endmember, $Th_{0.5}Ca_{0.5}PO_4$, (c), proportion of huttonite endmember, $ThSiO_4$. The remaining compositional parameter for monazite is $(REE)PO_4$. $p(REEPO_4)$[not shown] + p(cher) + p(hutt) =1. See Appendix S4.1 for data sources and S4.2 for full dataset. Surface is a lowess bisquare fit (span 15) through weighted average of each node in a *P T* grid with steps of 1 kbar and 10 °C. Greyed areas have no data to constrain the lowess model.

Chapter 5

This chapter is prepared for submission as:

Williams, M. A., Kelsey, D. E. & Spear, F. S. Phase equilibria modelling of monazite in a Th-bearing system

Statement of Authorship

Title of Paper	Phase equilibria modelling of monazite in a Th-bearing system
Publication Status	☐ Published ☐ Accepted for Publication ☐ Submitted for Publication ☑ Unpublished and Unsubmitted work written in manuscript style
Publication Details	

Principal Author

Name of Principal Author (Candidate)	Megan A Williams
Contribution to the Paper	Study design, assistance with model calibration, all calculations using thermodynamic model, all drafting of figures, manuscript/chapter writing.
Overall percentage (%)	90%
Certification:	This paper reports on original research I conducted during the period of my Higher Degree by Research candidature and is not subject to any obligations or contractual agreements with a third party that would constrain its inclusion in this thesis. I am the primary author of this paper.
Signature	Date 8/12/19

Co-Author Contributions

By signing the Statement of Authorship, each author certifies that:

i. the candidate's stated contribution to the publication is accurate (as detailed above);

ii. permission is granted for the candidate in include the publication in the thesis; and

iii. the sum of all co-author contributions is equal to 100% less the candidate's stated contribution.

Name of Co-Author	David E Kelsey
Contribution to the Paper	Thermodynamic model development and calibration, manuscript editing, project design
Signature	Date 29/11/19

Name of Co-Author	Frank Spear
Contribution to the Paper	Provision of phase equilibria software and initial thermodynamic dataset, assistance with thermodynamic model development and calibration.
Signature	Oct 31, 2019 Date

Phase equilibria modelling of monazite in a Th-bearing system

ABSTRACT

Integrating monazite into existing Pressure–Temperature frameworks is an essential step towards fully realising the significant potential of this mineral in petrochronology. To further this endeavour, we present a predictive and readily adaptable equilibrium thermodynamic calculation framework involving solid solution for monazite and other accessory phases. This framework comprises over 90 wt% oxide of the elemental components of these minerals (Y, La, Ce, Nd, Th, P, Si, Ca) and includes all of the major endmember substitutions. We investigate the response of monazite and other accessory phases to closed and open system melting processes and changes to the major and trace element composition of the whole rock. We find that the incorporation of additional elements into monazite (La, Nd, Th, Ca, P and Si) displaces both the lower and upper bounds of monazite stability to higher temperatures relative to previous estimates. Exploration of bulk composition changes reveals that both Al and Ca affect the size and shape of the accessory mineral stability fields, in line with previous studies. Decreases to bulk P have a limited effect on monazite stability and composition, but significantly decrease the temperature of the terminal stability boundary of apatite. We also show that increases to bulk LREE increase the mode and stability of monazite and decrease the proportion of the Th endmembers, cheralite and huttonite, in monazite. Changes to bulk Th have limited effect on the mode or stability field of monazite due to the generally low fraction of Th-endmembers in monazite, but do significantly change the total amount of Th-in-monazite. Apatite plays a key role in the stability of monazite above the solidus by saturating the rock in P. Therefore, compositions that are conducive to the stability of apatite at the expense of other Ca-bearing phases support correspondingly greater stability of monazite above the solidus. Our modelling shows that monazite can be stable to much higher temperatures than previously modelled, to >1100 oC in both open and closed systems, consistent with the natural rock record. Our models replicate the compositions and compositional trends from a natural dataset of over 5000 Pressure–Temperature-linked monazite analyses and present the first predictions of monazite growth above the solidus. We also present models for specific natural rock and monazite compositions which show considerable promise for the application of this framework to natural examples. The provision of this readily adaptable phase equilibria calculation framework adds an important new tool to the petrochronology toolbox.

1 INTRODUCTION

The rare earth element (REE) phosphate mineral monazite has substantial current and emerging utility in petrochronology. It is now routinely used in geochronological studies of high temperature tectonic processes and isotopic analysis shows that it can survive long periods of elevated temperatures (e.g. Rapp & Watson, 1986). Monazite is commonly zoned with respect to REEs, Th, U, Y, Si, Ca, P and ages (c.f. Engi, 2017; Williams, Jercinovic, & Hetherington, 2007). However, the relationship between the chemical zones and isotopic zones used for geochronology remains somewhat unclear, with some authors questioning whether the two systems could ever be fully integrated (e.g. Taylor, Kirkland, & Clark, 2016).

Monazite demonstrates a complex array of chemical and isotopic zoning textures which can be challenging to link to *P–T* conditions of growth or dissolution. Detailed monazite mineral chemistry is not routinely collected, for example by EPMA, by studies utilising monazite. This is in part because of our inability to link absolute mineral chemistry to specific locations along a P-T evolution path and further hampered by the need for different instrumentations to that for age analysis and long analysis times. For these reasons, Th + U + Pb chemical or isotopic information is typically collected from monazite but not much else. The recent improvements in the capacity and availability of LA–ICP–MS systems (including the advent of split stream LA+MC–ICP–MS) for the collection of accurate, detailed and low cost analysis of monazite chemistry, simultaneous with isotope geochronology, opens new avenues for petrology research with this utilitarian mineral. An important additional innovation required to expand monazite utility is a readily adaptable and predictive calculation

framework that can systematically link monazite chemistry to whole rock chemistry, mineralogy and *Pressure–Temperature* (*P–T*) conditions of formation.

Existing frameworks for calculating the stability and composition of monazite include Spear and Pyle (2010), Spear (2010) and Janots et al. (2007). These seminal studies were vitally important but were limited in their application by the restricted compositional space of the chemical systems. In addition, other existing efforts of modelling monazite abundance and composition show that, within the constraints of the modelling, prograde monazite growth in suprasolidus rocks is not possible (Kelsey, Clark, & Hand, 2008; Spear, 2010; Spear & Pyle, 2010; Yakymchuk, 2017; Yakymchuk & Brown, 2014a; Yakymchuk, Kirkland, & Clark, 2018). Instead, these studies suggest that in suprasolidus rocks monazite ages (and compositions) record cooling and crystallisation from melt (c.f. Yakymchuk & Brown, 2014a). This finding conflicts with several studies which persuasively show that monazite records prograde compositions and ages associated with heating and partial melting (e.g. Chapters 2 and 3; Foster et al., 2002; Rubatto, Williams, & Buick, 2001; Schulz, 2017; Skrzypek et al., 2018; Williams, 2001). Granulite facies terranes are commonly interpreted to have lost melt as a requirement to preserve their peak mineral assemblages (e.g. Brown, 2007; Palya, Buick, & Bebout, 2011; Powell & Downes, 1990; Redler, White, & Johnson, 2013; White & Powell, 2002). However, as yet, Yakymchuk (2017) is the only study to explore the response of monazite to open system melting but was not conducted with an equilibrium thermodynamic approach.

To this end, we aim to (1) create a thermodynamic calculation framework ('thermodynamic model') which explicitly incorporates the major elemental components of monazite (Ce, La, Nd, Th, Y, Ca, Si, P) and produces outputs for monazite composition that are consistent with available natural data (Chapter 4); (2) explore the composition and modal abundance of monazite in open and closed partial melt systems; (3) understand the key whole rock geochemical controls on monazite chemistry and stability in *P–T* space; and (4) apply the framework to natural rock compositions to model natural monazite compositions. These thermodynamic models are not intended to be definitive, however we are confident that the results presented below are consistent with the global trends in monazite composition (Chapter 4) so the thermodynamic models have some essential validity and therefore show considerable promise.

2 METHODS

2.1 Thermodynamic model development

The approach to developing the thermodynamic models follows the seminal work of Spear & Pyle (2010) and Spear (2010) for the calculated equilibrium thermodynamic stability of REE phases. In those studies, the thermodynamic properties for all but enthalpy for the accessory phases were taken from or calculated by summing published data (Robie et al. 1978; Robie & Hemingway 1995), and we follow the same approach here. That being the case, the enthalpy of formation for accessory phase end-members was calculated by a least squares procedure that entails using the combination of coexisting major and accessory phase compositions with the (known) thermodynamic properties of major phase end-members and the known enthalpy of formation for at least some trace element (TE)-bearing end-members. For our purposes, the enthalpies of formation that were assumed to be reliable were for monazite (see below) and this enabled least squares calculation of enthalpies for all remaining accessory phase end-members. In this way, the enthalpies of formation for all TE-bearing end-members are correlated to each other, ensuring the results are internally consistent. The list of all phase end-members and the corresponding thermodynamic data either developed in this study and/or used for phase equilibria calculations are presented in Table 1. In Table 1 the heat capacity terms are for the expression $Cp = a + b/(T^{0.5}) + c/T^2 + d/T^3 + f*T + g*T^2$. Data for the major phases are those of Spear & Pyle (2010), excepting YAG, NdAG and silicate melt. Silicate melt end-members are here defined to have 8 oxygens, except for h2oL as per Holland & Powell, (2011). This contrasts with Spear & Pyle (2010) that only had major component end-members of silicate melt defined this way. In the spirit of the way H_2O-in-melt is handled as h2oL by Holland & Powell (2011), we handle it identically here and also treat F analogously as CaF2L. Activity models for all phases except Th-in-monazite are defined the same as outlined in Spear & Pyle (2010). For the two Th end-members of monazite, huttonite and cheralite, the activities are defined on the basis of the fraction of Si, and

Table 1. Thermodynamic data used in calculation of equilibrium assemblage diagrams.

						Heat Capacity terms[a]							Volume terms			
Phase	**Component**	**formula**	**H**	**S**	**V**	**a**	**b**	**c**	**d**	**e**	**f**	**g**	**v1**	**v2**	**v3**	**v4**
Quartz	abQz	SiO_2	-910700	41.46	2.269	80.012	-240.276	-3546684	491568384	0	0	0	2.39×10^{-5}	0	-2.43×10^{-6}	1.01×10
Water	H_2O	H_2O	0	0	0	0	0	0	0	0	0	0	0	0	0	0
Kyanite	Ky	Al_2SiO_5	-2594221	82.43	4.412	262.68478	-2001.407	-1999740	-6.32×10^{7}	0	0	0	2.40×10^{-5}	0	-6.46×10^{-7}	0
Sillimanite	Sil	Al_2SiO_5	-2586090	95.93	4.983	256.73158	-1887.225	-2977353	250959080	0	0	0	1.34×10^{-5}	0	-7.53×10^{-7}	0
Andalusite	And	Al_2SiO_5	-2590260	91.4337	5.147	236.478	-1102.94	-7526810	936442000	0	0	0	2.34×10^{-5}	7.19×10^{-10}	-7.70×10^{-7}	1.92×10^{-12}
Plagioclase	Ab	$NaAlSi_3O_8$	-3921620	224.412	10.083	393.636	-2415.5	-7892830	1070640000	0	0	0	2.63×10^{-5}	3.24×10^{-9}	-1.94×10^{-6}	4.86×10^{-12}
	An	$CaAl_2Si_2O_8$	-4228730	200.186	10.075	439.369	-3734.15	0	-317023000	0	0	0	1.09×10^{-5}	4.20×10^{-9}	-1.27×10^{-6}	3.18×10^{-12}
K-feldspar	Kfs	$KAlSi_3O_8$	-3970790	214.145	10.869	381.372	-1941.045	-12037252	1836425472	0	0	0	1.51×10^{-5}	5.49×10^{-9}	-1.80×10^{-6}	5.11×10^{-12}
Garnet	Prp	$Mg_3Al_2Si_3O_{12}$	-6284734	268.8	11.311	640.72	-4542.07	-4701900	0	0	0	0	2.25×10^{-5}	3.70×10^{-9}	-5.76×10^{-7}	4.42×10^{-13}
	Alm	$Fe_3Al_2Si_3O_{12}$	-5278317	341.582	11.524	621.427	-3287.931	-15081040	2211865100	0	0	0	1.86×10^{-5}	7.47×10^{-9}	-5.70×10^{-7}	4.34×10^{-13}
	Sps	$Mn_3Al_2Si_3O_{12}$	-5641080	357.927	11.961	617.704	-3194.87	-12277000	1624210000	0	0	0	2.40×10^{-5}	0	-1.21×10^{-7}	0
	Grs	$Ca_3Al_2Si_3O_{12}$	-6632860	255.15	12.538	573.43	-2039.41	-18887200	2319310000	0	0	0	1.90×10^{-5}	7.98×10^{-9}	-6.54×10^{-7}	1.64×10^{-12}
	YAG	$Y_3Al_5O_{12}$	-7238751	275.92	13.126	574.99	-2470.1	-7514250	0	0	0.014700	0	0	0	0	0
	NdAG	$Nd_3Al_5O_{12}$	-6878217	365.155	13.282	567.01	-2470.1	-6524700	0	0	0.046466	0	0	0	0	0
Muscovite	Ms(Ms)	$KAl_3Si_3O_{11}(OH)_2$	-5976740	293.157	14.087	651.489	-3873.23	-18523200	2742470000	0	0	0	3.35×10^{-5}	0	-1.72×10^{-6}	4.29×10^{-12}
	Pg(Ms)	$NaAl_3Si_3O_{11}(OH)_2$	-5944210	277.699	13.216	577.569	-1472.8	-32214400	5050080000	0	0	0	3.94×10^{-5}	5.97×10^{-9}	-1.97×10^{-6}	4.93×10^{-12}
Biotite	Phlogopi	$KMg_3AlSi_3(OH)_2$	-6220355	325.924	14.971	610.38	-2083.78	-21533000	2841040000	0	0	0	3.44×10^{-5}	0	-1.70×10^{-6}	0
	Eastonit	$KMg_2Al_3Si_2(OH)_2$	-6335307	312.622	14.732	619.793	-2272.34	-22291160	3004744000	0	0	0	3.44×10^{-5}	0	-1.70×10^{-6}	0
	Annite	$KFe3AlSi3(OH)_2$	-5169560	405.01	15.487	727.208	-4775.04	-13831900	2119060000	0	0	0	3.44×10^{-5}	0	-1.70×10^{-6}	0
	Sideroph	$KFe_2Al_3Si_2(OH)_2$	-5617116	385	15.063	717.781	-4540.03	-15994640	2389879000	0	0	0	3.44×10^{-5}	0	-1.70×10^{-6}	0
	MnBiotit	$KMn_3AlSi_3(OH)_2$	-5458747	434.958	15.787	698.909	-4300.62	-9931330	1394790000	0	0	0	3.44×10^{-5}	0	-1.70×10^{-6}	0
Cordierite	MgCd	$Mg_2Al_4Si_5O_{18}$	-9177913	396	23.311	954.387	-7962.27	-2317260	-370214000	0	0	0	3.00×10^{-6}	1.80×10^{-9}	-1.16×10^{-6}	0
	WMgCrd	$Mg_2Al_4Si_5O_{18}$ H2O	-9489592	446	23.311	997.68	-7962.27	-2317260	-370214000	0	0	0	3.00×10^{-6}	1.80×10^{-9}	-1.16×10^{-6}	0
	FeCd	$Fe_2Al_4Si_5O_{18}$	-8454149	473	23.706	975.3	-8013.44	-9618520	1189280000	0	0	0	2.70×10^{-5}	0	-1.16×10^{-6}	0
	MnCd	$Mn_2Al_4Si_5O_{18}$	-8688528	473	24.027	975.3	-8013.44	-9618520	1189280000	0	0	0	2.70×10^{-5}	0	-1.16×10^{-6}	0
Apatite	OHAp	$Ca_5(PO_4)_3(OH)$	-6738500	390.4	15.96	387.8	1811	-12700000	0	0	0.118600	0	0	0	0	0
	FAp	$Ca_5(PO_4)_3(F)$	-6872000	387.9	15.756	754.3	-6201	-908400	0	0	-0.030260	0	0	0	0	0
	YOHAp	$Ca_4Y(PO_4)_2(SiO_4)(OH)$	-6978606	385.55	15.827	387.8	1811	-12700000	0	0	0.118600	0	0	0	0	0
	LaOHAp	$Ca_4La(PO_4)_2(SiO_4)(OH)$	-6932047	399.67	16.061	387.8	1811	-12700000	0	0	0.118600	0	0	0	0	0
	CeOHAp	$Ca_4Ce(PO_4)_2(SiO_4)(OH)$	-6935637	411.32	15.97	387.8	1811	-12700000	0	0	0.118600	0	0	0	0	0
	NdOHAp	$Ca_4Nd(PO_4)_2(SiO_4)(OH)$	-6936757	415.295	15.879	387.8	1811	-12700000	0	0	0.118600	0	0	0	0	0
	ThOHAp	$Ca_4Th(PO_4)(SiO_4)_2(OH)$	-7069354	384.92	15.519	387.8	1811	-12700000	0	0	0.118600	0	0	0	0	0
Monazite	Ce-mnz	$CePO_4$	-1967800	133.06	5.357	82.85	0	-852650	0	0	0.123130	0	0	0	0	0
	La-mnz	$LaPO_4$	-1970700	121.41	5.448	83.031	-117.09	-562600	0	0	0.113500	0	0	0	0	0
	Nd-mnz	$NdPO_4$	-1968400	137.035	5.266	75.39	0	-594150	0	0	0.127860	0	0	0	0	0
	Y-mnz	YPO_4	-1987700	107.29	5.214	78.05	0	-924000	0	0	0.117270	0	0	0	0	0
	Hutt	$ThSiO_4$	-2120900	106.69	4.906	115.98	0	-2054700	0	0	0.011331	0	0	0	0	0
	Cher	$Ca_{0.5}Th_{0.5}PO_4$	-1916400	109.47	5.127	80.421	-25.494	-901790	0	0	0.118580	0	0	0	0	0
Xenotime	Xen	YPO_4	-2004941	107.29	4.3	78.05	0	-924000	0	0	0.117270	0	0	0	0	0

Table 1 (cont.). Thermodynamic data used in calculation of equilibrium assemblage diagrams.

						Heat Capacity terms[a]							Volume terms			
Phase	**Component**	**formula**	**H**	**S**	**V**	**a**	**b**	**c**	**d**	**e**	**f**	**g**	**v1**	**v2**	**v3**	**v4**
Allanite	YEp	$CaYFeAl_2Si_3O_{12}(OH)$	-6645244	339.99	14.3	748.17	-6510.85	-106397	-115462976	0	0.004301	0	0	0	0	0
	LaAln	$CaLaFeAl_2Si_3O_{12}$ (OH)	-6626931	354.11	14.534	753.15	-6627.93	255003	-115462976	0	0.000529	0	0	0	0	0
	CeAln	$CaCeFeAl_2Si_3O_{12}$ (OH)	-6624435	365.76	14.443	752.97	-6510.84	-35047	-115462976	0	0.010158	0	0	0	0	0
	NdAln	$CaNdFeAl_2Si_3O_{12}$ (OH)	-6626257	369.73	14.352	745.51	-6510.84	223453	-115462976	0	0.014889	0	0	0	0	0
	ThEp	$Ca_{1.5}Th_{0.5}FeAl_2Si_3O_{12}$ (OH)	-6586331	336.3	13.9	770.58	-6712.002	-1705958	202134980	0	0.001890	0	0	0	0	0
	Czo	$Ca_2Al_3Si_3O_{12}$ (OH)	-6911712	287.076	13.673	749.17	-6509.28	-2380530	124858000	0	0	0	3.47×10^{-5}	0	-5.15×10^{-7}	1.29×10^{-12}
Melt	h2oL	H_2O	-295010	45.5	1.39	80	0	0	0	0	0	0	5.21×10-4	5.06×10^{4}	4.00	492
	qL4	Si_4O_8	-3684280	65.2	10.92	330	0	0	0	0	0	0	0	8.80×10^{5}	37.8	896
	abL	$NaAlSi_3O_8$	-3926520	149.9	10.858	358	0	0	0	0	0	0	3.37×10^{-5}	1.76×10^{5}	14.4	592
	kspL	$KAl\ Si_3O_8$	-3985190	129.2	11.431	368	0	0	0	0	0	0	4.93×10^{-5}	1.73×10^{5}	6.84	649
	anL	$CaAl_2Si_2O_8$	-4277970	29	10.014	430	0	0	0	0	0	0	5.14×10^{-5}	2.10×10^{5}	6.38	1.23×10^{3}
	silL85	$Si_{1.6}Al_{3.2}O_8$	-4172488	16	9.682	404.8	0	0	0	0	0	0	6.53×10^{-5}	3.52×10^{5}	10.2	1.38×10^{3}
	foL2	$Mg_4Si_2O_8$	-4530250	-124	8.624	538.8	0	0	0	0	0	0	1.84×10-4	7.24×10^{5}	20.1	-4.40×10^{3}
	faL2	$Fe_4Si_2O_8$	-2967348	192	8.054	487.4	0	0	0	0	0	0	2.14×10-4	5.80×10^{5}	20.8	528
	CaF2L	CaF_2	-1109771	137.74	4.908	155	0	0	0	0	0	0	4.93×10^{-5}	1.73×10^{5}	6.84	649
	Al2P2O8L	$Al_2P_2O_8$	-3461388	181.6	9.316	260	0	0	0	0	0	0	4.93×10^{-5}	1.73×10^{5}	6.84	649
	Y2P2O8L	$Y_2P_2O_8$	-3924174	214.58	8.601	284	0	0	0	0	0	0	4.93×10^{-5}	1.73×10^{5}	6.84	649
	La2P2O8L	$La_2P_2O_8$	-3857058	242.82	9.179	260	0	0	0	0	0	0	4.93×10^{-5}	1.73×10^{5}	6.84	649
	Ce2P2O8L	$Ce_2P_2O_8$	-3830088	266.12	9.031	300	0	0	0	0	0	0	4.93×10^{-5}	1.73×10^{5}	6.84	649
	Nd2P2O8L	$Nd_2P_2O_8$	-3811191	274.07	10.532	360	0	0	0	0	0	0	4.93×10^{-5}	1.73×10^{5}	6.84	649
	Th2Si2O8L	$Th_2Si_2O_8$	-4157267	213.38	9.812	285	0	0	0	0	0	0	4.93×10^{-5}	1.73×10^{5}	6.84	649
Staurolite	MgSt	$Mg_4Al_{18}Si_{7.5}O_{44}(OH)_4$	-25135000	898.255	44.196	2502.31	-14571	-66804200	9120510000	0	0	0	2.70×10^{-5}	0	-4.87×10^{-7}	0
	FeSt	$Fe_4Al_{18}Si_{7.5}O_{44}(OH)_4$	-23782364	1005	44.676	2577.674	-16265.359	-61185888	8692047872	0	0	0	1.79×10^{-5}	9.04×10^{-9}	-8.00×10^{-7}	0
	MnSt	$Mn_4Al_{18}Si_{7.5}O_{44}(OH)_4$	-24190000	1032.655	45.276	2534.82	-15039.6	-61185900	8527150000	0	0	0	2.70×10^{-5}	0	-3.31×10^{-7}	0

[a] Heat capacity expression is $Cp=a+b/(T^{0.5})+c/T^2+d/T^3+f*T+g*T^2$.

the fractions of Th and Ca, respectively. Apatite TE end-members were defined to contain OH rather than F so that preliminary calculations could be done in F-absent chemical systems. The Y, La and Nd end-members of allanite are defined analogously to Ce-allanite in Spear (2010) and ThEp is defined as specified in Table 1.

Thermodynamic data for the major element components of melt are those of Holland and Powell (2011) except enthalpy, which were re-derived via a least squares approach for a known melt-bearing composition at a fixed pressure and temperature in order to preserve internal consistency with other phases in the SPaC dataset, which is based largely on Berman (1988). All thermodynamic data for FAp and OHAp are taken directly from Robie, Hemingway, and Fisher (1978) and Robie and Hemingway (1995). Data for S, V and Cp terms for monazite, xenotime, apatite, allanite and TE-end-members of silicate melt and garnet were mostly derived via oxide sums using the data of Robie et al. (1978) and Robie and Hemingway (1995). However, to maintain consistency with the haplogranitic melt model of Holland and Powell (2011) all our silicate melt model end-members have Cp terms of zero, and for lack of data the volume terms for melt TE end-members are assumed to be the same as for kspL.

Enthalpies of formation for monazite Y, Ce, La and Nd end-members were taken directly from Ushakov, Helean, Navrotsky, and Boatner (2001) and were assumed to be reliable for the purpose of calculating H for other phase TE end-members. Enthalpies for huttonite (Mazeina, Ushakov, Navrotsky, & Boatner, 2005) and cheralite (Popa et al., 2008) were adjusted slightly (by –10,000 J and +20,000 J, respectively) from the published values to enable the natural trend in Th-in-monazite chemistry documented in Chapters 2, 3 and 4 to be replicated. The enthalpy of YPO_4–xenotime was calculated via least squares using the compositions of $CePO_4$–YPO_4 monazite and YPO_4 xenotime at 2 kbar , 500 °C and 5 kbar, 640 °C as per the experimentally defined miscibility gap in Gratz and Heinrich (1997).

Enthalpies of formation for apatite, melt and garnet TE end-members were calculated using a least squares approach for a reference assemblage shown in Table 2 that is from the Ivrea–Verbano Zone, Italy, for *P–T* conditions of 9 kbar and 840 °C (Chapter 4, appendix S5.2). The Y and Nd concentrations in garnet in Table 2 are the average of kinzigite compositions

Table 2. Reference assemblage and P T conditions for least squares calculation of H for apatite, melt, garnet TE endmembers.

Phase	Component	Formula	Mole Fr.
Quartz	abQz	SiO^2	1
Sillimanite	Sil	Al_2SiO_5	1
Plagioclase	Ab	$NaAlSi_3O_8$	0.711416
	An	$CaAl_2Si_2O_8$	0.288584
Garnet	Prp	$Mg_3Al_2Si_3O_{12}$	0.370087
	Alm	$Fe_3Al_2Si_3O_{12}$	0.585380
	Sps	$Mn_3Al_2Si_3O_{12}$	0.013877
	Grs	$Ca_3Al_2Si_3O_{12}$	0.030521
	YAG	$Y_3Al_5O_{12}$	0.000134
	NdAG	$Nd_3Al_5O_{12}$	7.50E-08
Biotite	Phlogopi	$KMg_3AlSi_3\ (OH)_2$	0.529293
	Eastonit	$KMg_2Al_3Si_2\ (OH)_2$	0.09083
	Annite	$KFe3AlSi3(OH)_2$	0.122671
	Sideroph	$KFe_2Al_3Si_2(OH)_2$	0.256505
	MnBiotit	$KMn_3AlSi_3(OH)_2$	0.000701
Apatite	OHAp	$Ca_5(PO_4)_3(OH)$	0.07451
	FAp	$Ca_5(PO_4)_3$ (F)	0.922348
	YOHAp	$Ca_4Y(PO_4)_2(SiO_4)(OH)$	0.0005
	LaOHAp	$Ca_4La(PO_4)_2(SiO_4)$ (OH)	0.000196
	CeOHAp	$Ca_4Ce(PO_4)_2(SiO_4)$ (OH)	0.000903
	NdOHAp	$Ca_4Nd(PO_4)_2(SiO_4)$ (OH)	0.00149
	ThOHAp	$Ca_4Th(PO_4)(SiO_4)_2(OH)$	0.000053
Monazite	Ce-mnz	$CePO_4$	0.458025
	La-mnz	$LaPO_4$	0.225783
	Nd-mnz	$NdPO_4$	0.179154
	Y-mnz	YPO_4	0.005911
	Hutt	$ThSiO_4$	0.031127
	Cher	$Ca_{0.5}Th_{0.5}PO_4$	0.1
Melt	h2oL	H_2O	0.482847
	qL4	Si_4O_8	0.119787
	abL	$NaAlSi_3O_8$	0.184521
	kspL	$KAl\ Si_3O_8$	0.179627
	anL	$CaAl_2Si_2O_8$	0.018762
	silL85	$Si_{1.6}Al_{3.2}O_8$	0.010573
	foL2	$Mg_4Si_2O_8$	0.001186
	faL2	$Fe_4Si_2O_8$	0.001632
	CaF2L	CaF_2	0.000205
	Al2P2O8L	$Al_2P_2O_8$	0.000682
	Y2P2O8L	$Y_2P_2O_8$	0.000006
	La2P2O8L	$La_2P_2O_8$	0.000042
	Ce2P2O8L	$Ce_2P_2O_8$	0.000084
	Nd2P2O8L	$Nd_2P_2O_8$	0.000032
	Th2Si2O8L	$Th_2Si_2O_8$	0.000013

T= 840 C; P= 9 kbar; Mole Fr., mole fraction.

presented in Bea and Montero (1999). Apatite F content was assumed to be ~0.92 (Table 2; Spear & Pyle, 2002) in this reference assemblage. For this reference assemblage the TE compositions of melt were calculated using the solubility equations of Harrison and Watson (1984) for the P_2O_5 contribution from apatite dissolution and Stepanov, Hermann, Rubatto, and Rapp (2012) for the Y, La, Ce, Nd, Th and P contributions from monazite dissolution.

It is acknowledged that the partitioning behaviour of F into haplogranitic melts for an aluminous metasediment system via apatite dissolution is not well constrained. Therefore, in the absence of strong information to the contrary (see for example Webster, Goldoff, Flesch, Nadeau, & Silbert, 2017), the partitioning of F (and all other elements in apatite) into melt followed

Table 3. Reference assemblage and P T conditions for least squares calculation of H for allanite.

Phase	Component	Formula	Mole Fr.
Quartz	abQz	SiO^2	1
Water	H2O	H2O	1
Plagioclase	Ab	$NaAlSi_3O_8$	0.617420
	An	$CaAl_2Si_2O_8$	0.382580
Garnet	Prp	$Mg_3Al_2Si_3O_{12}$	0.140718
	Alm	$Fe_3Al_2Si_3O_{12}$	0.726828
	Sps	$Mn_3Al_2Si_3O_{12}$	0.058437
	Grs	$Ca_3Al_2Si_3O_{12}$	0.070516
	YAG	$Y_3Al_5O_{12}$	0.0035
	NdAG	$Nd_3Al_5O_{12}$	0
Biotite	Phlogopi	$KMg_3AlSi_3 (OH)_2$	0.402322
	Eastonit	$KMg_2Al_3Si_2 (OH)_2$	0.128532
	Annite	$KFe3AlSi3(OH)_2$	0.275473
	Sideroph	$KFe_2Al_3Si_2(OH)_2$	0.191521
	MnBiotit	$KMn_3AlSi_3(OH)_2$	0.002152
Muscovite	Ms	$KAl_3Si_3O_{11}(OH)_2$	0.769259
	Pa	$NaAl_3Si_3O_{11}(OH)_2$	0.230741
Staurolite	MgSt	$Mg_4Al_{18}Si_{7.5}O_{44}(OH)_4$	0.197496
	FeSt	$Fe_4Al_{18}Si_{7.5}O_{44}(OH)_4$	0.796386
	MnSt	$Mn_4Al_{18}Si_{7.5}O_{44}(OH)_4$	0.006118
Apatite	OHAp	$Ca_5(PO_4)_3(OH)$	0.009504
	FAp	$Ca_5(PO_4)_3$ (F)	0.95557
	YOHAp	$Ca_4Y(PO_4)_2(SiO_4)(OH)$	0.022408
	LaOHAp	$Ca_4La(PO_4)_2(SiO_4)$ (OH)	0.002284
	CeOHAp	$Ca_4Ce(PO_4)_2(SiO_4)$ (OH)	0.006987
	NdOHAp	$Ca_4Nd(PO_4)_2(SiO_4)$ (OH)	0.003053
	ThOHAp	$Ca_4Th(PO_4)(SiO_4)_2(OH)$	0.000195
Monazite	Ce-mnz	$CePO_4$	0.489646
	La-mnz	$LaPO_4$	0.242121
	Nd-mnz	$NdPO_4$	0.163137
	Y-mnz	YPO_4	0.049183
	Hutt	$ThSiO_4$	0.04438
	Cher	$Ca_{0.5}Th_{0.5}PO_4$	0.011533
Xenotime	YPO4	YPO_4	1
Allanite	YEp	$CaYFeAl_2Si_3O_{12}(OH)$	0.024734
	LaAln	$CaLaFeAl_2Si_3O_{12}$ (OH)	0.099764
	CeAln	$CaCeFeAl_2Si_3O_{12}$ (OH)	0.202059
	NdAln	$CaNdFeAl_2Si_3O_{12}$ (OH)	0.081757
	ThEp	$Ca_{1.5}Th_{0.5}FeAl_2Si_3O_{12}$ (OH)	0.03
	Czo	$Ca_2Al_3Si_3O_{12}$ (OH)	0.561686

T= 640 C; P= 7.5 kbar; Mole Fr., mole fraction.

the simplest scenario, that of contributing at an equal 'rate' to P_2O_5. In other words, there is no built in preference for P_2O_5 dissolving into melt over F or vice versa.

Enthalpies of formation for all allanite end-members were calculated by least squares after all of the above was done so as to assume that the thermodynamics of monazite and apatite TE end-members were reliable. This used the reference assemblage in Table 3 that is based on the study of Goswami-Banerjee and Robyr (2015) at *P–T* conditions of 7.5 kbar and 640 °C.

It should be emphasized that the values of the enthalpies of formation were calculated to reproduce the two reference assemblages, and are only accurate to the extent that each represents an equilibrated assemblage. It should also be noted that the method of differential thermodynamics (i.e. the Gibbs method; Spear, 1993) makes use of identical reference assemblages, but does not formalize the calculation of individual enthalpies. Extracting individual enthalpies makes extrapolation of the results far simpler.

2.2 Phase equilibria modelling

In this study, calculations were performed using GIBBS v. 3(windows) (Spear, 2014; Spear & Menard, 1989) in the MnO–NaO–CaO–K_2O–FeO–MgO–Al_2O_3–SiO_2–H_2O–P_2O_5– Y_2O_3– La_2O_3–Ce_2O_3–Nd_2O_3–ThO_2–F chemical system, in order to investigate aluminous metasediments with phosphate phases in *Pressure–Temperature–Rock Composition* (*P–T–X*) space. This is an expansion on the MnNCKFMASH system to include the elements P, Y, La, Ce, Nd, Th and F. The phases included in the calculations were as follows: quartz, H_2O, kyanite, sillimanite, andalusite, plagioclase, K-feldspar, garnet, muscovite, biotite, staurolite, cordierite, apatite, monazite, xenotime, allanite and silicate melt.

Two published bulk compositions were modelled in both open and closed system scenarios to provide direct comparison to previous modelling studies exploring monazite stability (Table 4; Spear, 2010; Spear & Pyle, 2010). Preliminary exploration of two additional published bulk compositions produced similar equilibrium assemblage diagrams (EADs, Appendix S5.1; Kelsey et al., 2008; Yakymchuk et al., 2018) but did not provide the breadth of monazite and apatite stability that the Spear and Pyle (2010) and Spear (2010) compositions did and so were not considered further. EAD calculations for the two compositions in Table 4 allow the appraisal of the variability of the response of the accessory minerals to changes in thermodynamic model parameters (i.e. closed vs open systems and bulk rock composition).

Trace elements were added to these major element compositions to approximate the average pelite composition of Taylor and McLennan (1985). This was achieved by adding monazite, xenotime and trace element-free fluorapatite to the whole rock in such proportions that P, Ce, La, Nd, Y and Th approximated the Taylor and McLennan (1985) values. The stoichiometric monazite composition used was the average of over 5000 published analyses (Chapter 4) in a proportion of 0.00008. Stoichiometric flourapatite and xenotime were used in proportions of 0.00345 and 0.000017, respectively.

Open system processes were simulated by

Table 4. Bulk compositions used in calculation of phase equilibrium models.

Comp.	**C1 original**	**C1** P0 30	**C1** P0 10	**C1** P0 05	**C1** 2Ca	**C1** 0 5Ca	**C1** 1 5Al	**C1** 0 75Al	**C1** 2REE	**C1**0 5REE	**C1** 2Th	**C1** 0 5Th
Reference	[1]											
line colour	Fig 2a, 3a purple*	Fig 6a,c blue	Fig 6a,c red	Fig 6a,c pink	Fig 7a,c blue	Fig 7a,c red	Fig 8a,c blue	Fig 8a,c red	Fig 9a,c blue	Fig 9a,c red	Fig 10a,c blue	Fig 10a,c red
Major elements (wt%)												
SiO_2	56 05	56 65	56 71	56 54	55 64	59 32	50 95	56 24	56 23	56 24	56 24	56 05
Al_2O_3	20 65	20 87	20 89	20 83	20 50	16 39	28 15	20 72	20 72	20 72	20 72	20 65
MgO	3 09	3 12	3 13	3 12	3 07	3 27	2 81	3 10	3 10	3 10	3 10	3 09
FeO	10 15	10 26	10 27	10 24	10 07	10 74	9 23	10 18	10 18	10 18	10 18	10 15
MnO	0 41	0 41	0 41	0 41	0 41	0 43	0 37	0 41	0 41	0 41	0 41	0 41
CaO	1 46	0 62	0 56	0 74	2 33	1 34	1 17	1 28	1 28	1 28	1 28	1 46
Na_2O	0 68	0 68	0 69	0 68	0 67	0 72	0 62	0 68	0 68	0 68	0 68	0 68
K_2O	5 85	5 91	5 92	5 90	5 81	6 19	5 32	5 87	5 87	5 87	5 87	5 85
H_2O	1 33	1 34	1 34	1 34	1 32	1 40	1 21	1 33	1 33	1 33	1 33	1 33
F	0 026	0 008	0 004	0 013	0 013	0 014	0 013	0 013	0 013	0 013	0 013	0 026
P_2O_5	0 30	0 10	0 05	0 16	0 16	0 16	0 15	0 16	0 16	0 16	0 16	0 30
Trace elements (wt %)												
Y_2O_3	0 0034	0 0033	0 0033	0 0033	0 0033	0 0034	0 0034	0 0032	0 0034	0 0033	0 0034	0 0034
La_2O_3	0 0043	0 0043	0 0043	0 0043	0 0043	0 0043	0 0044	0 0042	0 0022	0 0086	0 0043	0 0043
Ce_2O_3	0 0088	0 0088	0 0088	0 0088	0 0088	0 0088	0 009	0 0085	0 0044	0 0176	0 0088	0 0088
Nd_2O_3	0 0035	0 0035	0 0035	0 0035	0 0035	0 0035	0 0036	0 0034	0 0017	0 007	0 0035	0 0035
ThO_2	0 0017	0 0017	0 0017	0 0017	0 0017	0 0017	0 0017	0 0016	0 0017	0 0017	0 0008	0 0034
Trace elements (ppm)												
Y	26	26	26	26	26	27	27	25	27	26	27	27
La	37	37	37	37	37	37	38	36	19	73	37	37
Ce	75	75	75	75	75	75	77	73	38	150	75	75
Nd	30	30	30	30	30	30	31	29	15	60	30	30
Th	15	15	15	15	15	15	15	14	15	15	7	30

Reference: [1] C1 = Spear & Pyle (2010) * Fig 6-10 only Comp, composition

Table 4(cont). Bulk compositions used in calculation of phase equilibrium models.

Comp.	**C2 original**	**C2** P0 30	**C2** P0 10	**C2** P0 05	**C2** 2Ca	**C2** 0 5Ca	**C2** 1 5Al	**C2** 0 75Al	**C2** 2REE	**C2**0 5REE	**C2** 2Th	**C2** 0 5Th
Reference	[2]											
line colour	Fig 2b, 3b purple*	Fig 6b,d blue	Fig 6b,d red	Fig 6b,d pink	Fig 7b,d blue	Fig 7b,d red	Fig 8b,d blue	Fig 8b,d red	Fig 9b,d blue	Fig 9b,d red	Fig 10b,d blue	Fig 10b,d red
Major elements (wt%)												
SiO_2	63 73	64 05	64 12	62 49	64 71	58 73	66 93	63 96	63 94	63 95	63 95	63 73
Al_2O_3	17 67	17 76	17 78	17 33	17 94	24 42	13 92	17 73	17 73	17 73	17 73	17 67
MgO	2 79	2 81	2 81	2 74	2 84	2 58	2 93	2 80	2 80	2 80	2 80	2 79
FeO	6 27	6 30	6 31	6 15	6 37	5 78	6 58	6 29	6 29	6 29	6 29	6 27
MnO	0 08	0 08	0 08	0 07	0 08	0 07	0 08	0 08	0 08	0 08	0 08	0 08
CaO	2 70	2 44	2 39	4 74	1 38	2 33	2 63	2 52	2 52	2 52	2 52	2 70
Na_2O	1 85	1 85	1 86	1 81	1 87	1 70	1 94	1 85	1 85	1 85	1 85	1 85
K_2O	3 76	3 78	3 79	3 69	3 82	3 47	3 95	3 78	3 78	3 78	3 78	3 76
H_2O	0 80	0 80	0 80	0 78	0 81	0 74	0 84	0 80	0 80	0 80	0 80	0 80
F	0 026	0 008	0 004	0 014	0 014	0 013	0 014	0 014	0 014	0 014	0 014	0 026
P_2O_5	0 31	0 10	0 05	0 16	0 16	0 16	0 17	0 16	0 16	0 16	0 16	0 31
Trace elements (wt %)												
Y_2O_3	0 0034	0 0034	0 0034	0 0034	0 0034	0 0034	0 0033	0 0035	0 0034	0 0034	0 0034	0 0034
La_2O_3	0 0044	0 0044	0 0044	0 0044	0 0044	0 0044	0 0042	0 0044	0 0022	0 0087	0 0044	0 0044
Ce_2O_3	0 0089	0 0089	0 0089	0 0089	0 0089	0 0089	0 0086	0 0091	0 0045	0 0178	0 0089	0 0089
Nd_2O_3	0 0035	0 0035	0 0035	0 0035	0 0036	0 0035	0 0034	0 0036	0 0018	0 0071	0 0035	0 0035
ThO_2	0 0017	0 0017	0 0017	0 0017	0 0017	0 0017	0 0017	0 0017	0 0017	0 0017	0 0009	0 0034
Trace elements (ppm)												
Y	27	27	27	27	27	26	28	27	27	27	27	27
La	38	38	38	38	38	36	38	19	74	38	38	38
Ce	76	76	76	76	76	73	78	38	152	76	76	76
Nd	30	30	30	31	30	29	31	15	61	30	30	30
Th	15	15	15	15	15	15	15	15	15	8	30	15

Reference: [2] C2 = Spear (2010) * Fig 6-10 only Comp, composition

using the automated melt extraction function available in GIBBS. This function calculates at each temperature step (2°C) along an isobaric section for each pressure step (herein 0.05 kbar), extracting melt when a specified threshold is reached. The user specifies both the upper melt volume % threshold which triggers melt extraction and also a lower melt volume % bound which dictates the amount of melt remaining in the rock after melt extraction. The upper and lower bounds used for all thermodynamic models in this study are 7 vol% and 1 vol%, respectively (see Yakymchuk & Brown, 2014b for discussion).

The bulk compositions were all run with excess H2O at the initial, low-T conditions (around 10% by weight). Along each isobaric path, the porosity was kept constant at a low value (0.1-1%) so that any evolved water would be removed from the system thus ensuring that there was little free water available at the H2O-saturated solidus.

Table 4(cont). Bulk compositions used in calculation of phase equilibrium models.

Composition	STF02B	IV16-07
Reference	[3]	[4]
	Fig. 11a,b	Fig. 11c,d
line colour		
Major elements (wt%)		
SiO_2	58.40	56.08
Al_2O_3	25.74	25.18
MgO	2.74	3.96
FeO	3.27	11.71
MnO	0.11	0.13
CaO	0.51	0.52
Na_2O	0.65	0.58
K_2O	7.00	1.42
H_2O	1.40	0.33
F	0.010	0.003
P_2O_5	0.13	0.05
Trace elements (wt %)		
Y_2O_3	0.0043	0.0037
La_2O_3	0.0065	0.0043
Ce_2O_3	0.0126	0.0084
Nd_2O_3	0.0046	0.0033
ThO_2	0.0019	0.0009
Trace elements (ppm)		
Y	34	46
La	55	40
Ce	108	79
Nd	39	31
Th	16	12

References: [3] Chapter 2; [4] Chapter 3

A small amount of melting occurred at the vapor-saturated solidus but the bulk of melting occurred as water was released by the melting of muscovite and/or biotite.

In this study, the range of pressures and temperatures in the calculations covers the known range of suprasolidus monazite stability (Chapter 4) and extends slightly beyond these temperatures and pressures to explore the high temperature limits to monazite stability. Both open and closed system processes are investigated and compared with natural data (Fig. 1). This allows assessment of controls on monazite stability and composition for both these processes.

3 EQUILIBRIUM ASSEMBLAGE DIAGRAMS

The *P–T* equilibrium assemblage diagrams (EADs) for the closed system scenario for the two modelled compositions (Table 4) are shown in Fig. 2 and for open systems in Fig. 3. The silicate mineral assemblages for both compositions are typical of those found in amphibolite and granulite facies metasedimentary rocks. The calculated terminal stability of monazite, apatite, allanite and xenotime for each scenario are shown by the bold and coloured lines in Figs. 2 and 3.

In the closed system, the predicted stability of

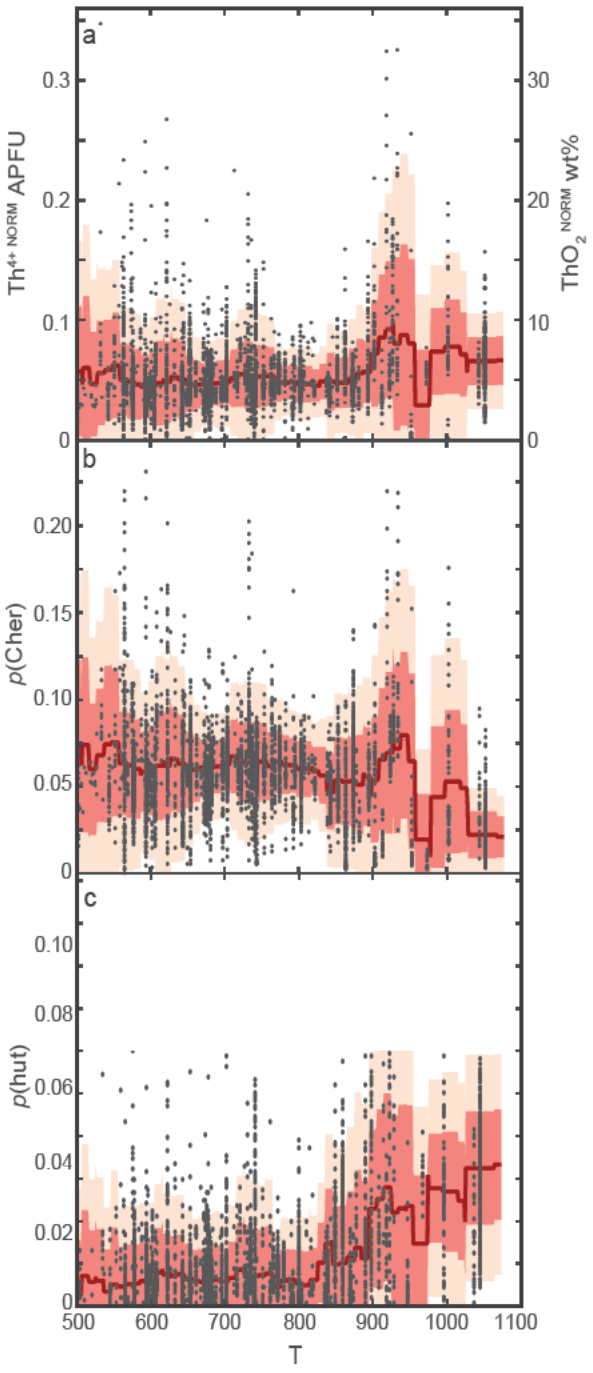

Figure 1. Natural monazite compositional data (Chapter 3) normalised to the modelling chemical system. Monazite compositional variable versus temperature: (a) Thorium in monazite (Th4+NORM) normalised to the modelling chemical system within the monazite A site (Y+Ce+La+Nd+Th+Ca=1) ; (b) the fraction of cheralite in monazite, p(Cher); and (c) the fraction of huttonite in monazite, p(hut).

the four accessory minerals is similar between the two compositions, with three key differences: (1) monazite in composition 1 (C1; Spear and Pyle, 2010) is stable over a smaller temperature window at low pressures than for composition 2 (C2; Spear, 2010); (2) apatite is stable to higher temperatures in C2 relative to C1; and (3) xenotime is stable to higher pressures in C2

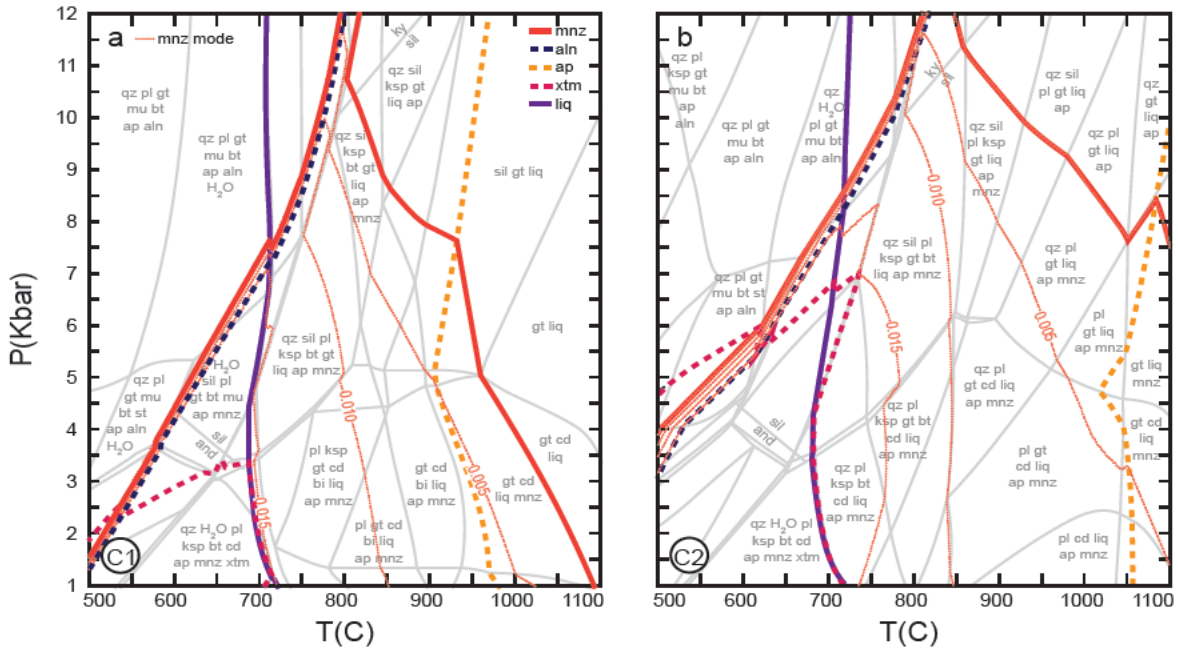

Figure 2. Closed system EADs with monazite modal proportion contours. Circled numbers refer to compositions C1 and C2 (table 4). Bold and bold dashed lines are zero mode boundaries (terminal stability) of phases as denoted on EAD. Orange dotted lines are monazite mode contours.

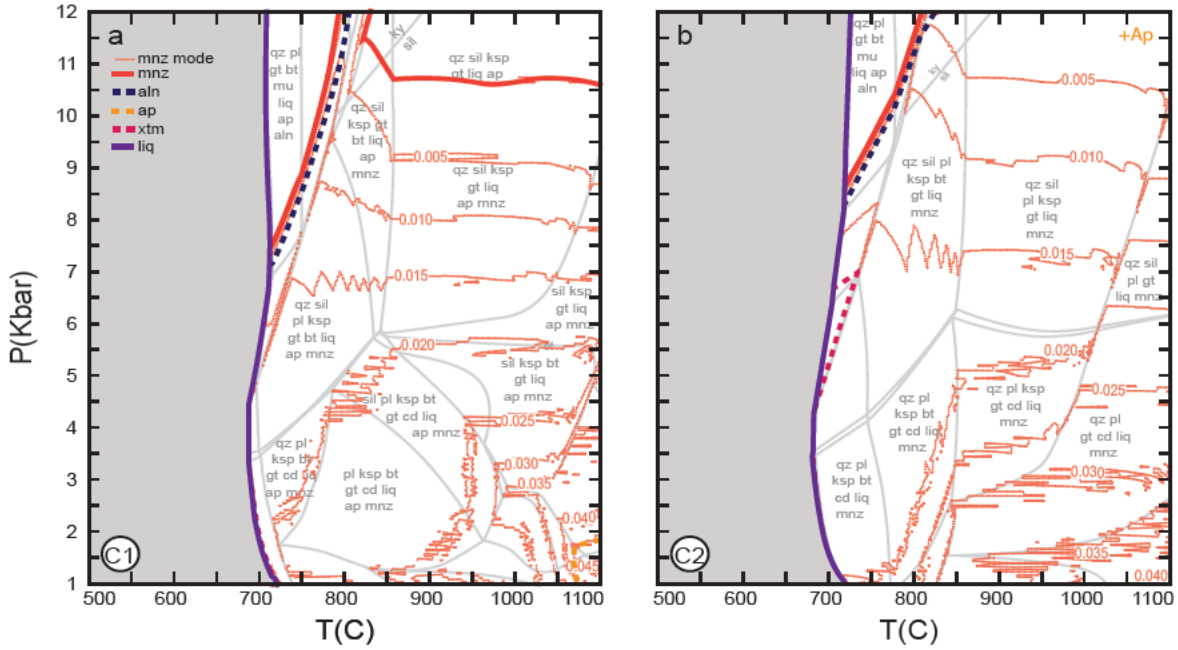

Figure 3. Open system EADs with monazite modal proportion contours. Circled numbers refer to compositions C1 and C2 (table 4). Bold and bold dashed lines are zero mode boundaries (terminal stability) of phases as denoted on EAD. Orange dotted lines are monazite mode contours. Contours appear jagged due to melt extraction algorithm.

relative to C1. In the closed system scenario for both compositions, monazite mode contours are largely vertical, indicating that monazite dissolution into melt is strongly temperature dependent (Fig. 2).

In the open system scenario, the subsolidus fields are identical to the open system and so have been excluded from the diagrams. The predicted stability of the accessory minerals is again similar between the two compositions, C1 and C2. The stability of monazite in C2 extends to higher pressures between ~800 and 1100 °C relative to C1. Additionally, in C1 there is a small region at low pressures and very high temperatures (<2 kbar and >1050°C) where apatite is not stable. Apatite is stable everywhere within the EAD bounds in C2. In contrast to the closed system, monazite modal abundance contours in the open system scenario are sub horizontal across most of the suprasolidus region (Fig. 3). This is

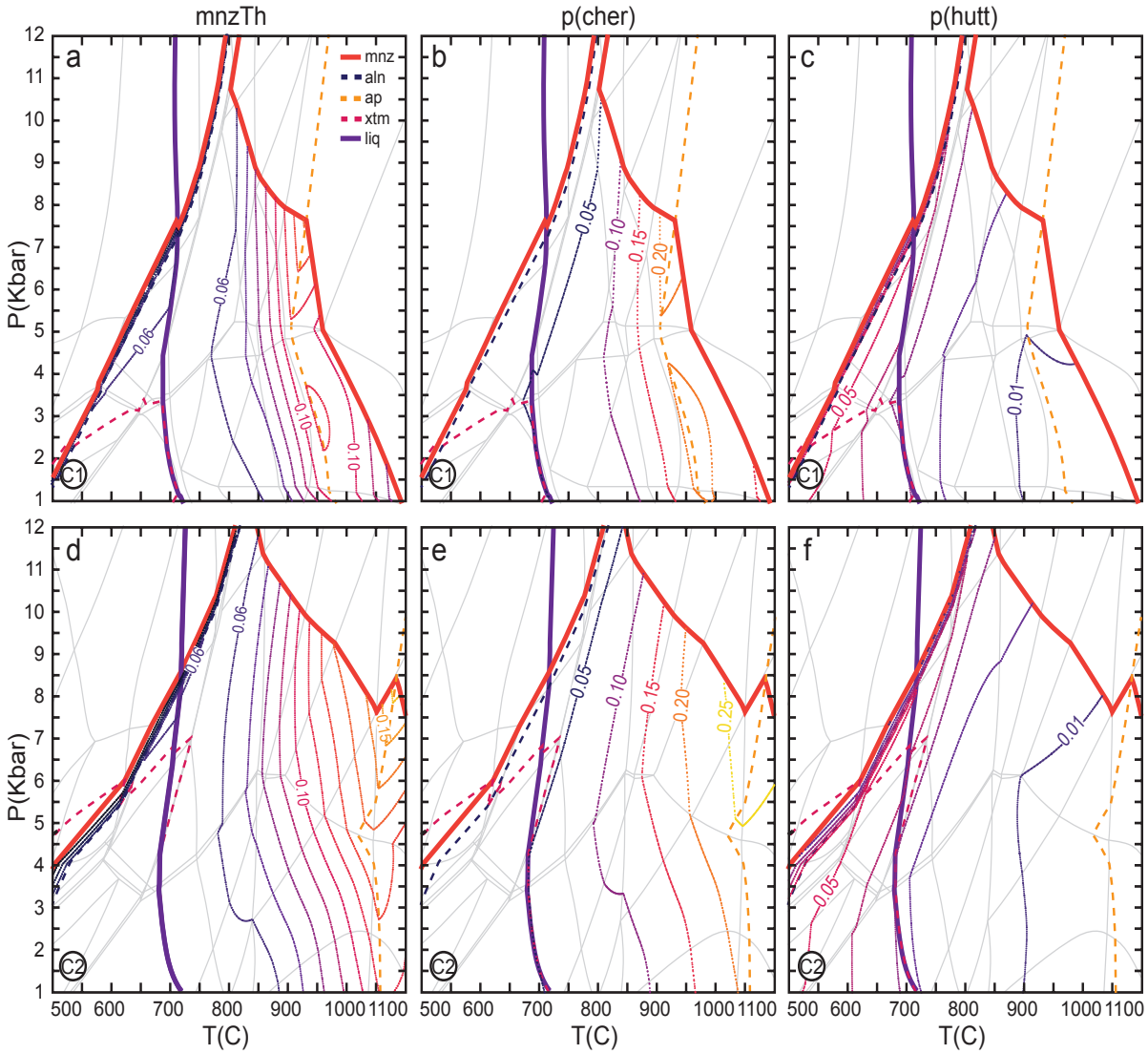

Figure 4. Monazite compositional contours for closed system EADs. (a) shows total mole fraction of Th in monazite (=p(hut)+0.5 x p(cher)) (b) cheralite fraction (c) huttonite fraction.

unexpected and notable because in this scenario, monazite abundance is predicted to remain effectively constant along isobaric heating paths and may even increase during prograde to peak metamorphism along low pressure isobaric paths or clockwise *P–T* paths.

Thorium compositional and endmember fraction contours for the closed system scenarios are shown in Fig. 4 and for the open system in Fig. 5. For both bulk compositions in the closed system scenario, Th-in-monazite contours are subvertical. Total Th-in-monazite fraction is at a minimum at the first (low temperature) appearance of monazite and is at a maximum at the terminal stability of apatite. This maximum in Th-in-monazite is largely a consequence of the cheralite fraction of monazite (Fig. 4). The maximum Th-in-monazite fraction is higher in C2 relative to C1 (0.16 and 0.13 APFU respectively), coincident with apatite being stable to higher temperatures in C2. The huttonite fraction of monazite increases rapidly from the first appearance of monazite to the terminal stability of allanite (temperature window ~10 °C wide). Huttonite fraction then decreases gradually with temperature for both compositions (Fig. 4).

In the open system scenario, Th-in-monazite contours are again sub vertical, but have a sawtooth shape due to the isobaric melt extraction calculation process (Fig. 5). High Th monazite is predicted at high *P–T*, near the terminal stability of monazite. Again, this high Th monazite is a consequence of cheralite fraction rather than huttonite fraction. The maximum concentrations of Th-in-monazite are higher in the open systems (Fig. 5) relative to the closed systems (Fig. 4). This is likely due to the greater stability of apatite in the open systems. Th-in-monazite contours

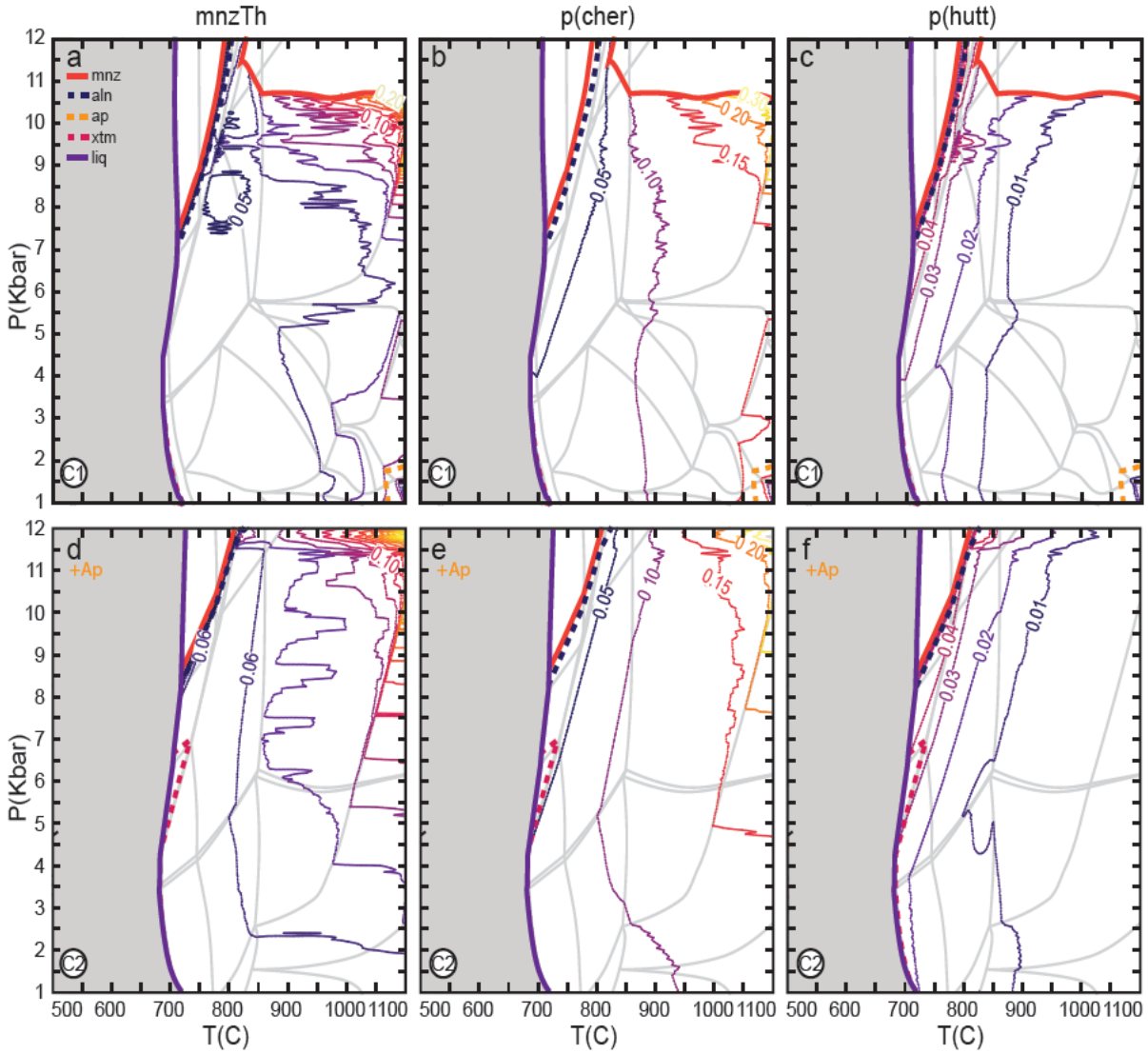

Figure 5. Monazite compositional contours for open system EADs. (a) shows total mole Fraction of Th in monazite (=p(hut)+0.5 x p(cher)) (b) cheralite fraction (c) huttonite fraction.

also follow the shape of the apatite-out line in C1. Th-in-monazite and cheralite contours are sub horizontal beyond the K-feldspar-out line. K-feldspar is unique among the major silicate minerals in its effect on monazite composition.

4 DISCUSSION

4.1 P T extent of monazite stability

The low-temperature appearance of monazite ('monazite-in' boundary) and allanite terminal stability ('allanite-out' boundary) are strongly linked and thus closely coincide in all EADs (Figs. 2–5), with a separation of these boundaries generally <10 °C at all pressures. This is consistent with natural rocks that preserve virtually no record of coexisting prograde allanite and monazite. At subsolidus temperatures, the allanite–monazite transition occurs within the region of the staurolite-out isograd (in EADs where staurolite occurs) consistent with previous estimates (e.g. Goswami-Banerjee & Robyr, 2015; Janots et al., 2008; Smith & Barreiro, 1990; Wing, Ferry, & Harrison, 2003). The allanite to monazite transition also occurs in the region of the first appearance of aluminosilicate in C1 and the high-temperature appearance of aluminosilicate in C2 (aluminosilicate stability field is more convoluted in C2) consistent with previous observations (e.g. Corrie & Kohn, 2008; Kohn & Malloy, 2004). Even in compositions that don't stabilise staurolite (e.g. K08; Appendix S5.1), the allanite to monazite transition occurs in much the same place, which indicates that the relationship between staurolite-out/aluminosilicate-in and the allanite to monazite transition is coincidental rather than causative (Fig. 2; see also appendix S5.1).

The terminal stability of monazite in pelitic compositions was previously calculated to occur

in the temperature range 720–845 °C (Kelsey et al., 2008; Yakymchuk, 2017; Yakymchuk & Brown, 2014a; Yakymchuk et al., 2018) and 840 to >950 °C for open system scenarios (Yakymchuk, 2017; Yakymchuk et al., 2018) based on the experimental solubility equations of Rapp, Ryerson, and Miller (1987) and Stepanov et al. (2012). Calculations from Yakymchuk (2017) and Yakymchuk et al. (2018) suggest that addition of Th to the modelling system increases the terminal stability of monazite by approximately 50 °C. The stability of monazite in closed systems has been extended again in our modelling, with the minimum temperature of the monazite-out line at ~850 °C at 12 kbar and increasing to at least 1100°C at 1 kbar (Fig. 2), and is even higher in the open system (up to 1100°C at 12 kbar for C2). This is most likely due to the extra elements included into our monazite model, particularly Th and Y, as well as the dynamic D values for element partitioning between monazite, melt and apatite with changing *P–T*. The monazite-out line was previously calculated to show a range of positive to vertical slopes (i.e. monazite is at least as stable at high pressures as low pressures; Kelsey et al., 2008; Yakymchuk & Brown, 2014a; Yakymchuk et al., 2018). Our EADs present the opposite slope (i.e. negative) of the monazite-out line (Figs 2–5) so that monazite solubility is more favoured at higher pressures for a given temperature.

There are important differences between the two original compositions modelled: (1) allanite to monazite transition has a steeper slope in C1 than C2; (2) the stability of both monazite and apatite extend to higher temperature in C2; and (3) xenotime stability extends to higher pressure in C2. Overall, C2 is more conducive to the expanded stability of phosphates, despite having the same amount of P, REE and Th as C1.

The slopes of monazite mode contours are distinctly different for closed and open systems. Monazite modal and compositional contours in closed systems are quasi-vertical, as monazite progressively dissolves into (progressively larger volumes of) melt. For the open system scenarios, monazite mode contours are approximately horizontal above the solidus. As such, monazite in these systems is not dissolved with progressive temperature increases, but may be consumed on a prograde path involving pressure increase. Monazite can be stable to very high temperatures in open systems, particularly at higher geothermal gradients.

Once biotite has left the assemblage the orientation of mode contours of major phases, namely garnet, K-feldspar, liquid/melt and plagioclase, becomes more horizontal. Therefore, monazite and apatite dissolution are still responding largely to the behaviour of melt, but there is a more complex interplay overall that involves other major phases as well. The finding that monazite and apatite modes are, at elevated pressures, nearly invariant of pressure is supported by studies that report little change to or increasing monazite mode with increasing temperature, at least up to a temperature around 800 °C or so, in melt-extracted migmatites (e.g. Chapters 2 and 3; Foster et al., 2002; Rubatto et al., 2001; Schulz, 2017; Williams, 2001). The decrease in monazite mode with increasing pressure can be understood by reference back to the closed system scenario. There, monazite mode at higher pressure isn't necessarily a function of greater solubility (c.f. Montel, 1986; Rapp et al., 1987; Rapp & Watson, 1986; Stepanov et al., 2012), but rather a function of the effect that allanite stability exerts on LREE and Th at earlier stages of heating above the solidus. This is an effect that carries over into the open system case to ultimately control monazite mode.

Contrary to previous modelling studies, our EADs present possibilities for monazite retention (and perhaps even growth) above the solidus along a prograde path, depending on the shape of the *P–T* path (Fig. 3). This is particularly true of clockwise *P–T* paths and open systems. Previous models could not predict monazite growth with heating above the solidus due to the nature of the definition of those modelling frameworks (Kelsey et al., 2008; Yakymchuk, 2017; Yakymchuk & Brown, 2014a; Yakymchuk et al., 2018). Studies of natural samples show that monazite mode commonly progressively increases above the solidus (e.g. Chapters 2 and 3; Foster et al., 2002; Franz, Andrehs, & Rhede, 1996; Rubatto et al., 2001; Schulz, 2017; Skrzypek et al., 2018; Williams, 2001) and this is an important observation to keep in mind when comparing forward models to natural rocks.

4.2 Th in monazite

There has been much speculation on the influence of Th on modifying the dissolution behaviour of monazite (e.g. Rapp et al., 1987; Rapp & Watson, 1986; Skora & Blundy, 2010; Stepanov et al., 2012;

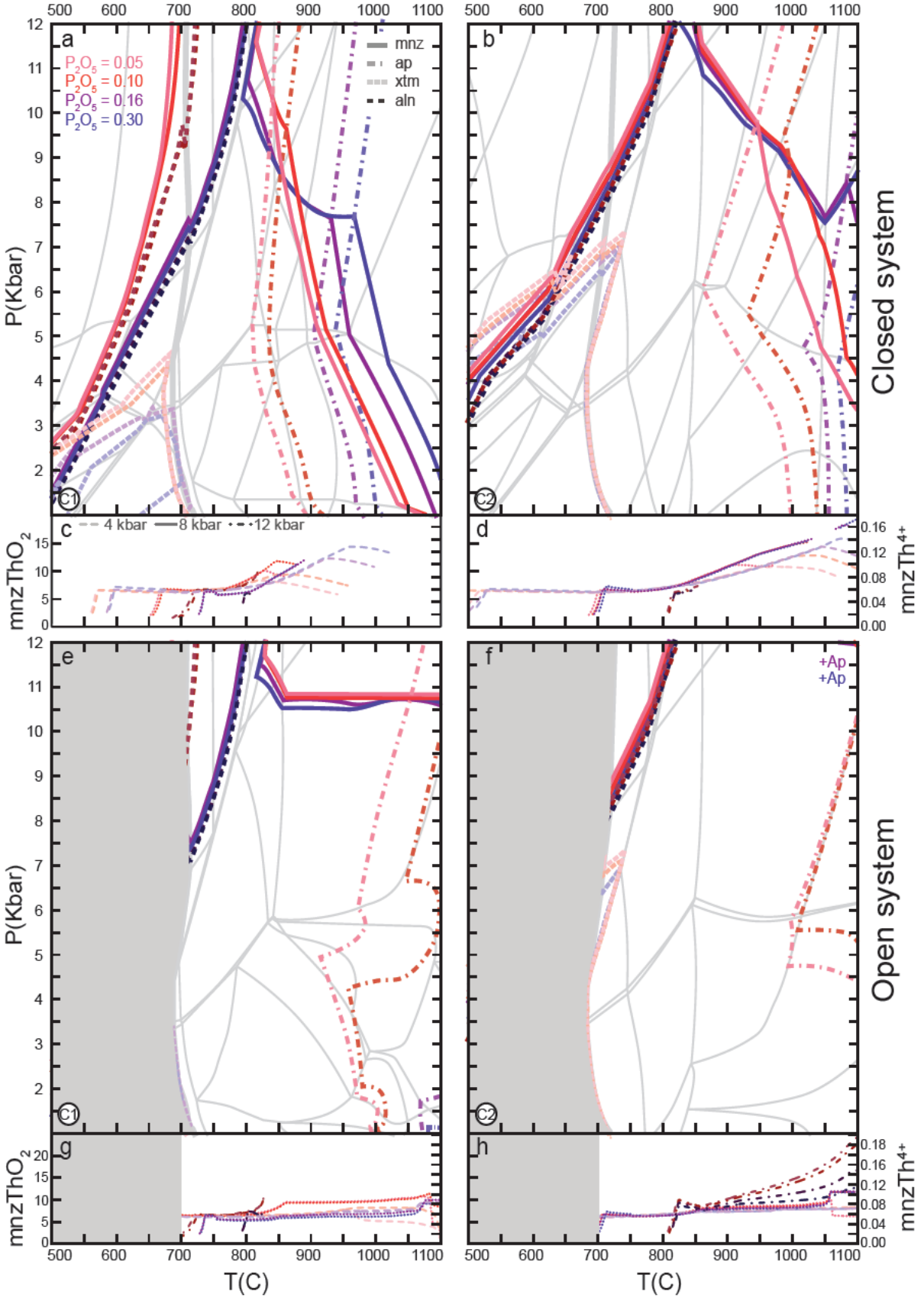

Figure 6. P T EADs at four different bulk P_2O_5 contents (see Table 4). Parts (a), (b), (e) and (f) show phosphate mineral stability and parts (c), (d), (g) and (h) show Th in monazite. Purple lines represent original C1 and C2 compositions presented in Table 4 and Figs. 2 5. P_2O_5 values (wt%) for all diagrams given in part (a).

Yakymchuk, 2017; Yakymchuk & Brown, 2019; Yakymchuk et al., 2018). Until now, this has proven difficult to quantify due to the absence of an adaptable, predictive thermodynamic framework such as that presented here. The thermodynamic models presented herein are the first explicitly incorporating Th as cheralite and huttonite into the calculated phase equilibria and thus provide the opportunity to understand the topology of the EADs and factors controlling the fractions of these components in monazite.

A trend of increasing total Th-in-monazite with temperature is predicted by Yakymchuk et al. (2018) in both open and closed systems. A similar trend in Th-in-monazite is observed in both C1 and C2 closed system EADs at all pressures. Both our EADs and those of Yakymchuk et al. (2018) show a similar flat-sloped Th-in-monazite trend with temperature in response to open system melting, except at high pressures (Fig. 6). The high pressure open system trends are similar to the increasing trends of the closed system EADs.

The concentration of Th-in-monazite at the solidus within the EADs presented in Fig. 2 is approximately 0.06 APFU (equivalent to ~6 wt%). This is slightly higher than the equivalent value from Yakymchuk et al. (2018) of 5 wt%. The modelling of Yakymchuk et al. (2018) shows that around 20% of the whole rock Th may be accounted for by the major silicate minerals at the solidus. This fraction decreases with increases in temperature, largely through interaction with melt. Our thermodynamic models do not account for Th included in the major silicate minerals, but we use similar bulk rock concentrations of Th to those of Yakymchuk et al. (2018). This extra 20% Th available to monazite in our models is reflected in the slightly higher composition of Th-in-monazite at the solidus, which is still well within the 1SD range of Th-in-monazite compositions from our global dataset (Fig. 1; Chapter 4).

Maximum Th-in-monazite predicted by our EADs in the closed system (0.13 and 0.16 Th^{4+} equivalent to 14 and 17 wt% ThO_2 for C1 and C2, respectively) occur at suprasolidus conditions and are somewhat lower than those predicted by Yakymchuk et al. (2018) (>20 wt% ThO_2). Notably, the maximum ThO_2 values in the modelling by Yakymchuk et al. (2018) occur at the final increment of dissolution of monazite into melt, whereas in our EADs the maximum ThO_2 is at the apatite-out boundary as previously stated.

For our EADs, the position of terminal apatite stability significantly changes the absolute maximum Th concentration and cheralite fraction in monazite. The apatite-out boundary occurs at higher temperatures in C2 which increases the maximum Th-in-monazite in C2 to greater than in C1 (see Fig. 4). Otherwise, the location of the same absolute fraction contours of Th-in-monazite and cheralite and huttonite fraction are very similar for C1 and C2. The C1 and C2 compositions have distinct differences in the major element chemistry (Table 4) but very similar trace element chemistry (by design). This suggests that Th-in-monazite is not overly affected by changes to the major element chemistry and is discussed further below.

Monazite rapidly changes composition from low Th (~0.03 Th^{4+}) to moderate Th (~0.06 Th^{4+}) monazite over the first ~10 °C of monazite stability. In line with these findings, natural monazite preserves highly variable Th contents at low temperatures (Fig. 1; Chapter 4). The common interpretation from the internal structure of natural monazite is that the first generation of monazite is very LREE-rich and Th-poor, rapidly followed by more Th-rich and LREE-poor monazite (e.g. Chapters 2 and 3; Corrie & Kohn, 2008; Gasser, Bruand, Rubatto, & Stüwe, 2012; Goswami-Banerjee & Robyr, 2015; Janots et al., 2008; Kohn & Malloy, 2004; Skrzypek et al., 2018; Smith & Barreiro, 1990), which is supported by the EADs presented here. Natural data commonly shows even higher Th contents in some low temperature monazite (up to 0.25 APFU Th at 550°C, Fig. 1), but the EADs presented here are not consistent with such high Th monazite at low temperature.

4.3 Bulk rock composition

Previous studies have explored the effect of changing whole rock composition on monazite stability (e.g. LREE, Kelsey et al., 2008; Al and Ca, Spear, 2010; P, Yakymchuk, 2017). To date, none have explored the role that Th plays. We explore the effect of each of these elements on monazite stability and total Th-in-monazite below.

4.3.1 Bulk P_2O_5

Changes to whole rock P_2O_5 have negligible effect on the position of the allanite to monazite transition (Fig. 6a and b), with the exception of the difference between 0.16% and 0.10% P_2O_5 in C1 (purple and red lines respectively; Fig.

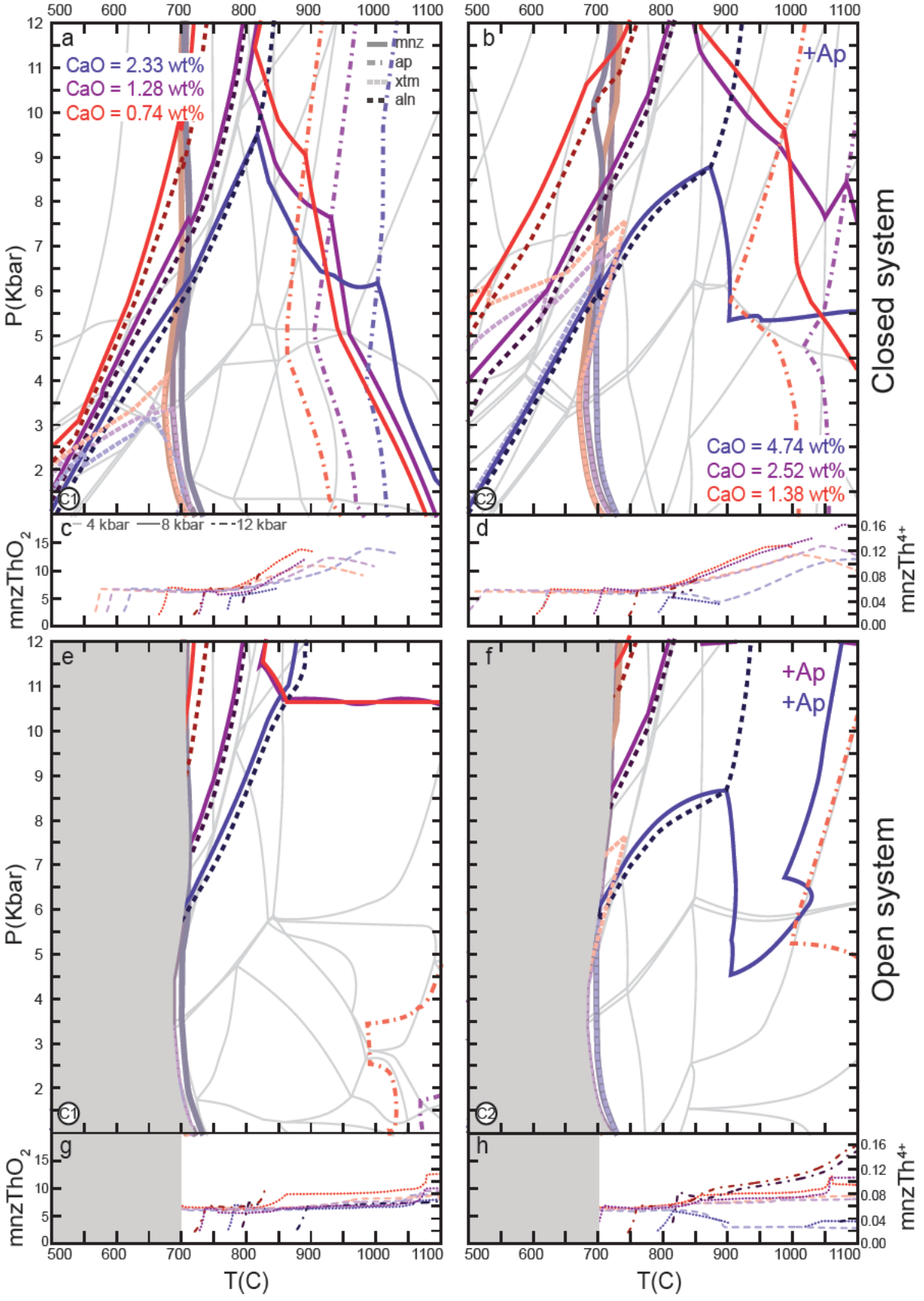

Figure 7.P T EADs at three different bulk CaO contents (see Table 4). Parts (a), (b), (e) and (f) show phosphate mineral stability and parts (c), (d), (g) and (h) show Th in monazite. Purple lines represent original C1 and C2 compositions presented in Table 4 and Figs. 2 5. CaO values (wt%) for all diagrams given in part (a).

6a). A decrease in whole rock P_2O_5 results in a modest decrease of monazite stability at high temperatures (>900 °C) and low to moderate pressures (<8 kbar; Fig. 6). This change has the opposite effect at higher pressures (>8 kbar), although the magnitude of the change is smaller at high pressures (Fig. 6). The inflection point between increased and decreased stability of monazite is the intersection of the monazite and apatite terminal stability contours.

Th-in monazite is ~0.06 Th^{4+} for all scenarios in Fig. 6 (whole rock P_2O_5 changes, open and closed systems) below ~ 800°C for all isobaric transects to highlight composition (4, 8 and 12 kbar; Fig. 6). At low pressures, the onset of monazite growth from allanite is marked by a rapid change from low (0.01 Th^{4+}) to moderate (0.06 Th^{4+}) Th concentrations in monazite (C1, Fig. 6, see above). Above ~800 °C, the response of Th-in-monazite to the variations of the bulk composition and melting parameters is much more heterogeneous. This onset of different responses closely coincides with the terminal stability boundary of plagioclase (Figs. 2 and 3). The range of P contents examined here is equivalent to that used in Yakymchuk (2017). More P expands monazite (and apatite) stability to higher temperature and reduces xenotime stability in our calculations.

4.3.2 Bulk CaO and Al_2O_3

Dependence of monazite stability on the bulk rock CaO content is apparent in Fig. 7 (see also Spear, 2010). Decreasing bulk CaO expands the stability of monazite to higher pressure, particularly around the solidus, but reduces mnz stability at high temperature, at least in the closed system scenario. The allanite to monazite transition moves significantly in each scenario, particularly at high pressure (Fig. 7). Increases to bulk CaO expand apatite stability to higher temperatures. This affects the shape and orientation of the monazite terminal stability boundary (e.g. Fig. 7b).

The high CaO bulk compositions in the open system scenarios present some interesting findings regarding monazite terminal stability. The high CaO scenario in C1 produces a monazite out boundary at >12kbar, at higher pressure than either the original or low Ca open system scenarios for C1. This is the opposite to how C1 responds to high CaO in the closed system scenario (i.e. the stability of monazite is constrained to lower pressures in higher CaO compositions). This seems to be a product of the unique organisation of the allanite to monazite transition relative to the muscovite to peritectic K-feldspar reaction for this composition. The high CaO scenario for C2 is also unusual, with a highly convoluted monazite terminal stability boundary (Fig. 7f). For a heating path, this stability field would produce discontinuous monazite growth.

Changes in whole rock Al_2O_3 have similar, but opposite effects to whole rock CaO (Fig. 8). The exception to this is that the allanite to monazite transition is less affected by changes in Al_2O_3 than CaO. The changes presented in Fig. 8 are consistent with the findings of Spear (2010).

4.3.3 Bulk LREE and Th

Monazite stability changes in response to bulk LREE are explored in Fig. 9 and are consistent with the findings of Kelsey et al. (2008) and Yakymchuk (2017). Higher LREE in the bulk composition expands the stability of monazite above the solidus. These changes in LREE make little difference to the location of the first (low temperature) appearance of monazite, but do increase the temperature difference between of the monazite-in and allanite-out boundaries (Fig. 9). The position of the apatite-out boundaries do not change with LREE and the effect on xenotime stability is limited.

By contrast, changes to bulk rock Th (Fig. 10) result in much less significant change to the position of the monazite terminal stability boundary, limited change to the location of the allanite to monazite transition and xenotime stability field, and no change to apatite terminal stability (Fig. 10). This result is somewhat surprising as the incorporation of Th and other elements into the model chemical system result in an overall increase in the temperature of: (a) the allanite to monazite transition compared to Spear (2010) and (b) the high-temperature terminal stability of monazite. However, both the sensitivity of monazite stability to changes in bulk LREE and the lack of change in response to bulk rock Th can be explained by monazite mode changes. Adding LREE to the bulk rock increases the mode of monazite as LREE are essential structural components of monazite. Conversely, changes to bulk Th have less effect because Th participates in solid solution, but the Th endmembers typically only constitute around 5–10% of total monazite (p(REEmnz) + p(cher) + p(hutt) = 1). This means that even doubling Th in

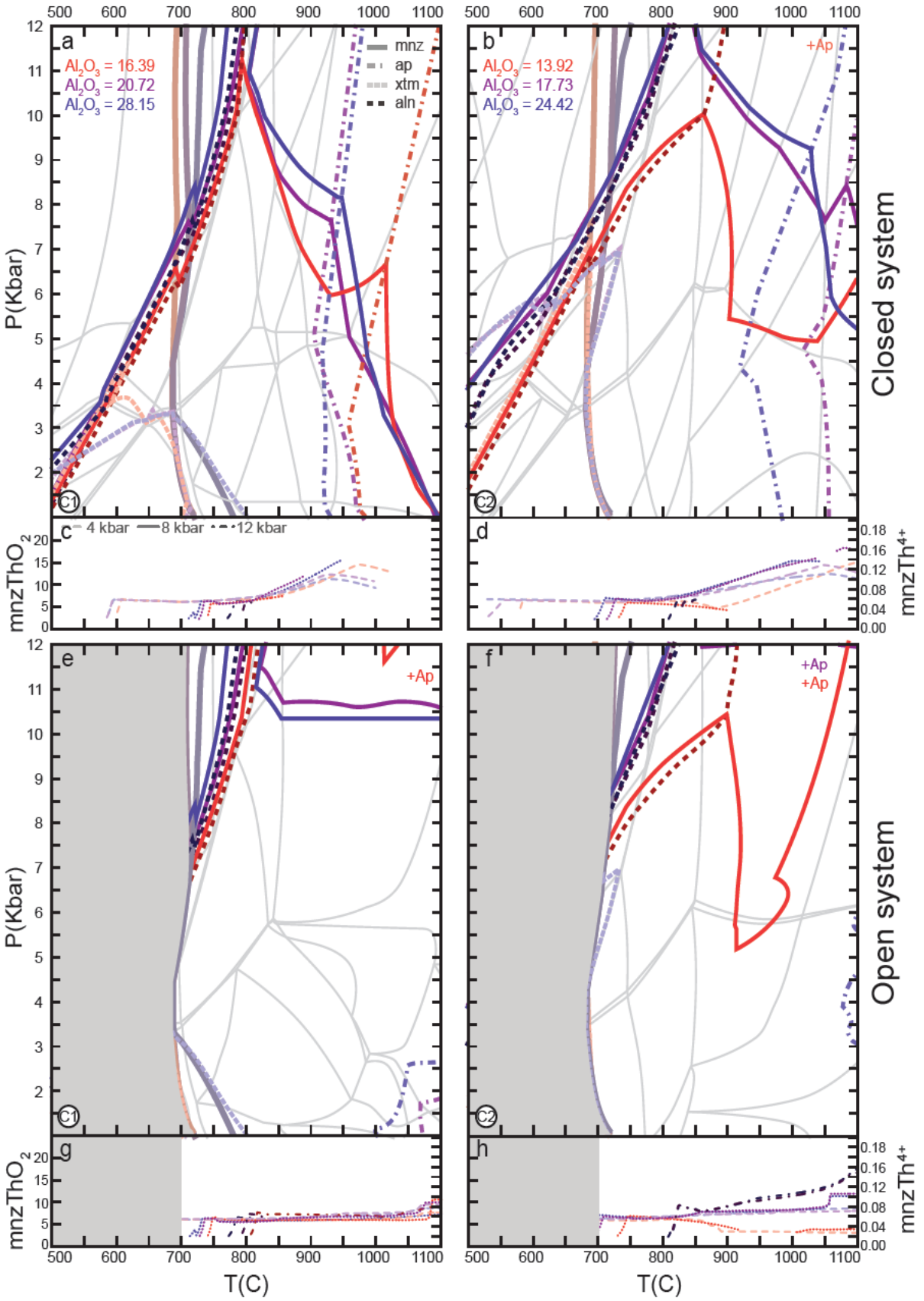

Figure 8. P T EADs at three different bulk Al_2O_3 contents (see Table 4). Parts (a), (b), (e) and (f) show phosphate mineral stability and parts (c), (d), (g) and (h) show Th in monazite. Purple lines represent original C1 and C2 compositions presented in Table 4 and Figs. 2 5. Al_2O_3 values (wt%) for all diagrams given in part (a).

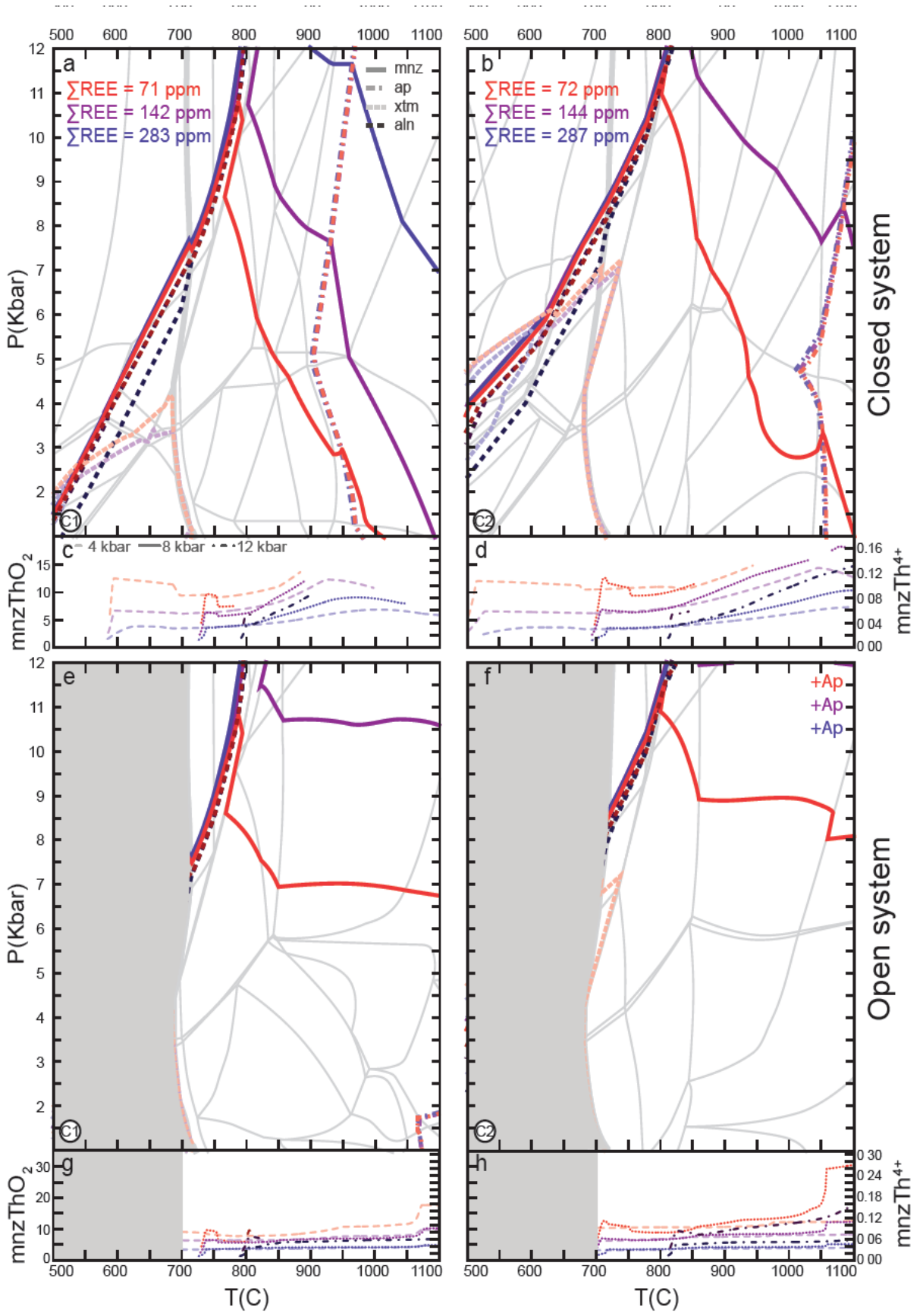

Figure 9. P T EADs at three different bulk ΣLREE contents (see Table 4). Parts (a), (b), (e) and (f) show phosphate mineral stability and parts (c), (d), (g) and (h) show Th in monazite. Purple lines represent original C1 and C2 compositions presented in Table 4 and Figs. 2 5. ΣLREE values (ppm) for all diagrams given in part (a). Note change in scale between mnzTh for closed and open scenarios.

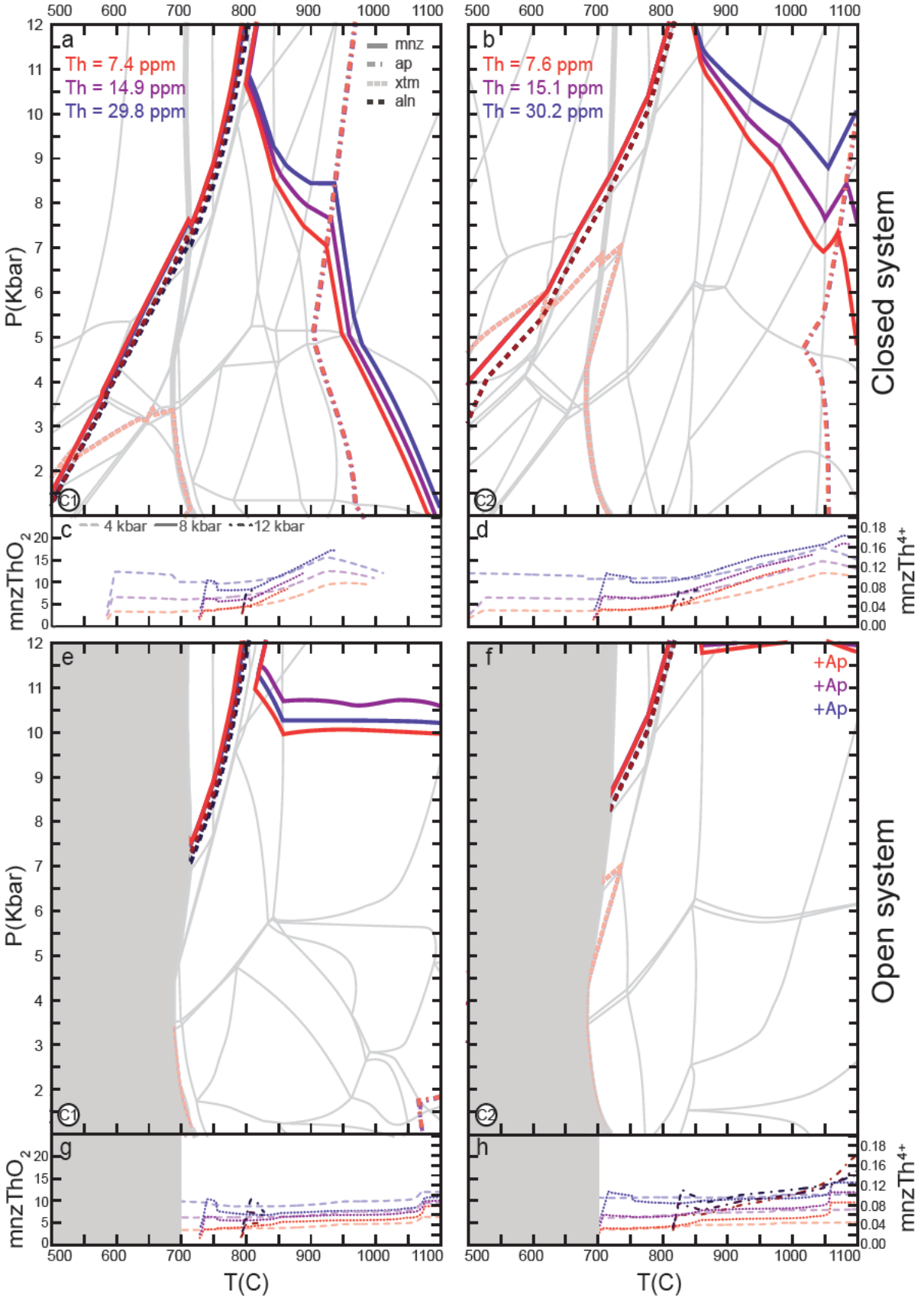

Figure 10. P T EADs at three different bulk Th contents (see Table 4). Parts (a), (b), (e) and (f) show phosphate mineral stability and parts (c), (d), (g) and (h) show Th in monazite. Purple lines represent original C1 and C2 compositions presented in Table 4 and Figs. 2 5. Th values (ppm) for all diagrams given in part (a).

the bulk composition only slightly increases the total mode of monazite but makes the monazite comparatively much more Th-rich (e.g. Fig. 10).

Higher whole rock LREE also decreases the amount of Th contained in monazite, even though the total whole rock Th does not change in these scenarios (Fig. 9). This is because increases in LREE causes increases to monazite mode which dilutes Th-in-monazite. Highly enriched Th concentrations are predicted in the open system scenario for the low LREE C2 composition (mnzThO_2 >30 wt% at 8kbar and >1050 °C; Fig. 9h). This super-enrichment of Th-in-monazite is consistent with low monazite mode owing to low bulk REE and in this case involves the loss of K-feldspar from the model system. This may represent a mechanism by which monazite can become highly enriched in Th (e.g. UHT monazite, Ivrea–Verbano Zone; Chapter 3). Despite the fact that changes to bulk rock Th have limited effect on the stability of monazite and the other phosphates, they have a similar (but inverse) effect on Th-in-monazite concentrations (Fig. 10). For example, low bulk rock Th translates to low Th-in-monazite compositions (Fig. 10). These observations highlight the crucial need for more monazite and other accessory mineral modal information to be included in natural studies to better understand chemical trends in these minerals.

4.4 Comparison to natural data

Comparison of the results presented here to >5000 published monazite compositions (Fig. 1; Chapter 4) is an essential check of the validity of our modelling approach. The EADs presented herein (Figs. 2–10) replicate both the total amount of Th-in-monazite and trend of Th-in-monazite with temperature from the large dataset from natural samples (Fig. 1). This can be seen by comparing the natural monazite data in Fig. 1 to calculated monazite compositions presented as isobaric transects in Figs. 7–10.

For the temperature interval 500–800 °C, the natural monazite data (Fig. 1) shows a fairly constant mean value of Th-in-monazite at ~0.05 APFU (approximately 5 wt% ThO_2). Over this interval, the standard deviation of the data reduces considerably, from 0.04 to 0.01 APFU. The reasonably constant average Th-in-monazite values over this interval are replicated by the relative flat-sloped trends in Th-in-monazite in the EADs here. There are two effects that likely account for the large variability in the data, particularly at the lower temperature end of this interval. The first is that bulk rock trace element composition has a considerable effect on the subsolidus Th-in-monazite concentration (Figs. 9 & 10). In the EADs we have calculated here for different bulk rock trace element values, subsolidus average Th-in-monazite (4 kbar) ranges from 0.03 to 0.10 APFU (3.1 to 11.4 wt% ThO_2; Figs. 9 & 10). This range is slightly larger than the 1SD range for the natural data over this temperature interval (0.01-0.09 APFU, Fig. 1), but sits within the 2SD range (0-0.13 APFU Th-in-monazite). This confirms that the chosen trace element range for the EADs is reasonable and relevant to the natural data. The second effect that could account for the scatter in the natural data in the temperature window 500-800 °C is the variable temperature of the allanite to monazite transition due to pressure (positive slope) and bulk composition effects. This transition is always accompanied by a sharp increase in the Th-in-monazite concentration over the first ~10°C of monazite stability. The fact that this transition would occur at different temperature in different natural samples (dependent on P-T path and bulk composition) can account for some of the scatter in the natural Th-in-monazite data over this temperature interval. This effect would be limited above approximately 820°C, as this is the maximum temperature of the monazite to allanite transition at 12kbar in our EADs. The first occurrence of monazite may form above these temperatures in some rocks, but such data is very limited within our dataset (Chapter 4).

For temperatures above 800°C, the Th-in-monazite trends for open and closed system melting EADs for the different bulk compositions are highly variable (Figs. 2-10). This is consistent with the increased variability of Th-in-monazite in the natural data, particularly in the temperature interval 800-1000°C. Three factors account for this variability: (1) closed versus open system melting; (2) bulk rock composition; and (3) transect pressure. Calculated monazite mode progressively decreases above the solidus in closed system EADs, particularly at high pressures (Fig. 2). This observation is important as it is very uncommon for natural samples to access and record the metamorphic assemblages at low pressures and UHT temperatures (i.e. extreme thermal gradients) and for this reason the high temperature monazite compositions

included in the natural dataset are for pressures >9kbar. No such decrease in monazite stability with temperature is observed in open system EADs. The natural dataset of monazite contains abundant suprasolidus and granulite facies monazite (Fig. 1). This is not entirely consistent with modelled closed system situations where monazite is progressively dissolved above the solidus. Open system behaviour is therefore likely to be an important reason for the persistence of monazite to high temperatures in anatectic rocks.

Natural UHT monazite that is particularly high in Th is replicated by calculations in low LREE, open systems where apatite is present. However, the Th fraction of monazite at high temperatures in the EADs is dominated by cheralite (e.g. Figs 4 and 5). In the natural data, there is a population of high-Th monazite enriched in the huttonite endmember, based on EPMA derived Si cations, (as well as the cheralite endmember) which is not replicated by these EADs. The compositions of UHT monazite in the natural dataset come from a small number of locations which may not be entirely representative of global monazite trends, particularly if the high variability of Th-in-monazite presented in these EADs is a true indication. The EADs also confirm the work of other studies which found that monazite mode in UHT samples is typically low (e.g. Chapter 3). This is replicated by the closed system EADs presented here and provides a compelling reason why UHT monazite should be, and typically is rare in nature. Further detailed investigation of monazite mode and compositions in known UHT locations would be welcome given the potential that such monazite could record UHT compositions (e.g. Chapter 3; Korhonen, Clark, Brown, Bhattacharya, & Taylor, 2013; Suzuki, Arima, Williams, Shiraishi, & Kagami, 2006; Walsh et al., 2015). However, the virtually impossible challenge in such terranes is knowing what the abundance of monazite was in lower-grade equivalents of the UHT rocks.

4.5 Application to Mt Stafford and the Ivrea Verbano Zone

Monazite as modelled in the preceding sections shows a range of compositions which are consistent in range and absolute amount to natural monazites within our global dataset. As such, these thermodynamic models may assist in understanding the complex zoning patterns seen in natural monazite. By specifically linking individual monazite compositional (and age) zones to *P–T* conditions, detailed *P–T–t* information can be extracted from monazite. Extracting *P–T* information directly from monazite may improve the precision and detail that can be extracted from individual monazite grains and reduces the reliance on finding monazite–xenotime or monazite–garnet grains which show equilibrium characteristics. This approach could also help to clarify when monazite grew relative to other minerals when textural or geochronological observations are unclear. Whereas this contribution has focussed on Th-in-monazite, other compositional endmembers of monazite and other minerals are all calculated simultaneously in this framework and can be assessed to understand the relationships between minerals of different compositions.

The application of the modelling framework to specific natural samples is a further useful check of whether these thermodynamic models are to be widely applicable. Here we explore the application of the thermodynamic models to one natural rock composition from Mt Stafford (STF) and the Ivrea–Verbano Zone (IVZ). This application will be restricted to subsolidus rocks for the sake of simplicity (particularly around open vs closed system melting). The selected compositions are both from amphibolite facies, subsolidus rocks (Table 4; Chapters 2 and 3). Both of these samples show multiple monazite chemical zones, described in full in chapter 2 (STF) and chapter 3 (IVZ) and summarised in Fig. 11 and appendix S5.3.

The peak mineral assemblage field for STF02B is consistent with the previous P–T estimate of 2.55 kbar and 620 °C for the sample (projected from White, Powell, & Clarke, 2003), but also extends to lower pressures and temperatures (Fig. 11a & b). The monazite composition range for zone B (rims of grains in STF02B) overlaps with the peak mineral assemblage field (Fig. 11b), and constrains the peak of metamorphism in this sample to <3.5 kbar and 460–600 °C, at slightly lower temperature than the previous estimate for this sample. The monazite compositional range for zone A (low temperature metamorphic origin, cores of grains in STF02B; Chapter 2) occurs near the first appearance of monazite at lower temperatures (~360 °) and slightly higher pressures than zone B. The current field of overlap for two of Ce, Th and Y (lowest temperature light yellow field; Fig. 11a) is consistent with the location of zone A in cores of grains in STF02B

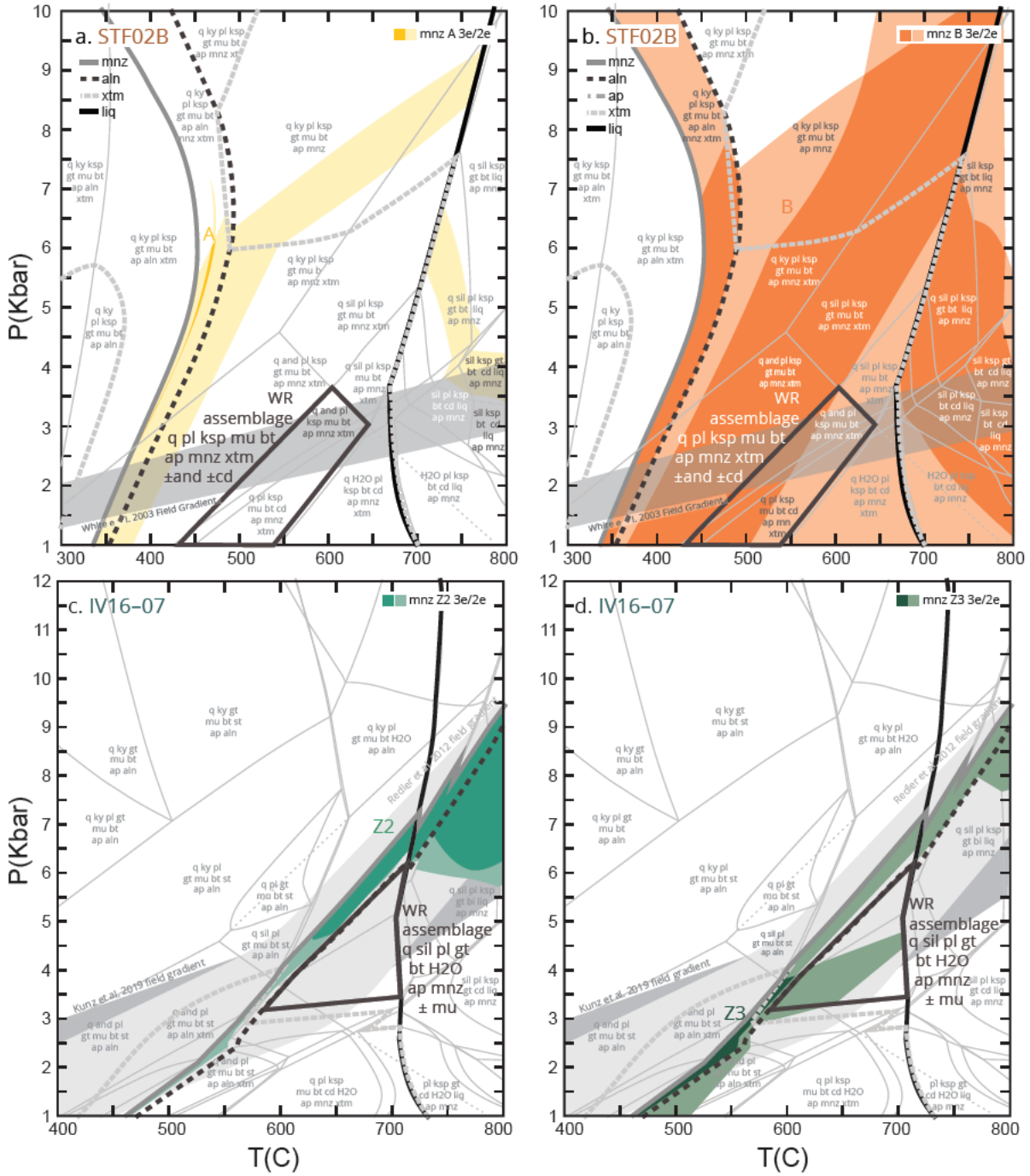

Figure 11. Closed system EADs for bulk compositions from Mt Staff ord and the Ivrea Verbano Zone. Coloured regions show the fi elds of overlapping calculated monazite compositional contours (Ce, Y and Th) equivalent to the measured composition of monazite. Compositional contours are plotted for the 2SD range on the mean measured for each element and zone as defi ned in Chapters 2 and 3. An additional 75% Th error has been added to Ce and Th contours to account for error in WR Th values (see appendix S5.3). Bold colours indicate regions where Ce, Y and Th contours overlap ('3e'); pale colours indicate regions where two compositional contours overlap ('2e'). Grey bands indicate the previous constrained P T gradients for the terranes (Redler, Johnson, White, & Kunz, 2012; White, Powell, & Clarke, 2003). Compositional contours shown are: (a) Mt Staff ord, Zone A (cores of grains in STF02B); (b) Mt Staff ord, Zone B (rims of grains in STF02B); (c) Ivrea Verbano Zone, zone Z2 (cores of grains in IV16 07); and (d) Ivrea Verbano Zone, zone Z3 (rims of grains in IV16 07). Peak mineral assemblages for STF02B (a & b) and IV16 07 (c & d) are shown by bold dark grey lines.

and the ubiquitous presence of zone A monazite in the lowest grade samples from the sequence (Chapter 2).

The peak mineral assemblage field for IV16-07 is consistent with previous P-T estimates of 5.4 kbar and 680 °C for IV16-07 (Fig. 11 c & d; Kunz & White, 2019; Redler, Johnson, White, & Kunz, 2012)NW Italy, but also extends to lower pressures and temperatures. The monazite compositional ranges for both Z2 and Z3 monazite occur at least partly down temperature of the whole rock assemblage field for IV16-07. The field of compositional overlap (3 contours) for Z2 monazite (Fig. 11c) occurs at higher pressures than Z3 monazite (Fig. 11d).

The location of the Z3 monazite compositional range, down pressure from the Z2 range indicates that this zone most likely formed on the retrograde part of a clockwise path. This is at odds with our initial interpretation of the relationship of these two zones: that both Z2 and Z3 were formed on the prograde path. The original assumption in chapter 3 was that monazite and xenotime grew in equilibrium with each other as they occupy the same microstructural location (solely within the matrix). It was also assumed in the original interpretation in chapter 3 that Y-in-monazite was correlated with temperature, and thus that Z3 monazite (with much higher Y-in-monazite) must have formed at higher temperatures than Z2 (e.g. Pyle & Spear, 2003).

The EADs for STF02B produce a very small field of overlap between the compositional contours (Ce, Th and Y) for monazite zone A (Fig. 11a) and a very large field of overlap for monazite zone B (Fig. 11b). It is expected that more precise whole rock geochemistry would produce a field of overlap between Th, Ce and Y for zone A which extends further down pressure adjacent to the first appearance of monazite. More precise bulk geochemistry would also likely decrease the area of overlap for zone B. This is because monazite composition is quite sensitive to trace element chemistry, particularly Th (see Fig. 10). An increase of Th-in-monazite results in a commensurate decrease in REE-in-monazite (Y-in-monazite is largely unaffected). Therefore if bulk Th is too high, as is expected to be the case here (see appendix S5.3), its impact is to change the position of both the Ce and the Th contours. Where monazite composition changes rapidly, such as near the first (low-temperature) appearance of monazite (e.g. STF zone A), this can result in the compositional contours of monazite not overlapping. In the case of IV16-07, lower bulk Th would result in regions of overlap for Z2 and Z3 compositional contours which also overlap the whole rock assemblage field. This would be more consistent with the interpretations from the rock that monazite grew concurrently with the peak mineral assemblage (Chapter 3).

If the errors on the bulk rock Th are very large, as is the case here, it can result in very large fields in areas where monazite composition is relatively unchanging (e.g. STF zone B, Fig. 11b). It may also be that in natural rocks there is some incorporation of the trace elements into silicate minerals which is not accounted for in these thermodynamic models. This is mostly thought to be the case for garnet, which is not present in sample STF02B but is present in IV16-07, so can only have an effect in the latter (see Yakymchuk & Brown, 2019).

Although these thermodynamic models aren't necessarily definitive, we have shown that within the limitations (uncertainty) of measured whole rock geochemistry they have competently predicted the integrated monazite and major mineral evolution of these two natural rocks. This is a very pleasing outcome, therefore these thermodynamic models represent an important step towards integrating monazite geochemistry (and geochronology) with *P–T* modelling and show promise for this endeavour moving forward.

4.6 Implications for accessory mineral petrology

This equilibrium thermodynamics approach is a major step forward for integrating accessory minerals into modern metamorphic petrology approaches. The integration of accessory minerals into phase equilibria modelling was discussed in Engi (2017) as being one of only three key directions for future development in accessory mineral petrology and petrochronology research. The thermodynamic model framework we have developed already provides some powerful benefits over existing techniques: (1) the four major phosphate and accessory minerals (monazite, allanite, apatite and xenotime) are all included; (2) calculations involving accessory minerals are fully integrated into the calculation of the EAD, rather than calculated externally and separately as a function of melt composition; (3) the calculations, including the melt loss routine, are automated, reducing the

calculation time to minutes or hours for diagrams such as presented here; (4) the calculations are readily adaptable to any realistic aluminous metasedimentary and granitic bulk composition; and (5) the monazite activity–composition (*a–x*) model includes the vast majority of the major compositional components of monazite, which typically comprise over 90 wt% of the total oxide of natural monazite compositions. More targeted petrological experiments on apatite and/or monazite behaviour in granitic melt-bearing systems could be conducted to improve future iterations of these thermodynamic models.

The ability to readily conduct these calculations opens up a range of potential applications in petrochronology. They allow investigation of subsolidus and prograde metamorphic processes involving accessory minerals. The thermodynamic models can be applied to better understand the formation of specific phosphate microstructures where detailed petrographic analysis has shown the evolution of the phosphate assemblage or composition (e.g. Chapters 2 and 3). The most powerful application for this framework will be by combining this modelling with geochronology to better assess geospeedometry, i.e. putting absolute time into *P–T–t*(*–D*) paths. This application has the potential to significantly further our understanding of the rates of tectonic processes, particularly in the deep crust. As melt is calculated to contain trace element, our modelling framework opens up the study of magmatic processes tracked via trace elements such as Y, La and Th.

The calculated composition field for STF monazite zone B (Fig. 11b) provides a possible explanation for the observations that monazite chemical zones can contain more than one isotopic (age) zone. This same compositional zone intersects the previously established P-T path for Mt Stafford (White et al., 2003) three times below the peak temperature for the terrane (820°C; Fig. 11b; White et al. 2003). This could indicate that in the highest temperature rocks in the region, the same apparent compositional zone, when taken as a range as we have done here, could contain as many as 6 isotopic zones or ages (3 prograde and 3 retrograde) depending on the reactivity and preservation of monazite. Future, detailed studies of monazite chemical and isotopic composition could leverage this modelling technique to improve the understanding of monazite growth in complex or indistinct cases. Overall, these EADs show just how varied the response of monazite chemistry could be to metamorphism depending on bulk chemistry, *P-T* path and melting conditions. It also provides the tool for examining these complex behaviours.

5 CONCLUSIONS

Calculated equilibrium thermodynamic EADs show that monazite is stable over the *P–T* range 1–12 kbar and 500 –1000 °C in a closed system. The monazite stability field is approximately triangular, with monazite stable over a restricted temperature range at high pressures that intersects with the solidus. In open systems, monazite is stable to >1100°C up to ~10 kbar and sometimes higher. Low Th monazite occurs in a narrow field immediately up temperature of the first appearance of monazite, corresponding to the area where allanite and monazite coexist. High Th monazite occurs at high pressures and temperatures in open systems. Total Th-in-monazite is relatively stable over the temperature range 600–800 °C regardless of pressure, open or closed melting regimes or major element bulk rock chemistry. Th-in-monazite is variable above ~800 °C, affected by pressure, closed vs open system melting and bulk rock composition. Bulk rock Al_2O_3 and CaO affect the stability of monazite, in line with previous studies, but have a limited effect on Th-in-monazite. The opposite of this is true for bulk rock Th. Bulk rock LREE affects the suprasolidus stability of monazite and also Th-in-monazite. The modelling results presented here closely replicate the results from a recent compilation of >5000 *P–T* linked monazite analyses. This thermodynamic modelling framework shows additional promise in application to natural samples. The monazite compositions from two subsolidus samples were replicated within the uncertainty of the measured monazite and whole rock compositions. This new framework is a powerful tool for investigating a wide range of petrology questions.

SUPPORTING INFORMATION

Appendix S5.1: Spear & Pyle (2010) (C1) and Spear (2010) (C2) diagrams

Appendix S5.2: Additional diagrams and bulk compositions

Appendix S5.3: IVZ + STF modelling methods and diagrams

REFERENCES

Bea, F., & Montero, P. (1999). Behavior of accessory phases and redistribution of Zr, REE, Y, Th, and U during metamorphism and partial melting of metapelites in the lower crust: an example from the Kinzigite Formation of Ivrea Verbano, NW Italy. *Geochimica Et Cosmochimica Acta*, 63(7 8), 1133 1153.

Berman, R. G. (1988). Internally consistent thermodynamic data for minerals in the system Na2O K2O CaO MgO FeO Fe2O3 Al2O3 SiO2 TiO2 H2O CO2. *Journal of Petrology*, 29(2), 445 522.

Brown, M. (2007). Crustal melting and melt extraction, ascent and emplacement in orogens: mechanisms and consequences. *Journal of the Geological Society*, 164(4), 709 730.

Corrie, S. L., & Kohn, M. J. (2008). Trace element distributions in silicates during prograde metamorphic reactions: Implications for monazite formation. *Journal of Metamorphic Geology*, 26(4), 451 464.

Engi, M. (2017). Petrochronology based on REE minerals: monazite, allanite, xenotime, apatite. *Reviews in Mineralogy and Geochemistry*, 83(1), 365 418.

Foster, G., Gibson, H., Parrish, R., Horstwood, M., Fraser, J., & Tindle, A. (2002). Textural, chemical and isotopic insights into the nature and behaviour of metamorphic monazite. *Chemical Geology*, 191(1 3), 183 207.

Franz, G., Andrehs, G., & Rhede, D. (1996). Crystal chemistry of monazite and xenotime from Saxothuringian Moldanubian metapelites, NE Bavaria, Germany. *European Journal of Mineralogy*, 8(5), 1097 1118.

Gasser, D., Bruand, E., Rubatto, D., & Stüwe, K. (2012). The behaviour of monazite from greenschist facies phyllites to anatectic gneisses: an example from the Chugach Metamorphic Complex, southern Alaska. *Lithos*, 134, 108 122.

Goswami Banerjee, S., & Robyr, M. (2015). Pressure and temperature conditions for crystallization of metamorphic allanite and monazite in metapelites: a case study from the Miyar Valley (high Himalayan Crystalline of Zanskar, NW India). *Journal of Metamorphic Geology*, 33(5), 535 556.

Gratz, R., & Heinrich, W. (1997). Monazite xenotime thermobarometry: Experimental calibration of the miscibility gap in the binary system CePO4 YPO4. *American Mineralogist*, 82(7 8), 772 780.

Harrison, T. M., & Watson, E. B. (1984). The behavior of apatite during crustal anatexis: equilibrium and kinetic considerations. *Geochimica Et Cosmochimica Acta*, 48(7), 1467 1477.

Holland, T., & Powell, R. (2011). An improved and extended internally consistent thermodynamic dataset for phases of petrological interest, involving a new equation of state for solids. *Journal of Metamorphic Geology*, 29(3), 333 383.

Janots, E., Engi, M., Berger, A., Allaz, J., Schwarz, J. O., & Spandler, C. (2008). Prograde metamorphic sequence of REE minerals in pelitic rocks of the Central Alps: implications for allanite monazite xenotime phase relations from 250 to 610 C. *Journal of Metamorphic Geology*, 26(5), 509 526.

Kelsey, D. E., Clark, C., & Hand, M. (2008). Thermobarometric modelling of zircon and monazite growth in melt bearing systems: Examples using model metapelitic and metapsammitic granulites. *Journal of Metamorphic Geology*, 26(2), 199 212.

Kohn, M. J., & Malloy, M. A. (2004). Formation of monazite via prograde metamorphic reactions among common silicates: implications for age determinations. *Geochimica Et Cosmochimica Acta*, 68(1), 101 113.

Korhonen, F., Clark, C., Brown, M., Bhattacharya, S., & Taylor, R. (2013). How long lived is ultrahigh temperature (UHT) metamorphism? Constraints from zircon and monazite geochronology in the Eastern Ghats orogenic belt, India. *Precambrian Research*, 234, 322 350.

Kunz, B. E., & White, R. W. (2019). Phase equilibrium modelling of the amphibolite to granulite facies transition in metabasic rocks (Ivrea Zone, NW Italy). *Journal of Metamorphic Geology*.

Mazeina, L., Ushakov, S. V., Navrotsky, A., & Boatner, L. A. (2005). Formation enthalpy of ThSiO4 and enthalpy of the thorite huttonite phase transition. *Geochimica Et Cosmochimica Acta*, 69(19), 4675 4683.

Montel, J. M. (1986). Experimental determination of the solubility of Ce monazite in SiO2 Al2O3 K2O Na2O melts at 800 C, 2 kbar, under H2O saturated conditions. *Geology*, 14(8), 659 662.

Palya, A. P., Buick, I. S., & Bebout, G. E. (2011). Storage and mobility of nitrogen in the continental crust: Evidence from partially melted metasedimentary rocks, Mt. Stafford, Australia. *Chemical Geology*, 281(3), 211 226.

Popa, K., Shvareva, T., Mazeina, L., Colineau, E., Wastin, F., Konings, R. J., & Navrotsky, A. (2008). Thermodynamic properties of CaTh (PO4) 2 synthetic cheralite. *American Mineralogist*, 93(8 9), 1356 1362.

Powell, R., & Downes, J. (1990). Garnet porphyroblast bearing leucosomes in metapelites: mechanisms, phase diagrams, and an example from Broken Hill, Australia *High temperature metamorphism and crustal anatexis* (pp. 105 123): Springer.

Pyle, J. M., & Spear, F. S. (2003). Four generations of accessory phase growth in low pressure migmatites from SW New Hampshire. *American Mineralogist*, 88(2 3), 338 351.

Rapp, R. P., Ryerson, F., & Miller, C. F. (1987). Experimental evidence bearing on the stability of monazite during crustal anatexis. *Geophysical Research Letters*, 14(3), 307 310.

Rapp, R. P., & Watson, E. B. (1986). Monazite solubility and dissolution kinetics: implications for the thorium and light rare earth chemistry of felsic magmas. *Contributions to Mineralogy and Petrology*, 94(3), 304 316.

Redler, C., Johnson, T., White, R. W., & Kunz, B. (2012). Phase equilibrium constraints on a deep crustal metamorphic field gradient: metapelitic rocks from the Ivrea Zone (NW Italy). *Journal of Metamorphic Geology*, 30(3), 235 254.

Redler, C., White, R. W., & Johnson, T. E. (2013). Migmatites in the Ivrea Zone (NW Italy): Constraints on partial melting and melt loss in metasedimentary rocks from Val Strona di Omegna. *Lithos*, 175, 40 53.

Robie, R., & Hemingway, B. (1995). Thermodynamic properties of minerals and related substances at 298.15 K and 1 bar (10^5 Pascals) pressure and at higher temperatures (Vol. 2131): US Government Printing Office. pp.

Robie, R., Hemingway, B., & Fisher, J. (1978). Thermodynamic properties of minerals and related substances at 298.15 K and 1 bar (105 Pascal) pressure and at higher temperatures. *US Geol. Surv. Bull.*, 1452, 298 310.

Rubatto, D., Williams, I. S., & Buick, I. S. (2001). Zircon and monazite response to prograde metamorphism in the Reynolds Range, central Australia. *Contributions to Mineralogy and Petrology*, 140(4), 458 468.

Schulz, B. (2017). Polymetamorphism in garnet micaschists of the Saualpe Eclogite Unit (Eastern Alps, Austria), resolved by automated SEM methods and EMP Th U Pb monazite dating. *Journal of Metamorphic Geology*, 35(2), 141 163.

Skora, S., & Blundy, J. (2010). High pressure hydrous phase relations of radiolarian clay and implications for the

involvement of subducted sediment in arc magmatism. *Journal of Petrology*, 51(11), 2211 2243.

Skrzypek, E., Kato, T., Kawakami, T., Sakata, S., Hattori, K., Hirata, T., & Ikeda, T. (2018). Monazite behaviour and time scale of metamorphic processes along a low pressure/high temperature field gradient (Ryoke belt, SW Japan). *Journal of Petrology*, 59(6), 1109 1144.

Smith, H. A., & Barreiro, B. (1990). Monazite U Pb dating of staurolite grade metamorphism in pelitic schists. *Contributions to Mineralogy and Petrology*, 105(5), 602 615.

Spear, F. (1993). Metamorphic phase equilibria and pressure temperature time paths (Vol. 1): Mineralogical Society of America Monograph. 799 pp.

Spear, F. S. (2010). Monazite allanite phase relations in metapelites. *Chemical Geology*, 279(1 2), 55 62.

Spear, F. S. (2014). Program GIBBS. from http://ees2.geo.rpi.edu/MetaPetaRen/Software/GibbsWeb/Gibbs.html

Spear, F. S., & Menard, T. (1989). Program GIBBS; a generalized Gibbs method algorithm. *American Mineralogist*, 74(7 8), 942 943.

Spear, F. S., & Pyle, J. M. (2002). Apatite, Monazite, and Xenotime in Metamorphic Rocks. *Reviews in Mineralogy and Geochemistry*, 48(1), 293 335.

Spear, F. S., & Pyle, J. M. (2010). Theoretical modeling of monazite growth in a low Ca metapelite. *Chemical Geology*, 273(1), 111 119.

Stepanov, A. S., Hermann, J., Rubatto, D., & Rapp, R. P. (2012). Experimental study of monazite/melt partitioning with implications for the REE, Th and U geochemistry of crustal rocks. *Chemical Geology*, 300, 200 220.

Suzuki, S., Arima, M., Williams, I. S., Shiraishi, K., & Kagami, H. (2006). Thermal history of UHT metamorphism in the Napier Complex, East Antarctica: Insights from zircon, monazite, and garnet ages. *The Journal of Geology*, 114(1), 65 84.

Taylor, R. J. M., Kirkland, C. L., & Clark, C. (2016). Accessories after the facts: Constraining the timing, duration and conditions of high temperature metamorphic processes. *Lithos*, 264, 239 257.

Taylor, S. R., & McLennan, S. M. (1985). The continental crust: its composition and evolution.

Ushakov, S., Helean, K., Navrotsky, A., & Boatner, L. (2001). Thermochemistry of rare earth orthophosphates. *Journal of Materials Research*, 16(9), 2623 2633.

Walsh, A. K., Kelsey, D. E., Kirkland, C. L., Hand, M., Smithies, R. H., Clark, C., & Howard, H. M. (2015). P T t evolution of a large, long lived, ultrahigh temperature Grenvillian belt in central Australia. *Gondwana Research*, 28(2), 531 564.

Webster, J. D., Goldoff, B. A., Flesch, R. N., Nadeau, P. A., & Silbert, Z. W. (2017). Hydroxyl, Cl, and F partitioning between high silica rhyolitic melts apatite fluid (s) at 50 200 MPa and 700 1000 C. *American Mineralogist*, 102(1), 61 74.

White, R., & Powell, R. (2002). Melt loss and the preservation of granulite facies mineral assemblages. *Journal of Metamorphic Geology*, 20(7), 621 632.

White, R. W., Powell, R., & Clarke, G. L. (2003). Prograde metamorphic assemblage evolution during partial melting of metasedimentary rocks at low pressures: migmatites from Mt Stafford, Central Australia. *Journal of Petrology*, 44(11), 1937 1960.

Williams, I. (2001). Response of detrital zircon and monazite, and their U Pb isotopic systems, to regional metamorphism and host rock partial melting, Cooma Complex, southeastern Australia. *Australian Journal of Earth Sciences*, 48(4), 557 580.

Williams, M. L., Jercinovic, M. J., & Hetherington, C. J. (2007). Microprobe monazite geochronology: understanding geologic processes by integrating composition and chronology. *Annual Review of Earth and Planetary Sciences*, 35(1), 137.

Wing, B. A., Ferry, J. M., & Harrison, T. M. (2003). Prograde destruction and formation of monazite and allanite during contact and regional metamorphism of pelites: petrology and geochronology. *Contributions to Mineralogy and Petrology*, 145(2), 228 250.

Yakymchuk, C. (2017). Behaviour of apatite during partial melting of metapelites and consequences for prograde suprasolidus monazite growth. *Lithos*, 274, 412 426.

Yakymchuk, C., & Brown, M. (2014a). Behaviour of zircon and monazite during crustal melting. *Journal of the Geological Society*, 171(4), 465 479.

Yakymchuk, C., & Brown, M. (2014b). Consequences of open system melting in tectonics. *Journal of the Geological Society*, 171(1), 21 40.

Yakymchuk, C., & Brown, M. (2019). Divergent behaviour of Th and U during anatexis: Implications for the thermal evolution of orogenic crust. *Journal of Metamorphic Geology*. 37, 899 916.

Yakymchuk, C., Kirkland, C. L., & Clark, C. (2018). Th/U ratios in metamorphic zircon. *Journal of Metamorphic Geology*, 36(6), 715 737.

Supporting information

APPENDIX S5.1: SPEAR & PYLE (2010) (C1) AND SPEAR (2010) (C2) DIAGRAMS

Diagrams for C1 and C2 in text (Figs. 2-10) are composite figures. The original output datafile for each modelled variation of C1 (Spear & Pyle, 2010) and C2 (Spear, 2010) are included as separate files (S5.2.X). ".All" files can be opened using a standard text reader.

Electronic supplementary files:

S5.1.1 C1 closed system model, "SP10DSM.All"

S5.1.2 C1 open system model, "SP10DSM_ME.All"

S5.1.3 C1 closed system model, P=0.30, "SP10DSM_P30.All"

S5.1.4 C1 closed system model, P=0.10, "SP10DSM_P10.All"

S5.1.5 C1 closed system model, P=0.05, "SP10DSM_P05.All"

S5.1.6 C1 open system model, P=0.30, "SP10DSM_P30_ME.All"

S5.1.7 C1 open system model, P=0.10, "SP10DSM_P10_ME.All"

S5.1.8 C1 open system model, P=0.05, "SP10DSM_P05_ME.All"

S5.1.9 C1 closed system model, 2Ca, "SP10DSM_Ca2.All"

S5.1.10 C1 closed system model, 0.5Ca, "SP10DSM_Ca05.All"

S5.1.11 C1 open system model, 2Ca, "SP10DSM_Ca2_ME.All"

S5.1.12 C1 open system model, 0.5Ca, "SP10DSM_Ca05_ME.All"

S5.1.13 C1 closed system model, 1.5Al, "SP10DSM_Al15.All"

S5.1.14 C1 closed system model, 0.75Al, "SP10DSM_Al75.All"

S5.1.15 C1 open system model, 1.5Al, "SP10DSM_Al15_ME.All"

S5.1.16 C1 open system model, 0.75Al, "SP10DSM_Al75_ME.All"

S5.1.17 C1 closed system model, 2REE, "SP10DSM_REE2.All"

S5.1.18 C1 closed system model, 0.5REE, "SP10DSM_REE05.All"

S5.1.19 C1 open system model, 2REE, "SP10DSM_REE2_ME.All"

S5.1.20 C1 open system model, 0.5REE, "SP10DSM_REE05_ME.All"

S5.1.21 C1 closed system model, 2Th, "SP10DSM_Th2.All"

S5.1.22 C1 closed system model, 0.5Th, "SP10DSM_Th05.All"

S5.1.23 C1 open system model, 2Th, "SP10DSM_Th2_ME.All"

S5.1.24 C1 open system model, 0.5Th, "SP10DSM_Th05_ME.All"

S5.1.25 C2 closed system model, "S10DSM.All"

S5.1.26 C2 open system model, "S10DSM_ME.All"

S5.1.27 C2 closed system model, P=0.30, "S10DSM_P30.All"

S5.1.28 C2 closed system model, P=0.10, "S10DSM_P10.All"

S5.1.29 C2 closed system model, P=0.05, "S10DSM_P05.All"

S5.1.30 C2 open system model, P=0.30, "S10DSM_P30_ME.All"

S5.1.31 C2 open system model, P=0.10, "S10DSM_P10_ME.All"

S5.1.32 C2 open system model, P=0.05, "S10DSM_P05_ME.All"

S5.1.33 C2 closed system model, 2Ca, "S10DSM_Ca2.All"

S5.1.34 C2 closed system model, 0.5Ca, "S10DSM_Ca05.All"

S5.1.35 C2 open system model, 2Ca, "S10DSM_Ca2_ME.All"

S5.1.36 C2 open system model, 0.5Ca, "S10DSM_Ca05_ME.All"

S5.1.37 C2 closed system model, 1.5Al,

"S10DSM_Al15.All"

S5.1.38 C2 closed system model, 0.75Al, "S10DSM_Al75.All"

S5.1.39 C2 open system model, 1.5Al, "S10DSM_Al15_ME.All"

S5.1.40 C2 open system model, 0.75Al, "S10DSM_Al75_ME.All"

S5.1.41 C2 closed system model, 2REE, "S10DSM_REE2.All"

S5.1.42 C2 closed system model, 0.5REE, "S10DSM_REE05.All"

S5.1.43 C2 open system model, 2REE, "S10DSM_REE2_ME.All"

S5.1.44 C2 open system model, 0.5REE, "S10DSM_REE05_ME.All"

S5.1.45 C2 closed system model, 2Th, "S10DSM_Th2.All"

S5.1.46 C2 closed system model, 0.5Th, "S10DSM_Th05.All"

S5.1.47 C2 open system model, 2Th, "S10DSM_Th2_ME.All"

S5.1.48 C2 open system model, 0.5Th, "S10DSM_Th05_ME.All"

APPENDIX S5.2: ADDITIONAL DIAGRAMS AND BULK COMPOSITIONS

Preliminary modelling of two additional pelite compositions was completed. These compositions were initially published in Kelsey, Clark, and Hand (2008) and Yakymchuk, Kirkland, and Clark (2018). The original output data file (.All files; see below, S5.2.X) for each of these compositions are included as separate files and the modelled compositions are summarised in Table S5.2. Note that these two compositions were modelled using an earlier version of the dataset which favours Th-in-monazite much more strongly than Th-in-allanite at low temperatures. ".All" files can be opened using a standard text reader.

Electronic supplementary files:

S5.2.1 K08 closed system model, "K08DSM.All"

S5.2.2 Y18 closed system model, "Y18DSM.All"

Table S5.2. P T Additional bulk compositions used in exploratory calculation of phase equilibrium models. Major elements reported as wt % oxide and trace elements as ppm element. K08, Kelsey et al. (2008); and Y18, Yakymchuck et al. (2018).

	K08	Y18
Major elements(wt%)		
SiO_2	65.29	60.70
Al_2O_3	18.46	21.78
MgO	1.61	3.49
FeO	4.81	4.52
MnO	0.11	0.19
CaO	3.01	1.86
Na_2O	1.71	1.94
K_2O	3.82	4.34
H_2O	0.99	0.99
F	0.014	0.014
P_2O_5	0.16	0.16
Trace elements(wt%)		
Y_2O_3	0.0034	0.0034
La_2O_3	0.0044	0.0044
Ce_2O_3	0.0089	0.0089
Nd_2O_3	0.0035	0.0035
ThO_2	0.0017	0.0017
Trace elements(ppm)		
Y	27	27
La	37	37
Ce	76	75
Nd	30	30
Th	15	15

APPENDIX S5.3: MT STAFFORD AND IVREA–VERBANO ZONE MODELLING METHODS AND DIAGRAMS

The modelling for natural rock compositions from Mt Stafford and the Ivrea–Verbano Zone (STF02B and IV16-07 respectively) were modelled using principally the same method as the C1 and C2 compositions as described in section 2.2 (main text). The only difference was the method of adding trace elements to the major element compositions. These two samples have measured Ce, La, Y and Th values (Chapters 2 and 3), but not F or Nd. For Ce, La, Y and Th, trace elements equal to the measured values were used.

Bulk Nd values were not analysed, so appropriate bulk Nd values were substituted. Nd values used for both STF02B and IV16-07 models were calculated from La values for those compositions using the average La/Nd ratio from studies of upper crustal rocks (average La/Nd = 0.89; Condie, 1993; Gromet, Haskin, Korotev, & Dymek, 1984; McLennan, 2001; Plank, 2014; Rudnick & Gao, 2003; Taylor & McLennan, 1985; Wedepohl, 1995). The Nd values used in calculations are given in Table 4. F was added by the same method as for C1 and C2, but the measured P value was used.

Original output diagrams from which Figure 11 were drawn are provided in Figs. S5.3.1 –S5.3.8 (See also electronic supplemenatry files). The original output data file (.All files; see below, S5.3.1 and S5.3.2) for each of these compositions are included as separate files. ".All" files can be opened using a standard text reader.

Electronic supplementary files:

S5.3.1 STF02B closed system model, "ST02BR. All"

S5.3.2 IV16-07 closed system model, "IV07BR. All"

Figures S5.3.1–S5.3.8

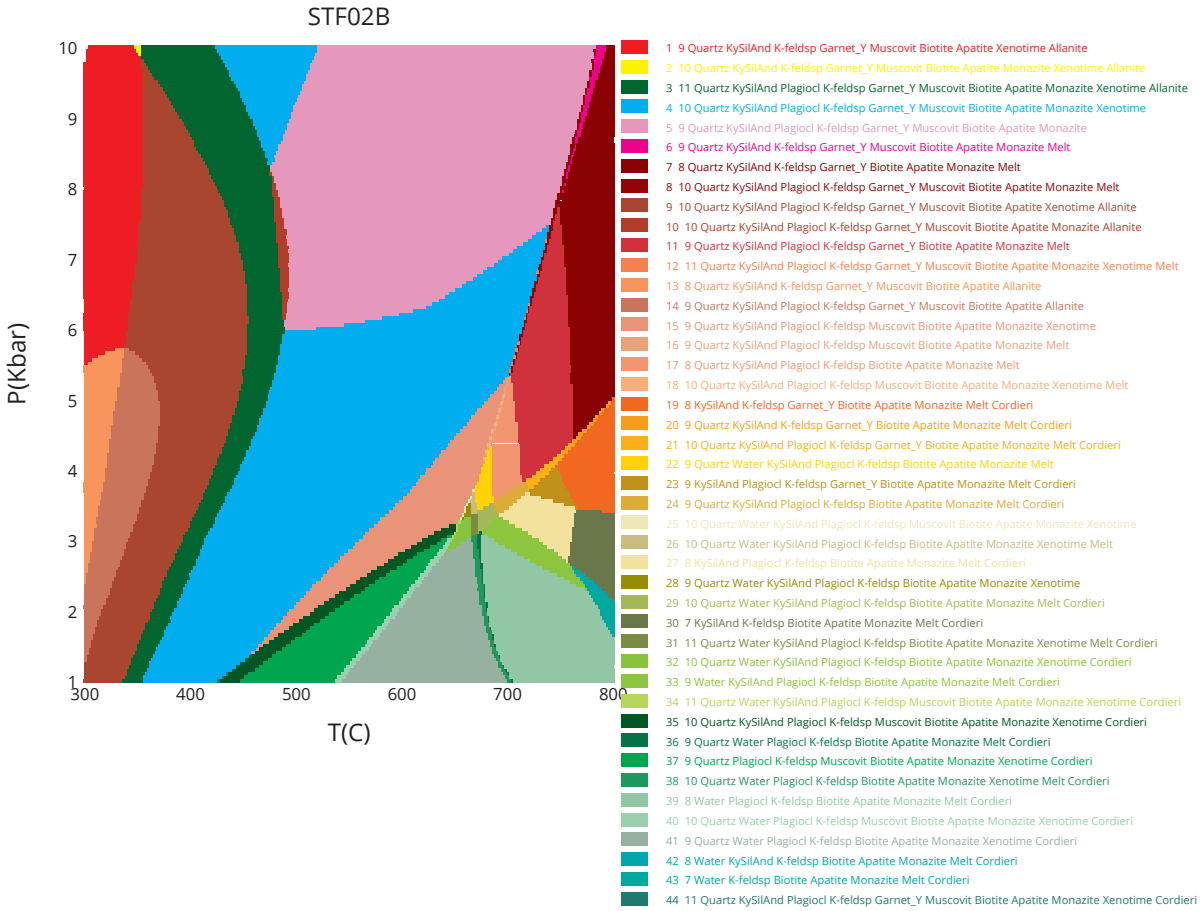

Figure S5.3.1. EAD for STF02B as output by MADplotter program.

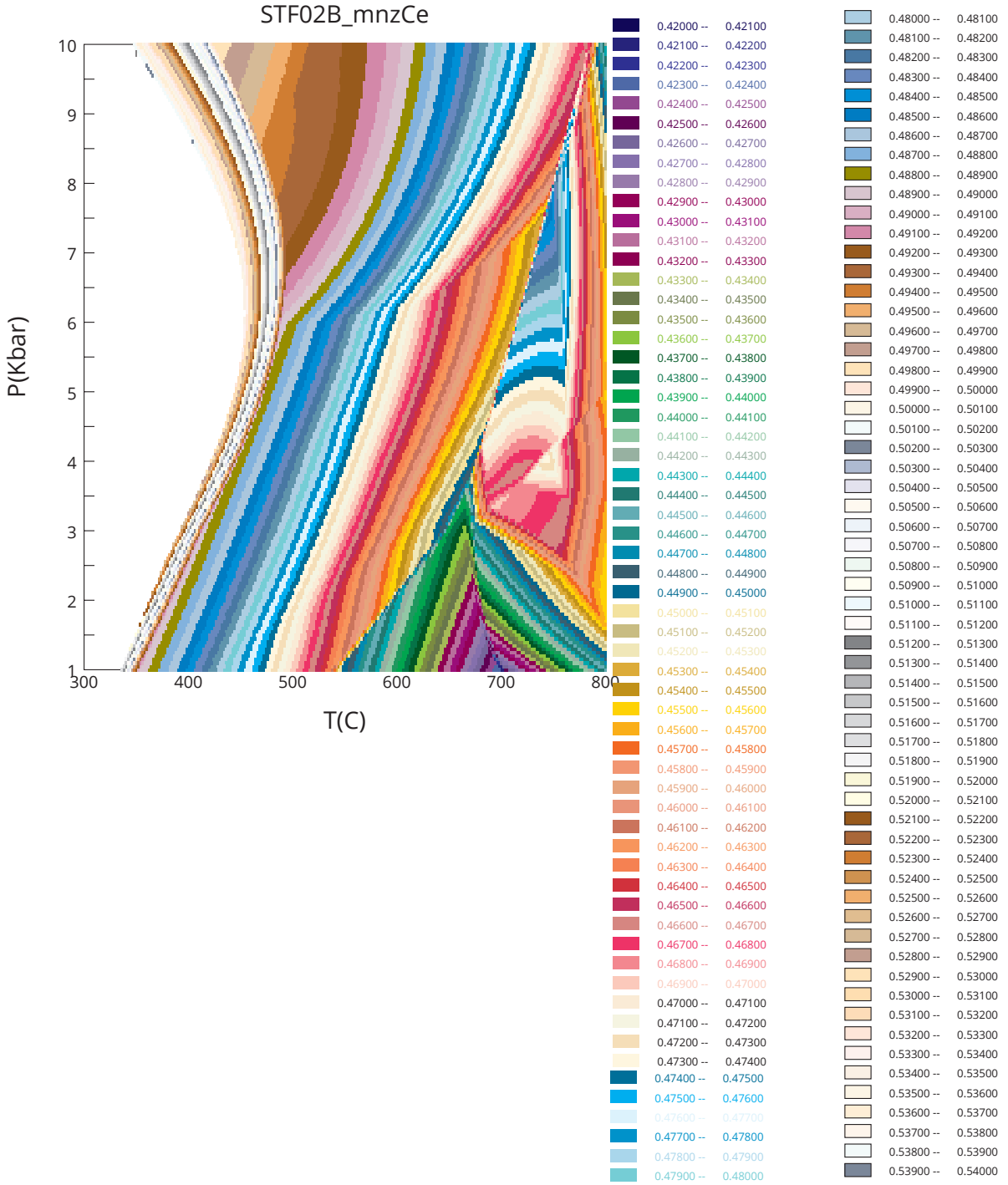

Figure S5.3.2. Contours of Ce in monazite for STF02B as output by MADplotter program. Contour increments are 0.001 APFU. Coloured area indicates extent of monazite stability.

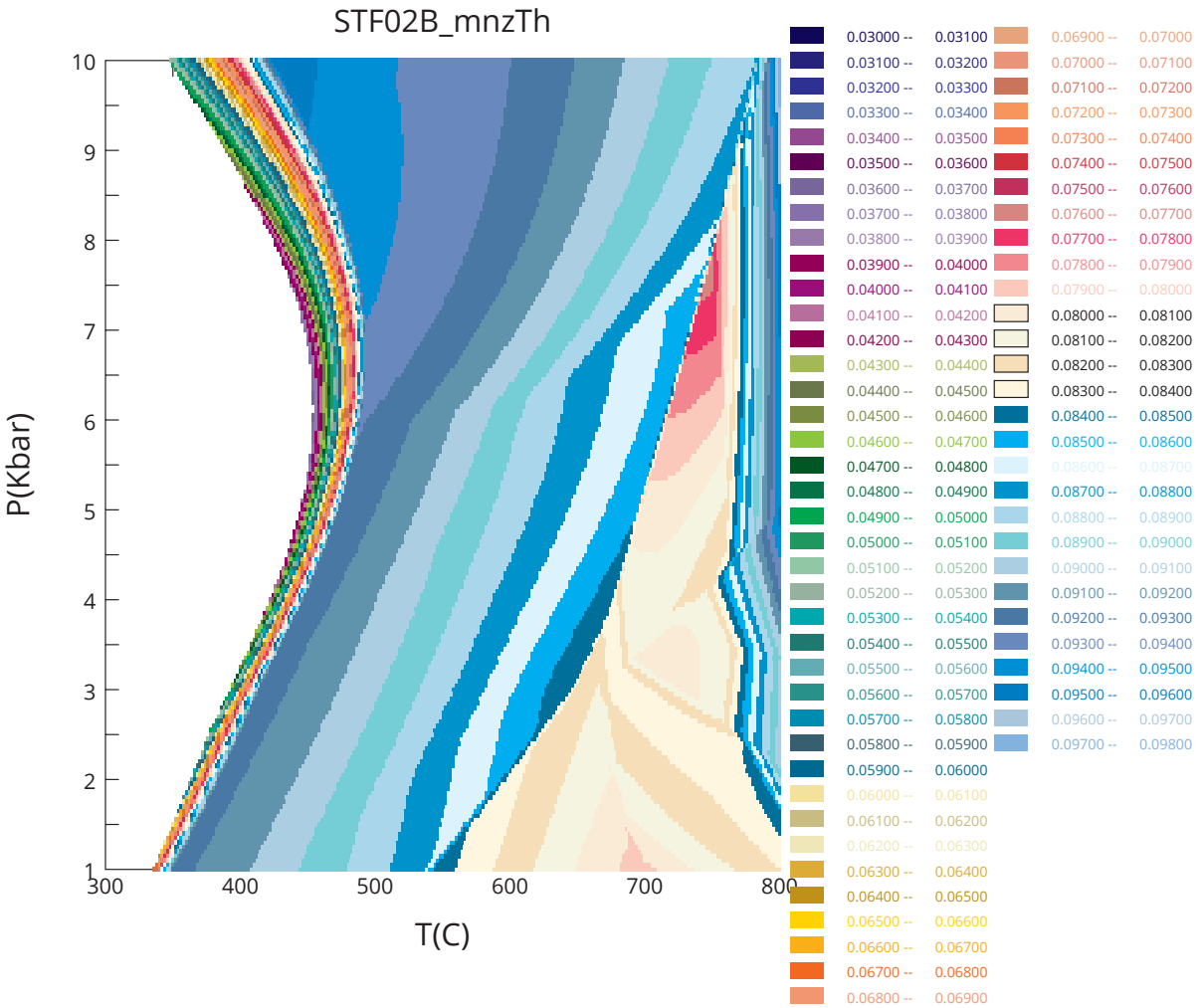

Figure S5.3.3. Contours of Th in monazite for STF02B as output by MADplotter program. Contour increments are 0.001 APFU. Coloured area indicates extent of monazite stability.

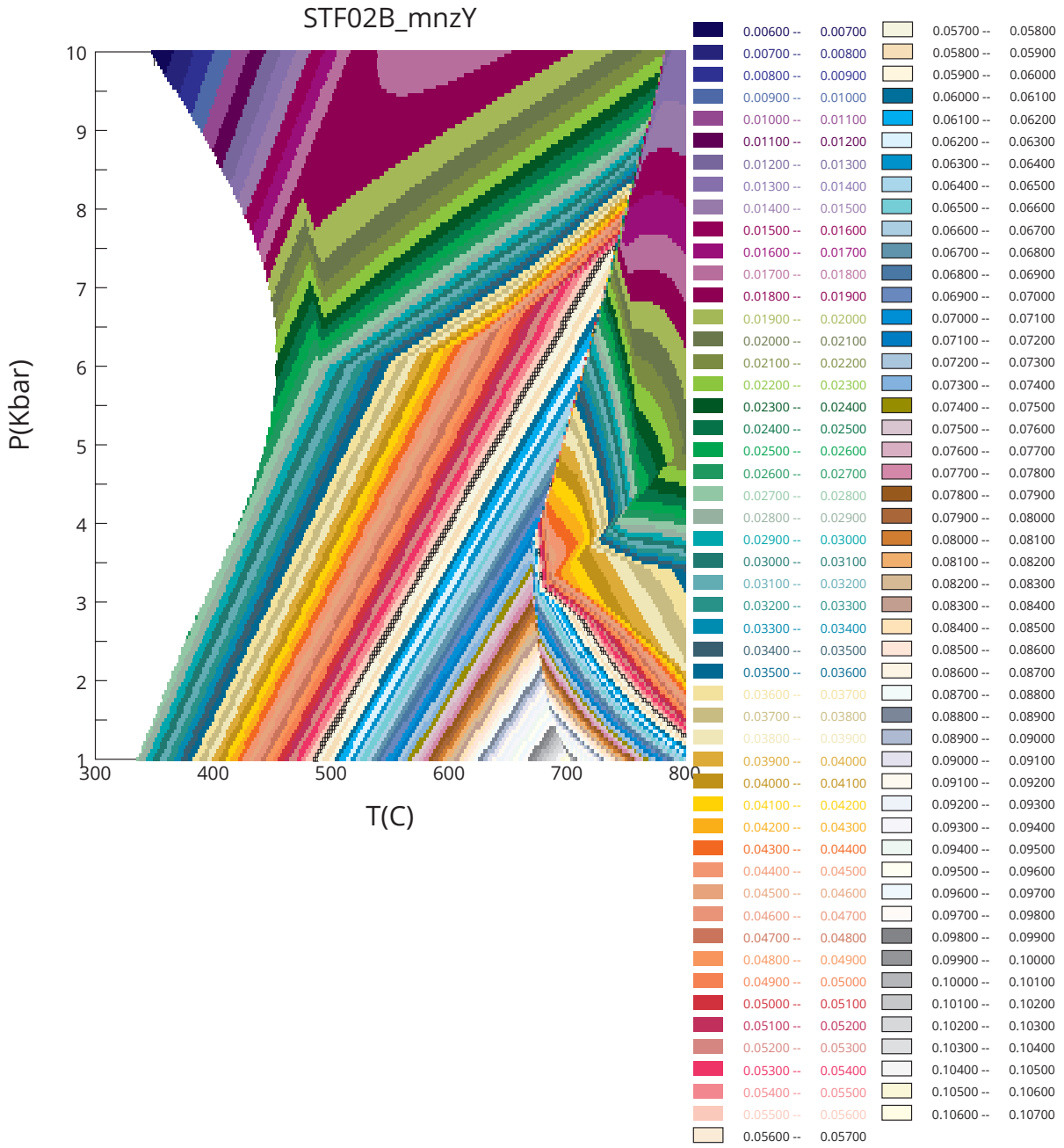

Figure S5.3.4. Contours of Y in monazite for STF02B as output by MADplotter program. Contour increments are 0.001 APFU. Coloured area indicates extent of monazite stability.

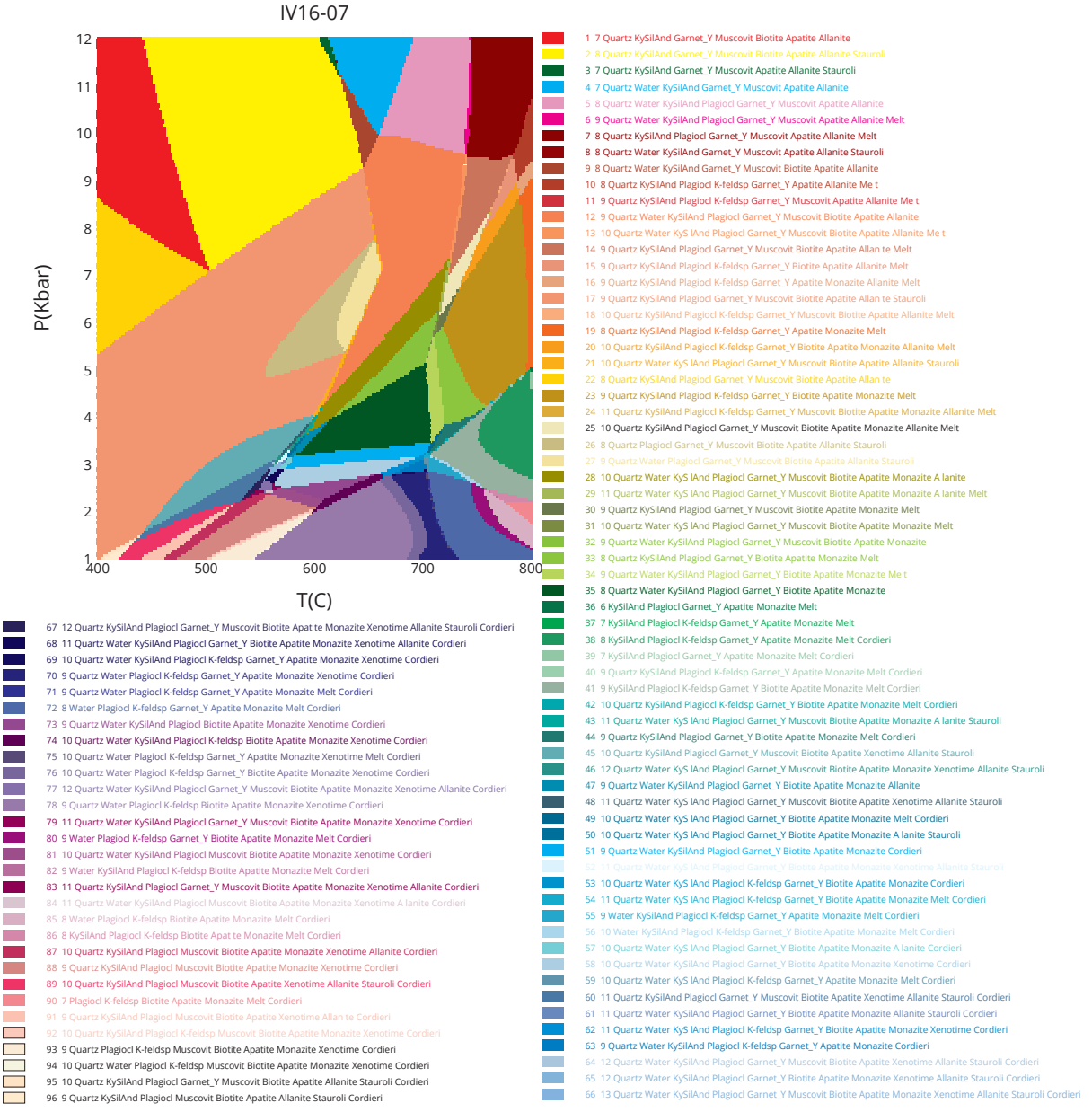

Figure S5.3.5. EAD for IV16 07 as output by MADplotter program.

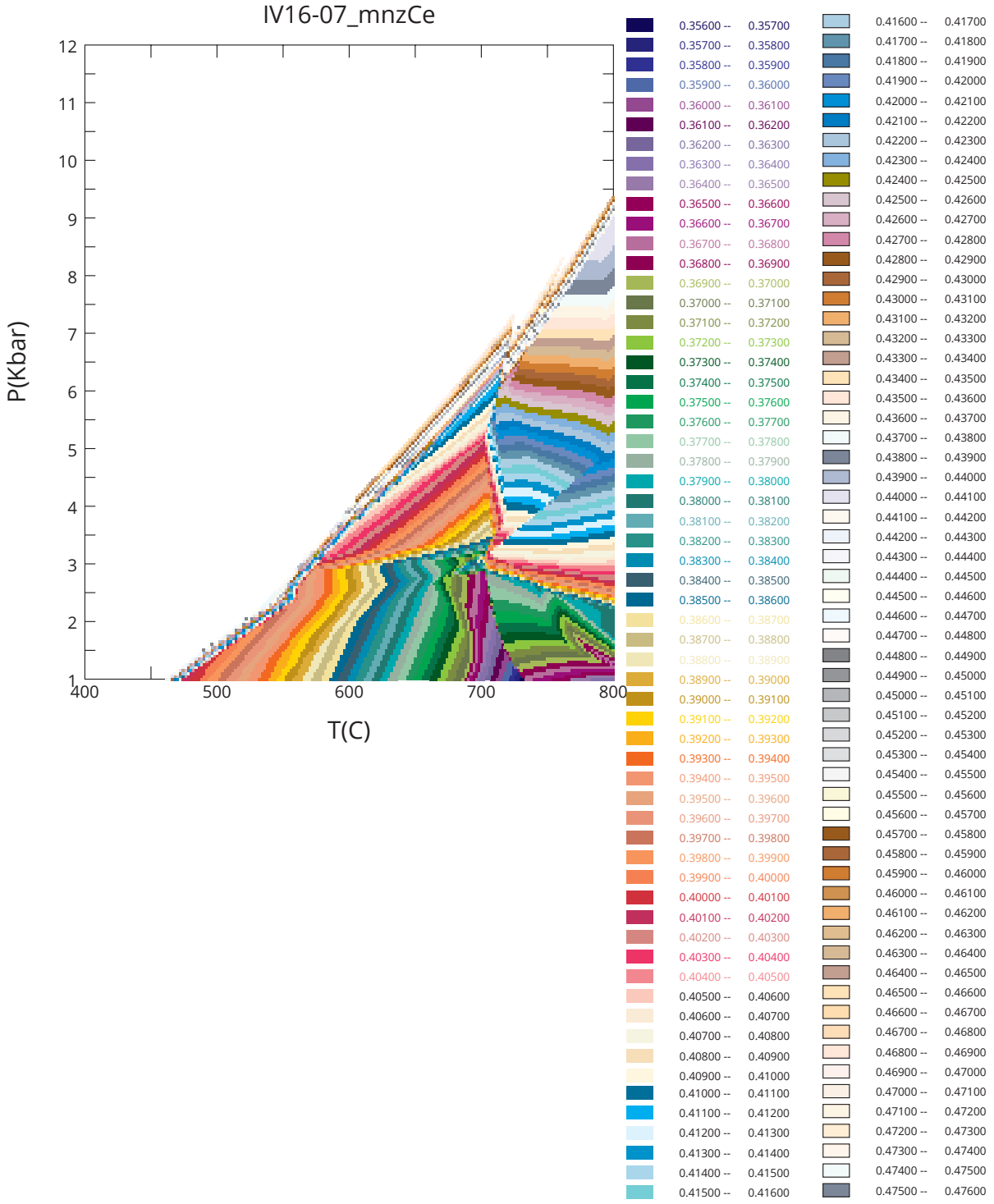

Figure S5.3.6. Contours of Ce in monazite for IV16 07 as output by MADplotter program. Contour increments are 0.001 APFU. Coloured area indicates extent of monazite stability.

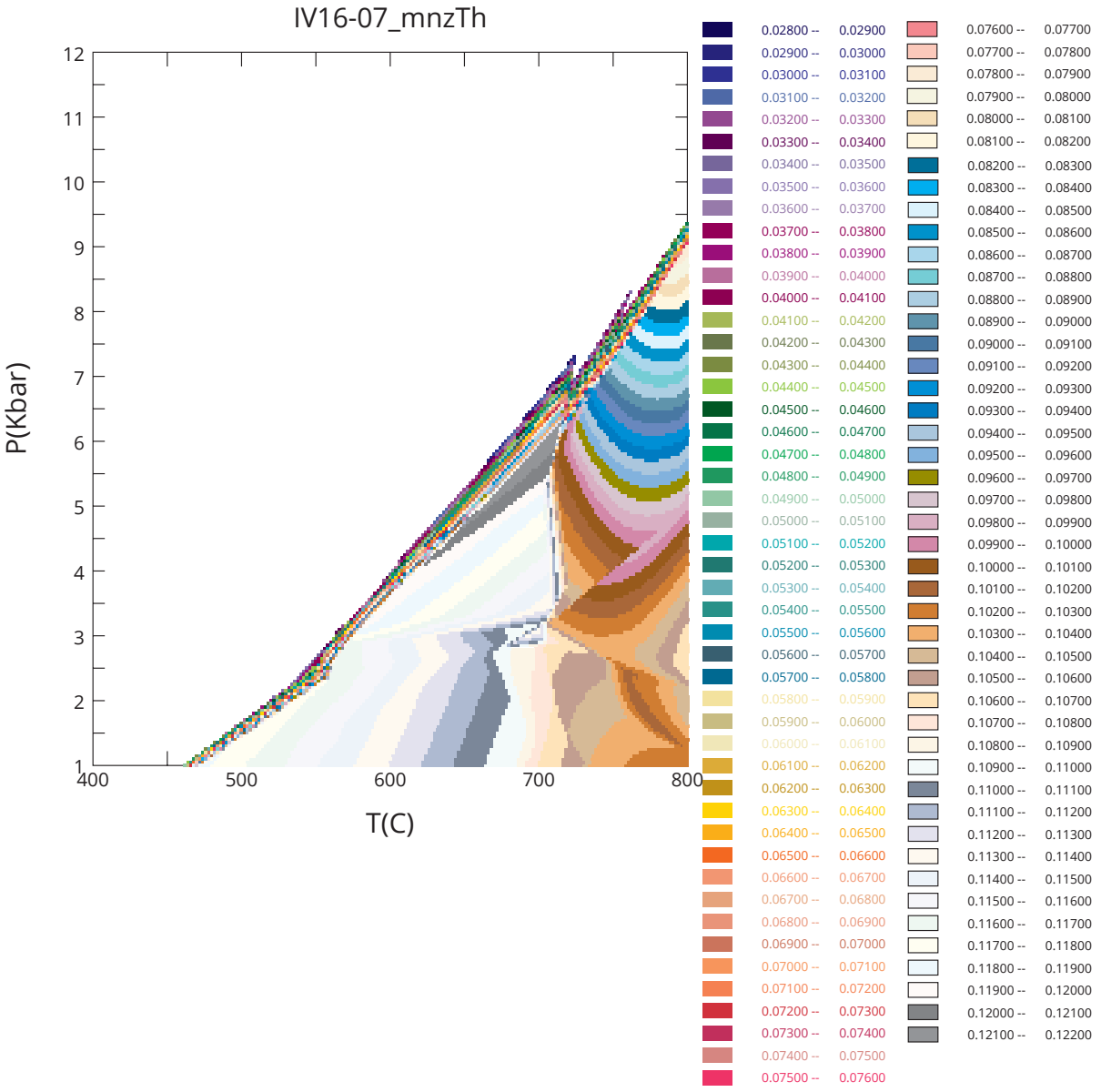

Figure S5.3.7. Contours of Th in monazite for IV16 07 as output by MADplotter program. Contour increments are 0.001 APFU. Coloured area indicates extent of monazite stability.

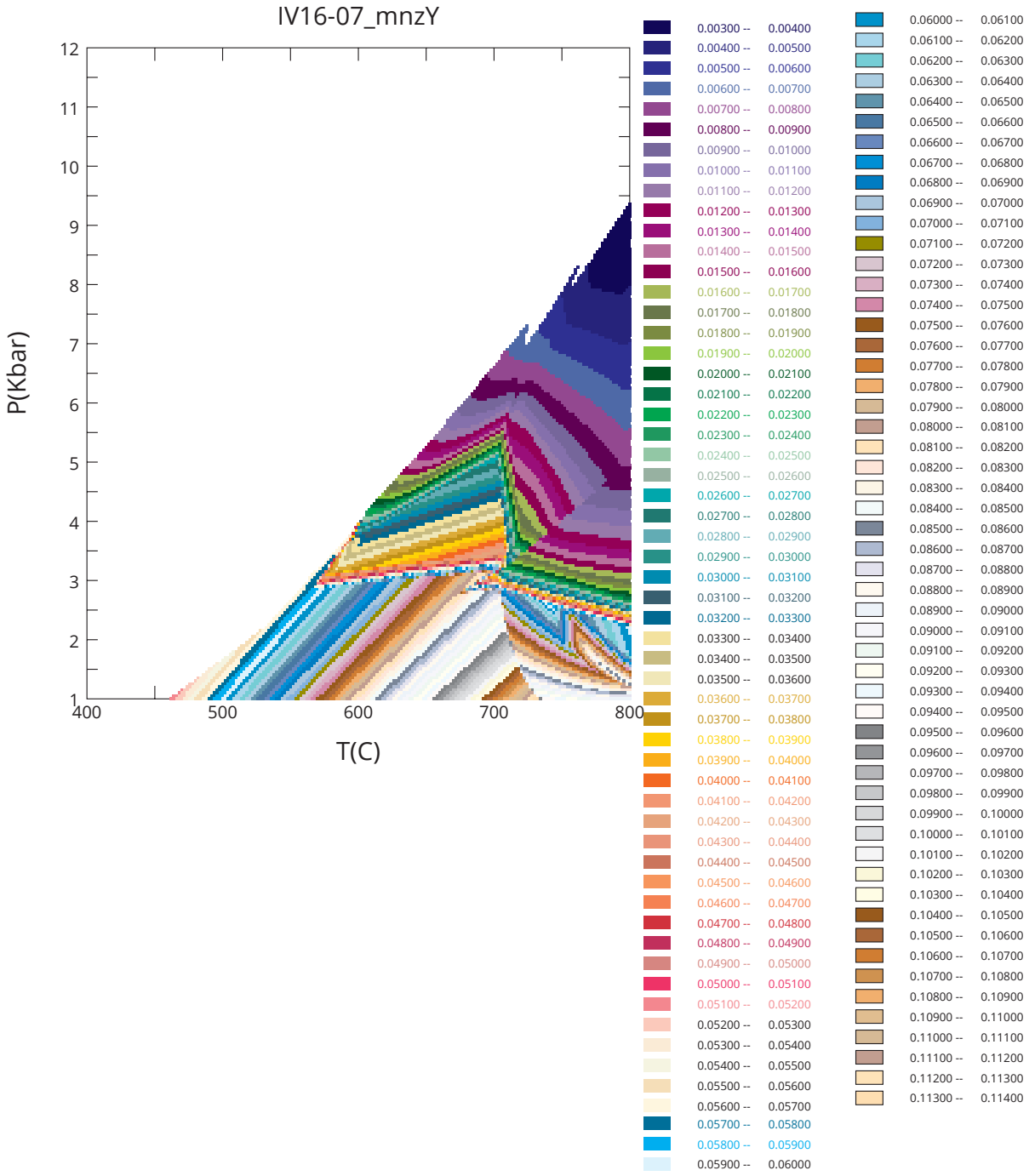

Figure S5.3.8. Contours of Y in monazite for IV16 07 as output by MADplotter program. Contour increments are 0.001 APFU. Coloured area indicates extent of monazite stability.

REFERENCES

Condie, K. C. (1993). Chemical composition and evolution of the upper continental crust: Contrasting results from surface samples and shales. Chemical Geology, 104(1), 1 37.

Gromet, L. P., Haskin, L. A., Korotev, R. L., & Dymek, R. F. (1984). The "North American shale composite": Its compilation, major and trace element characteristics. Geochimica Et Cosmochimica Acta, 48(12), 2469 2482.

Kelsey, D. E., Clark, C., & Hand, M. (2008). Thermobarometric modelling of zircon and monazite growth in melt bearing systems: Examples using model metapelitic and metapsammitic granulites. Journal of Metamorphic Geology, 26(2), 199 212.

McLennan, S. M. (2001). Relationships between the trace element composition of sedimentary rocks and upper continental crust. Geochemistry, Geophysics, Geosystems, 2(4).

Plank, T. (2014). The Chemical Composition of Subducting Sediments. In Ralph F. Keeling (Ed.), Treatise on geochemistry (pp. 607 629). Amsterdam: Elsevier.

Rudnick, R., & Gao, S. (2003). Composition of the continental crust. Treatise on geochemistry, 3, 659.

Spear, F. S. (2010). Monazite allanite phase relations in metapelites. Chemical Geology, 279(1 2), 55 62.

Spear, F. S., & Pyle, J. M. (2010). Theoretical modeling of monazite growth in a low Ca metapelite. Chemical Geology, 273(1), 111 119.

Taylor, S. R., & McLennan, S. M. (1985). The continental crust: its composition and evolution.

Wedepohl, K. H. (1995). The composition of the continental crust. Geochimica Et Cosmochimica Acta, 59(7), 1217 1232.

Yakymchuk, C., Kirkland, C. L., & Clark, C. (2018). Th/U ratios in metamorphic zircon. Journal of Metamorphic Geology, 36(6), 715 737.

Chapter 6

Summary and Conclusions

Thesis summary and conclusions

This thesis aims to develop an understanding of: (1) how Th concentration in monazite changes as a function of progressive metamorphism; and (2) what the controls on these changes are at both the mineral and outcrop scale. In the preceding chapters, the natural monazite record of two metamorphic terranes were investigated, compared with global trends and then placed within a mineral equilibria calculation framework in order to address the principle aims of this thesis. The following discussion summarises the key outcomes and presents a concise summary of the role that monazite plays in retaining Th in melt-depleted granulite-facies pelites.

Aim 1: Comprehensively characterise the natural record of thorium in monazite and rocks in different tectonic settings in detail to understand the interplay between the behaviour of thorium in monazite and in the bulk rock as a function of metamorphism, partial melting and melt loss;

Chapters 2 and 3 present two of the most detailed studies to date with focus on the distribution of Th within and between monazite grains as a function of metamorphic grade. The two studied terranes—Mt Stafford (central Australia) and the Ivrea–Verbano Zone (NW Italy)—were chosen because they have continuous metamorphic field gradients, an abundance of pelite layers (known for having a high propensity to grow monazite) and well constrained pressure–temperature (*P–T*) conditions of evolution. Although they share these similar characteristics, they have distinctly different metamorphic field gradients. Mt Stafford is a low-strain sequence with a very high metamorphic field gradient, whereas the Ivrea–Verbano Zone has a higher-pressure and higher-strain history, and thus a lower metamorphic field gradient. The whole rock Th trends in both terranes have similarities, with Th increasing from the lowest grade rocks to the granulite facies. The Ivrea–Verbano Zone also contains UHT granulite facies rocks (septa within a large mafic body) which have very low Th concentrations. This allows the appraisal of monazite and bulk Th trends in different tectonic settings.

Chapters 2 and 3 show that each of these terranes preserve several successive monazite chemical zones, which can be observed across multiple samples and therefore across differences in metamorphic grade. At Mt Stafford, these zones are preserved from the lowest grades of metamorphism (mid amphibolite facies) to the peak of regional granulite facies metamorphism. The first generation of metamorphic monazite has highly variable Th contents. Monazite compositional zones from higher metamorphic grades have higher Th than low temperature monazite. In the Ivrea–Verbano Zone, amphibolite-, granulite-facies and UHT monazite show distinctly different chemical zoning patterns. Similar chemical zones are observed between samples of similar metamorphic grade, but are not preserved in higher grade rocks. This may be a function of the higher strain regime in the Ivrea–Verbano Zone creating conditions which favour wholescale monazite recrystallisation (**Chapter 3**) whereas, in the lower strain Mt Stafford rocks, monazite zoning has a greater preservation potential (**Chapter 2**). This finding suggests that there are multiple processes which may be responsible for the formation of preserved monazite textures. Such processes may be governed by the interplay of melt presence and melting style (open versus closed), the *P–T* gradient of the terrane, the positive slope of the allanite-to-monazite reaction limiting the amount of subsolidus monazite that can grow at higher pressures, the amount of strain experienced by samples, residence time at high temperatures, cooling path and the relative timing of monazite formation relative to other minerals.

In both terranes, monazite volume proportion increases with metamorphic grade to the granulite facies, although monazite modal proportion is very low in the UHT samples (Ivrea–Verbano Zone). This monazite volume increase can be used to reconcile the trend of reasonably constant Th-in-monazite concentration from the mid amphibolite facies (~600 °C) with the trend from the whole rock geochemistry of increasing Th with metamorphic grade.

In order to more fully understand monazite compositional trends with metamorphic grade,

it is crucial to have an understanding of how the two Th-bearing endmembers of monazite (cheralite, $Ca_{0.5}Th_{0.5}PO_4$, and huttonite, $ThSiO_4$) change with metamorphic grade. The cheralite to huttonite ratios for monazite in these two terranes are explicitly and quantitatively described for the first time in **chapters 2 and 3**. These observations show that cheralite is the dominant Th endmember, with huttonite playing a more minor role. UHT samples from the Ivrea–Verbano Zone have a population of monazites with high proportions of both huttonite and cheralite. Importantly, partial melting does not decrease the fraction of Th endmembers of monazite nor the bulk Th in either terrane, except at UHT (i.e. extreme) conditions.

A large range of additional analytical data, such as apatite and silicate major and trace element chemistry, monazite trace element chemistry from LA–ICP–MS, multi-element EPMA maps of monazite grains and additional monazite geochronology, was collected for the Mt Stafford and Ivrea–Verbano Zone samples and is provided in the appendices to **chapters 2 and 3** and to this thesis. Whereas this data was not explored in detail herein, it could be an invaluable resource for future research on monazite formation, REE, Th and U partitioning or other questions in these or other terranes.

Aim 2: Establish the global trends in monazite chemistry with pressure and temperature, including understanding the solid-solution chemistry changes and the relative proportions of the two Th-bearing endmembers of monazite;

Chapter 4 builds on **chapters 2 and 3** by providing a dataset of over 5000 monazite chemical analyses spanning 1.0 to 41.5 kbar and 250 to 1080 °C. From this dataset we have ascertained that Th-in-monazite shows a clear increasing trend with temperature and limited pressure dependence. Within this trend are three segments over different temperature windows: (1) Th-in-monazite increases from first-formed monazite to ~550 °C; (2) Th-in-monazite is effectively constant in the window 550 to 800 °C ; and (3) Th-in-monazite increases again above 800 °C. Cheralite is the dominant Th endmember of monazite, but ultra-high temperature monazite incorporates increasingly large proportions of huttonite. At temperatures below ~600 °C we have identified the possible presence of a solvus between cheralite and huttonite, which favours the occurrence (coexistence) of thorite and more cheralite-rich monazite (although total Th-in-monazite at these temperatures tends to be low).

The trends in the dataset largely replicate trends observed in **Chapters 2 and 3** as well as in the recent detailed study of Th-in-monazite from the Ryoke Belt, Japan, by Skrzypek et al. (2018). This shows that the trends in these three detailed studies are representative of global trends and processes which govern the incorporation of Th into monazite. This large monazite compositional dataset has been provided in Appendix S2 to Chapter 4 as a resource for future studies of monazite chemistry.

Chapters 2 and 3 together (19 samples) account for about a third of the samples with monazite chemistry linked to comprehensive major and trace element chemistry and more than half of the linked monazite volume estimates. This type of data is crucial for understanding the controls on monazite formation with progressive metamorphism and how these differences manifest in the microstructures and chemical domains recorded by monazite. Studies which investigate these controls are crucial to more fully and precisely understanding monazite as a geochronometer.

Aim 3: Create a readily adaptable thermodynamic calculation framework that explicitly incorporates the major elemental components of monazite (Ce, La, Nd, Th, Y, Ca, Si and P) and systematically predicts the pressure, temperature and rock composition (P–T–X) controls on the stability of Th-bearing phases including monazite;

The phase equilibria modelling framework presented in **Chapter 5** represents an important innovation in the modelling of accessory phase relations. The majority of previous attempts to model monazite stability and composition do so using the results from solubility equations superimposed on calculated phase diagrams for the silicate minerals (e.g. Kelsey et al., 2008; Yakymchuk and Brown, 2014; Yakymchuk et al., 2018). A thermobarometric framework for monazite exists, but is limited in its application due to the incorporation of only a small number of elements in the dataset. **Chapter 5** presents new solid-solution monazite, apatite, xenotime, allanite and melt thermodynamic models which have an expanded suite of elements, enabling more realistic application of the models to replicate natural monazite compositions. The software environment has also been complied for use on

both Windows and Mac machines, expanding the accessibility of the program. The ability to link *P–T* information to absolute time using these new monazite models will enable a much more precise discussion of the formation of monazite and geospeedometry in high temperature rocks. This will lead to a better understanding of the rates of tectonic processes. A significant outcome of **chapters 2 and 3** is to provide the necessary datasets for calibration of thermodynamic models for monazite and associated minerals. Additionally, **chapter 4** provides the global context of monazite chemistry trends which are used to test the models from representative pelite samples in **chapter 5** (from Spear, 2010; Spear and Pyle, 2010). The calculated models in **chapter 5** replicate well the general trends in natural data identified in **Chapter 4**, with the only exception being the increase in the huttonite component at UHT conditions. This may be the result of a bulk compositional or melt-loss control, but further work is needed to understand the specific conditions which lead to huttonite enrichment.

Aim 4: Apply the thermodynamic model to determine P–T–X (metamorphic reaction) controls on monazite chemistry and stability in representative and natural bulk compositions;

Chapter 5 explores the *P–T–X* controls on monazite stability and Th-in-monazite using the phase equilibrium framework that we have developed. We show that in the closed system case, monazite has a quasi-triangular shaped stability field, with the apex approximately at the solidus. The shape of the monazite field is controlled by allanite stability at low temperatures, with the allanite to monazite transition having a positive slope. At high temperatures, monazite gradually dissolves in silicate melt, with the modal abundance of monazite at the solidus playing a role in its stability in the anatectic realm. This means that in contrast to experimental and previous modelling studies, monazite is predicted by our models to be more stable at lower pressures rather than higher pressures in partially melted rocks. Apatite stability seems to be an important factor for sustaining monazite stability to high temperatures, with compositions that favour apatite stability at high temperatures (e.g. high P, high Ca and low Al) also resulting in expanded stability of monazite above the solidus. Apatite also has a role to play in attaining high Th concentrations in monazite, with the maximum Th-in-monazite reached at the apatite 100% dissolution boundary (**Chapter 5**). Bulk LREE and Th both change the proportion of Th endmembers in monazite, as monazite is the main host of these elements at low pressures and above the solidus. Increasing bulk LREE has an additional effect of increasing the stability field of monazite, which has been shown in previous modelling studies.

Chapter 5 also provides the proof-of-concept that this modelling framework can be applied to natural samples. We have shown that models using actual sample bulk compositions from the Ivrea–Verbano Zone and Mt Stafford can produce both the bulk silicate assemblage and monazite compositions in agreement with observations from these samples. We have also shown that although monazite compositions only change by small magnitudes during progressive metamorphism, these compositions are sufficiently different to define unique fields using Ce, Th and Y compositional parameters. The main aim of **Chapter 5** is to demonstrate that the highest grade/temperature monazite compositions recorded in the natural samples can be replicated in approximately the same location as the peak field for a specific sample within the errors of the natural data.

The thermodynamic framework is applied to two subsolidus natural samples from **chapters 2** (STF02B) **and 3** (IV16-07). This modelling gives further insight into the potential controls on the preservation (or not) of prograde monazite chemical zones. In Mt Stafford sample STF02B, the bulk composition and *P–T* path for the terrane results in a window of subsolidus monazite growth spanning ~300 °C (**Chapter 5**). The model is consistent with measured monazite chemistry in that the model is able to closely predict the Y + REE + Th chemistry of monazite with increasing temperature from zones A and B. Within this range, the natural data (**chapter 2**) shows that there are distinct phases of growth commonly recorded by monazite (e.g. during allanite consumption or near peak metamorphic conditions). These may be the result of either how rapidly monazite mode changes at certain *P–T* conditions or how long the rock remained at such conditions (i.e. how equilibrated it was). In contrast to Mt Stafford, the bulk composition and *P–T* path for Ivrea–Verbano Zone sample IV16-07 shows a window of only ~50°C for the subsolidus growth of monazite (**Chapter 5**) due to the positive slope of the monazite-to-allanite

reactions. Although the chemistry of other samples in the Ivrea–Verbano Zone sequence may be more conducive to prograde monazite growth, this small window of subsolidus monazite growth may go some way to explaining why the record from the Ivrea–Verbano Zone generally lacks prograde (and Variscan) monazite (**Chapter 3**) in granulite-facies samples.

In the Ivrea–Verbano Zone sample, IV16-07, the modelling provides some important clues about the formation of monazite in the terrane which were not considered in the initial study (**Chapter 3**). In particular, the modelling suggested that Z3 monazite (rims of amphibolite facies grains) was likely a retrograde zone. This was overlooked in **Chapter 3** because of the assumption that monazite and xenotime grew in equilibrium, and therefore that Y-in-monazite could be used as a proxy for temperature where microstructural setting was ambiguous. This finding simplifies the timeline for the Ivrea–Verbano zone somewhat, indicating that the peak of metamorphism (Z2) in the sample occurred slightly before or coincident with the emplacement of the Mafic Complex at the base of the metamorphic sequence. While the models are not necessarily definitive, this provides a nice example of the clarity which can be provided by observations of monazite chemistry combined with the modelling technique in situations where observations of mineral textures are ambiguous.

The monazite compositions for 'zones' are averaged between grains and samples for natural samples in **chapter 5** produces large regions of P–T space that these compositions span within the models. This is in part necessary to produce realistic models for the measured rock compositions. There are also instances where the fields for monazite compositional zones appear more than once along the published *P–T* path. This indicates that monazite with statistically similar compositions may have grown at different times. This could well be the reason that multiple ages can be observed within a single apparent chemical 'zone' (see also Williams et al., 2007). This may be exacerbated by the averaging of monazite zone compositions between several analyses and grains. A potential solution to this issue would be to model individual monazite analyses, which could therefore directly and precisely link geochronology and *P–T* constraints. This would give many more *P–T–t* points and would eliminate the imprecision introduced by averaging the compositions, but would require that both the bulk and mineral chemistry have good precision, with the error on measured bulk chemistry being a major source of uncertainty herein.

Aim 5: Apply the thermodynamic model to determine P–T–X controls on retention versus extraction of Th from the lower crust during metamorphism involving crustal melting.

The thermodynamic modelling framework presented in **chapter 5** is readily adaptable, has quick calculation times and automated melt-loss routines. These features make it an ideal tool for investigating the controls on Th retention versus extraction from granulite facies rocks.

Chapters 2 and 3 provide compelling evidence that the retention of Th in the lower crust is directly linked to the presence or not of monazite. This was further explored by Yakymchuk et al. (2018), who showed that the difference in solubility between monazite (which hosts Th) and zircon (which hosts U) could be used to explain the frequent observation of increased Th/U ratios in lower crustal rocks with respect to their protoliths (e.g. Alessio et al., 2018; Bea and Montero, 1999). The modelling of representative pelite compositions (C1 and C2) presented in **chapter 5** shows that the inclusion of Th in the modelling chemical system has a stabilising effect on monazite at high temperatures over and above simple calculations considering only LREE+Y in previous modelling contributions (e.g. Kelsey et al., 2008; Yakymchuk and Brown, 2014; Yakymchuk et al., 2018), which supports a monazite control on Th retention in the lower crust. This was the case in **chapter 5** even when bulk Th was low (~7.5 ppm; pelite average is ~14.6; Taylor and McLennan, 1985).

The modelling framework takes into account the findings of Stepanov et al. (2012), who showed that $D^{Th}_{mnz/liq}$ increasingly favoured Th to remain in monazite over melt with increasing temperature. This is replicated by the models up to the point that apatite disappears from the modelled assemblages. In the case of the melt-loss melting scenarios explored in **chapter 5**, apatite was stable to >1100°C at most pressures, and this resulted in regions of the equilibrium assemblage diagrams where Th-in-monazite became super concentrated, particularly at high pressures (>9 kbar) and temperatures (>1000 °C). When melt loss routines were combined with low bulk LREE

(La+Ce+Nd = 72 ppm), monazite compositions with ThO_2 of ~30% were calculated (>1050 °C, 8kbar). This Th enrichment is equivalent to the highest Th contents included in the monazite chemical database explored in **chapter 4**.

The modal abundance of monazite at the solidus appears to be a strong control on the retention of monazite (and therefore Th) in the residuum as melting progresses (**Chapter 5**). This is most evident in the higher pressure part of our models, where the allanite to monazite transition occurs near or above the solidus. In closed system melting scenarios where monazite abundance is low at the solidus (i.e. at high pressures), monazite dissolves into melt more rapidly than at lower pressures. For opens system scenarios at similar pressures, monazite abundance remains low for isobaric heating paths. Where allanite is the Th-bearing phase at the first melting increment, the Th is quickly lost to melt because allanite generally only remains stable over a small temperature window above the solidus. Therefore, in contrast to experimental studies that claim monazite solubility is diminished at higher pressures, we have found that when allanite is taken into account monazite solubility actually increases with increasing pressure. Further investigation of different modelling parameters could enhance our understanding of these processes and controls.

Future directions and unresolved questions

In **chapter 5**, the mechanism for calibrating the models relies on the use of the solubility equations for apatite and monazite. However, given the importance of apatite to monazite solubility and P-in-melt, it is curious that no experiments have been done directly on full-system (Ca–P–F–NCKFMASH) peraluminous rocks to understand apatite composition and dissolution behaviour as a detailed function of *P–T–X*. Similarly for monazite, the Stepanov et al. (2012) experiments are the only ones which include Th in full-system peraluminous melts. However, it is not possible to fully interrogate their datasets and results because they don't present bulk composition mixes for the specific experiments and trace element compositions of monazite are normalised to a constant Ce value. Therefore, the success of the thermodynamic modelling included in this thesis is at the mercy of trusting that the dissolution expressions that these studies provided are universally applicable, which they may not be. To some extent, the dissolution expressions used to calibrate these models must be valid because the equilibrium assemblage diagrams calculated in **chapter 5** seem reasonable in terms of geological interpretation and in application to specific samples. However, further experimental study of monazite, apatite and associated phases on full-system peraluminous rocks would improve the applicability and reliability of the models presented in this thesis.

Whereas the Yakymchuk et al. (2018) study (see also Yakymchuk, 2017; Yakymchuk and Brown, 2014; Yakymchuk et al., 2017) uses the solubility expressions to predict accessory mineral behaviour external to the phase equilibrium framework for the major phases, the approach used in **chapter 5** is based on explicitly incorporating the accessory minerals and their requisite elements into the same phase equilibria calculations as for the major minerals and elements. That is, having thermodynamic (*a-x*) models for the end-members that span compositional space of the accessory minerals. The latter is advantageous in that it allows for: (1) dynamic partition coefficients for elements between phases as a function of *P–T–X* (e.g. $D^{Th}_{mnz/liq}$); (2) the behaviour of accessory phases to be modelled simultaneously with the major phases and components; and (3) the solid-solution chemistry of accessory phases to be calculated as a function of *P–T–X*, including specific REEs and also the subdivision of Th into the two end-members for monazite. Though we concede that accessory minerals and trace elements may not behave in a perfectly equilibrium manner, the evidence provided in this thesis is that there sufficient systematic – predictable – behaviour to monazite composition as a function of *P–T–X* that accessory minerals appear to behave in an at least close-to-equilibrium manner.

In focussing on monazite compositions, particularly Th-in-monazite, there is limited discussion in **chapter 5** of other compositional parameters output by these models. These parameters include the other components of monazite (i.e. Y, La, Ce, Nd), modal proportions for all of the phases in the modelling system, endmember proportions for the other mineral and melt phases, melt compositions and volume of melt loss. The models generate far more information than can be assessed in a single contribution, but future studies focussing on each of these important parameters would

be valuable to further validate these models. Such studies could also explore more of the functionality embedded in the framework using, for example, other rock compositions or different melt extraction parameters. They could also explore the utility of the framework in investigating broader questions within petrology and petrochronology, for example, investigating magma petrogenesis (e.g. Iles et al., 2018) or post-peak melt-rock interaction (e.g. Prent et al., 2019). Investigation of these processes typically involves using trace element signatures and ratios between accessory and major minerals. Modelling of such systems using the framework developed here would enable a deeper exploration of the controls on these processes for specific rock compositions and *P–T* histories. The automated nature of the modelling framework makes model calculation quick and straightforward, lending itself to applications where modelling multiple scenarios is key to success.

Future efforts could address aspects such as trace elements in xenotime and a stronger focus on Y-in garnet within this framework. These were not the focus of the current study, particularly as we were looking to develop a toolkit which didn't rely on the growth of monazite, xenotime and garnet in equilibrium with one another, and could be applied to garnet-free rocks (e.g. Mt Stafford; **Chapter 2**). Given the keen interest in garnet chemistry and the large amount of garnet data which is routinely collected, more precise/directed calibration of the models with focus on Y-in-garnet would increase the utility of this framework.

Uranium is not included in the current version of the modelling database, but incorporation of U into future versions would provide a powerful tool for investigating a range of open questions, particularly regarding Th/U partitioning in both monazite and crustal rocks. Although U is not the focus of this work, all of the necessary natural data for calibration of a U-bearing system is presented in the Mt Stafford and Ivrea–Verbano Zone case studies and monazite compositional database (**chapters 2-4**). However, U might be somewhat more challenging to reliably calibrate due to its low whole rock concentration and lower concentration (than Th) in monazite, apatite, xenotime and therefore melt. It would be logical to add zircon and therefore Zr, if U were to be added to the models. Some calibrations already exist for zircon dissolution (Kelsey & Powell 2011; Watson & Harrion 29183; Boehnke et al 2012). The addition of Th–U-bearing zircon would allow for addressing questions regarding Th/U partitioning in melt-bearing rocks. Uranium is the final outstanding major heat producing element to be added to equilibrium thermodynamic framework and its addition would open up a powerful tool for investigating radiogenic heat production in the crust. This would allow linkage of our understanding of heat production in a geophysical and broad scale geochemical point of view to a specific and testable minerals-focussed point of view. Additionally, this system being hosted within the GIBBS program allows large numbers of models to be created with ease to investigate the geochemical and mineralogical controls on the movement of heat producing elements in the crust. This framework could also be used in future to examine other types of open system processes, such as melt reintegration (e.g. Yakymchuk and Brown, 2019) or melt loss along specific *P–T* paths.

Conclusions

This thesis provides a significant contribution to petrology research by presenting a strong empirical case from two different terranes for changes to monazite chemistry with increasing metamorphic grade. On the basis of that, supported by the largest (to date) global dataset of monazite compositions that show the same trends, we have presented a readily adaptable thermodynamic framework for the calculation of monazite phase equilibria modelling. This is an important advancement which will facilitate a better understanding of the specifics of monazite formation in natural samples.

References

Alessio, K.L., Hand, M., Kelsey, D.E., Williams, M.A., Morrissey, L.J., Barovich, K., 2018. Conservation of deep crustal heat production. Geology 46, 335 338.

Bea, F., Montero, P., 1999. Behavior of accessory phases and redistribution of Zr, REE, Y, Th, and U during metamorphism and partial melting of metapelites in the lower crust: an example from the Kinzigite Formation of Ivrea Verbano, NW Italy. Geochimica Et Cosmochimica Acta 63, 1133 1153.

Iles, K.A., Hergt, J.M., Woodhead, J.D., 2018. Modelling Isotopic Responses to Disequilibrium Melting in Granitic Systems. Journal of Petrology 59, 87 113.

Kelsey, D.E., Clark, C., Hand, M., 2008. Thermobarometric modelling of zircon and monazite growth in melt bearing systems: Examples using model metapelitic and metapsammitic granulites. Journal of Metamorphic Geology 26, 199 212.

Prent, A.M., Beinlich, A., Morrissey, L.J., Raimondo, T.,

Clark, C., Putnis, A., 2019. Monazite as a monitor for melt rock interaction during cooling and exhumation. Journal of Metamorphic Geology 37, 415 438.

Skrzypek, E., Kato, T., Kawakami, T., Sakata, S., Hattori, K., Hirata, T., Ikeda, T., 2018. Monazite behaviour and time scale of metamorphic processes along a low pressure/high temperature field gradient (Ryoke belt, SW Japan). Journal of Petrology 59, 1109 1144.

Spear, F.S., 2010. Monazite allanite phase relations in metapelites. Chemical Geology 279, 55 62.

Spear, F.S., Pyle, J.M., 2010. Theoretical modeling of monazite growth in a low Ca metapelite. Chemical Geology 273, 111 119.

Stepanov, A.S., Hermann, J., Rubatto, D., Rapp, R.P., 2012. Experimental study of monazite/melt partitioning with implications for the REE, Th and U geochemistry of crustal rocks. Chemical Geology 300, 200 220.

Taylor, S.R., McLennan, S.M., 1985. The continental crust: its composition and evolution.

Williams, M.L., Jercinovic, M.J., Hetherington, C.J., 2007. Microprobe monazite geochronology: understanding geologic processes by integrating composition and chronology. Annual Review of Earth and Planetary Sciences 35, 137.

Yakymchuk, C., 2017. Behaviour of apatite during partial melting of metapelites and consequences for prograde suprasolidus monazite growth. Lithos 274, 412 426.

Yakymchuk, C., Brown, M., 2014. Behaviour of zircon and monazite during crustal melting. Journal of the Geological Society 171, 465 479.

Yakymchuk, C., Brown, M., 2019. Divergent behaviour of Th and U during anatexis: Implications for the thermal evolution of orogenic crust. Journal of Metamorphic Geology. 37, 899 916.

Yakymchuk, C., Clark, C., White, R.W., 2017. Phase relations, reaction sequences and petrochronology. Reviews in Mineralogy and Geochemistry 83, 13 53.

Yakymchuk, C., Kirkland, C.L., Clark, C., 2018. Th/U ratios in metamorphic zircon. Journal of Metamorphic Geology 36, 715 737.

Appendix A1

Additional publications by the author:

Williams, M. A., Kelsey, D. E., Hand, M., Raimondo, T., Morrissey, L. J., Tucker, N. M., & Dutch, R. A. (2018). Further evidence for two metamorphic events in the Mawson Continent. *Antarctic Science*, **30**(1), 44 65.

Alessio, K. L., Hand, M., Kelsey, D. E., **Williams, M. A.**, Morrissey, L. J., & Barovich, K. (2018). Conservation of deep crustal heat production. *Geology*, **46**(4), 335 338.

Williams, M. A., Kelsey, D. E., Hand, M., Raimondo, T., Morrissey, L. J., Tucker, N. M., & Dutch, R. A. (2018). Further evidence for two metamorphic events in the Mawson Continent. *Antarctic Science*, **30**(1), 44 65. doi.org/10.1017/S0954102017000451

LIBRARY NOTE:

The following article (pages 145-166) has been removed due to copyright.

Williams, M. A., Kelsey, D. E., Hand, M., Raimondo, T., Morrissey, L. J., Tucker, N. M., & Dutch, R. A. (2018). Further evidence for two metamorphic events in the Mawson Continent. Antarctic Science, 30(1), 44 65.

It is available online to authorised users at: doi.org/10.1017/S0954102017000451

Alessio, K. L., Hand, M., Kelsey, D. E., **Williams, M. A.**, Morrissey, L. J., & Barovich, K. (2018). Conservation of deep crustal heat production. *Geology*, **46**(4), 335 338. doi.org/10.1130/G39970.1

LIBRARY NOTE:

The following article (pages 168-171) has been removed due to copyright.

Alessio, K. L., Hand, M., Kelsey, D. E., Williams, M. A., Morrissey, L. J., & Barovich, K. (2018). Conservation of deep crustal heat production. Geology, 46(4), 335-338.

It is available online to authorised users at:
doi.org/10.1130/G39970.1

Appendix A2

Additional data for Mt Stafford samples

ADDITIONAL DATA FOR MT STAFFORD SAMPLES

Additional data files for Mt Stafford (STF) samples are provided as electronic appendices as follows:

A2.1 STF EPMA data (raw)

A2.2 STF silicate laser traces

A2.3 STF monazite laser (raw)

A2.4 STF geochronology

A2.5 STF monazite EPMA maps

A2.6 STF monazite MLA maps

A2.7 STF apatite MLA maps

Appendix A3

Additional data for Ivrea–Verbano Zone samples

ADDITIONAL DATA FOR IVREA–VERBANO ZONE SAMPLES

Additional data files for Ivrea–Verbano Zone (IVZ) samples are provided as electronic appendices as follows:

A3.1 IVZ EPMA data (raw)

A3.2 IVZ silicate laser traces

A3.3 IVZ monazite EPMA maps

A3.4 IVZ monazite MLA maps

A2.5 IVZ apatite MLA maps